

Cage-like Proteins as Bioink Components for 3D Bioprinting

by

Adrian Delgado

A thesis

presented to the University of Waterloo

in fulfillment of the

thesis requirement for the degree of

Master of Science

in

Chemistry (Nanotechnology)

Waterloo, Ontario, Canada, 2018

© Adrian Delgado, 2018

AUTHOR'S DECLARATION

I hereby declare that I am the sole author of this thesis. This is a true copy of the thesis, including any required final revisions, as accepted by my examiners.

I understand that my thesis may be made electronically available to the public.

Abstract

Hydrogel matrices have been used as structural surrogates in 3D bioprinting as a mechanism to provide the appropriate environment for cell adhesion and proliferation. In this research, the preparation and optimization of a hydrogel bioink containing a cage protein was investigated; specifically a Horse Spleen Ferritin (HSF)-poly (ethyleneglycol) diacrylate (PEGDA)-based bioink was developed. Studies were also undertaken to optimize the formulation of these bioinks for use in 3D bioprinting strategies, to develop techniques to precisely deposit cage proteins in hydrogels while maintaining their quaternary protein structures. In addition, the rheological properties of these various bioinks were evaluated. Finally, an optimized set of hydrogels was studied with respect to their effects on the growth of *E. coli* expressing a green fluorescent protein variant (His-tag GFP-S65T). Confocal microscopy experiments employed the presence of the bacterially expressed GFP fluorescence to follow bacterial cell migration in bioprinted and casted hydrogel constructs. Evaluation of cell viability within these constructs was also determined. Results indicated that the system had good potential for fabricating hydrogel scaffolds with high accuracy, fidelity and resolution.

Acknowledgements

I would like to state my full appreciation to the Government of Costa Rica, especially to the PINN program hosted by the Science, Technology and Telecommunications Ministry (MICIT), which sponsored my whole education abroad aiming to provide better quality professionals for Costa Rica. Furthermore, I would like to express, to the greatest extent, my gratitude and appreciation to Dr. John Honek who took me from Costa Rica and guided me through this process of becoming a better researcher.

Special thanks to my committee members Dr. Mario Gauthier and Dr. Shirley Tang, who gave me advice and guidance when it came to understand how to build a bioink system. Likewise, I definitely need to give my most candid thanks to Dr. Richard Smith and Ms. Val Goodfellow, who always helped me to understand the nuisances of mass spectrometry, and other techniques that I needed to master during my stay at the University of Waterloo.

I would not be graduating without the help of so many individuals who took me under their wing and provided professional, emotional or academic support. I would like to say that without my family, close friends and lab co-workers this experience would have not been as exciting as it was.

Pura Vida!

Table of Contents

List of Figures	ix
List of Tables	xvi
List of Abbreviations	xviii
Chapter 1 . Introduction	1
1.1 Cage proteins	1
1.1.1 Virus-like proteins.....	3
1.1.2 Ferritins	6
1.1.3 Chaperonins.....	15
1.2 Bioconjugation of proteins	17
1.3 Ferritin polymer-protein conjugates	26
1.3.1 Ferritin polymer-protein conjugates by “Grafting-to”	28
1.3.2 Ferritin polymer-protein conjugates by “Grafting-from”.....	30
1.3.3 Ferritin polymer-protein conjugates by “Grafting-through”.....	31
1.4 Protein-polymer conjugates for PEGDA-based hydrogels.....	32
1.4.1 PEGDA	33
1.4.2 Thickening Agents (TA).....	34
1.5 3D molecular bioprinting.....	36
1.5.1 3D bioprinting.....	37
1.6 Summary and research objectives	52
Chapter 2 Protein Scaffold Engineering	55
2.1 Introduction	55

2.2 Modification of HSF at the ϵ -amine of lysine residues	57
2.3 Materials and methods	58
2.3.1 Materials	58
2.3.2 Instrumentation	59
2.3.3 Methods	62
2.4 Results and Discussion	69
2.4.1 Bioconjugation Effects.....	69
2.4.2 Temperature effect.....	79
2.4.3 Verification of vinylic moieties on HSF quaternary structure	86
2.5 Conclusions.....	89
Chapter 3 Rheological properties of polysaccharide-polymer blends	90
3.1 Introduction	90
3.2 Materials and Methods	92
3.2.1 Materials	92
3.2.2 Instrumentation	92
3.2.3 Methods	94
3.3 Results and discussion.....	103
3.3.1 Linear dynamic viscoelastic properties.....	103
3.3.2 Bioprinting Fidelity.....	119
3.4 Conclusions.....	124
Chapter 4 Bioprinting of bacterial cells on aHSF-based PEG hydrogels	125
4.1 Introduction	125

4.1.1 Bacterial cell bioprinting	126
4.1.2 Hydrogel scaffold properties	128
4.2 Materials and methods	133
4.2.1 Materials	133
4.2.2 Instrumentation	134
4.2.3 Methods	135
4.3 Results and Discussion	145
4.3.1 aHSF Hydrogel Properties	145
4.3.2 <i>E. coli</i> growth on aHSF hydrogel networks	163
4.4 Conclusions.....	179
Chapter 5 Future directions	180
5.1 Introduction	180
5.1.1 Evaluation of modified polysaccharides for three-dimensional network generation.....	181
5.1.2 Variation of the polymer-protein conjugate approach.....	183
Letters of Copyright Permissions.....	185
Bibliography.....	196
Appendix	222
Appendix A. Rheology Theory	223
Appendix B. Iron determination of ferritin hydrogels	229
Appendix C. Bioprinting Conditions.....	233
Appendix D. ANOVA for k and n determinations.....	235

Appendix E. ANOVA for detailed declustering studies.....	239
Appendix F. Iron diffusion from PEGDA-Based hydrogels.....	243
Appendix G. Swelling Capacity of Hydrogels determined by TGA.	245
Appendix I. ImageJ Code to analyze porosity SEM images.....	246
Appendix J. ImageJ Code to analyze confocal images.....	250

List of Figures

- Figure 1. Depiction of CLP of different sizes. A) CCMV b) HSF c) DNA binding protein from starved cells (DPS). PDB: 1CWP, 2W0O, and 1DPS structure files were utilized for protein structure display. 2
- Figure 2. Cryo-electron micrograph reconstructions of several representative spherical viruses (T values between 3 and 25). Reproduced with permission from Johnson *et al.* ¹² 4
- Figure 3. Ribbon diagram showing the tertiary structure of the CCMV. Reproduced with permission from Speir *et al.*¹⁴ 6
- Figure 4. The tertiary structure of recombinant horse L HSF subunit, PDB 2v2i, and shown are four α -helices forming a bundle and a short C-terminal α -helix. Reproduced with permission from Crichton *et al.* ¹⁸ 9
- Figure 5. Depiction of the: (A) 4-fold and (B) 3-fold channels of human ferritin with the key amino acids that allow Fe(II) intake. Adapted with permission from Bou-Abdallah *et al.* Copyright 2017 American Chemical Society.²⁵ 11
- Figure 6. Schematic view of the di-iron ferroxidase centre on the four-helix of the H-chain Human Ferritin. Adapted with permission from Bou-Abdallah *et al.* Copyright 2017 American Chemical Society.²⁵ 13
- Figure 7. Structure of the GroEL–GroES–ADP₇ complex. (a) Representation of the complex. (b) Representation of a cross-section of the complex. Reproduced with permission from Lund *et al.* ⁴¹ 16

Figure 8. Average pKa value and abundance of bioconjugate groups on RNase A (PDB ID: 2QCA). Reproduced with permission from Rosen <i>et al.</i> ⁵⁴	19
Figure 9. Modification reactions for the bioconjugation of amino acids. (a) N-terminus of Lysines: NHS ester conjugation. (b) Cysteines: thiol–maleimide or halogen-substituted acetamide coupling. (c) Glutamic and aspartic acid: EDC/NHS coupling. (d) Tyrosine: oxidative coupling of a phenylenediamine derivative, or oxidation through a diazonium coupling reaction. (e) Tryptophan and (f) para-Amino-L-phenylalanine: oxidative coupling of a phenylenediamine derivative. (g) Homopropargylglycine and (h) Azidohomoalanine: click chemistry between the alkyne and an azide. Reproduced with permission from Rosen <i>et al.</i> ⁵⁸ . 20	20
Figure 10. Activated ester peptide bond formation. Reproduced with permission from El-Faham <i>et al.</i> ⁶²	22
Figure 11. Scheme for the modification of tyrosine: (a) reaction with diazonium salts, (b) three-component mannich reaction, (c) reaction with preformed imines, and (d) ene-type reaction with diazodicarboxylate reagents. Reproduced with permission under CC license from Boutureira <i>et al.</i> ^{71s}	25
Figure 12. Repeating units of polysaccharides used as thickening agents: A) Xanthan Gum, B) Carboxymethylcellulose, and C) Sodium Alginate. ¹¹⁵	36
Figure 13. Representation of A) stereolithography-based, B) Laser-based, C) Inkjet-based, and D) Extrusion-based bioprinting methodologies.	39
Figure 14. Graphical representation of laser-based bioprinting. Reproduced with permission from Malgorzata <i>et al.</i> ¹²⁸	41

Figure 15. A) Thermal- and B) Piezoelectric-based systems for inkjet bioprinting. Reproduced with permission from Malgorzata <i>et al.</i> ¹²⁸	43
Figure 16. A) pneumatic-, B) mechanical- and C) solenoid-based systems for extrusion-based bioprinting. Reproduced with permission from Malgorzata <i>et al.</i> ¹²⁸ ..	43
Figure 17. Polymer-protein conjugates approaches (1) grafting-to, (2) grafting-from, or (3) grafting-through. Based from Grover <i>et al.</i> ¹⁷⁷	56
Figure 18. Strategy for the synthesis of a ferritin-conjugated monomer	62
Figure 19. X-ray structural diagram of HSF with subunits presented in HSF and the indication of a HSF subunit with all the exposed lysines according to Zhen <i>et al.</i> Reproduced with permission from Zhen <i>et al.</i> ¹⁸⁶	70
Figure 20. Mass spectra from HSaF using ESI mass spectrometry.	75
Figure 21 Acryloylated lysine residue yield employing increasing concentrations of different bioconjugation reagents (NAS, MMA and GMA) where the mass difference is evaluated from the WT-HSF average MW = 20000 Da to the highest frequency point on the weight distribution.....	78
Figure 22. Effect of number of aliquots (~1500 mEq/aliquot) effect of bioconjugation reagent on modified HSF at 4 °C and 23 °C.....	80
Figure 23. DLS determinations of the temperature effect on aggregation on modified HSF by the addition of aliquots of bioconjugation reagent (1500 mEq/aliquot) shown as A) Z-average and B) polydispersity index.	82

Figure 24. TEM studies for the evaluation of quaternary structure preservation as a result of bioconjugation with A) 1500 mEq of NAS, B) 10500 mEq of NAS, C)1500 mEq of MMA, and D) 10500 mEq of MMA.	84
Figure 25. SDS-Page gel with WT-, acryloylated and polymerized ferritins.	85
Figure 26. ATR-FTIR for the evaluation of the presence of vinyl moieties produced by of bioconjugation.	87
Figure 27. ¹ H-NMR evaluation of the presence of vinyl moieties because of bioconjugation with NAS and MMA.	88
Figure 28. BioBots 1 bioprinter used for the studies of the aHSF-PEGDA-TF based bioinks.	93
Figure 29. Synthesis proposed by Majima <i>et al.</i> to yield lithium acyl phosphinate from ethyl (2,4,6-trimethylbenzoyl)phenylphosphinate (P-1). ²¹⁰	95
Figure 30. Schematic of bioprinting models used for testing resolution capabilities of the BioBots 1 bioprinter	102
Figure 31. Log scale plot of the loss modulus as a function of the stress for a) XG and b) CMC at a range of frequencies 0.05-5.00[Hz], the LVR is indicated here. .	106
Figure 32. Log scale plot of the viscosity as a function of the frequency of the TA.	109
Figure 33. Dependency of Power Law model constants on thickening agent concentration.....	113
Figure 34. Evaluation of the viscoelastic properties G' and G'' for A) xanthan gum, B) alginate, C) Pluronic F127 and D) carboxymethylcellulose.....	118

Figure 35. Images of A) top view and B) side view used to analyze the bioprinting fidelity of a 12% PEGDA and 4% XG gel using ImageJ.	121
Figure 36. Designed nine plate well to guarantee gels with 12 mm wide, 12 mm long and 2 mm thick using the blender 2.76 program.	138
Figure 37. Thermo-gravimetric profile of PEGDA M_n 700 variation in aHSF-PEGDA hydrogels prepared with different TA.....	147
Figure 38. Protein concentration effect on aHSF-based hydrogels.	148
Figure 39. Swelling of PEGDA Based Hydrogels by TA (Appendix G).....	150
Figure 40. HSF concentration dependency on Fe^{2+} diffusion of aHSF PEGDA-based hydrogel networks	152
Figure 41. PEGDA concentration dependency on Fe^{2+} diffusion from HSF bioconjugated PEGDA-Based hydrogels for A) CMC, B) XG, C) ALG and D)NTA (Data shown in Appendix F).	154
Figure 42. Coarse-declustering profiles of bioconjugated HSF in PEGDA networks for denaturing conditions.	156
Figure 43. Detailed-declustering profiles of bioconjugated HSF in PEGDA networks. .	158
Figure 44. SEM image of a 20% PEGDA-aHSF hydrogel (400- μ m image recorded in ESEM mode, high vacuum, 30 kV).....	159
Figure 45. Images for A) 100 μ m image recorded in ESEM mode, low vacuum and 30 kV, and B) Negative threshold pore identification by the ImageJ software for porosity determination.	160

Figure 46. Pore size dependency of HSF-PEGDA based hydrogels on the presence of thickening agent.	162
Figure 47. Qualitative assessment of GFP- <i>E. coli</i> growth on 124.0 μm cross section of aHSF-8% PEGDA-Based hydrogel construct.....	164
Figure 48. Evaluation of the effects of PEGDA concentration on cell density of a 1.25×10^5 cells cm^{-3} hydrogels construct immersed in LB with 0.5 mM of IPTG for 96 hours.	167
Figure 49. Evaluation of the effects on cell density (2.4×10^4 , 1.25×10^5 , and 2.5×10^5 cells cm^{-3}) for 8 % PEGDA hydrogels immersed in A) LB with 0 mM of IPTG and B) LB with 0.5 mM of IPTG.	169
Figure 50. Time dependency for mean intensity versus cell colonies count for PEGDA hydrogels (Red: without protein and Blue: with protein) immersed in A) LB with 0 mM of IPTG and B) LB with 0.5 mM of IPTG.....	171
Figure 51. Time dependency for mean volume for PEGDA hydrogels (Red: without protein and Blue: with protein) immersed in A) LB with 0 mM of IPTG and B) LB with 0.5 mM of IPTG.	172
Figure 52. Time dependency of the cell growth inside A) Carboxymethylcellulose 10%, B) Xanthan Gum 4% and C) Alginate 7% hydrogel constructs with and without aHSF.	175
Figure 53. Spheroid volume change over time inside A) Carboxymethylcellulose 10%, B) Xanthan Gum 4% and C) Alginate 7% hydrogel constructs with and without aHSF.	178

Figure 54. Diagram of an aHSF-based hydrogel with controlled aHSF concentration.	184
Figure 55. Particle motion profile for shear and extensional flow. ²⁸³	223
Figure 56. Viscosity as a function of shear rate for time dependent and time independent non-Newtonian fluids.	225
Figure 57. Absorption sweep for the determination of the wavelength of maximum absorption of the Iron-Phenanthroline complex.	231
Figure 58. Iron absorbance determination at 510 nm for the Fe ²⁺ -O-phenanthroline complex.	232

List of Tables

Table 1. Accepted mechanisms of iron (II) oxidation.....	14
Table 2. Properties of ferritin mineral cores from some species.....	15
Table 3. Summary of the different bioprinting methodologies	45
Table 4. Summary of some properties of hydrogels with references on their use for bioprinting.....	50
Table 5. Preliminary evaluation of bioink printability at different pneumatic pressures..	97
Table 6. Composition of the initially tested bioinks for rheological studies	98
Table 7. Settings for the Bohlin Rheometer to measure the respective bioink's LVR....	99
Table 8. Frequency range and Maximum Stress Values for Oscillation Experiments .	100
Table 9. One Way ANOVA results for the variation of the linear regression for consistency as a function of TA percentage over a range of PEGDA concentrations....	112
Table 10. Power law model values for the determination of the viscosity as a function of shear stress.....	115
Table 11.Length measurements for bioprinted features	122
Table 12.Height Measurements for bioprinted Features	122
Table 13. Stock formulations for the hydrogel constructs to be analyzed.....	136
Table 14. Prepared HSF-based hydrogels for swelling studies.....	138
Table 15. Calibration curve for the iron determination in ferritin based hydrogel.....	230
Table 16. Statistical results of linear regression for the iron absorbance determination at 510 nm for the Fe ²⁺ -O-Phenanthroline complex.....	232

List of Abbreviations

Acronym	Description
AfFtn	<i>A. Fulgidus</i> ferritin
aHSF	Acryloylated HSF
AI	Arabinose isomerase
Alg	Sodium alginate
AM	Additive manufacturing
ANOVA	Analysis of variance
APS	Ammonium persulphate
ATRP	Atom transfer radical polymerization
Bfr	Bacterioferritin
BSA	Bovine serum albumin
BSED	Backscattered electron detection
CAD	Computer-aided design
CCMV	Cowpea chlorotic mottle virus
CLP	Cage-like proteins
CMC	Sodium carboxymethylcellulose
CTA	Chain transfer agent
dECM	Decellularized extracellular matrices
DLS	Dynamic light scattering

Acronym	Description
DMF	Dimethylformamide
DMIAAm	2-(Dimethyl maleinimido)-N-ethyl acrylamide
DMSO	Dimethyl sulfoxide
DoD	Drop-on-demand
Dps	DNA-binding protein from starved cells
ECM	Extracellular matrix
ESED	Environmental secondary electron detector
ESEM	Environmental scanning electron microscope
f	Frequency
FRP	Free radical polymerization
FTIR	Fourier-transform infrared spectroscopy
G''	Loss modulus
G'	Storage modulus
GMA	Glycidyl methacrylate
GSED	Gaseous secondary electron detectors
¹H-NMR	Proton nuclear magnetic resonance
HEPES	4-(2-Hydroxyethyl)-1-piperazineethanesulfonic acid
HSaF	Horse spleen apoferritin
HSF	Horse spleen ferritin
HSP	Heat shock protein

Acronym	Description
IPN	Interpenetrating networks
k	Consistency
LAP	Lithium acyl phosphinate
LB	Luria-Bertani
LIFT	Laser-induced forward transfer
MALDI	Matrix assisted laser desorption ionization
MEK	2-Butanone
MMA	Methacrylic acid N-hydroxysuccinimide ester
MOPS	3-(N-Morpholino)propanesulfonic acid
MPC	Methacryloyloxyethyl phosphorylcholine
MPL	Multi-photon lithography
MsDps1	DPS protein from <i>Mycobacterium smegmatis</i>
MWCNT	Multi-walled carbon nanotubes
n	Power law index
NAA	Natural amino acids
NAS	N-Acrylosuccinimide ester
NHS	N-Hydroxysuccinimides
NHS esters	N-Hydroxysuccinimide esters
NMP	Nitroxide-mediated polymerization
NNAA	Non-natural amino acids

Acronym	Description
PBS	Phosphate buffered saline
PEG	Poly (ethyleneglycol)
PEGDA	Poly (ethyleneglycol) diacrylate
PEG-DAA	PEG diacrylamide
PEGDMA	Poly (ethyleneglycol) methacrylate
PETA	Pentaerythritol triacrylate
PL	Pluronic F127
PNIPAAm	Poly(N-isopropyl acrylamide)
PVA	Poly (vinyl alcohol)
RAFT	Reversible addition–fragmentation chain transfer polymerization
RC	Regenerated cellulose
RDRP	Reversible-deactivation radical polymerization
RH	Hydrodynamic radius
SEC	Size-exclusion chromatography
SEM	Scanning electron microscopy
TA	Thickening agents
tan δ	Mechanical loss angle
TEM	Transmission electron microscopy
TFP	Tetrafluorophenol esters
TGA	Thermo gravimetric analysis

Acronym	Description
TMEDA	N,N,N',N'-Tetramethylethylenediamine
VLP	Virus-like proteins
XG	Xanthan gum
XI	Xylose isomerase

Chapter 1. Introduction

1.1 Cage proteins

The frequency at which nanotechnology has turned to biological systems in the search for an adequate template for reactions has risen over the last few years. Additionally, supramolecular chemistry has prioritized the development of systems that can render specific architectures, which can be assembled or disassembled systematically in response to changes in the biochemical environment.¹ Therefore, scientists have used hierarchical structures such as cage-like proteins (CLP) to satisfy these needs. These are self-assembled hollow protein spheres that are usually between 10-100 nm in diameter, which are structurally comprised of an assembly of a limited number of subunits to form robust nanostructures.¹ They can be genetically engineered, resulting in alteration of their amino acid sequence and the ability to place certain amino acid residues in well-defined three-dimensional space.² Considering that CLP's offer distinct attributes such as enhanced physicochemical stability, periodic and monodispersed size ranges, capability of bioconjugation with other molecules on either their inner or outer surfaces, enhanced biological recognition and most importantly, well-defined assembly-disassembly pathways, it can be concluded that they are ideal structures to be used as constrained reaction vessels with biological recognition capabilities.^{3,4,5}

Their symmetries usually have been used to classify CLP's. For instance, 12-mers and 24-mers can assemble themselves into tetrahedral and octahedral symmetries,

respectively, whereas 60-mers or multiples of the latter tend to self-assemble into icosahedral symmetries.⁶ Robust CLP's can range from virus-like, ferritin-like, and chaperonin proteins and have been employed as templates to render functional biomaterials.⁴ Further examples of these CLP are the icosahedral, tetrahedral, or octahedral symmetric proteins such as cowpea chlorotic mottle virus (CCMV), horse spleen ferritin (HSF), and heat shock protein (HSP), respectively (Figure 1).¹

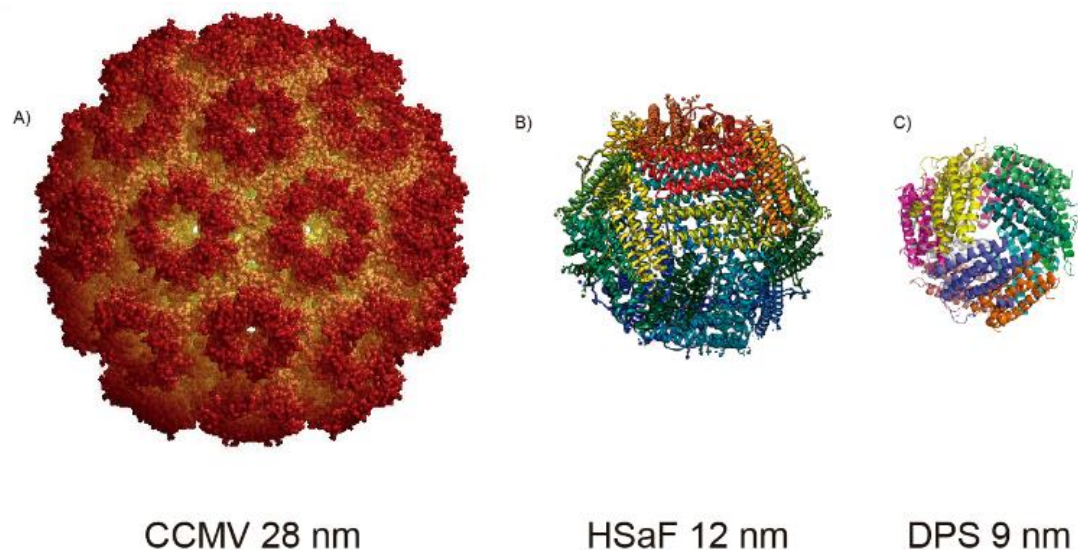


Figure 1. Depiction of CLP of different sizes. A) CCMV b) HSF c) DNA binding protein from starved cells (DPS). PDB: 1CWP, 2W0O, and 1DPS structure files were utilized for protein structure display.

Over time, these, and many other proteins have been utilized as size-constrained reaction vessels or platforms to be chemically or physically modified at precisely known locations in order to generate libraries of protein cage architectures available for scientists.⁵ An understanding of the advantages provided by CLP's is of primary

importance, because it enables one to correctly choose the appropriate building blocks or pathways for self-assembly of a desired CLP. ⁷

1.1.1 Virus-like proteins

Since their discovery virus-like proteins (VLP), derived from icosahedral viruses, have been studied for theoretical considerations on the principles of how these biomolecules aggregate.⁸ Furthermore, VLPs find applications outside their natural environment when they are devoid of their nucleic acid. This can be achieved via natural routes using recombinant DNA technology, to produce a non-infectious VLP, taking advantage of the biocompatibility of a multimeric ensemble to reduce the inherent toxicity.⁹ Many VLPs are of paramount importance because they have an increased ability to hold cargo, resist harsh conditions needed for inner or outer bioconjugation, have increased biocompatibility and in-vivo targeting and stability characteristics.⁹ Additional support has been given to VLPs because they have the potential to act as the protein shell for size- and shape-constrained reaction vessels, which can be used for chemical synthesis and catalysis (Figure 2).¹⁰ However, this is not the only type of use that they can be given. Numerous reports state that VLPs could be used as molecular containers, reaction vessels, nano templates and as synthetic platforms for nanoparticles.¹¹ Hence the potential applications of these biomolecular vessels are of interest.⁹

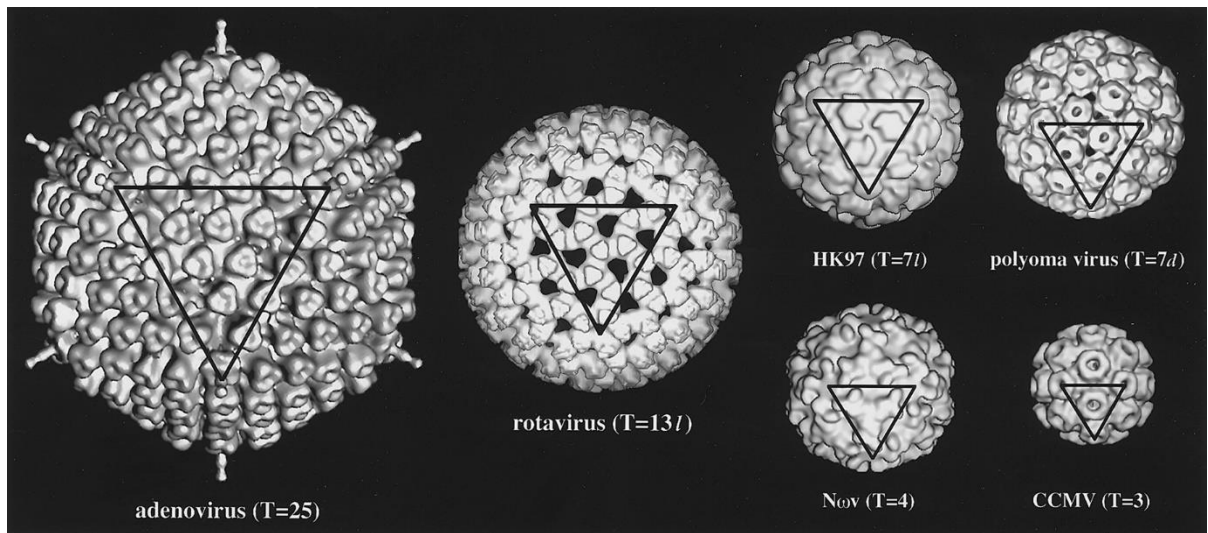


Figure 2. Cryo-electron micrograph reconstructions of several representative spherical viruses (T values between 3 and 25). Reproduced with permission from Johnson *et al.*¹²

It has been known for many years that VLPs are multimeric self-assembly-capable proteins that undergo dynamic structural transitions induced by defined chemical triggers, to provide unique gating mechanisms and control of the load-unload pathways of entrapped materials.¹⁰ Furthermore, VLPs can be assembled or disassembled from wild-type or mutant subunits under *in vitro* conditions.¹² However, it is of crucial importance to choose the best expression system for the desired VLP. It is vital to also consider the requirements for proper folding of the protein subunits and their possible requirement for post-translational modifications. Fuenmayor *et al.* presented a comprehensive review of the advantages and disadvantages of the different VLP production platforms, where the term “chimeric VLPs” is introduced to describe a hierarchical complex VLP that is composed of two different VLP.¹³

For example, examination of the structure of the CCMV capsid was carried out using x-ray crystallography and cryo-electron microscopy, which it revealed that the capsid was tied together via a carboxy-terminal extension of the subunit, residues 27 to 35, and a hydrophobic intracapsomere contact amongst dimers resulting in a stable and modular arrangement of subunits.⁷ The CCMV's outer diameter is 28 nm, with an inner diameter of 18 nm and is composed of an assembly of 180 identical subunits (19800 Da;190 amino acids) which, as previously mentioned, renders an icosahedral lattice upon self-assembly.¹¹ The virus subunit adopts a canonical virus β -barrel fold (Figure 3). Structurally, it has been reported by Johnson *et al.* that CCMV could have polymorphism, on which the structure can interchange between quasi-equivalent structures, where it has the potential to interchange between hexamers and pentamers in the presence of Ca^{2+} ions.¹² Furthermore, CCMV possesses a desirable feature: It undergoes irreversible pH-dependent swelling, which results in almost a 10% increase in its natural volume.¹⁰

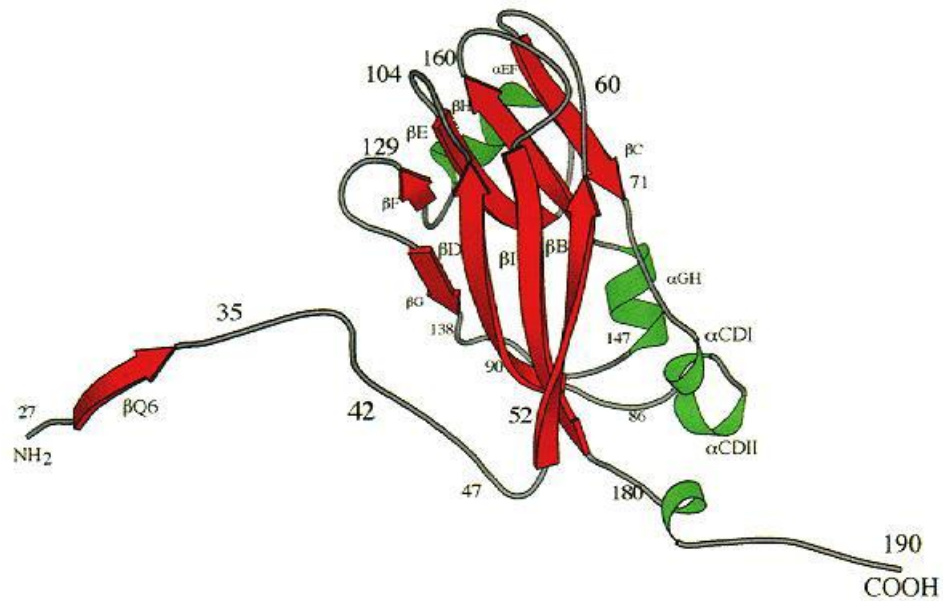


Figure 3. Ribbon diagram showing the tertiary structure of the CCMV. Reproduced with permission from Speir *et al.*¹⁴

The applications of VLPs are quite varied, for example: In the field of medicine, VLPs are devoid of any nucleic acid to produce vaccines that represent no danger of accidental infection for diseases such as hepatitis B, malaria, HPV, influenza virus A, HIV, human parvovirus and others.¹³

1.1.2 Ferritins

Iron is a ubiquitous and essential element for life that is involved in major biological functions, most of them crucial for organisms, such as DNA synthesis, nitrogen reduction, oxygen transport as found in hemoglobin, and redox reactions. The term “ferritins” was first used in 1937 by Laufberger to describe a family of iron-containing proteins.¹⁵ Ferritins are located, for the most part, inside cells, and their structure is highly preserved and

consists of an Fe^{3+} -storage cavity surrounded by a protein capsid which mediates biological Fe^{2+} transport processes into the cavity with oxidative precipitation of iron(III) oxide. These storage proteins are present in almost all life forms such as eubacteria, archaea and eukaryotes.¹⁶ Interestingly, because they can come from different sources, there is structural variation among them. Examples of members of the ferritin superfamily are human heart ferritin, HSF, bacterioferritin (Bfr), DNA-binding protein from starved cells (DPS) and archaeoferritin, among others.¹⁷

1.1.2.1 Ferritin Structure

The basic building block from the ferritin family is the ferritin subunit, about 50 Å long and 25 Å wide, which may vary in size depending on the source of the subunit.¹⁸ Furthermore, as shown on Figure 4, it is composed of a four-helix bundle with a C-terminal extension which lies at a 60° angle roughly perpendicular to that of the central axis of the four-helix bundle.¹⁹ Ferritins, for the most part, are hollow tetra-helical ensembles.²⁰ In general, ferritins have 12-13 nm outer diameters, 7-8 nm inner diameters and molecular weights of approximately 450 kDa.²¹ However, there are different sized ferritins. First, 24-subunit ferritins are present in plant and animal tissues. However, 12-subunit ferritins also exist and it is believed that their role is to protect DNA from oxidative damage.²² This difference between the two types of ferritin involve a change from a structure containing twenty-four, α -bundle subunits arranged in a 4-3-2 symmetry stable cage-like structure that can hold up 4000 ferric atoms in an inorganic ferric oxide-phosphate complex;²² to a twelve, α -bundle subunits in a 4-3-2 symmetry stable cage-like structure that can hold up

500 ferric atoms.¹³ Therefore, HSF and Bfr are termed Maxi-Ferritin, that is they possess a 24-subunit structure whereas DPS are termed a Mini-ferritin due to its 12-subunit structure.²³

It is also worthy to note that some ferritins can be composed of different subunits, and this is dependent on the particular tissue it is isolated from. For example, the mammalian ferritin cage may have two distinct types of subunits, which mainly differ in their amino acid sequences. First, there is the heavy ferritin chain subunit (H-chain) which is more predominant in the mammalian heart, and its main characteristic is the presence of a di-iron ferroxidase centre, which oxidizes cellular iron from Fe^{2+} to Fe^{3+} . Secondly, there is the light ferritin chain subunit (L-chain), which is found predominantly in mammalian livers and is mainly involved in iron core nucleation processes.¹⁸ The H-chain (21 kDa) and the L-chain (19 kDa) lengths are 182 and 175 amino acids respectively, being 90% and 85% identical to human ferritin, respectively.²⁴ Going further away from mammalian ferritins, less similarity is found amongst the subunits. Such is the example of the bacterioferritins, being only 22-24% identical to H-chain and 18-21% identical to L-chains of mammals.²¹ Due to the multiple differences in the ferritin sequences, it is unlikely that ferritin subunits in mammals form homopolymeric structures. This results in a large number of isoferritins, that is composite ferritins, existing.¹⁵ To be more precise, some isoferritins may present the following combinations of H- and L-chain subunits: human placenta (~ 20% H, 80% L), human spleen (~ 10% H, 90% L), human liver (~ 50% H and , 50% L), horse spleen (~ 8% H, 92% L), and rat liver (~ 35% H, 65% L).²⁵

As well, the most substantial difference between ferritins and bacterioferritins is the presence of 12 heme moieties which are present in the bacterioferritins.²³

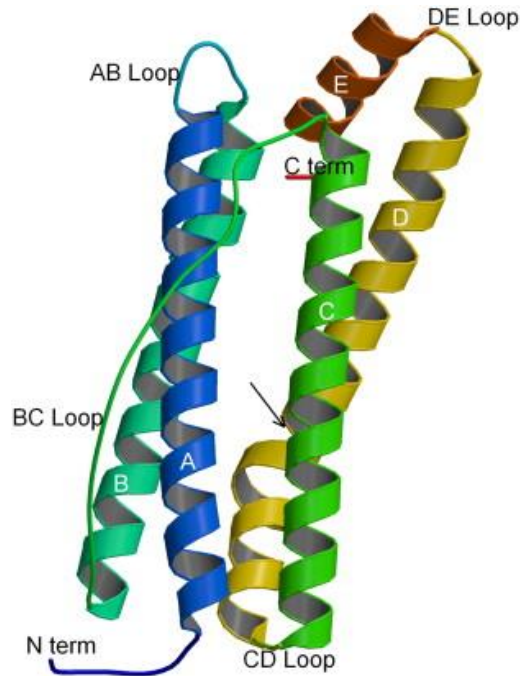
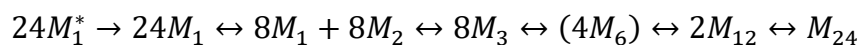


Figure 4. The tertiary structure of recombinant horse L HSF subunit, PDB 2v2i, and shown are four α -helices forming a bundle and a short C-terminal α -helix. Reproduced with permission from Crichton *et al.* ¹⁸

1.1.2.2 Ferritin cage assembly

The ferritin cage is a structure that undergoes self-assembly. However, understanding how the formation of the supramolecular complex occurs facilitates mechanistic insight. Gerl *et al.* reported the mechanism of how HSaF assembles using intrinsic fluorescence, far-UV circular dichroism and glutaraldehyde cross-linking experiments. The overall proposed scheme takes into consideration the steps of how the protomers assemble themselves to render the cage-like protein.²³



The process starts with 24 unfolded ferritin subunits ($24M_1^*$) that fold themselves into the appropriate conformation, to then associate into eight monomers ($8M_1$) and eight dimers ($8M_2$). The next step is the formation of trimeric protomer ($8M_3$) followed by the formation of four hexamers ($4M_6$). The final two steps are the formation of two twelve-mers ($2M_{12}$) to associate on the protein cage (M_{24}) finally. Several studies have been made to understand how the cage-like protein assembles. Sato *et al.* reported a time-resolved small angle x-ray scattering study for *E. coli* ferritin A to verify what Gerl *et al.* reported, with the main difference that they were unable to discard the presence of 8-, 10-, or 14-mers during the process of the formation of the cage-like protein. Their findings showed that the ferritin could dissociate and associate reversibly with no large aggregates being formed during the reassembly reaction.²⁶

In support of the disassembly/reassembly of the protein cage, it is well known that ferritin subunits in aqueous solutions are stable between pH 3-10 due to strong hydrogen bonding interactions at the intra- and inter-subunit contacts, as well as through hydrophobic interactions. In dilute salt buffers another interaction contributes, namely a salt bridge between K59 and E104, which is believed to further enhance quaternary structure stability.²⁷ Ferritin oligomers further undergo a well-known dissociation process at pH below 3 and pH above 10. Below pH 3, ferritins suffer a stepwise disassembly that is not entirely reversible, causing ferrihydrite core aggregation at pH 2.10, followed by subunit aggregation at pH 0.80. It has been shown that dimers can be found between pH values of 3.4 and 0.8.²⁷ However, further dissociation from dimeric ferritin subunits to

monomers is not possible (e.g. in strong acids or at high salt concentrations). As a result, a solution with a pH below 0.8 results in an inhomogeneous and polydispersed ferritin subunit solution.²⁸ For basic pH values above 10.6, there is irreversible dissociation due to hydrolysis of some of the peptide bonds.²⁹ In conclusion, it is of utmost importance to understand which are the essential elements that facilitate the mechanism of self-assembly and disassembly of the CLP.

1.1.2.3 Iron (II) intake and Iron (III) mineralization

As previously mentioned, the assembled cage-like protein has a 4-fold, 3-fold and 2-fold symmetry axis. The 4-fold axis renders a largely hydrophobic structure.⁴ In contrast, it is known that for higher organisms, hydrophilic residues such as three aspartate and three glutamates mainly compose the 3-fold axis. This trend is not seen for some invertebrate protein sequences, because this 3-fold axis also has some hydrophobic residues which, as a result, inhibit metal binding.²¹

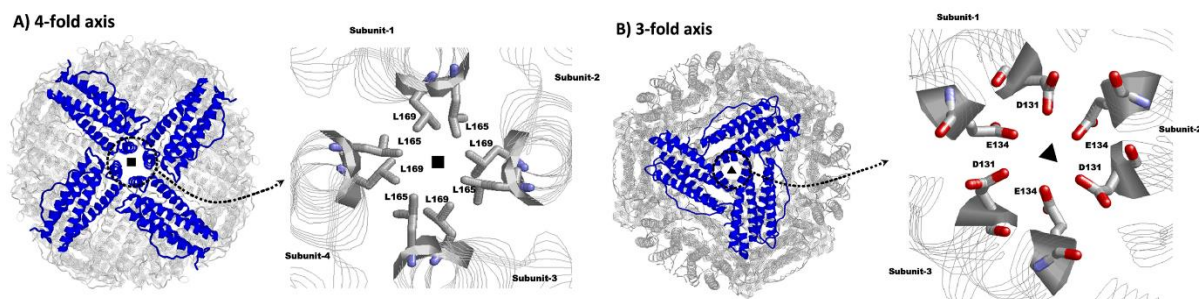


Figure 5. Depiction of the: (A) 4-fold and (B) 3-fold channels of human ferritin with the key amino acids that allow Fe(II) intake. Adapted with permission from Bou-Abdallah *et al.* Copyright 2017 American Chemical Society.²⁵

Therefore, special attention should be given to the 3-fold axis for the mammalian H-chain ferritin subunit. It facilitates a channel that connects the outer with the inner environment, which has been proposed as the main route for iron transport across the protein shell to the site of Fe(II) oxidation.²¹

In the early 1990s, studies conducted by Desideri *et al.* and Stefanini *et al.* concluded that Fe(II) enters the molecule through this threefold axis, and the iron is oxidized inside the cage's hollow cavity.³⁰ To support this statement, several studies attempting substitution of the carboxylate residues by other residues resulted in complete quenching of the iron uptake into the ferritin cage.³¹ Likewise, iron intake has been corroborated by X-ray crystallography studies using Cd²⁺, Zn²⁺, Tb³⁺ or Ca²⁺.³¹ Nevertheless, the intake of iron(II), or other metals, can be quenched by high concentrations of chelators such as phosphate (PO₄³⁻) anions, since there is a binding preference for Fe²⁺ to PO₄³⁻ ions rather than to ferritin cage structures.³² To further understand quenching studies, the interactions of [Cr(N(CH₂CH₂NH₂)₃(H₂O)(OH)]²⁺, a Cr(III) amine complex (Cr(TREN)) and Tb(III) have been studied. It was found that Cr(TREN) inhibits the intake of iron(II) by obstructing the routes of metal uptake. Also, Tb(III) cannot interfere with Cr(TREN) binding, whereas the inverse interaction could occur.³³

As previously mentioned, ferritin cages facilitate iron intake through the 3-fold channel. However, the migration across the shell is the first step of the process for iron storage inside the ferritin cage. Several authors have reported that iron mineralization and iron ferroxidation, the other two key steps for iron storage inside the cage, take place

in the L-type subunits and at the ferroxidase centre of the H-type subunits, respectively.^{30,34,35} The steps of iron uptake, oxidation and core formation have been studied to understand the process of migration of the iron through the protein shell of several ferritins over time using specialized techniques such as time-resolved fluorescence,³⁶ Fe Mössbauer spectroscopy,³¹ diferric transferrin formation spectroscopy,³⁵ spectrophotometric assays, oximetry and elemental analysis,³² among other techniques. The ferroxidase centre, as depicted in Figure 6, is an iron binding and oxidation centre exclusively found within the four-helix bundle of H-type subunits. However, it is not entirely clear how this centre operates.³⁷ Nevertheless, it has been shown that to facilitate the oxidation/mineralization process, a ratio of L-type and H-type subunits must be present, the optimal ratio being 30% H-type and 70% L-Type.²⁵

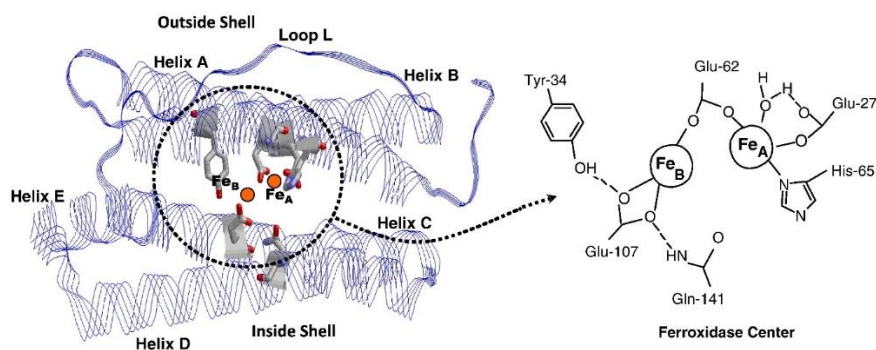


Figure 6. Schematic view of the di-iron ferroxidase centre on the four-helix of the H-chain Human Ferritin. Adapted with permission from Bou-Abdallah *et al.* Copyright 2017 American Chemical Society.²⁵

As a result, three reasonable models have been proposed: a ferroxidation model, a mineralization model, or a combination of both, as shown in **Table 1**.³⁸

Table 1. Accepted mechanisms of iron (II) oxidation

Mechanism	Chemical Reaction
Ferroxidation	$2\text{Fe}^{2+} + \text{O}_2 + 4\text{H}_2\text{O} \rightarrow 2\text{FeOOH}_{\text{core}} + \text{H}_2\text{O}_2 + 4\text{H}^+$
Mineralization	$4\text{Fe}^{2+} + \text{O}_2 + 6\text{H}_2\text{O} \rightarrow 4\text{FeOOH}_{\text{core}} + 8\text{H}^+$
$\text{Fe}^{2+} + \text{H}_2\text{O}_2$ detoxification	$2\text{Fe}^{2+} + \text{H}_2\text{O}_2 + 2\text{H}_2\text{O} \rightarrow 2\text{FeOOH}(\text{core}) + 4\text{H}^+$

*Adapted from Bou-Abdallah *et al.*²⁵

The mechanism that takes place depends on the amount of iron present at specific times and the subunit composition. It has been reported that when a small number (~50 atoms per addition) of iron (II) is present, the ferroxidation mechanism occurs whereby two iron (II) atoms are oxidized per O₂ molecule. On the other hand, when large amounts (~1000 atoms per addition) are added, the dominant mechanism is mineralization, where four iron (II) atoms are oxidized per O₂ molecule. When an intermediate quantity of iron (II) is added, the mechanism that takes over is the Fe²⁺ + H₂O₂ detoxification, where the H₂O₂ produced by the ferroxidase centre oxidizes more Fe(II) by the detoxification reaction.³⁹

The ferritin cage has been proven as an active site for iron mineralization, where it provides a microenvironment that can mineralize ferrihydrite (5Fe₂O₃·9H₂O) cores with large surface to volume ratio, enabling the protein to be used as a nanoreactor.³¹ However, the properties of the ferritin ferrihydrite cores may vary depending on the ferritin source; some examples are shown in Table 2. This behaviour allows the possibility to take advantage of these properties when other nanoparticle mineral cores of ferritin need to be synthesized.

Table 2. Properties of ferritin mineral cores from some species

Ferritin Source	Average no. Fe Atoms	Mean Core Size (nm)	Crystallinity
Horse spleen	2000	-	Good
Bacterium (<i>Pseudomonas aeruginosa</i>)	800	6,0-6,5	Amorphous
Mollusc (<i>Acanthopleura hirtosa</i>)	1500-2500	8,0-8,5	Limited
Pea seed (<i>Pisum sativum</i>)	1800	5,2-6,5	Amorphous

*Data points were taken from Chasteen *et al.*³¹

1.1.3 Chaperonins

The term chaperonin is used to describe a group of CLP that aid protein folding and protein stabilization inside a cell when it has been exposed to environmental or physiological stress.⁴⁰ The first chaperonins reported were the *E. coli* chaperonins GroEL and the co-chaperonin GroES as proteins that facilitate unfolded or partially folded proteins to achieve their fully folded and active state.⁴¹ Their structure is mainly characterized by monomers of 60 kDa subunits of heat shock proteins that oligomerize into arrangements between 800-1000 kDa into two rings placed back to back that are not connected to each other as shown in **Figure 7**.

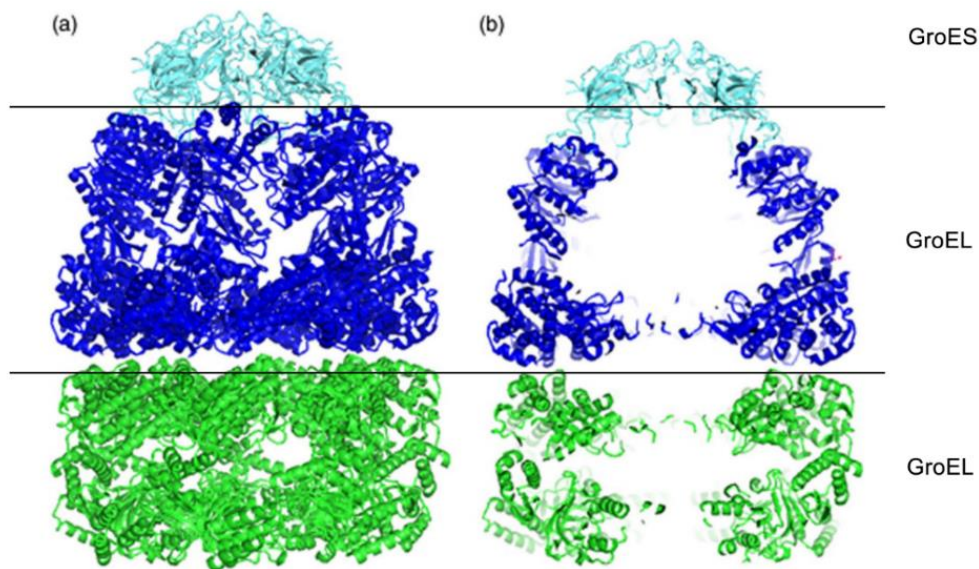


Figure 7. Structure of the GroEL–GroES–ADP₇ complex. (a) Representation of the complex. (b) Representation of a cross-section of the complex. Reproduced with permission from Lund *et al.*⁴¹

Chaperonins have been classified into two groups according to their structure and origin. Group I chaperonins, found in eubacteria, mitochondria and chloroplasts, feature a detachable co-chaperonin as a lid that closes the cavity, whereas group II chaperonins, found in archaeal cytoplasm and eukaryotic cytosol, have proteinaceous lids built into their structure which gates the large pores.⁴² Chaperonins have found applications facilitating the functional expression of heterologous enzymes, where *E. coli* xylose isomerase (XI) and arabinose isomerase (AI) are being coexpressed with bacterial GroE in *Saccharomyces cerevisiae* to overcome the mismatch that occurs when bacterial proteins are overproduced in eukaryotic systems in the absence of HSP60.⁴³ Equally important is that chaperonins have also found an application in the medical field, by

reducing amyloid formation in Alzheimer's disease by recognizing non-native protein molecules and facilitating their refolding.⁴⁴

1.2 Bioconjugation of proteins

The functional and structural properties of proteins make them important scaffolds for medicine as well as materials science. Efficient strategies to covalently attach additional molecules to their surfaces is of importance.⁴⁵ As a consequence, many strategies have been encompassed into a class of reactions addressed as bioconjugation, to introduce new chemical functionalities onto proteins by modifying endogenous amino acid residues through chemical or biochemical reactions, while maintaining functionality and structure.⁴⁶ For instance, it is known that protein assemblies using disulfide bonds, flexible genetic linkers or protein-protein interactions deliver polydispersed materials.⁴⁷ Therefore, bioconjugation has been used to reduce this effect, while exploiting its advantages such as increased availability to synthesize building blocks of advanced complexity, enhanced control over the assembly of the desired product, and accurate control over modularity for a single subunit of the construct.⁴⁷

Complex bioconjugation strategies can be utilized to modify proteins.⁴⁵ An obstacle for bioconjugation is the need to be able to facilitate high selectivity within a complex substrate, such as a protein that contains many different amino acid side chains.⁴⁸ Therefore, to increase the production of the desired protein conjugate several factors need to be accounted for such as the abundance of the targeted endogenous amino acid residues, their surface exposure, and the selectivity of the modification reagent.⁴⁹ As well,

the extent of labeling can be varied by controlling the concentration of the modification reagent; but excess reagent can result not only in over modification of the protein, but also in a reduction in regioselectivity.⁴⁵

1.2.1.1 Bioconjugation techniques

As mentioned previously, multiple chemical reactions have been developed to covalently link synthetic molecules to natural proteins. The design of these reactions has allowed the study of the behaviour of these proteins. The most common approach is to use electrophilic reagents that interact with the nucleophilic amino acid side chains. Hence, peptide residues with a more significant nucleophilic behaviour such as aspartic acid, glutamic acid, lysine, arginine, cysteine, histidine and tyrosine in the unprotonated state are most likely to be modified (Figure 8).⁵⁰

Not only endogenous amino acids are targets for bioconjugation, but positions such as the N-terminus, natural amino acids (NAA) and non-natural amino acids (NNAA) that are exposed on the surface of the proteins also can be conjugated readily.⁵¹ A thorough review of all the available reactions for bioconjugation has been published by deGruyter *et al.*⁵² On the other hand, there is constant development of new bioconjugation and modification reactions, which can be put into play in the bioprinting process and can render materials suitable for a broader range of applications and processing routes that apply to 3D bioprinting.⁵³

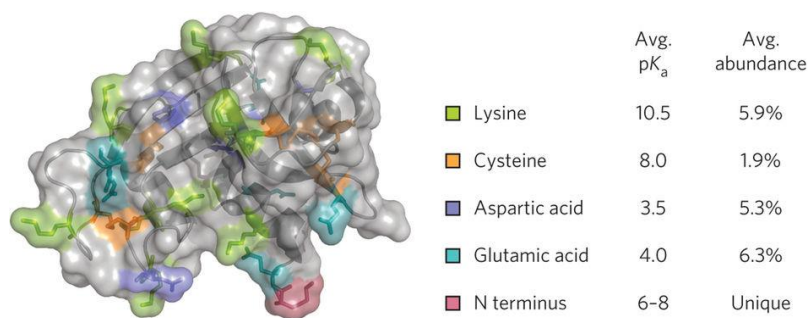


Figure 8. Average pKa value and abundance of bioconjugate groups on RNase A (PDB ID: 2QCA). Reproduced with permission from Rosen *et al.* ⁵⁴

1.2.1.1.1 N-terminus modifications

It has been reported that the N-terminus of a protein can be selectively modified with bioorthogonal functional groups *via* transamination reactions, pH-controlled N-terminal selective acylations or oxidations and reductive alkylations, all of these being very selective and having minimal side reactions.⁵⁵ Factors such as the loss of bioactivity, commercial availability, loss of charge at the N-terminus or the generation of unwanted derivatives, respectively, need to be weighed in to guarantee an adequate bioconjugation level.⁵⁵ More so, the N-terminus is unique for protein chemical modification, being basic but charged at physiological pH.

1.2.1.1.2 Exposed natural amino acid modification

Creating a covalent link between molecules is the most common approach for conjugation; other approaches that bridge molecules without the need of a covalent link, employ affinity-based systems or protein co-factors.⁵⁶ The available sites for modification can be determined by targeted amino acids, protein morphology, the electrostatic

environment, the accessibility of the substrate to the modification site, residue availability, and the pH at which the posttranslational modification is carried out.⁵⁷ An overview of the major conjugation strategies is shown in Figure 9.

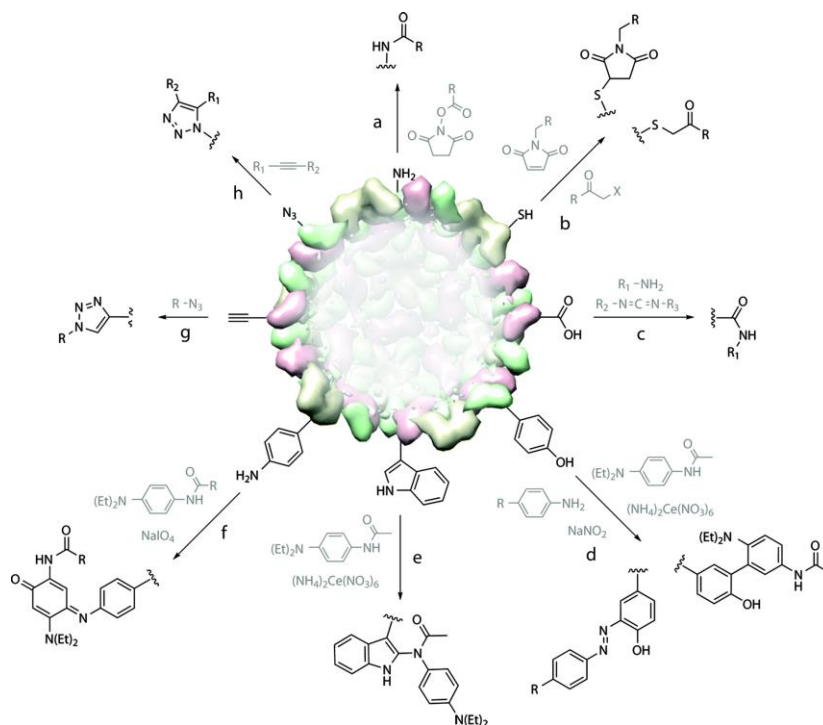


Figure 9. Modification reactions for the bioconjugation of amino acids. (a) N-terminus of Lysines: NHS ester conjugation. (b) Cysteines: thiol–maleimide or halogen-substituted acetamide coupling. (c) Glutamic and aspartic acid: EDC/NHS coupling. (d) Tyrosine: oxidative coupling of a phenylenediamine derivative, or oxidation through a diazonium coupling reaction. (e) Tryptophan and (f) para-Amino-L-phenylalanine: oxidative coupling of a phenylenediamine derivative. (g) Homopropargylglycine and (h) Azidohomoalanine: click chemistry between the alkyne and an azide. Reproduced with permission from Rosen *et al.*⁵⁸

1.2.1.1.2.1 Lysine modification

Primary amino groups are a major target for bioconjugation due to their frequent occurrence on the surface of proteins (up to ~6%), yet the selective modification of a specific lysine side chain can be difficult.⁵⁷ Amino groups can be divided into two groups: the α -amino group, situated at the N-terminus of most polypeptide chains and the ϵ -amino group of a lysine residue, with pKa values of 8 and 10, respectively.⁵⁹ These residues are often involved in vital structural and functional processes, intra-, interdomain, and interprotein interactions such as cation- π , hydrogen bonds, and salt bridges, for which a net charge is essential. Interestingly, available approaches historically used for side chain and amine tagging, such as activated esters (fluorophenyl esters, N-hydroxysuccinimides (NHS), sulfo-NHS, acyl azides), isothiocyanates, isocyanates, aldehydes, anhydrides, sulfonyl chlorides, carbonates, fluorobenzenes, epoxides and imidoesters, eliminate the native charge at the lysine.⁶⁰ Instead, methods that employ reductive alkylation, using an aldehyde or ketone combined with a reducing agent such as sodium borohydride and sodium cyanoborohydride, have been proven to preserve the lysine charge.⁶¹ In general, deprotonated primary amines are one of the most reactive functional groups in proteins (cysteine thiol groups being more reactive), to maintain a deprotonated state; the pH needs to be adjusted in buffers, so that a free amine state is obtained for either α -amino-, ϵ -amino- or both groups. Equally importantly, an adequate amine-selective reagent has to be selected, because it will react with nucleophilic surface residues. Despite selecting the right conditions for the reaction to be carried out, the reaction rates will be affected by depletion of the amine-reactive reagent due to hydrolysis in aqueous solutions.⁵⁹

In terms of available strategies for lysine residue bioconjugation, the most used strategy is the use of activated esters, a strategy developed in 1963 by Anderson *et al.* to generate a peptide bond.⁵² The goal of this approach is to use a compound of intermediate stability that can be an acyl halide, azide or a mixed or symmetric anhydride, as shown in Figure 10, where the intermediate undergoes a process of aminolysis to generate a new peptide bond.⁶²

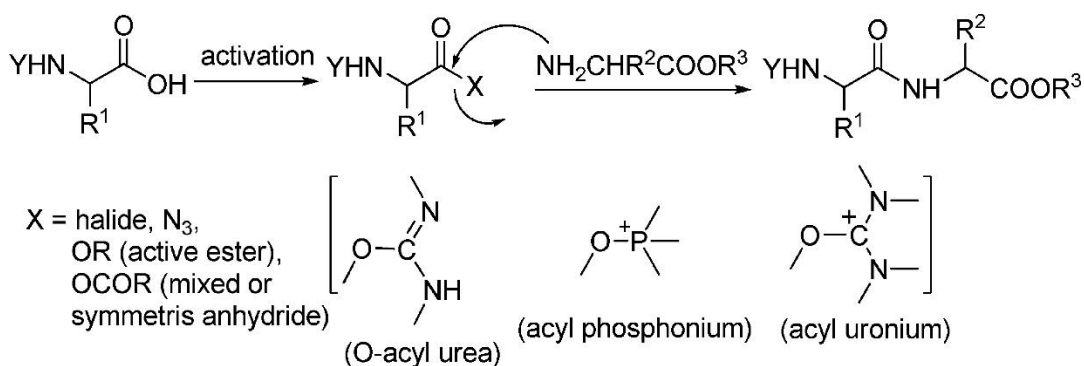


Figure 10. Activated ester peptide bond formation. Reproduced with permission from El-Faham *et al.*⁶²

It has been reported that for activated esters, a high concentration of nucleophilic thiols need to be avoided because they increase the rate of degradation due to the formation of thioesters, which subsequently hydrolyze.⁵⁹ The most frequent types of active esters used have been the ones derived from p-hydroxamic active esters such as o-phthalimido esters or the widely used, water soluble and easy to remove from solution, N-hydroxysuccinimide esters (NHS esters).⁶²

1.2.1.1.2.2 Cysteine modification

Solvent-exposed cysteine residues are easily modified due to the high nucleophilicity of their sulfhydryl side chain, and with high selectivity because of their low abundance in proteins.⁵⁹ Likewise, at pH 9, cysteine residues react faster than lysine due to the higher nucleophilicity of thiols over lysines, resulting in a selective modification of cysteine over lysine residues.⁶³ There are two well-known methods, such as maleimide-thiol Michael additions and activation with halogen-substituted acetylamides.⁵⁸

Generating maleimide-thiol conjugates is one of the most commonly used methods for bioconjugation, on which a thiolate (RS^-) undergoes Michael addition to the double bond of a maleimide to form a succinimidyl thioether. These reactions are desired due to their specificity to thiols, fast aqueous reaction kinetics, lack of byproducts, and the stability of the thioether addition product.⁶⁴ In many cases, in the absence of excess thiols, retro-Michael additions revert the thioether adducts to the starting materials. However, in the presence of an excess of thiol ($\text{R}'\text{S}^-$) new conjugates (RS^-) are permanently substituted by ($\text{R}'\text{S}^-$). This behaviour has been well characterized for antibody-drug conjugates, where the products are required to have a long shelf life.⁶⁵

Interestingly, maleimide reagents are not adequate solutions for applications where high stability and the size of the generated linkage is crucial. Instead, the use of haloacetyl-mediated conjugations are preferred with haloacids such as iodoacetate, bromoacetate, 3-bromopropionate, 2-bromopropionate and 2-bromobutyrate.⁵⁹ It has been reported that with smaller halogens, fewer side reactions are present, such as when

chloroacetamide is used instead of iodoacetamide to reduce adduct formation in the alkylation of cysteine-containing peptides.⁶⁴

1.2.1.1.2.3 Glutamic and aspartic acid Modifications

Carboxylic acids in aqueous solutions exhibit lower reactivity. These functionalities are found on the C-terminus of proteins, or as side chains in glutamic and aspartic acids located internally to the protein sequence.⁵⁹ The modification is carried out in the presence of carbodiimides and primary amines, with the disadvantage of decreased site specificity due to the frequent presence of primary amines on proteins.⁵⁸ Carbodiimides react with a carboxylic acid to generate a reactive species, an O-acylisourea that undergoes aminolysis in the presence of a nucleophilic component, a primary amine. A side reaction in these reactions is the formation of N-acyl urea byproducts, which can be avoided utilizing an excess of hydroxybenzotriazole.⁶³

1.2.1.1.2.4 Tyrosine and tryptophan modifications

In general, tyrosine residues are less frequently occurring protein residues, which can be introduced by site-directed mutagenesis without changing the electrostatic environment or redox sensitivity dramatically.⁶⁶ Interestingly, it has been reported that tyrosine residues are often overrepresented on binding sites of proteins.⁶⁷ For this reason, they can be used as a desirable residue to switch the protein target between its active and inactive states, using procedures such as the reversible addition of phosphate groups.⁶⁸ Even though tyrosine residues are less reactive than aliphatic amines at neutral

pH, the pKa (4.75) difference between amine and phenolic groups can be exploited to allow tyrosine side chains to also react with amine-reactive reagents at lower pH.⁵⁹

Furthermore, the phenolic group of tyrosine provides a distinct reactivity, which can be utilized to modify the side chain *via* a palladium-catalyzed allylic alkylation using an electrophilic π -allyl intermediate in aqueous solution.⁶⁹ Likewise, it can be modified at the *ortho* position using a myriad of reactions such as three-component Mannich reactions, diazonium salts bearing electron-withdrawing para substituents and oxidative coupling reactions using Ni(II), ceric ammonium molybdate ($\text{CeH}_8\text{Mo}_3\text{N}_2\text{O}_{12}$), and $\text{Ru}(\text{bpy})_3$ catalysts (Figure 11).^{66,67,70} Nonetheless, the modifications of tyrosine requires surface exposure and compete with both exposed tryptophan (Trp) residues and reduced disulfides.⁷¹

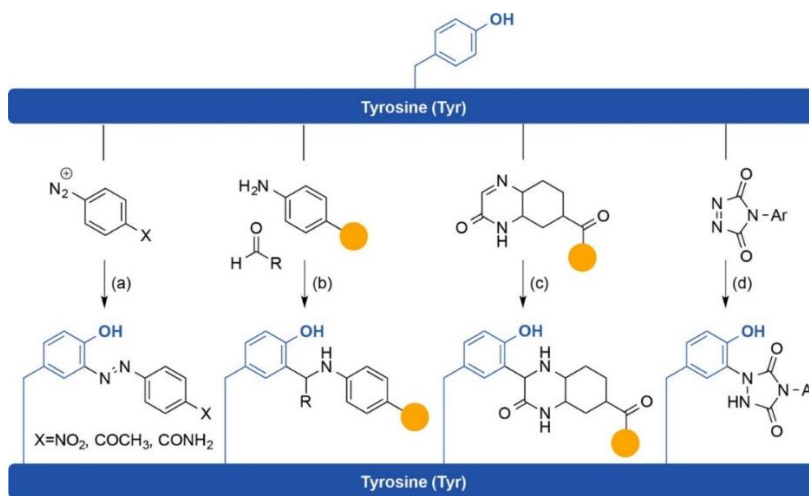


Figure 11. Scheme for the modification of tyrosine: (a) reaction with diazonium salts, (b) three-component mannich reaction, (c) reaction with preformed imines, and (d) ene-type reaction with diazodicarboxylate reagents. Reproduced with permission under CC license from Boutureira *et al.*^{71s}

In contrast, tryptophan, one of the least frequently present amino acids in proteins, provides a unique centre for specific bioconjugation reactions. It has been reported that a viable conjugation can be done through the in situ generation of a rhodium carbenoid reagent, which produces an alkylated indole. This reaction is possible since the reaction with tryptophan can outcompete hydrolysis of the rhodium reagent. However, this reaction requires a highly acidic pH (1.5-3.5), which could cause protein unfolding and denaturation.^{67,71}

1.3 Ferritin polymer-protein conjugates

The ferritin family provides an versatile shell that can be used as a multivalent scaffold. To recapitulate, ferritins are a family of proteins that have been investigated for applications as nano-carriers for drug therapy, vaccine development, chemical catalyst and imaging surrogates, that minimize toxicity in the body while maximizing absorption.⁷²⁻⁷⁴ Furthermore, ferritins, being proteins, can stabilize several particles inside their cavities, and are able to be engineered to prevent any immunogenic response towards many substances.⁷² Hence, the well-defined ferritin structure makes it an excellent particle for derivatization. It is possible to derivatize the protein shell by genetic, combinatorial or chemical methods, which will depend on the desired product.¹⁶

Even the overall quaternary structure of ferritin itself can be controlled, as evidenced by multiple studies carried out on ferritins from different organisms. For example, for a genetic mutation of *A. fulgidus ferritin* (AfFtn), a tetrahedral ferritin, it was shown that a mutation at K150A and R151A was sufficient to shift the quaternary structure

from the tetrahedral to the canonical octahedral symmetry of the vertebrate and bacterial ferritin cage proteins. The reason for the morphological change was attributed to the loss of hydrogen bonding and a decrease in the positive electrostatic charge.⁷⁵ In the same manner, DPS protein from *Mycobacterium smegmatis* (MsDps1) was mutated at an invariant residue F47 to E47 as described by Chowdhury *et al.*, ultimately eliminating the formation of dodecamers in solution and increasing the flexibility at the AB α -helices loop. It was shown through X-ray crystallography that in the crystalline state, MsDps1 could undergo 24mer formation.⁷⁶

In terms of chemical derivatization of ferritins, the ability of ferritins to be grafted onto surfaces was explored. Such is the case reported by Dominguez-Vera *et al.*, where HSF was grafted onto an N-succinimidyl-3-(2-pyridyldithio)propionate–modified gold surfaces.⁷⁷ In a similar way, Halfer *et al.* modified alumina particles with -COOH moieties to use EDC/NHS ester and further graft HSF to them.⁷⁸ These approaches can facilitate the control of the fraction of residues that can be modified while maintaining structural composition. Many reagents have been proven useful for protein functionalization. As previously mentioned, the most common residues are cysteine residues and lysine residues. Cysteine residues can also serve to employ click-type chemistry using azide-alkyne Michael additions, whereas lysine residues are modified by taking advantage of their reactivity in alkaline media using NHS esters, NHS carbonates, NHS carbamates, thiazolidine-2-thiones, pentafluorophenyl esters, anhydrides, acid halogenides and amidination reagents.⁷⁹

1.3.1 Ferritin polymer-protein conjugates by “Grafting-to”

Lysine residues are one of the most common sites for the functionalization of ferritin. The labeling efficiency is defined by the surface exposure of the lysine side chains and their reactivity. For example, to graft to HSF, Gálvez *et al.* used NDB, a family of nitrobenzofurazans that react preferably with primary and secondary amino groups under alkaline conditions, to understand the labeling capacity of this protein.⁸⁰ It was successfully shown that two out of three reactive lysines could be modified per subunit: the K83 and K97 sites, whereas the more hindered K104 remained unlabeled.

Furthermore, ferritin-antibody conjugates have been synthesized by Kishida *et al.* reporting a comparison of the effectiveness of adding activated moieties to a ferritin subunit by reaction with a water-soluble carbodiimide and N-hydroxysuccinimide, or with an excess of glutaraldehyde.⁸¹ It was shown that EDC/NHS lysine residue modification resulted in ferritin-ferritin polymers, high hydrolysis rates of the activated ester at pH 8 and a dependence of the reaction time. Likewise, glutaraldehyde and reactive amino groups formed ferritin-ferritin polymers by the linkages of the glutaraldehydes, the formation of stable Michael-type adducts or both. Hu *et al.* demonstrated grafting onto ferritin surfaces by NHS terminated methacryloyloxyethyl phosphorylcholine (MPC) and PEGMA monomers.⁸² It was shown that the reaction occurs within 1 hour, and more prolonged incubation times facilitated the aggregation of the conjugated samples. Furthermore, short polymer chains, such as NHS-polyPEGMA, are readily conjugated in comparison with NHS-polyMPC. This appears to demonstrate that molecular weight is a critical aspect that affects the reaction kinetics.

To support this statement, Spa et al. derivatized HSF with NHS-fluorescent dyes (Cy3 and Cy5 dyes); however, low yields were achieved. Instead, the NHS moieties were exchanged for tetrafluorophenol esters (TFP) to reduce competitive hydrolysis, achieving 11 and 15 molecules of Cy3 and Cy5, respectively, per ferritin cage.⁸³ However, the functionalization of ferritins can also lead to shifting in the net charge of the resulting chemically-modified protein. Wonga *et al.* then synthesized a hydrophobic ferritin by EDC coupling with long chain (C₉, C₁₂, C₁₄) primary amines.⁸⁴ This reaction was carried out in conditions under which ferritins are usually unstable such as organic solvents (DCM, ethyl acetate, and toluene). Conjugation with long-chain alkyl amines led to a net positive charge, due to the excess of surface lysine and arginine residues that remained unaffected by the coupling reaction.

Ferritins offer such a flexible platform that they have been used by Bhattacharyya *et al.* to synthesize a three-part complex system of protein-CNT-polymer conjugates.⁸⁵ The functionalization of multi-walled carbon nanotubes (MWCNT) was achieved by oxidation of the surface to provide –COOH moieties, which underwent reaction with the primary amines of ferritin once the EDC/O-acylisourea intermediate was formed. Once the modification was made, these adducts were used as additives for polymer strengthening, such as in the preparation of modified (polyvinyl alcohol) (PVA).

1.3.2 Ferritin polymer-protein conjugates by “Grafting-from”

A “grafting-from” approach has been reported *vía* an ATRP reaction combining a chain transfer agent (CTA), by attaching 2-bromo-isobutyric acid (BIBA) to the amino groups of the protein shell, and further copolymerization of thermoresponsive poly(N-isopropyl acrylamide) (PNIPAAm) and photo-crosslinkable 2-(dimethyl maleinimido)-N-ethyl acrylamide (DMIAAm) groups from the protein surface without any variation of the original protein dimensions to form an emulsion stabilizer.⁸⁶ It was found that characterization of the products became more complex as the reaction was incubated for longer times, due to the modification of the protein quaternary structure and the high polydispersity of the protein-polymer product. However, it was also demonstrated that this bioapplication could be useful for the construction of polar-apolar interfaces by decreasing the interfacial tension due to the presence of hydrophobic/hydrophilic moieties. Likewise, Hu et al. demonstrated that ATRP CTA agents could be grafted to ferritin (~2 tertiary bromide initiators) by NHS ester chemistry in pH 9.0 PBS buffer (with 20% DMSO) at 4 °C for 24 h, followed by a polymerization in aqueous solution with CuBr and 2,2'-bipyridine (bpy), using MPC and PEGMA monomers. These monomers addressed the drawbacks of the addition of PEG has and supplies hydrophilic moieties with greater biocompatibility.⁸²

1.3.3 Ferritin polymer-protein conjugates by “Grafting-through”

Danon *et al.* reported the preparation of a polycationic derivative using EDC/DMPA.⁸⁷ Ferritin was derivatized under physiological conditions without a change in morphology of the native molecules. Furthermore, labeling was controlled by changing the surface charge, which could be adjusted according to the needs of a particular experiment. To further this discovery of a cationized ferritin, Mann *et al.* modified the external surface of ferritin by attaching DMPA to aspartic and glutamic acid residues using EDC chemistry, followed by the addition of an anionic polymeric surfactant $C_9H_{19}-C_6H_4-(OCH_2CH_2)_{20}O(CH_2)_3SO_3^-$, resulting in the formation of a solvent-free liquid protein nanoconstruct.⁸⁸ Using this approach, it was possible to attach approximately 4 surfactant molecules per subunit, which was found to be sufficient to increase protein stability by 30%, and increase its decomposition temperature from 315°C to 405°C.

Transmission electron microscopy (TEM) and dynamic light scattering (DLS) were used to study complex arrays of HSF polymers through channel-directed electrostatic interactions with poly(α , L-lysine) in the presence of urea.^{89,90} This system relied on the positive charge present on the side chain of the lysine residues and the head-to-tail orientation of the polymers, in contrast to the branched arrangement produced by most free radical polymerizations (FRP).

1.4 Protein-polymer conjugates for PEGDA-based hydrogels

Natural polymers offer mild gelation properties and provide adequate environments for cell encapsulation under physiological conditions. However it is often necessary to add synthetic and photocrosslinkable reagents, such as the ones based on polyethylene glycol (PEG), to provide greater control over the final macroscopic hydrogel properties.⁹¹ PEGDA-based hydrogels have been used in bioprinting applications due to their hydrophilic, biocompatible and highly tunable nature.⁹² However, there have been developments on developing peptide-binding proteins in polymeric networks to use them as detection methods in complex mixtures.⁹³ The crosslinking of PEGDA-based hydrogels are done preferably using water-soluble photoinitiators that are nontoxic. Multiple authors have used the photoinitiator Irgacure 2959 in low concentrations (~0.05%).⁹⁴ It can be activated in the upper spectrum of the UV region (>350 nm). However, this wavelength has been reported to damage cells.⁹⁵ As an alternative, the use of mild photoinitiators with the capacity to be photopolymerized at longer wavelengths (~400 nm), resulting in lower cytotoxicity and high cell survival (>95%), is desirable. Acylphosphine oxide photoinitiators have demonstrated these requirements while increasing the gelation rate up to ten times in contrast with the hydrogels obtained utilizing Irgacure 2959.⁹⁶

However, PEGDA hydrogels present drawbacks such as low mechanical strength and potentially rapid degradation of the photocrosslinkable polymers.⁹⁷ Therefore, various approaches have been explored to improve the mechanical strength and structural stability of these PEG-based gels. The first approach is that of physical blending (i.e.,

PEGDA/HEMA improves the viscosity of the hydrogel).⁹⁸ Nonetheless, blended hydrogels are challenging in that it is difficult to identify the contributions of the individual components to the overall physical properties of the gel. The second approach is to chemically or biochemically crosslink the polymer chains (i.e., molecular strands).⁹⁸ The third approach allows one to independently tune the gel's properties by using interpenetrating networks (IPN), the addition of a second polymer network entangled on the chains of the first polymer to reinforce the mechanical properties of hydrogels. This method has employed polysaccharides and PEGDA-based polymers (e.g., agarose-, xanthan gum-, and alginate-PEGDA).^{99–101}

1.4.1 PEGDA

PEGDA is a reagent that is used extensively in the field of therapeutics, protein stabilization, and drug delivery. It was patented by Lee pharmaceuticals in 1973 as a composition of aromatic and alicyclic polyacrylates (~25-90% wt).¹⁰² They can be synthesized by addition of linear PEG polymer chains into a nonpolar solvent (e.g., DCM or toluene) containing acryloyl chloride. The reaction is followed by precipitation of the product polymers in cold diethyl ether (4°C).¹⁰³

In general, PEG-based polymers offer increased biocompatibility, low biofouling, and drug delivery capabilities. For PEGDA-based hydrogels, the hydrophobicity is closely correlated with the porosity of a sample. Also, as the wt % of PEGDA increases, the average mesh size decreases.¹⁰⁴ PEGDA offers many attributes that are useful for bioprinting applications; however, as described by Mazzoccoli *et al.*, PEGDA blends

require a combination of long and short chains to facilitate viscoelastic behavior. This is achieved by varying the processing conditions during polymerization or combining various polymers to manufacture a hydrogel with a desired set of mechanical characteristics.¹⁰⁵ Despite all the advantages, PEGDA ester linkages introduced upon acrylation of the PEG diol are susceptible to slow degradation in vivo by hydrolytic cleavage of the ester linkages (~ months to years).⁹¹ To reduce the degradation rate of PEGDA hydrogels, Browning *et al.* synthesized PEG diacrylamide (PEG-DAA).¹⁰⁶ It was shown that the amide bond, instead of the hydrolytically degradable ester bond, changes the polymer's structure; however, there is no significant change in the gel's rheological properties. It was demonstrated that the elastic moduli increase with the decrease of the polymer chain polymerization and that swelling decreases with increasing PEG weight fraction.

1.4.2 Thickening Agents (TA)

Carboxymethylcellulose is a derivative of cellulose which is water soluble. It has been used in the production of bioinks for biomedical applications (Figure 12). To obtain these hydrogels, chemical crosslinking is achieved by the use of bifunctional crosslinkers containing chemical groups such as aldehydes, dicarboxylic acids, and PEG.¹⁰⁷ Likewise, alginates are a naturally derived linear copolymer of 1,4 linked β -D-mannuronic acid and α -L-guluronic acid residues repeated at irregular intervals. These systems are called G-blocks.¹⁰⁸ The formation of a hydrogel from these biomolecules will depend on the type of alginate used and the method of crosslinking. Traditionally, the alginates undergo physical crosslinking with divalent cations such as Ca^{2+} ions.¹⁰⁹ It has been

reported that the resulting alginate-based gel has a structural conformation described by the egg-box model, which arise when Ca^{2+} ions are chelated by G blocks of greater than 20 units.¹⁰⁸ Furthermore, xanthan gum is a cellulose-based polymer, substituted on the O-3 of alternate backbone residues by charged trisaccharide side-chains of β -D-mannose-1,4- β -D-GlcAp-1,2- α -D-mannopyranose to give a branched pentasaccharide repeating unit.¹¹⁰ It is a non-gelling biopolymer that exists in aqueous media with an ordered rigid chain conformation which is able to form highly viscous solutions even at low concentrations.¹¹¹ Lastly, Pluronics F127 is a water soluble triblock copolymer formed by poly(ethylene oxide)–poly(propylene oxide)–poly(ethylene oxide) (PEO–PPO–PEO) which can exhibit a thermoreversible behavior.¹¹² The gelation mechanism of these solutions is reported as a physical crosslinking, which is dominated by the PPO block, on which the solubility is decreased in aqueous solutions above 15 °C.¹¹³ Pluronics solutions are liquid before cross-linking and beyond the gelation point, a physical network is formed which continue to increase as the temperature is increased. Furthermore, this behavior is desired for the incorporation of drugs due to increased circulation time and enhanced metabolic stability.¹¹⁴

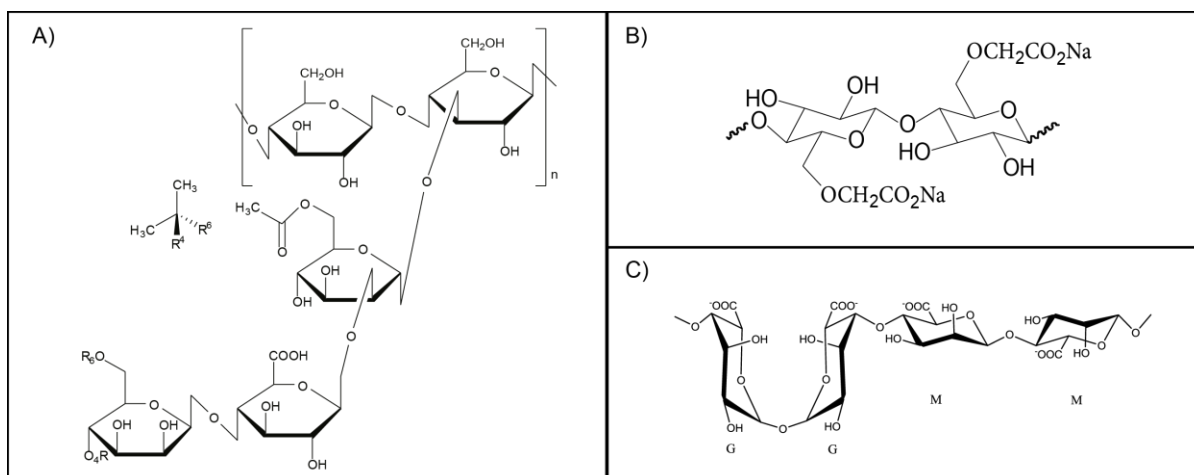


Figure 12. Repeating units of polysaccharides used as thickening agents: A) Xanthan Gum, B) Carboxymethylcellulose, and C) Sodium Alginate. ¹¹⁵

1.5 3D molecular bioprinting

3D Bioprinting technology, also referred to as Additive Manufacturing (AM), is a technology that facilitates the fabrication of complex constructs altogether instead of by the conventional predefined assembly of several pieces cast over predefined moulds. It was first introduced by Charles Hull in the early 1980's, in response to extended fabrication processes and manufacturing imperfections in prototype development.¹¹⁶

In general, the process for 3D bioprinting follows a set of predefined steps, which starts by creating the desired tridimensional model on any designated software with all the desired morphology. Secondly, the generated model is converted to the STL format that encompasses the geometry information of the model. Third, the model is processed using a 3D printer software, which slices the 3D model into an array of 2D layers stacked one on top of the other. Lastly, the model is bioprinted to generate the 3D object that was

designed. Once all the stages have been made, some post processing can be needed for the model to be ready to be used in the desired application.¹¹⁷ AM provides great flexibility and applicability, where it utilizes a layer-by-layer stepwise approach employing computer-aided design (CAD), allowing for rapid prototyping and the fabrication of custom parts. It has been used in many industrial applications such as in materials science, with the rapid production of microfluidic devices with complex geometric features; in biomedical engineering, for scaffold fabrication for cultivation of mesenchymal stem cells; and in nanotechnology, for the small-scale production of stretchable and flexible conductors, among others.¹¹⁸

1.5.1 3D bioprinting

3D Bioprinting is a methodology that physically deposits a biomaterial, using a 3D printer, which is further stabilized or immobilized by melt-cure, chemical or physical crosslinking. This approach can precisely deposit biomaterials such as bioactive molecules, biopolymers or even cells at specific spatial sites.^{119,120} 3D bioprinting has an unprecedented advantage over conventional 2D strategies, providing biocompatible and biodegradable 3D scaffolds, namely extracellular matrices (ECMs), which can be classified into two main groups: scaffolds of complex geometries that are directly fabricated using biocompatible materials, which may or may not be seeded with cells, and artificial tissues that are directly fabricated with cells encapsulated during the bioprinting process.^{120–122}

Currently, since there are no synthetic multicellular 3D structures that can mimic *in vivo* conditions, research is focused on the latter. As a result, new biomaterials and desired substrates are being developed that facilitate cell positioning in a specific spatial arrangement capable of rendering specific physiological properties of the environment only biological structures can deliver.¹²³ Furthermore, 3D bioprinting is a challenging task, since the physical properties of the desired biomaterial for bioprinting will define the 3D bioprinting technology needed. For that reason, desirable techniques that provide simultaneous material deposition, viable cell-laden constructs, unhindered cell-transport structures and post-seeding for multiple material types are constantly being developed.¹²³

1.5.1.1 Bioprinting methodologies

Bioprinting, a methodology that arises at the intersection where engineering meets medicine and science, has been a tool employed for diverse applications from promoting self-repair of endogenous tissue to reconstruction using a biomimetic tissue.¹²⁴ Formally it has been described as a process of bioprinting biological systems made of cells, growth factors, and biomaterial scaffolds.¹²⁵ In the past, methods such as electrospinning, fibre deposition, freeze-drying, and gas foaming have been used, all of which lack the required control to synthesize an advanced scaffold.¹²⁰ In general, the goal is to design novel bioinks that facilitate an adequate scaffold fabrication process that can grow and maintain a set of physiological functions. However, an adequate bioprinting process employs a suitable combination of a bioink with an adequate bioprinting methodology.¹²⁶ Therefore, the development of techniques that can facilitate the complex production of multi

cellularized scaffolds has been of interest. Many authors have reviewed the available techniques and have agreed that the methods are grouped as stereolithography-based, laser-based, inkjet-based, and extrusion-based bioprinting (Figure 13).^{120,126–128} Less known classifications are either the direct-write or thermal-inkjet bioprinting methods.¹²⁹ For practical purposes, to address the different methodologies available, the descriptions are going to be made according to what most of the authors have agreed as relevant (Table 3). Despite the advantages of the 3D bioprinting methodologies, inaccuracies in resolution (~20 to 85 μm) and material mixing can lead to material variability and distribution of defects.¹³⁰

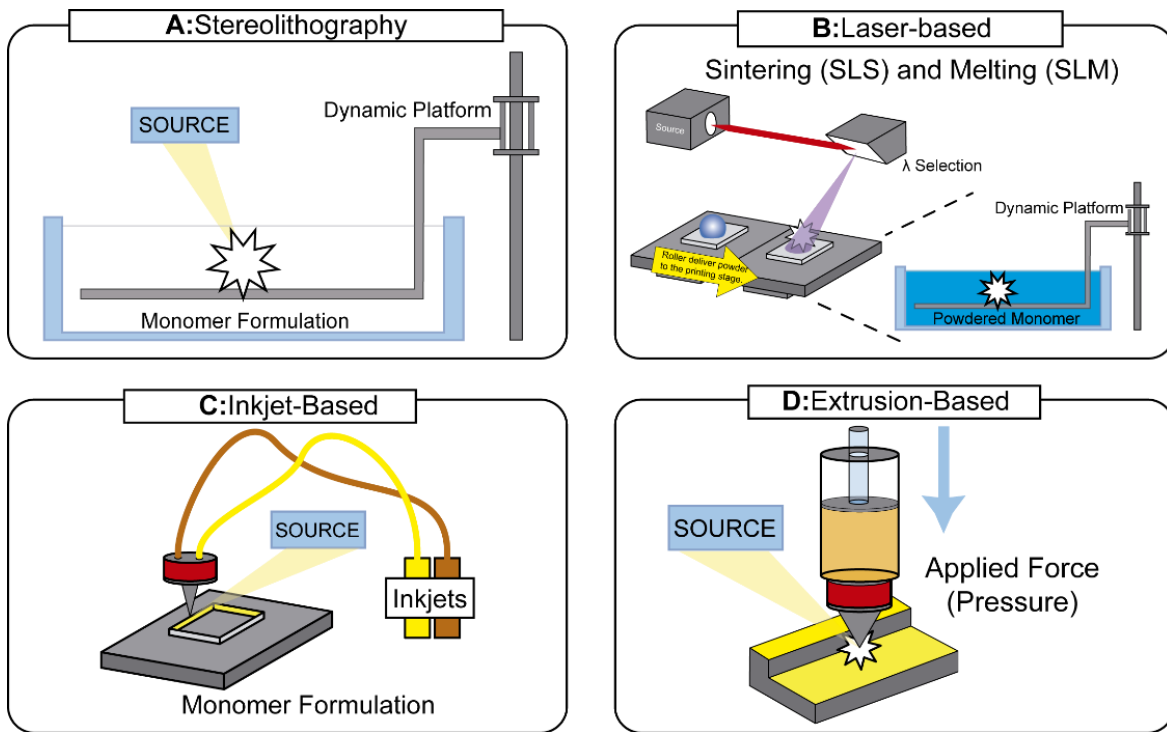


Figure 13. Representation of A) stereolithography-based, B) Laser-based, C) Inkjet-based, and D) Extrusion-based bioprinting methodologies.

A) Stereolithography-based approaches

This methodology employs a laser source to solidify a photosensitive polymer in a selective layer-by-layer fashion. This technique delivers a high-resolution product. As a result, and taking advantage of the method's flexibility, it has been used to create moulds and anatomical models for cell deposition.¹²⁴ However, due to the nature of this bioprinting method, the application of live cell bioprinting is restricted.¹²⁵ Several toxic materials such as acrylics and epoxies have been used to develop this model.¹²⁷ To overcome the cellular toxicity of these resins, high molecular weight polymers which can hydrolyze in vitro and in vivo, such as D,L-lactide and poly(propylene) fumarate, have been used. Likewise, polymers such as poly-(ethyleneglycol)-diacrylate (PEGDA) and poly-(ethyleneglycol)-metacrylate (PEGDMA) have been used to develop scaffolds using stereolithography-based bioprinting.¹²⁵

B) Laser-based approaches

Laser-induced forward transfer (LIFT) is a technique that has been used due to its ability to deposit cells at a density of 10^8 cells/mL. It consists of three main parts: a pulsed laser source, a ribbon coated with a biomaterial that coats a metal film, and a receiving substrate.¹²⁰ It operates by a pulsed beam that is focused on a designed area such as a glass absorbing layer.¹³¹ Once the pulsed beam hits the layer's surface, it creates a high-pressure bubble on the other side that propels cell-laden material onto a collector substrate that can be controlled using an elevator system.¹²⁵ This methodology is convenient due to its accuracy, precision and reproducibility without the need of using a

nozzle. Furthermore, it avoids direct contact between the dispenser and the bioinks. As a result, it does not cause mechanical stress to the cells, which results in high cell viability (usually higher than 95%).¹³² However, the viability of the cells contained in the bioink can be compromised according to the intensity of the pulsed beam. In addition, the technique is time consuming.¹³³

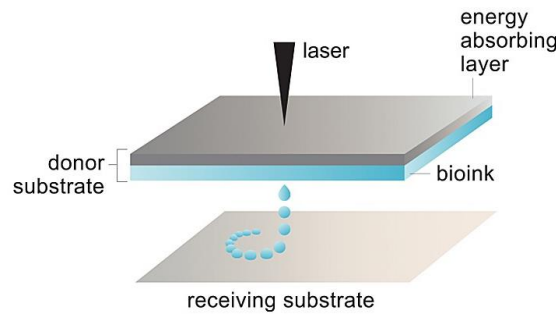


Figure 14. Graphical representation of laser-based bioprinting. Reproduced with permission from Malgorzata *et al.*¹²⁸

C) Inkjet-based approaches

Inkjet bioprinting is a technique that deposits droplets over a surface to produce 2D and 3D structures.¹³³ It is the most common type for biological and non-biological bioprinting application.^{134,135} Pragmatically, it is called “inkjet” bioprinting because the biomaterial is placed inside a cartridge altogether with other additives that allow the bioprinting process over an electronically controlled stage.¹³³ The bioprinting process is activated by either a thermal or a piezoelectric drop-on-demand (DoD) actuator that enables the flow of biomaterial from the cartridge to the platform.¹³⁴ In the case of the thermal actuator, it uses heat to generate small air bubbles that collapse within the pinhead to provide pressure pulses that eject the bioink out of the nozzle. It generates

heat for about 2 μs , causing an overall temperature rise of 4–10 $^{\circ}\text{C}$ above ambient temperatures. It has been reported that the droplet size cannot be controlled (~ 10 to 150 μL) as a result of the temperature gradient applied, the current pulse frequency, and the viscosity of the bioink itself. A common drawback is needle clogging due to material aggregation.¹²⁵ On the contrary, the piezoelectric actuator, which does not use heat or cause needle clogging, uses high frequencies to propel the droplets from the needle. This allows for control of the direction and size of the droplets.¹²⁰ However, some of their frequencies can cause cell damage and lysis. Therefore, the thermal actuator is preferred for bioprinting applications when an inkjet bioprinter is the desired method of printing.¹³⁶ Bioinks with lower viscosities must be used because higher viscosity bioinks are unable to form picoliter droplets to produce satisfactory deposition materials on any surface by this approach.¹³³ Furthermore, inkjet bioprinters facilitate the integration of multiple bioprinting heads, which enables deposition of multiple cell types.¹³⁶ This methodology offers advantages such as a reduced cost due to the similarity with other available printers, high cell viability ($\sim 80\text{-}90\%$) and relatively high bioprinting speed.¹³² However, the main restrictions are the low upper limit for the viscosity of the bioink (0.1 Pa s^{-1}), making the deposition of highly viscous hydrogels and extracellular matrix (ECM) difficult.¹³⁶

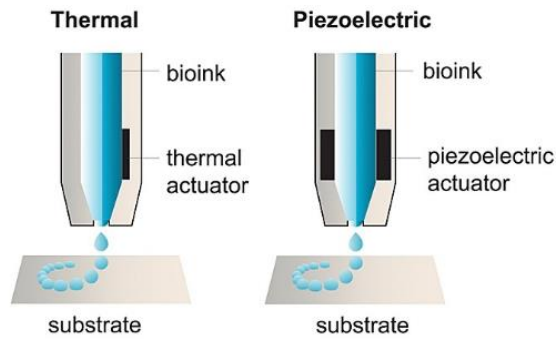


Figure 15. A) Thermal- and B) Piezoelectric-based systems for inkjet bioprinting. Reproduced with permission from Malgorzata *et al.*¹²⁸

D) Extrusion-based approaches

Extrusion-based bioprinting is a technique to dispense bioinks using force to flow materials through an orifice. Materials such as solutions, pastes or dispersions are extruded using either a pneumatic- or mechanic-based system, as shown in Figure 16.¹²⁰ Each method offers unique advantages. However, all use high shear and extensional forces or higher temperatures, which can compromise cell viability.¹²⁴

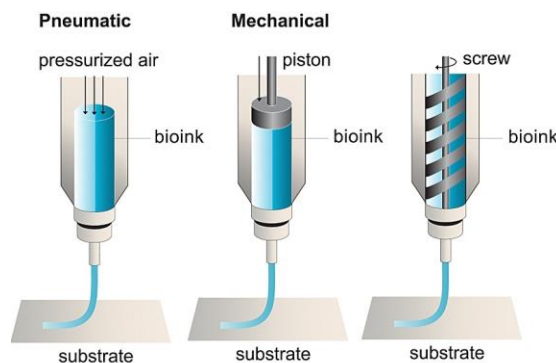


Figure 16. A) pneumatic-, B) mechanical- and C) solenoid-based systems for extrusion-based bioprinting. Reproduced with permission from Malgorzata *et al.*¹²⁸

Pneumatic-based systems offer considerable control over the amount of pressure applied to bioinks. However, when it comes to high viscosity bioinks, a different approach must be taken into consideration. Approaches such as a screw or piston driven mechanical approaches are also used. These actuators offer great spatial control and precision regarding the dispensing process of the bioinks. Nonetheless, they can generate higher pressures which may degrade the bioinks.¹³⁷ As a rule, pneumatic systems are better for high viscosity materials, while mechanical systems outperform the latter on low viscosity materials.¹²⁹ Also, the final product depends on the filament extruded, which, at the same time, is a function of needle diameter, material flow rate, bioprinted filament height and write speed.¹²⁹

Table 3. Summary of the different bioprinting methodologies

	Stereolithography ^{138,139}	LIFT ^{126,140}	Inkjet bioprinting ^{120,126,140}	Extrusion bioprinting ^{126,140}
Viscosity bioink	n.a.	1–300 mPa s	<10 mPa s	30–6 × 10 ⁷ mPa s
Cell density	Medium 10 ⁷ cells/ml	Medium (10 ⁸ cells ml ⁻¹)	Low <10 ⁶ cells ml ⁻¹	High, cell spheroids
Resolution	1.2–200 μm	10–100 μm	10–50 μm	200–1000 μm
Single cell control	High	Medium	Low	Medium
Fabrication speed	Fast (<40,000 mm/s)	Medium (200–1600 mm/s)	Fast (100 000 droplets/s)	Slow (700 mm/s – 10 μm/s)
Cell viability	>90 %	>95%	>85%	80%–90%
Advantages	<ul style="list-style-type: none"> • Complex internal features • Growth factors and cell loading possible 	<ul style="list-style-type: none"> • Supports vascular channels • Nozzle-free technology enables less cell damage • High precision (1cell/droplet) 	<ul style="list-style-type: none"> • low cost • high resolution • high printing speed • ability to introduce concentration gradients 	<ul style="list-style-type: none"> • Independent movement with high resolution • Support is not required
Disadvantages	<ul style="list-style-type: none"> • Toxic photoresins • Possible shrinking • Need of support structure 	<ul style="list-style-type: none"> • Expensive • Difficult to print multi cellularized cellular scaffolds • Limited commercial viability 	<ul style="list-style-type: none"> • Thermal and mechanical stress to cells • limited printable materials 	<ul style="list-style-type: none"> • Expensive • Optimization of bioink properties is crucial

1.5.1.2 Bioinks

The bioprinting methods previously described provide a myriad of strategies for bioprinting applications. Moreover, the bioprinted product's functionality will depend on the combination of a bioprinting method and an adequate bioink for the application. In general, each bioprinted construct will need a bioink that can successfully comply with the requirements of the needed geometry. As a result, the dependence on structural composition and functionality extends the need to develop novel bioinks further using nano-dimensional biomaterials such as proteins, polysaccharides, polymers and micelles to improve mechanical and chemical properties.

Bioinks are usually classified into two main categories, depending on their bioprinted processes: **(1)** Scaffold-based bioinks, which are curable polymers that possess mechanically robust and durable materials and **(2)** scaffold-free bioinks, where soft materials, such as hydrogels, usually with a high water content, provide a viable environment for cell multiplication.^{131,141,142} While this classification is the most widely used, it is important to emphasize that point **1** comprises the type of bioinks used on "Top Down" approach, where the scaffolds are seeded with cells after bioprinting. In contrast, point **2** comprises the bioinks used in a "Bottom up" approach, where highly hydrated polymers are combined with cells prior to bioprinting.¹⁴³ In general, a bioink's potential to be used in the field will depend on the printability, crosslinking ability, mechanical properties, biocompatibility degradation controllability and formation of by-products after biodegradation occurs.¹²⁵

1.5.1.3 Scaffold-based bioinks

The scaffold-based bioprinting approach is the most widely used approach to date because it provides an area for cell adhesion and a biological cue for cell differentiation.¹⁴² There are three categories that encompass the scaffold-based bioinks: hydrogels, decellularized extracellular matrices (dECM) and micro carriers.

1.5.1.3.1 Hydrogels

Attempts to work under physiological conditions have been satisfied using hydrogels. El-Sherbiny *et al.* define hydrogels as “three-dimensional networks composed of hydrophilic polymers crosslinked either through covalent bonds or held together via physical intramolecular and intermolecular attractions”.¹⁴⁴ Hydrogels are desirable materials in bioprinting applications due to their ability to provide enhanced printability, cytocompatibility, address low biomaterial viability, provide homogenous distribution of substrates, and facilitate diffusion of molecular oxygen required for cell viability.¹⁴⁵ These materials have a high content of hydrophilic moieties, provide fast gelation times and enhanced mechanical strength which can support 3D-structures.^{146,136} However, to provide a microenvironment with proper mechanical properties for cellular activities it is crucial to preserve the original 3D structure. Therefore, it is of utmost importance to select a crosslinking mechanism that does not have a negative impact on the desired structure. Various crosslinking processes have been developed for hydrogels, including thermal-, chemical-, and photo-crosslinking.¹⁴⁷

Hydrogels used for bioprinting are usually classified with respect to whether they contain natural or synthetic polymers. Natural polymers are preferred over synthetic polymers because of cell affinity and resemblance to the ECM. However, natural polymers undergo uncontrollable degradation and possess poor mechanical stability.¹²⁶ In contrast synthetic polymers, provide relatively consistent chemical and mechanical properties that exceed the ones natural polymers can provide.¹²⁵ Many authors have described the available bioinks extensively.¹³¹ However, some examples of frequently used bioinks are provided in Table 4.

1.5.1.3.2 Decellularized ECM

Novel research has been focused on developing naturally derived materials that overcome biocompatibility, cytocompatibility and diffusivity issues. As a result, dECM, a material that retains the components and complexity of natural ECM, has been used as a bioink. ¹²⁵ dECM has been collected thoroughly from sources such as human skin, nerve, and demineralized bone.¹⁴⁸

To facilitate the use dECMs as a bioink, the chosen ECM needs to undergo minimal damage. There are two general approaches for isolating dECM and utilizing it as a biomaterial: a) organ decellularization and recellularization, and b) isolation and processing of tissue and organ-specific dECM into a separate, distinct, biomaterial form before utilization. The second approach is desirable because it can be fully recellularized with enhanced cell control to make a functional tissue, and does not require sufficiently functional organs before decellularization.¹⁴⁸ Furthermore, it is of paramount importance

to remove residual DNA after decellularization (less than 50 ng dsDNA per mg dry weight and 200 base pair DNA fragment length) which, may cause an immune response.¹⁴⁹ In most cases, the decellularization process is based on gentle methods that dissolve cell membranes which maintain the structural integrity of the monolayers. They involve the use of NH₄OH and Triton X-100 solutions in phosphate buffered saline (PBS).¹⁵⁰ Furthermore, Kim *et al.* reported a thorough review of ECM decellularization.¹⁴⁹

1.5.1.4 Scaffold-free bioinks

Scaffold-free bioinks have been used as a method to facilitate rapid fabrication of bio-mimetically developed tissues.¹⁵¹ It is a developing method which has been unable to provide a reliable and reproducible approach for the production of custom-shaped scaffolds while maintaining control of the bioprinted shape when multicellular constructs are needed.¹⁵² To our knowledge, there are three types of scaffold-free bioinks for extrusion bioprinting: tissue spheroids, cell pellets and tissue strands.¹⁴²

Table 4. Summary of some properties of hydrogels with references on their use for bioprinting.

<i>Type of bioink</i>	<i>Biomaterial</i>	<i>Composition.</i> ¹⁵³	<i>bioink composition</i>	<i>Crosslinking method</i>	<i>Applications</i>	<i>Advantages</i>	<i>Drawbacks</i>
<i>Natural</i>	Alginate. ¹⁵⁴	Polyanionic copolymers derived from brown sea algae and comprising 1,4-linked B-D-mannuronic (M) and α-L-guluronic acid (G) residues in varying proportion	Alginate-TEMPO-oxidized cellulose nanofibrils (TCNF)-glycerin	CaCl ₂	Wearable sensors and drug releasing materials.	Hydrogels without glycerin are stable at room temperature	Instability under moist conditions for prolonged use
<i>Natural</i>	Agarose. ¹⁵⁵	repeating units of alternating β-d-galactopyranosil and 3,6-anhydro-α-l-galactopyranosil groups	3% agarose / 1:1:1 (Agarose:Collagen: Mesenchymal Stem Cells)	Melt-cure	Fabrication of bone, cartilage, fat, and capillaries.	Higher proliferation rate of MSC's	Limited applications because they force a physical and subsequent phenotypic cell
<i>Natural</i>	Collagen. ¹⁵⁶	Component of the ECM found in all connective tissues	0.12% Collagen	Riboflavin crosslinking	bovine chondrocytes differentiation	Increased rheological properties on low collagen hydrogels.	The crosslinking method affects the cell viability (~77%)
<i>Natural</i>	Chitosan. ¹⁵⁷	linear polysaccharide consisting of β-1,4 linked 2-acetamido-2-deoxy-β-d-glucopyranose units and 2-amino-2-deoxy-β-d-glucopyranose units	2% Chitosan Solution	Thermal cross-linking reaction	Bone tissue engineering	pH dependent gelation	Cells cannot be printed due to acidic environment
<i>Natural</i>	Fibrin. ¹⁵⁸	A natural major protein component of blood clots	0.25% Fibrinogen solution	CaCl ₂	In vitro-engineered substitutes of human skin	allow efficient production of collagen that allow efficient production of collagen	Poor control on cell deposition.
<i>Natural</i>	Gelatin. ¹⁵⁹	A mixture of peptides and proteins produced by partial hydrolysis of collagen	Gelatin/hepatocyte	2.5% glutaraldehyde solution	Large scale-up hepatic tissues	Provide nutrients and space for cell growth and aggregation	Necrosis occurred during the whole culture period
<i>Natural</i>	Hyaluronic Acid. ¹⁶⁰	A linear anionic polysaccharide comprising [α-1,4-D-glucuronic acid-β-1,3-N-acetyl-D-glucosamine] _n , a naturally occurring high molecular weight hydrophilic glycosaminoglycan	1%-3% Methacrylate Hyaluronic Acid	UV-cross-linked	Osteogenic differentiation	Excellent spontaneous osteogenic differentiation	Low cell viability (~65%)

<i>Type of bioink</i>	<i>Biomaterial</i>	<i>Composition.</i> ¹⁵³	<i>bioink composition</i>	<i>Crosslinking method</i>	<i>Applications</i>	<i>Advantages</i>	<i>Drawbacks</i>
<i>Natural</i>	Matrigel. ¹⁶¹	A gelatinous protein mixture derived from mouse sarcoma	1:1 Matrigel:Cells solution	Thermal cross-linking reaction at 4°C	radiation testing	Facilitates the creation a new sensor	Limited cell type applications
<i>Synthetic</i>	Pluronics F127. ¹⁶²	PEO–PPO–PEO tri-block copolymers	15-40%w/v Pluronics F127	Thermal cross-linking reaction at 37°C	support materials (Fugitive Inks)	fast gelation in physiological conditions	Limited gelation integrity
<i>Synthetic</i>	Methacrylated Gelatin. ¹⁶³	Methacrylated peptides and proteins from partial hydrolysis of collagen	5-15% GelMA macromers	UV-cross-linked	3D drug discovery platform	High cell viability (80%)	Does not allow for dispensing of continuous fibers
<i>Synthetic</i>	Poly(ethyleneglycol). ¹⁶⁴	non-ionic polyester PEG diol with two hydroxyl end groups	3-20% PEGDA	UV-cross-linked	Cell encapsulation studies	Ease for functionalization	Lack of protein binding sites and low degradability.
<i>Synthetic</i>	poly-lactic acid. ^{165,166}	Thermoplastic aliphatic polyester with a starting compound of lactic acid.	100% Poly-lactic acid	UV-cross-linked	fetal femur-derived cells differentiation	Increased interconnectivity	Not applicable for direct write applications
	poly(lactic-co-glycolic acid). ¹⁶⁷	biodegradable synthetic copolymer of Poly-(glycolic acid) (PGA) and poly-(lactic acid) (PLA)	PLGA 97%-3% Alginate	Melt-cure 140°C	Cell encapsulation studies	Able to print with other blends	Not applicable for direct write applications

1.6 Summary and research objectives

The role of CLP has been established in the Honek laboratory through the study of several interactions both outside and inside the quaternary structures.

The host-guest encapsulation properties of bacterial ferritin (Bfr), a HSF analogue, was studied by generating a protein which had a poly histidine amino acid sequence (His₆-tag) presented on the internal surface of the Bfr cage. Once the Bfr His₆-tag was prepared, it was used to investigate strategies to encapsulate a range of guest molecules (fluorescent dyes, intact proteins and gold nanoparticles) linked to the Ni²⁺-nitrilotriacetic acid (NTA) functionality. The investigations confirmed that successful encapsulation of a guest molecule(s) within the cavity of an engineered Bfr depends strongly on the multisubunit structure of Bfr, and slight variations can cause a decrease on the encapsulation success.²⁴ Furthermore, the factors that controlled the host-guest capabilities were studied using fluorescence quenching experiments and transmission electron microscopy (TEM). Analyses of TEM data obtained on several host-guest systems verified encapsulation of the above guest molecules.¹⁶⁸

Additionally, the Bfr outer surface has also been engineered by utilizing recombinant DNA techniques and carrying out enzymatic surface modifications. Furthermore, large centimeter-sized macro porous ferritin gels reported by Kumari *et al.* has been synthesized.¹⁶⁹ These results were obtained by forming a cross-linked network of poly (ethylene glycol)-diglycidyl ether and HSF, which formed a gel-like material that could be used as a nanoreactor for chemical reactions.

The purpose of the research was to design a biocompatible HSF-based bioink system, capable of photo-polymerizing, which presented host-guest interaction capabilities to release a cargo of interest, that was suitable for direct extrusion from a 3D bioprinter.

To do so, HSF was functionalized on the surface with NHS esters via controlled modification of primary amines. The reaction conditions such as protein concentration, pH levels and bioconjugation degree on HSF were studied to verify the impact on the protein solution when high levels of bioconjugation were achieved.

The functionalized HSF was mixed with a biocompatible prepolymer, such as PEGDA to generate a bioink, in different ratios to gather relevant data on the printing capabilities. Furthermore, a rheological investigation of the prepolymer mix was made to understand the printability of the material. This investigation demonstrated the need to increase the viscosity of the solution by the addition of additives that allow direct writing from the designated bioprinter. As a result, three polysaccharides, known for their biocompatibility were considered: sodium alginate, carboxymethylcellulose and xanthan gum. To gather relevant data on these systems, a rheological assessment was done considering the linear viscoelastic region, apparent viscosity, loss and storage moduli of each sample. The results confirmed successful viscosity ranges for direct-write of the bioink on a surface.

Once the rheological assessment was carried out, the hydrogel constructs' physical properties such as sol-gel fraction, porosity, swelling capacity, host-guest

capabilities were evaluated by leaching studies, SEM, thermal gravimetric analysis (TGA), and transmission electron microscopy (TEM) respectively.

Once the hydrogel constructs were characterized appropriately, *E. coli* cells expressing green fluorescent protein were blended with the bioinks. These bioinks were bioprinted using the BioBots 1 printer. In order to evaluate the impact of the bioprinting process, quantitative assessment of the hydrogels using confocal microscopy techniques were used. The investigations confirmed that successful cell viability depends on the porosity of the materials that facilitate the nutrient migration on the hydrogel construct. Further variations of the bioconjugation modifications on guest-containing CLP were explored to optimize the position and release characteristics of molecular cargo after incorporation into 3D bioprinted structures.

Chapter 2 Protein Scaffold Engineering

2.1 Introduction

Proteins play an essential role in biomedical research due to their biological activity and specificity.¹⁷⁰ However, there are shortcomings associated with the use of proteins for therapeutic use, such as short *in vivo* half-life, poor stability in humans and possibly low solubility.¹⁷¹ Protein structure and stability can also be affected by pH, ionic strength, temperature, and solvent additives.¹⁷¹ Variants of a protein can be made by genetic manipulation of the protein residues (e.g., site directed mutagenesis) or by chemical modification of residues such as the ones described in section 1.2.1.1.

Polymer-protein conjugates have been the focus of interest by many researchers since these conjugates provide the ability to incorporate a variety of properties to the protein, and are produced by coupling reactive moieties to protein residues.¹⁷² Polymer-protein conjugates have been successfully synthesized using either (1) grafting-to, (2) grafting-from, or (3) grafting-through approaches. The approach to be selected will depend on the application of the material and the precision needed for the desired synthesis (

Figure 17).¹⁷³ For **1**, a pre-formed reactive polymer is conjugated to a protein; **2**, a polymer chain is grown from a protein macro initiator; and **3**, protein reactive groups are incorporated in a polymer which can react with the proteins after polymerization.^{172,174} In terms of advantages from these methods we could describe that grafting-from enables a high degree of protein modification and the advantage of natural purification of the product

by dialysis.¹⁷³ Nonetheless, this process is challenging due to the difficulty in preserving protein structure while attaching long polymer chains.¹⁷⁵ In contrast, grafting-to approaches facilitate the control of the polydispersity and the chemical structure. However, the resulting grafting density is strongly dependent on the molar mass of the polymer chains.¹⁷⁶ For the grafting through approach,¹⁷⁶ there is no guarantee that only one reactive moiety will react with exclusively one group of the desired peptide, a situation which increases the complexity of the product.⁷⁹

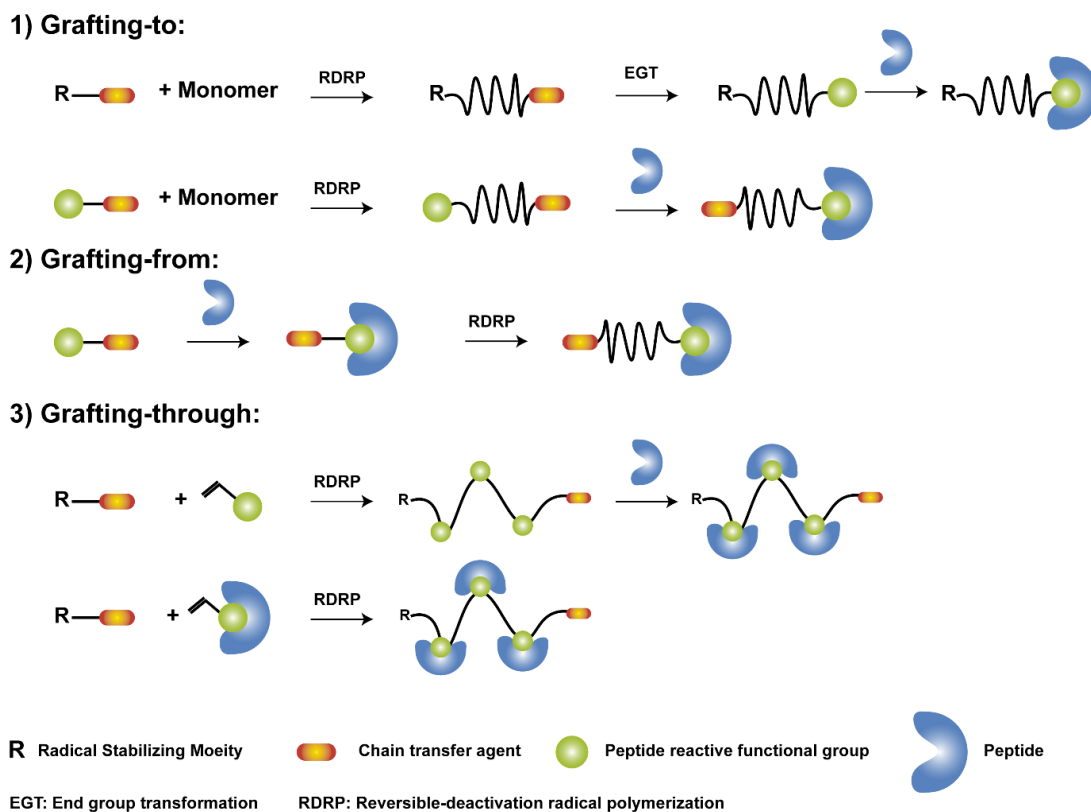


Figure 17. Polymer-protein conjugates approaches (1) grafting-to, (2) grafting-from, or (3) grafting-through. Based from Grover *et al.*¹⁷⁷

To control the polymerization degree in grafting-from methods, reversible-deactivation radical polymerization (RDRP) techniques have been developed with the objective to facilitate the formation of a product with a well-defined composition, site-specific functionalities and controlled architecture.¹⁷⁸ The three most common methods employed in RDRP reactions are methods such as reversible addition–fragmentation chain transfer polymerization (RAFT), atom transfer radical polymerization (ATRP) and nitroxide mediated polymerization (NMP).¹⁷⁵ Likewise, for grafting-to methods, click-type reactions are preferred, on which a cysteine or an unnatural amino acid with an alkynyl residue can undergo active-ester-mediated amide couplings, thiol-maleimide Michael additions, or copper-catalyzed and strain-promoted 1,3-dipolar azide-alkyne cycloadditions.¹⁷⁹

2.2 Modification of HSF at the ϵ -amine of lysine residues

This chapter will outline and discuss the methods for the preparation and the characterization of a HSF-based protein-polymer conjugate and its properties. This protein will be studied initially by the modification of the HSF at the ϵ -amino group of lysine residues using three different reagents: N-acrylosuccinimide ester (NAS), methacrylic acid N-hydroxysuccinimide ester (MMA) and glycidyl methacrylate (GMA). In order to verify successful bioconjugation, a range of biophysical techniques such as proton nuclear magnetic resonance (¹H-NMR) and matrix assisted laser desorption ionization (MALDI) mass spectrometry were utilized. Furthermore, Fourier-transform infrared

spectroscopy (FTIR) was used to corroborate the presence of acrylic moieties provided by the derivatization reaction. Dynamic light scattering (DLS) was used to determine the aggregation degree and hydrodynamic radius increase (R_H) with increasing functionalization of the protein. To further understand the behavior of mHSF with increased bioconjugation, transmission electron microscopy (TEM) was employed to analyze large structural changes that might result from these approaches.

2.3 Materials and methods

2.3.1 Materials

HSF, bovine serum albumin (BSA), lithium bromide (LiBr), 2-butanone (MEK), dimethyl formamide (DMF), dimethyl sulfoxide (DMSO), sodium chloride (NaCl), sodium bicarbonate (NaH_2CO_3), sodium carbonate (Na_2CO_3), PEGDA (M_n : 700,2000,6000), uranyl acetate, molybdic acid, ammonium persulphate (APS), N,N,N',N'-tetramethylethylenediamine (TMEDA), 2,4,6-trinitrobenzenesulfonic acid (TNBS), deuterium oxide (D_2O), N-acrylosuccinimide ester (NAS), methacrylic acid N-hydroxysuccinimide ester (MMA) and glycidyl methacrylate (GMA) were purchased from Aldrich (Milwaukee, USA) and used without further purification. MILLI-Q water was prepared freshly by reverse osmosis. Lithium acyl phosphinate (LAP), ethyl (2,4,6-trimethyl benzoyl) phenylphosphinate (CAS: 84434-11-7) was purchased from AK Scientific (Union City, CA; USA) and used without any further purification. Copper grids (300 mesh) with a carbon-formvar coating were purchased from CANEMCO-MARIVAC (QC, Canada). Standard regenerated cellulose (RC) membrane dry spectra/por®4

Dialysis Tubing 12-14 kDa MWCO was purchased from Spectrum Labs (Rancho Dominguez, CA, USA). Horse spleen apoferritin (HSaF) was prepared following the procedure described by Wonga *et al.*⁸⁴

2.3.1.1 Safety Statement

All uranyl acetate used with TEM was disposed of properly through the waste management facility.

2.3.2 Instrumentation

2.3.2.1 DLS

DLS spectra was recorded employing Malvern Instrument Zetasizer Nano ZS at a 173° (back angle) scattering angle, using a quartz cuvette Spectrosil Precision Cell QS 3.0 mm (Thermal Syndicate LTD, Northumberland, USA). Ten series of 10-second experiments were averaged for the acquisition of the correlation function.

2.3.2.2 NMR Spectra

Proton (¹H) NMR (600 MHz) spectra were recorded in 10% D₂O on a 600 MHz High-resolution UltraShield™ Bruker spectrometer (Bruker Daltonics Inc. Billerica, MA, USA). For a 7" tube (NE-HL5-7") 1.00 mL of sample is prepared according to the following procedure. Typical concentrations are: 10-mg (¹H) or 50 mg (¹³C) for 300 MHz, 5 mg (¹H) 20 mg (¹³C) for 400 MHz.

2.3.2.3 FTIR Studies

Samples were analyzed by ATR-FTIR using a Bruker Tensor 37 FTIR unit equipped with a BioATR II cell. All protein concentrations were adjusted to a concentration of 2 mg/mL in MQ water. The analysis was made at room temperature, controlled by a water bath. All the samples were run on a window from 800 to 4000 cm^{-1} through 512 scans to increase the signal to noise ratio.

2.3.2.4 MALDI

An AutoFlex Speed MALDI-TOF/TOF (Bruker Daltonics Inc. Billerica, MA, USA) was utilized for mass spectrometric analysis. The data analysis was performed using FlexAnalysis software (Bruker Daltonics Inc.). A saturated solution of sinapinic acid was prepared in TA30 solvent (30:70 [v/v] acetonitrile: 0.1% TFA in water). All samples were desalted using a C-18 ZipTip activating them with 3 washes of 10 μL 100% acetonitrile, 3 washes of 10 μL 0.1% formic acid, 10 washes of 10 μL of the sample, the sample was further cleaned with 6 washes of 10 μL 0.1% formic acid, and then the analyte was eluted them with 10 washes of 60% acetonitrile/40% 0.1% formic acid. The samples were mixed in a ratio of 1:2.5 with the matrix solution and 1 μL was spotted on the plate. A protein solution was used as an internal standard that was composed of cytochrome *c* (12360 Da), Protein A (22307 Da) and trypsinogen (23982 Da).

2.3.2.5 Electrospray Ionization

All protein samples were buffer exchanged for water using Pall Nanosep® 10 kDa cut-off spin columns and then diluted to a final concentration of 3-10 μM in a 50 μL solution

of 1:1 water:MeCN with 0.2% formic acid. Protein samples were run on a Q-Exactive hybrid quadrupole-Orbitrap™ detection mass spectrometer (Thermo Scientific, Waltham, MA, USA). Spectra were collected between 600-1500 m/z.

2.3.2.6 UV/Vis absorption spectra

SpectraMax M5 (Molecular Devices, Sunnyvale, CA, USA) equipped with SoftMax® Pro Enterprise software was utilized to record UV/vis absorption spectra.

2.3.2.7 Lyophilization

A FreeZone 4.5 Liter Benchtop Freeze Dry System (Labconco Corporation, Kansas City, MO, USA) was utilized.

2.3.2.8 TEM

TEM was performed on a CM10 Philips microscope modified with an Advanced Microscopy Techniques image capturing CCD camera. The accelerating potential was set to 100 keV for imaging in bright field mode.

2.3.2.9 Size Exclusion Chromatography

BioRad DuoFlow (Hercules, California, USA) equipped with GE Sephacryl™ S-300 HR column was utilized to undertake protein purifications.

2.3.3 Methods

2.3.3.1 Bioconjugation studies

To study the effect of increasing acryloylated lysines on the surface of the protein, three different acryloylation reagents were used: NAS and MMA as proposed by Hermanson *et al.*, and GMA proposed by Xu *et al.*^{50,180} All the protein concentrations were measured using Bradford Assay.¹⁸¹

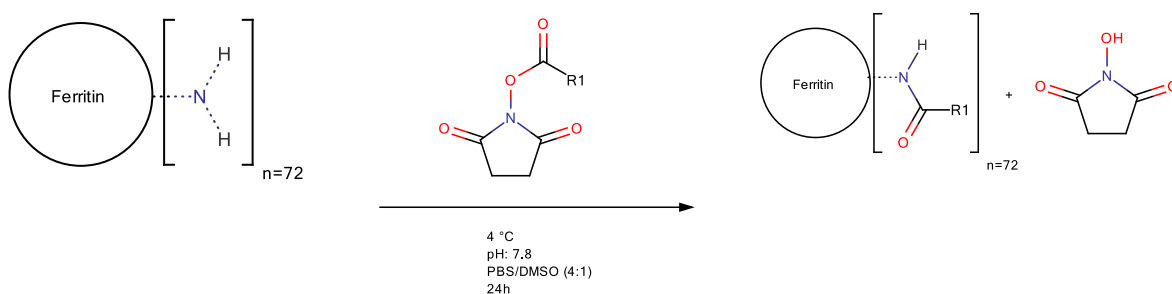


Figure 18. Strategy for the synthesis of a ferritin-conjugated monomer

2.3.3.2 Optimal parameter determination

The procedure proposed by Hermanson *et al.* was followed to evaluate the impact of changing the solvent percentage on the bioconjugation of the protein with either MMA or NAS. One mEq HSF solution was mixed with 7200 mEq of bioconjugation reagent (MMA and NAS) varying the concentration of solvent from 0.00%, 7.50%, 10.00% and 20.00% (v/v) topped to 1 mL with a PBS buffer pH 7.8. The effect of the molar excess concentration on the bioconjugation was also evaluated using the procedure proposed by Hermanson *et al.* changing the molar excess on the bioconjugation of either MMA or NAS on the protein. HSF (1 mEq) solutions were mixed with 100, 500, 1000, 2500, 5000 or

7200 mEq of bioconjugation reagent (MMA and NAS) in a 7.50% DMF topped to 1.00 mL with PBS buffer pH 7.8. Furthermore, the optimization parameters were evaluated using other solvents such as DMSO instead of DMF. The acryloylated protein solutions were dialyzed (15 mM NaCl, pH 7.0) for 4 hours twice at 4 °C. MALDI analysis was employed to verify the number of lysine residues covalently modified on the surface of each cage-like protein.

2.3.3.3 Primary amine determination: TNBS Assay

To measure the bioconjugation degree, a colorimetric assay that measured the N-nitrophenylation of primary amines was used.¹⁸² A 0.01% TNBS in NaH₂CO₃ buffer (0.1 M, pH 8.5), 1.00 M HCl, and 10% SDS solutions were prepared. To verify assay validity, several primary amine standards at a concentrations of 20-200 µg/mL (large proteins) or of 2-20 µg/mL for small molecule (amino acids) were prepared. A 1 mg/mL lysine solution, 5 mg/mL HSAF solution and 5 mg/mL BSA solution were utilized. A 6 point standard calibration point was made by adding from 0.00 µL to 60 µL in 10 µL increments, 30 µL for the unknown samples, 250 µL of the TNBS solution and bringing the solution to a volume of 625 µL with a NaH₂CO₃ buffer (0.1M, pH 8.5) followed by 2 hours of incubation at 37.0°C. Then, 250 µL of the SDS solution and 125 µL of the HCl was added to stop the reaction. The measurements were made at a wavelength of 345 nm.

2.3.3.4 Acryloylation of HSF for TNBS Analysis

1. MMA and NAS

The bioconjugation reactions using either NAS or MMA as described by Hermanson *et al.*¹ were carried out using 7200 mEq of a NAS-DMF (0.091 g of reagent in 0.9558 g of solvent) and added to 1 eq. (1 mL) of the HSF solution (45 mg/mL HSF) and the mixture was incubated at room temperature with stirring for 12 hours. Each hour, a sample of 50 μ L was taken to measure acrylates using the primary amine TNBS analysis described in section 2.3.3.3.

2. GMA

The bioconjugation using GMA proposed by Xu *et al.*² was carried using a sodium bicarbonate buffer at pH 9.5, 0.100 M. In order to carry out the bioconjugation, 100 μ L of a GMA-DMF solution (0.1109 g of acryloylation reagent in 0.954 g of solvent) to make up for 7200 mEq, was added to 1 mL of the HSF solution (45 mg/mL HSF) and the mixture was incubated at 35 °C with stirring for two hours. The bioconjugation was followed using the primary amine TNBS analysis described in section 2.3.3.3 which involved extracting a 50 μ L every hour to measure acryloylation. The acrylated protein solution was dialyzed against phosphate buffer (100 mM, pH 7.4) at 4°C overnight before TNBS analysis was undertaken.

2.3.3.5 Acryloylation of HSF using NAS or MMA

HSF (200 μ L of a 53 mg/mL solution pure HSF) was combined a sodium phosphate buffer (800 μ L, 500 mM NaH₂PO₄, pH 8.01) to produce a 10 mg/mL HSF solution. This solution was chemically acryloylated employing ~7200 mEq (60 μ L of acryloylation

reagent (NAS or MMA; 100 mg/mL in DMF)) which was slowly added (30 μ L every hour) and incubated for 2 h at 4°C, finally producing acryloylated HSF (aHSF). The unreacted acryloylation reagent was eliminated by dialysis in sodium phosphate buffer (2 L, 15 mM NaH₂PO₄, pH 7.41) and incubated for 4 h at 4 °C, followed by a second dialysis in four hours at 4 °C.

2.3.3.6 Acryloylation effects of using molar excess on bioconjugation reactions

To study the effects of increasing acryloylated lysines on the surface of the protein, three different acryloylation reagents were used: GMA, NAS and MMA as proposed by Xu *et al.* and Hermanson *et al.* respectively. Initially, 100 mg/mL stock solutions were prepared from each of the bioconjugation reagents in DMF. Seven samples per bioconjugation reagent were prepared using 0.5 mL of a 20 mg/mL of HSF (2.2×10^{-8} mEq), followed by cooling the sample down to 4 °C with constant stirring. The samples were prepared by adding between 25 μ L up to 175 μ L of the bioconjugation reagent (e.g., 25 μ L, 50 μ L or 75 μ L) in 25 μ L increments. Each increment was slowly added (25 μ L every 2 hours) to the protein solution, and the mixture was incubated for 14 h at 4 °C. The protein solution was topped up to 1 mL with sodium carbonate buffer (0.1M, pH 9.5) or sodium carbonate buffer (0.1 M, pH 8) for GMA or NHS activated esters respectively. The acryloylated protein solution was then dialyzed (15 mM NaCl, pH 7.0) twice, for 4 h each time, at 4 °C. MALDI analyses were made to verify the number of lysine residues covalently modified on the surface of each CLP.

2.3.3.7 Acryloylation density studies to evaluate protein diameter change

To study the effect of increasing acryloylated lysines on the surface of the protein, two different acryloylation reagents were used: NAS and MMA as proposed by Hermanson *et al.*¹ Two conditions were tested: the effect of a) bioconjugation at room temperature and b) bioconjugation at 4 °C. First, 100 mg/mL bioconjugation solutions of NAS and MMA were prepared in DMF. Likewise, an HSF solution (12.6 mg/mL measured by the Bradford assay) was prepared by diluting one mL of a stock solution of HSF (50 mg/mL) to 4 mL using a 500 mM phosphate buffer pH 8 solution. To carry the bioconjugation studies, four 200 µL HSF samples per treatment were prepared, for a total of 16 samples. The samples were reacted with either one, three, five or seven aliquots of 20 µL of the corresponding bioconjugation reagent every 45 minutes, respectively. To keep the volume constant, once the desired amount of bioconjugation reagent aliquot was added, 20 µL aliquots of DMF was added to the solution to complete to add up to a total of 140 µL in the mixture. The samples were later purified using Amicon Ultra 0.5 mL MWCO 10K spin column (Millipore, Billerica, MA, USA) doing four 500 µL interchanges at 10,000g for 10 minutes. Finally, both, the filtrate and the unfiltered solution were characterized using MALDI analysis and DLS studies.

2.3.3.8 Surface bioconjugation studies

Kinetics of the reactions were followed by high resolution 600 MHz ¹H NMR. Spectra (64 scans with 120 s delay) were recorded in 10% D₂O on a 600 MHz Bruker spectrometer as described by Imani *et al.* The reagents were screened before the

reaction to verify the signals. The observed changes in the intensity of the vinyl protons were determined as a function of time. All runs were performed at room temperature. One mL of 4.0 mM of TMEDA and 10 mg/mL of protein conjugate was poured into a 7 mm diameter NMR tube. An aliquot of 50 μ L of a 125 mM APS was added to initiate the polymerization, and immediately the tube was transferred to the NMR instrument.

2.3.3.9 DSC studies of modified proteins

Differential scanning calorimetry studies were carried out according to what is described by Zhang *et al.*¹⁸³ The samples prepared in section 2.3.3.6 were analyzed using a VP-DSC micro calorimeter equipped with degassing equipment. The samples were dialyzed three times with 50 mM NaH₂PO₄, pH 7.2, prior to analysis. Then, each sample was degassed for 5 minutes. The operating conditions were optimized for 30 scans for a temperature range from 20 to 110 °C on a scan rate of 90 °C/h. The Post-cycle thermostat threshold was set to 25 °C, and the pre- and post-scan thermostat times were set to 15 and 0 minutes respectively.

2.3.3.10 TEM studies of modified proteins

Preparation of samples for TEM were performed using 300 mesh copper grids with a carbon-formvar coating. Molybdic acid ((NH₄)₆Mo₇O₂₄), and Uranyl acetate (UO₂(CH₃COO)₂) stains were prepared and used as both 0.7 % and 0.5 % solutions. Both stains were used to determine which gave better resolution. The protein samples were prepared to a concentration of approximately 1.0 mg/mL, and buffer exchanged using dialysis tubes in Milli-Q water. Grids were prepared by placing a 10 μ L sample droplet,

two 10 μ L droplets of water and one droplet of stain on Parafilm®. The sample droplet was placed on top of the grid to form a layer of solution on the grid. The samples were washed by placing the grid on the water droplet while waiting a minute at a time. The grid was placed onto the stain solution for 10 seconds followed by blotting the grid on the filter paper. The final step was to wash the sample on the water droplets for 10 seconds followed by dabbing the grid on the filter paper. Each grid was left, covered, at room temperature to dry for 24 hours.

2.3.3.11 SEC purification of labeled HSF

The separation of the labeled HSF samples was made using GE Sephacryl™ S-300 HR resin. The running solution was 100 mM potassium phosphate dibasic buffer at pH 8.0. AHSF was added in 500 μ L injection volumes and run at a flow rate of 40 ml/hr with a collection of 8 mL fractions. The first eluted peak was collected and used directly for further experiments.

2.4 Results and Discussion

2.4.1 Bioconjugation Effects

The scope of the project was to bioconjugate the HSF to introduce reactive moieties that could undergo a grafting mechanism that could be subsequently incorporated into a hydrogel network. Initially, two vinyl-based NHS esters were chosen: NAS and MMA. There are four reasons why acrylate-based monomers were chosen for HSF bioconjugation: 1) the ability to undergo radical polymerization, 2) low cost, 3) good aqueous solubility, and 4) potentially adjustable hydrogel properties which could be adjusted by the monomer concentration used and which could lead to interesting physical properties (e.g., transparency and glass transition temperature).¹⁸⁴

It has been challenging to identify the chemoselectivity of the NHS esters for HSF. For example, it was first reported that HSF had approximately 3.3 ± 0.3 surface lysine residues per subunit that are chemically addressable and that can be used for bioconjugation.¹⁸⁵ However, to prove accurate reactivity of lysine groups, Zeng *et al.* modified a HSF analogue with 5-carboxyfluorescein NHS followed by tryptic digestion of HSaF. Analysis of the results of these experiments indicated that K97, K83, K104, K67 and K143 residues are actually modified per lysine subunit.¹⁸⁶

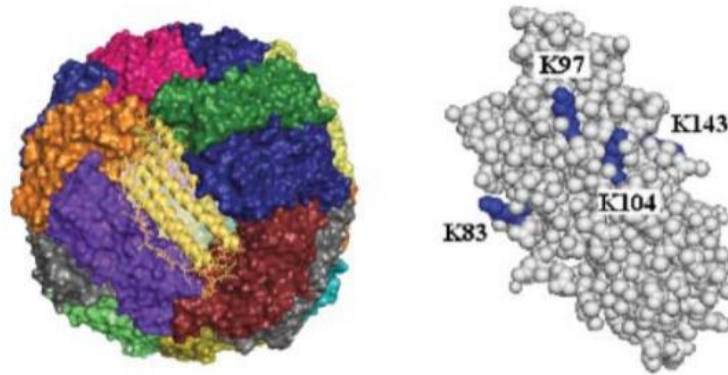


Figure 19. X-ray structural diagram of HSF with subunits presented in HSF and the indication of a HSF subunit with all the exposed lysines according to Zhen *et al.* Reproduced with permission from Zhen *et al.* ¹⁸⁶

It was shown that once the lysines are modified with a CTA, and soluble PEGMA was added by ATRP, an amphiphilic hydrogel resulted; showing that by controlling the chemoselectivity of derivatization it is possible to affect the particle's surface affinity towards a specific moiety. To further the studies of lysine modification, Zeng *et al.* derivatized apo-HSF employing a 200-fold excess of 5-(propargylamino)-5-oxopentanoic acid NHS ester (200-fold excess) in a phosphate buffer (0.1 M, pH 7.8) and DMSO, at a 4:1 (v/v) ratio, for 24 h. Analysis of the combination of MALDI studies with trypsin and V8 protease digestion showed that there are five addressable lysines per subunit instead of the previously reported four: K97, K83, K104, K67 and K143 on apo-HSF (L-chain). Furthermore, it has been demonstrated that as bioconjugate steric hindrance increases, a decrease in the number of labeled lysines results.¹⁸⁷ This chemoselectivity on lysine residues results in versatile methods to alter the properties of HSaF particles, which can

be extended to other protein nanoparticles. On average, this result gave perspective on the number of lysine residues that could be modified on the ferritin surface by using different bioconjugation reagents under different conditions.

Our first approach to bioconjugate HSF was made following the procedure describe by Böker *et al.*⁸⁶ Commercially-available equine ferritin was purified by size-exclusion chromatography (SEC) to isolate non-aggregated ferritin. Subsequently, the non-aggregated ferritin was reacted with a NHS ester at 500-fold excess with respect to the addressable amino groups per ferritin cage (3 residues on the surface per subunit and 24 subunits per HSF) and left to react for 24 h at 4 °C in a 1:5 (v/v) DMF:PBS buffer (0.1 M, pH 8). The final step was to dialyze the mixture in PBS buffer (0.1 M, pH 7.4) to remove any non-reacted NHS ester. This resulted in the formation of protein precipitates that were not possible to resolubilize even after extensive dialysis. The aggregation could have been prevented adding a stabilizing osmolyte or a non-denaturing detergent. However, because the bioconjugation of the HSF was critical to introduce reactive moieties that could undergo a grafting mechanism in one-step. It was desired to optimize the reaction conditions in order to reduce aggregation while facilitating a successful bioconjugation by varying the solvent used to solubilize the NHS ester, the buffer pH, the reagent concentration (both NHS ester and protein concentration), and reaction times.

To assess the impact of solvent volume percent, DMF and DMSO were selected because NHS esters have high solubility in non-aqueous solvents. Furthermore, DMSO was selected due to the lack of nucleophilic groups that might react with the NHS esters. Although DMF is generally an unreactive solvent, a frequently present impurity in

commercial DMF is dimethylamine, which is reactive towards NHS esters. Therefore, fresh DMF was needed to do carry out the reaction. Concentrations ranging from 0-20% of organic solvent (DMF or DMSO) were used to verify the maximum amount of solvent tolerated by the reaction while keeping constant the other conditions (25 mg/mL (0.05 mM) HSF, pH 8, 500-fold excess, 4 °C and 24 h reaction time). Our findings demonstrated that the presence of DMSO did not improve the bioconjugation process, and possibly increased the aggregation of HSF in comparison with DMF. In addition, it was evident that extended periods (>12 h) in contact with these solvents completely precipitated the protein from solution even at 4 °C, an observation also described by others.⁵⁰

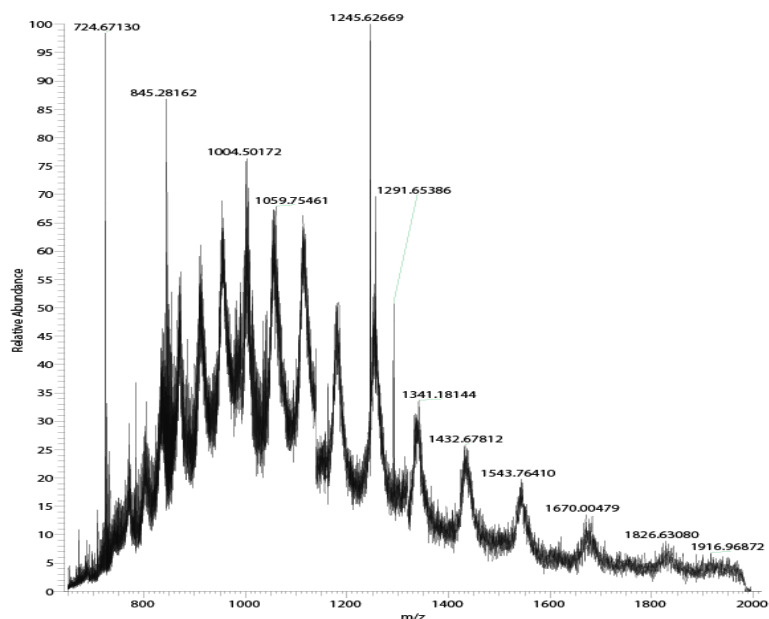
The buffer pH was evaluated, as there is a correlation of the pH and the NHS esters hydrolysis rates in aqueous media. The half-life of NHS esters decrease from 4-5 hours to under 10 minutes as the pH is increased from 7.0 to 8.6. It was reported that at pH 8 the $t_{1/2}$ is roughly 1 hour.⁵¹ From this, an assumption that at pH 9, NHS-activated esters have a $t_{1/2}$ of only a few minutes made it evident that the incubation had to be done at the lower pH and lower temperature. As a result, multiple buffers were tested to regulate the pH at which the reaction was carried: acetate buffer (1 M, pH 7.88), sodium bicarbonate buffer (0.1 M, pH 8.5) and phosphate buffer (0.5 M, pH 8). Sodium phosphate buffer (0.5 M, pH 8) was chosen because it assists in protein stabilization and free Fe^{2+} complexation.¹⁸⁸ Moreover, successful bioconjugation has been reported using (4-(2-hydroxyethyl)-1-piperazineethanesulfonic acid) (HEPES) and (3-(N-morpholino)propanesulfonic acid) (MOPS) for bioconjugation of some proteins.¹⁸⁹

Furthermore, a buffer with reactive primary amines, such as TRIS (0.1 M, pH 8), was used to quench the labeling reaction.

To gain more insight concerning the HSF bioconjugation procedure, variation of the molar ratios of acryloylation reagents:protein were tested starting from 5:1, 10:1, 25:1, 50:1, and 500:1. To verify the protein bioconjugation, the different assays were first purified using Nanosep® Spin Columns MWCO: 10 kDA. The purification was carried out with bioconjugated and non-bioconjugated protein using a phosphate buffer (50 mM, pH 7.4, 15 mM NaCl). The use of ultracentrifugation procedures resulted in high aggregation rates and difficulty in resolubilization as well. It is known that ultracentrifugation will result in a higher local protein concentration, facilitating precipitation, which could lead to unfolding and an increase in non-specific protein-protein and protein-membrane interactions, ultimately causing a blockage in the membrane, increasing the ultrafiltration times. To reduce the nonspecific binding, 50 µM of Tween 20 was added.¹⁹⁰ However, the presence of detergents is detrimental for MS analysis, resulting in low sensitivity of the protein analyte.¹⁹¹ As an alternative method, dialysis in phosphate buffer (50 mM, pH 7.4, 15 mM NaCl) was chosen using two exchanges of 4 hours and one final exchange overnight. Neither of these procedures gave positive results for the bioconjugation process, instead, it favored an increased reagent waste at the beginning of the synthesis.

Initial analysis of the samples was carried using the Thermo Scientific Q-Exactive™ Orbitrap mass spectrometer using positive ion mode (spectrum scan range was collected between 650-2500 m/z for 2 minutes at 17500 MHz resolution) which gave unsuccessful results. The ESI-MS spectra showed a large distribution of ions

corresponding to a high distribution of molecular weights from the bioconjugated HSF (Figure 20). The reason supporting this behavior is the composition of HSF that has two different subunits (L- and H-chain). In addition, bioconjugated HSF led to inhomogeneous modified ϵ -lysine residues. As a result, multiple charged species were identified when analyzed using ESI-MS. At first, this variation was attributed to the source of the protein, which may be glycosylated as reported in the literature.¹⁹² To discard this possibility, HSaF was acquired from another commercial source (EMD Millipore Inc.) with a stated protein purity of $\geq 90\%$. This protein led to the same result of multiple charged ions with similar charges, making it impossible to deconvolute the ESI-MS spectra. It was hypothesized that L- and H-chain would ionize to the same degree, because of the protein similarities, making ESI an inadequate method to analyze reaction completion. Furthermore, it has been reported, that the molecular characterization of the polymer–ferritin conjugates imposes many challenges because of their high molecular weights.⁸⁶



A)

Figure 20. Mass spectra from HSAF using ESI mass spectrometry.

Due to the difficulties found with the NAS and MMA, other alternatives were explored. Xu *et al.* introduced the use of GMA as an alternative to acryloylated proteins.¹⁸⁰ However, GMA can undergo self-hydrolysis under basic conditions.¹⁹³ Furthermore, when GMA in DMF (100 mg/mL solution) was added to the protein solution, two phases were formed due to low solubility of GMA in water, requiring the use of an increased amount of solvent for the bioconjugation reaction.

The bioconjugated proteins modified with NAS, MMA and GMA were first studied by the use of the well-known TNBS colorimetric assay (see section 2.3.3.3).¹⁸⁰ This assay addressed the detection and quantitation of unreacted terminal amines on the ferritin shell. This was accomplished employing HSF and BSA as a control proteins. BSA contains 60 addressable lysine residues, while HSF has an average of 55 and up to 72

addressable lysine residues on the exterior of HSF that were modified by NHS-ester/GMA acylation.¹⁹⁴ GMA bioconjugation was studied first by adding 100-fold excess towards HSF lysine residues. BSA showed an enhanced bioconjugation capability using the bioconjugation approach because all the lysine residues are somewhat exposed to the solution environment.¹⁹⁵ According to the experimental results, 13 out of 60 lysine residues can be acryloylated under 2 hours for BSA. In comparison, only 3 out of 7 lysine residues of the HSF can be acryloylated. The reaction was carried out over 18 hours. It was found that 32.6 (~50%) of the available lysine residues of BSA react, while only 10 (~14%) lysine residues are bioconjugated. Likewise, NAS was evaluated to show that 59 of BSA and 40 of HSF lysine residues can be modified under 14 hours. This difference can be attributed to the lower reactivity of GMA in comparison with NAS. This demonstrated that the nucleophilic substitution is favored with NHS esters in comparison with the ring opening that the glycidyl group undergoes. However, the modification of the protein with GMA allows the reaction of the glycidyl group with the ϵ -primary amine while preserving the net charge of the protein, favoring its stability and keeping the isoelectric point constant.¹⁹⁴ Thus, decreasing aggregation. The TNBS analysis was accurate as a tool to determine the amount of bioconjugated lysine residues, however, it was a time-consuming technique. During the development of the project, the chemistry department at the University of Waterloo acquired an Ultraflex, MALDI mass spectrometer. This technique can be used for high throughput analysis for proteomics at a low cost. As a result, TNBS analysis was no longer pursued.

A set of bioconjugation reactions utilizing NAS, MMA and GMA were proposed to understand the influence of the bioconjugation reagent over a time span of 14 hours. The experiment was carried out by adding (15 μ mol, 25 μ L of 100 mg/mL solution) of bioconjugation reagent into the protein solution every two hours to study how many lysine residues could be modified (1200 mEq excess towards total lysine residues per aliquot). This experiment was studied using MALDI, as shown in Figure 21.

After 14 hours GMA (142.15 g/mol) MMA (183.16 g/mol) and NAS (169.13 g/mol) could modify an average of 1.41 ± 0.50 , 2.28 ± 0.38 and 3.86 ± 1.20 lysine residues per ferritin subunit respectively. It was demonstrated that two aliquots of the bioconjugation reagent were enough to achieve more than 60% of the maximum lysine bioconjugation that could be achieved with each of the bioconjugation reagents. As a result, a minimum of two aliquots (3000 mEq, 50 μ L of 100 mg/mL solution) spaced by 45 minutes was required to produce an acceptable bioconjugated protein. Although the GMA was correctly quantified, the use of the GMA reagent for further experiments was not pursued because of the low number of bioconjugated lysine residues achieved after 14 hours of reaction.

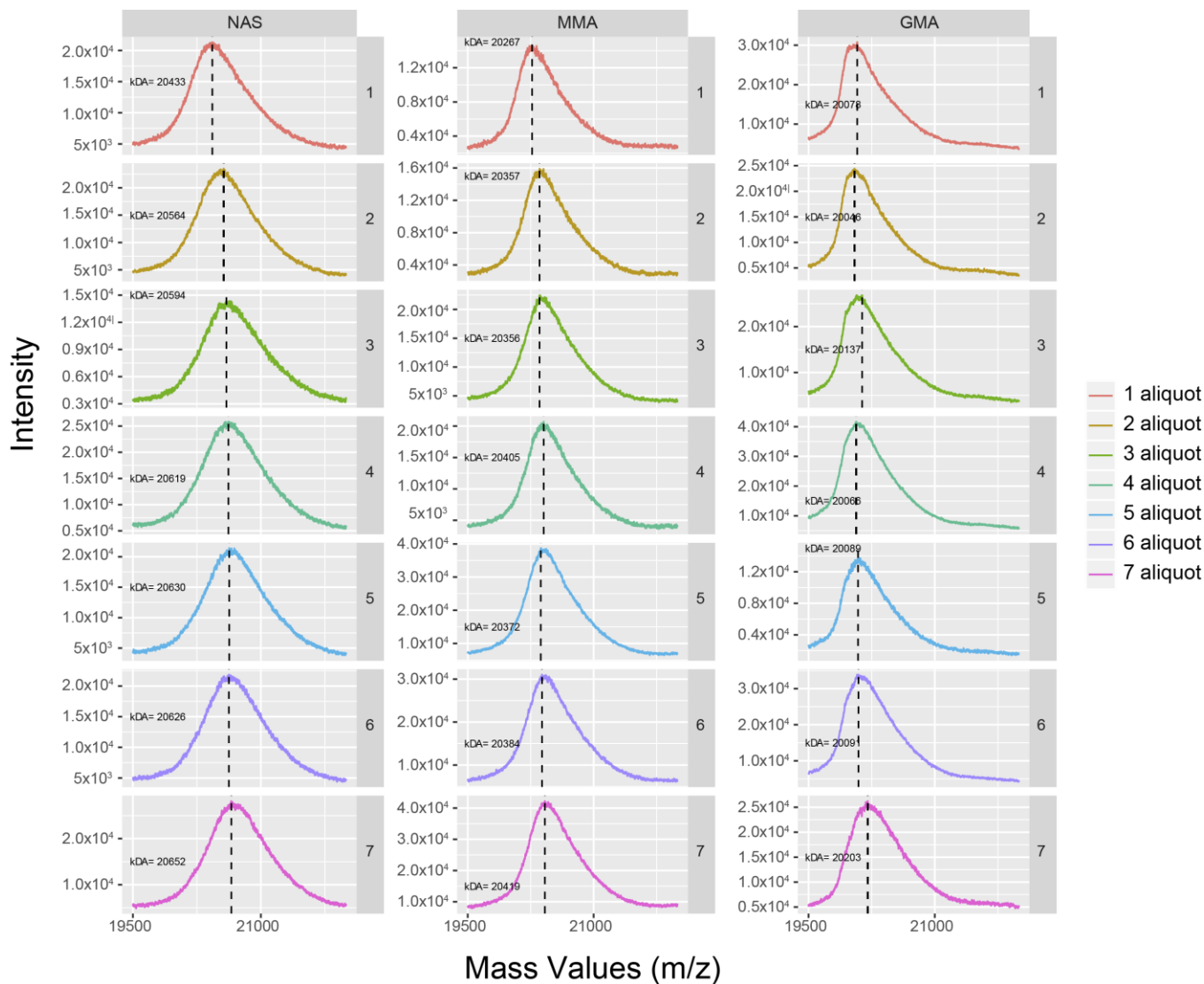


Figure 21 Acryloylated lysine residue yield employing increasing concentrations of different bioconjugation reagents (NAS, MMA and GMA) where the mass difference is evaluated from the WT-HSF average MW = 20000 Da to the highest frequency point on the weight distribution.

2.4.2 Temperature effect

Amidation reactions have been reported to be made under room temperature and at 4 °C.¹⁹⁶ It is expected that a decrease in temperature will reduce the hydrolysis of the ester group. However, the reaction rate decreased as well, it was expected that the rate was going to be sufficient enough to improve the efficiency of the coupling chemistry and increasing the degree of bioconjugation.¹⁹⁷ Figure 22 showed that lower temperatures produce lower bioconjugation, which showed that it was needed to determine the effect of the decreased hydrolysis rate on the bioconjugation studies. Despite this, it was clear that there is a linear relationship between the aliquots added to the mixture and the degree of labeling. It was desirable to explore the effectiveness of this reaction under various experimental conditions. To do so, a few researchers have proposed that the determination of free NHS by UV absorbance at 260 nm is a powerful method to follow the reaction.¹⁹⁸ This monitoring technique was unsuccessful to probe the presence of free NHS esters within the reaction to help verify the optimal time interval to carry out the reaction. After many failed measuring trials, a heuristic approach was made and reconfirmed that to make a successful labeling reaction the optimal time interval between aliquots was 45 minutes.

As previously mentioned, there is an evident increase on the labeling of the HSF when using NAS instead of MMA. This behavior may be attributed to the methyl group, which causes a decrease in the reactivity in comparison with the NAS reagent. However, this behavior is desirable because it facilitates a repeatable method to control the amount of lysine groups that can be modified on the ferritin shell.

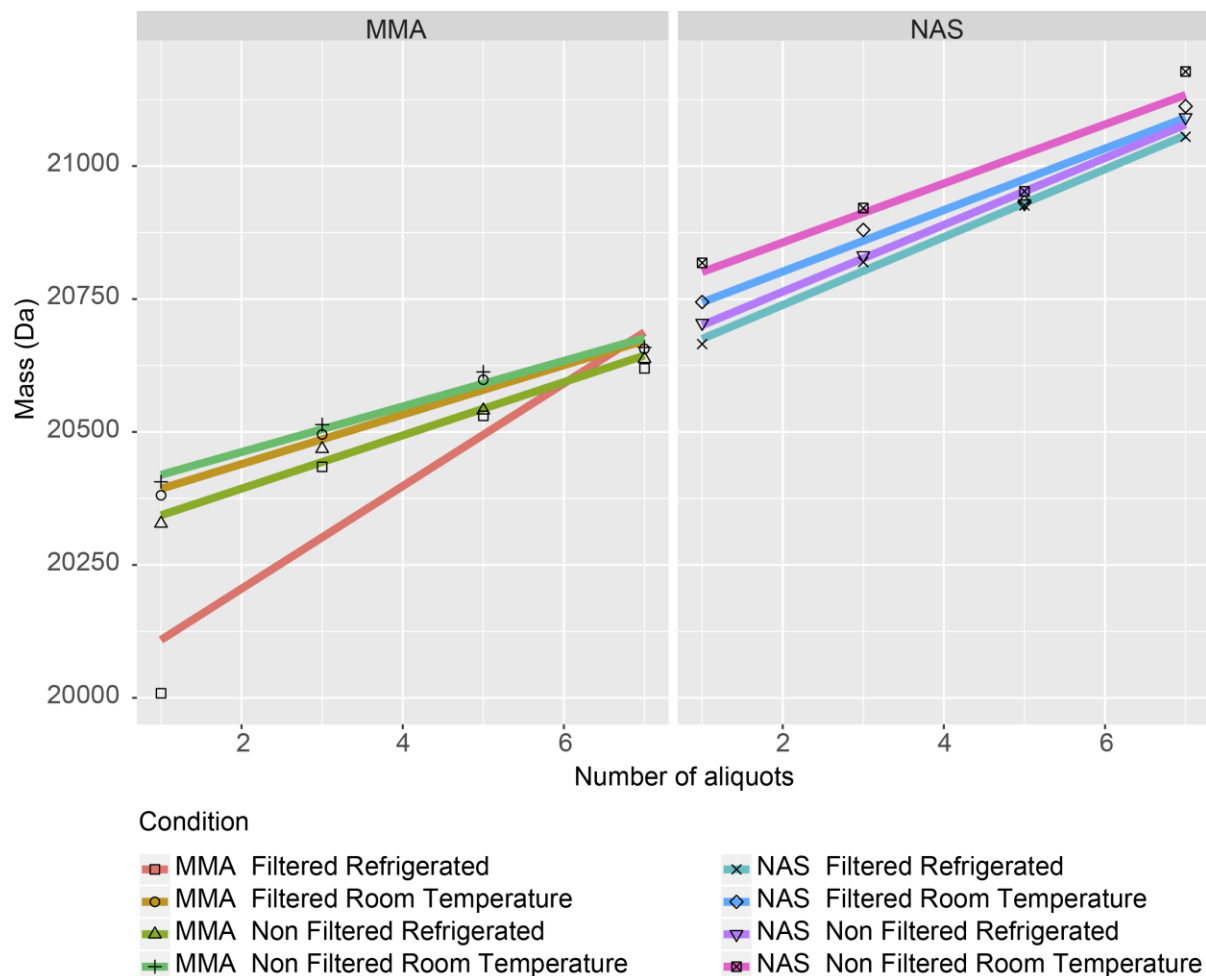


Figure 22. Effect of number of aliquots (~1500 mEq/aliquot) effect of bioconjugation reagent on modified HSF at 4 °C and 23 °C.

In addition to the temperature conditions explored above, it was necessary to gain further insight into the aggregation profile using DLS. The hydrodynamic radius (R_H) is affected by the bioconjugation of the HSF (Figure 23). It is important to note that HSF and HSAF have the same hydrodynamic radius.¹⁹⁹ However, it is shown that the greatest increase in the hydrodynamic radius was achieved using NAS as a bioconjugation reagent, which is in accordance with the fact that NAS is the reagent that covalently

modified the most acrylates on the ferritin surface. A trend was observed; MMA bioconjugation rendered a higher value of polydispersity index (PDI) of hydrodynamic radius for the modified ferritin compared to NAS, this will affect the cross-linking density of the hydrogel once the bioink has been polymerized.

Surface labeling of HSF had been achieved in the past.²⁰⁰ The labeling of charged groups of the HSF causes an irreversible change of their charge. In this case, due to the loss of primary amine moieties at physiological pH, the modified protein's pI will be decreased. Additionally, when there is a high degree of labeling, an increase in the polydispersity of the modified proteins will result. This in turn would make it more difficult to purify to homogeneity a unique protein with only one molecular weight. As mentioned above, the increase in temperature will have an effect on the extent of labeling. Furthermore, an increase of the temperature of the reaction will also affect the amount of protein aggregation over the amount of added aliquots to the reaction.

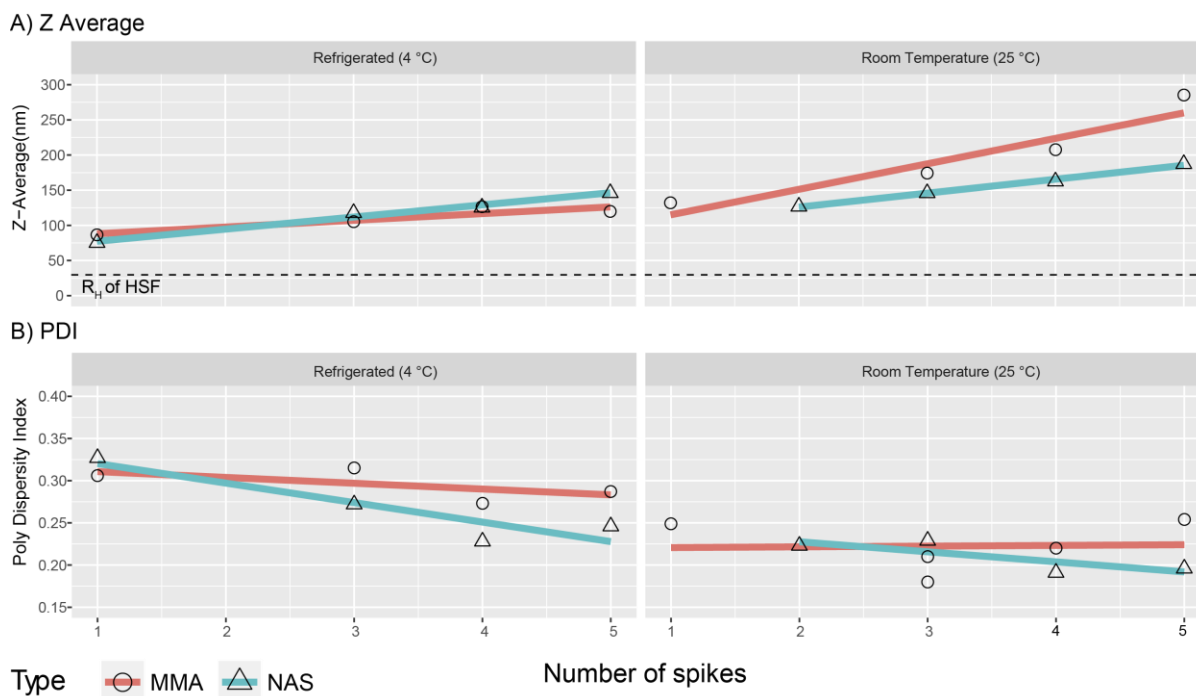


Figure 23. DLS determinations of the temperature effect on aggregation on modified HSF by the addition of aliquots of bioconjugation reagent (1500 mEq/aliquot) shown as A) Z-average and B) polydispersity index.

It was assumed that CLP conformation is preserved after the protein labeling; nonetheless, it is not guaranteed that the cage-like structure prevails for most subunits. To determine the integrity of the CLP, SEC of protein structure was utilized. More importantly, the intact 24-mer of the HSF CLP will had a retention time similar to WT-HSF. This finding suggested that the structure prevailed after surface functionalization.

However, it was necessary to correlate the aggregation with the intact structure by evaluating the HSF with a series of molar blending ratios of 1 through 7 aliquots (1500 mEq per aliquot) in increasing concentration steps of acryloylation reagents (MMA and NAS). The NHS labeled proteins were then screened by employing TEM. This technique

had been successfully utilized to visualize encapsulated guest molecules within Bacterioferritin.¹⁶⁸ Two TEM stains were used: uranyl acetate and molybdic acid, to determine the structure and the aggregation profile of the modified HSF. It was expected that the modified HSF appeared as a shell because the stains can penetrate all the protein channels (eight 3-fold and six 4-fold) by connecting the inner cavity to the solution with pore sizes between 0.3 and 0.4 nm.⁹⁰ After a few trials, uranyl acetate was discarded, and molybdic acid was selected as the method to use for TEM screening. Instead, as shown on panel A of Figure 24, commercial HSAF showed stain penetration within the inside of the capsule protein. The penetration of stain confirmed that single atom stains were small enough to transit across the native pores. In addition, the negative stain facilitates the determination that the protein shell remains intact through the labeling process, regardless of the amount of lysine residues being modified. For example, panels B and D show NAS and MMA modified proteins that had approximately 2.1 and 2.8 lysine residues modified respectively. However, there are distinct protein shells that are observable. In contrast, at higher labeling, there are no single protein shells that are observable, suggesting that aggregation is likely when higher labeling is achieved. These TEM studies showed that the cage-like structure is likely preserved (Figure 24).

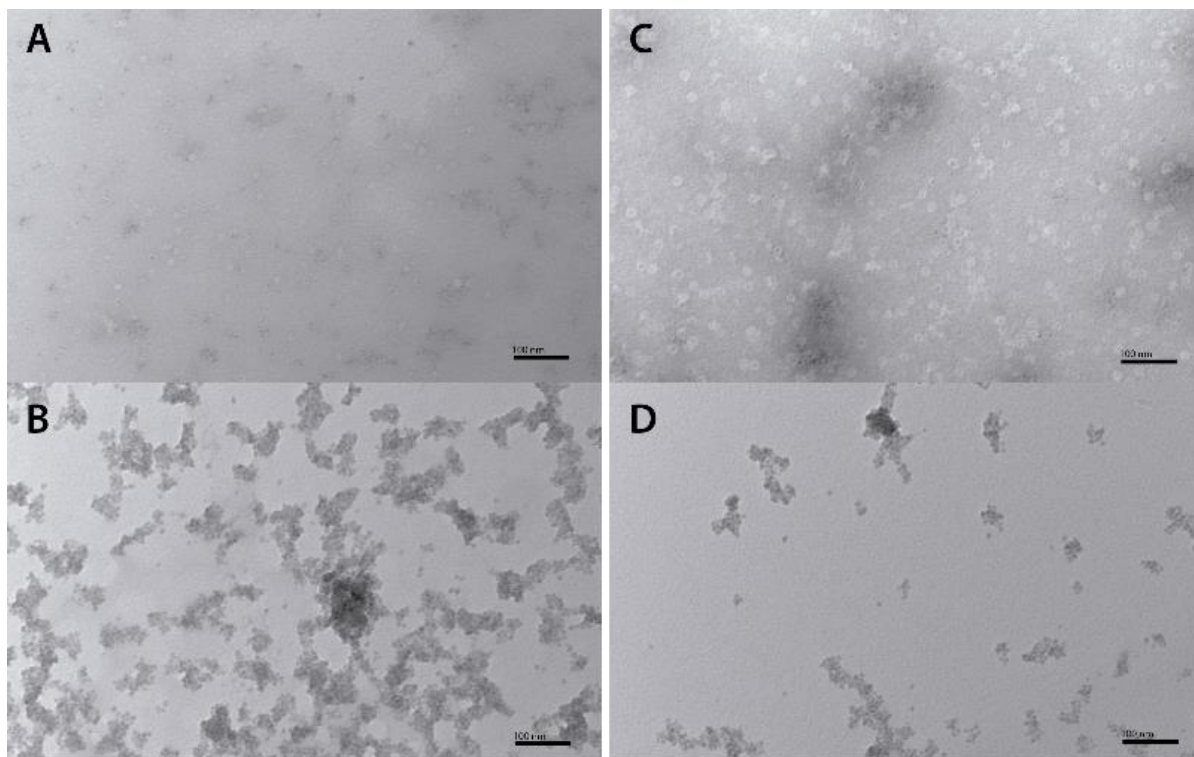


Figure 24. TEM studies for the evaluation of quaternary structure preservation as a result of bioconjugation with A) 1500 mEq of NAS, B) 10500 mEq of NAS, C) 1500 mEq of MMA, and D) 10500 mEq of MMA.

Further information from the bioconjugated protein was needed, as a result, SDS-page analyses were made on MMA-, NAS-bioconjugated and self-cross-linked HSaF using LAP. This experiment was done to confirm that bioconjugation was successful, and to explore the capabilities of the ferritin to undergo self-polymerization once it is exposed to FRP conditions. It can be interpreted from Figure 25 that not only the acryloylated ferritins (N026A, M026A) showed an increased molecular weight due to the addition of several acrylate groups, but also when the acryloylated ferritins were exposed to UV-light (406nm) under the presence of LAP, they may undergo self-polymerization. This theory

was supported by analyzing the gel band where polymerized N026A and M026A occurred. That is, there was a decreased intensity of the band near the trypsin inhibitor at 20,100 Da, whereas on the top of the well there was observed a broadening of the band, which had the same concentration as the acryloylated ferritins that were not exposed to the UV light. This suggested that a polymer with much larger molecular weight was not able to penetrate into the acrylamide gel.

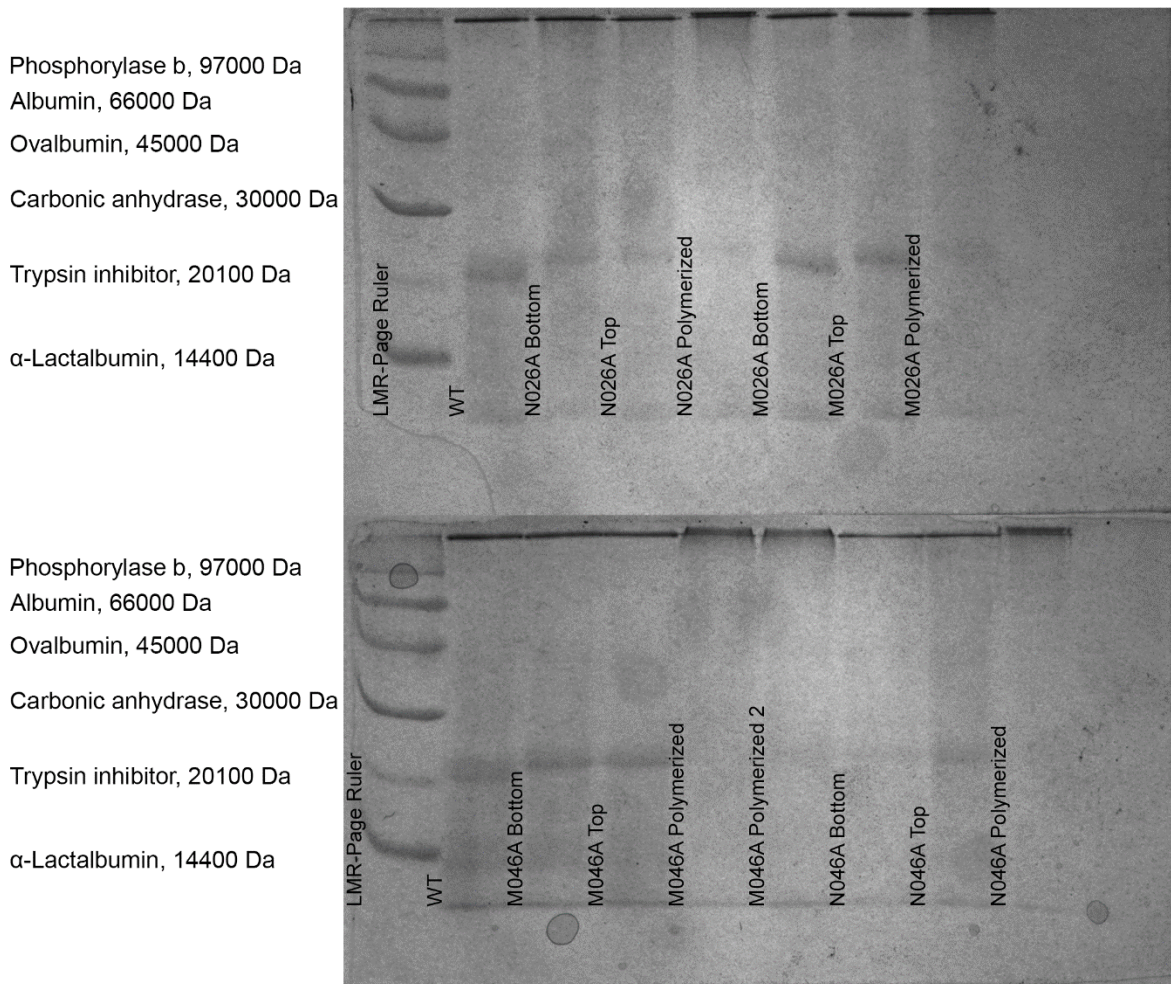


Figure 25. SDS-Page gel with WT-, acryloylated and polymerized ferritins.

2.4.3 Verification of vinylic moieties on HSF quaternary structure

NAS- and MMA-NHS esters were chosen to label HSF due to their capabilities to provide vinylic moieties that function as anchoring points for a free radical polymerization (FRP) with other vinylic moieties or Michael additions with thiol moieties. This stage was relevant because it defined the cross-linking density and the intermolecular hindrance of the modified proteins. At first, it was presumed that a simple method such as the use of a 5% KMnO_4 aqueous solution to screen for the oxidation of the vinyl moieties was sufficient.²⁰¹ However, the maroon protein solution of labeled HSF protein made it difficult to confirm if the vinylic moieties were present, or if they had undergone self-polymerization.

Furthermore, to analyze protein structural changes, DSC studies were carried out on the modified proteins (1-7 aliquots) as described in section 2.3.3.9. The proteins were purified using SEC as shown in section 2.3.2.9. However, unrepeatable results were achieved for these multiple runs. Therefore, the DSC evaluation of modified HSF was abandoned as a suitable mechanism to provide insights on the protein stability due to the acryloylation of the exterior of the protein cage. Instead, an instrumental approach was followed using ATR-FTIR and $^1\text{H-NMR}$ to verify if the labeled proteins had reactive vinylic moieties available to be further cross-linked in a second step.

It was possible to characterize the acryloylated ferritins by FTIR. This method monitors the formation of the C=C band 1380–1420 cm^{-1} vibration band due to symmetric bond stretching.

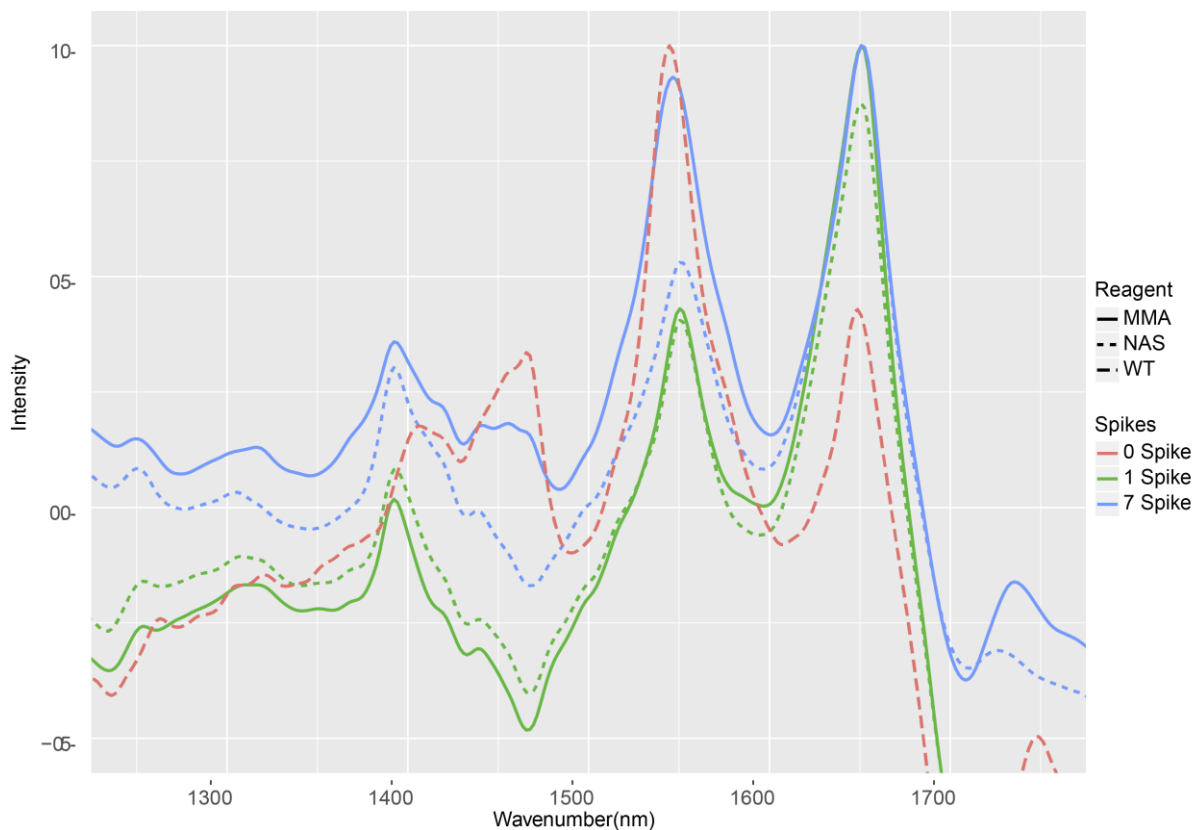


Figure 26. ATR-FTIR for the evaluation of the presence of vinyl moieties produced by of bioconjugation.

Supporting evidence for a successful bioconjugation was achieved through the analysis of $^1\text{H-NMR}$, where acrylic protons are shown near the 6 ppm range $^1\text{H-NMR}$. The signals are very distinct for each of the reagents. MMA-HSF [$^1\text{H-NMR}$ (600MHz, D_2O) δ 6.25 (d, 2H), 5.85 (d, 2H), 4.10 (m, 3H)], and NAS-HSF [$^1\text{H-NMR}$ (600MHz, D_2O) δ 6.40 (d, 2H), 6.20 (m, 2H), 6.02 (m, 2H), 5.85 (m, 2H)], show the presence of vinylic moieties, excluding the signals that come from the pure NAS and MMA which have been identified in Figure 27 in accordance to literature.^{202,203}

Furthermore, a ^{13}C -NMR analysis was attempted in a solution for 5 mg/mL of modified protein. After 7 hours of analysis, using ^{13}C proton-decoupled NMR, no observable resonances were present. This was likely due to the much lower abundance of the ^{13}C nucleus present in the sample, and much longer NMR experiments would have been required. These were not pursued.

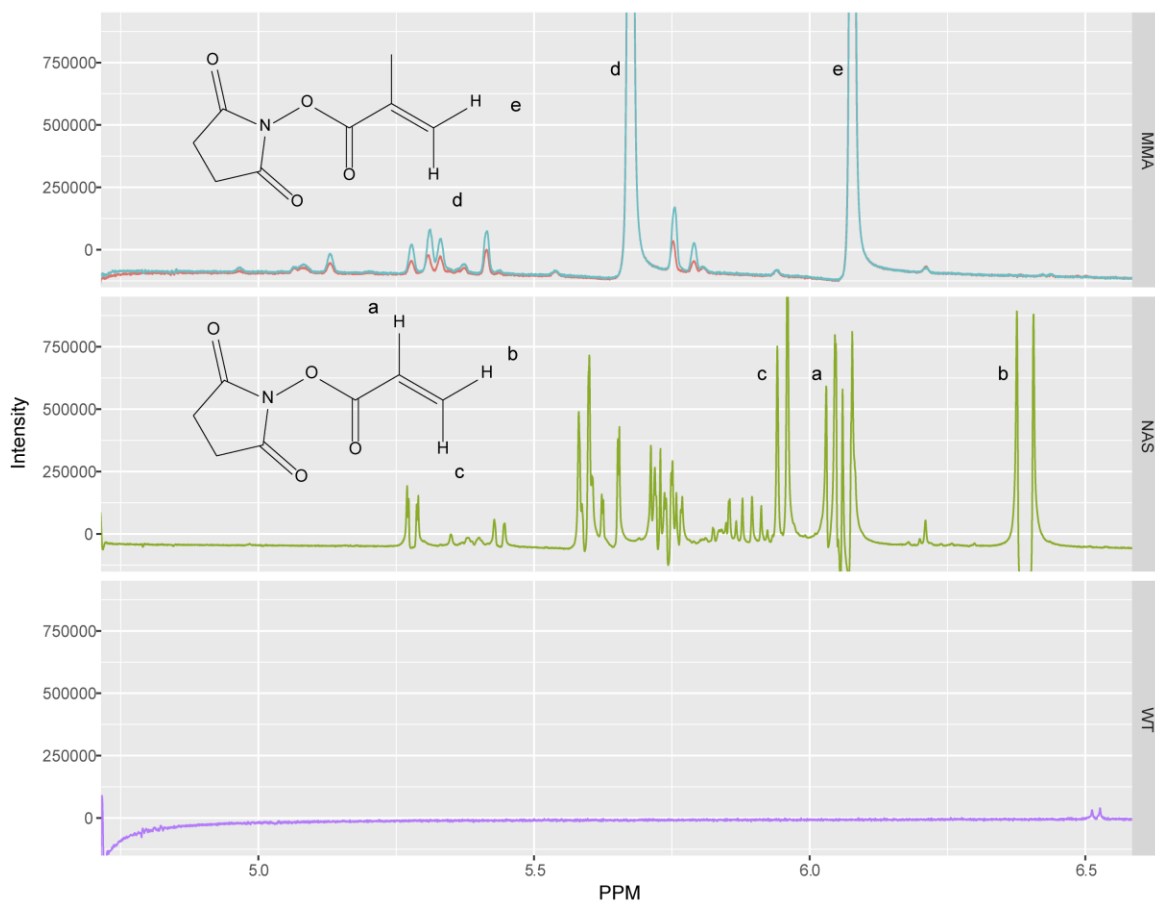


Figure 27. ^1H -NMR evaluation of the presence of vinyl moieties because of bioconjugation with NAS and MMA.

2.5 Conclusions

Here it has been shown that lysine residues of HSF can be chemically modified with different bioconjugation reagents (MMA, NAS and GMA), two of which gave high bioconjugation yields. The resulting modified capsule was a mixture of different modified lysine residues. It was shown that there was undesired aggregation effect as the bioconjugation degree (Addition of aliquots) was increased or as the reaction temperature was increased. Furthermore, it was discovered that the use of high levels of bioconjugation reagent led to irreversible aggregation and precipitation of the protein, which made it unsuitable for long-term storage. In addition, it was shown that vinylic moieties do not undergo Michael addition and remain available to undergo polymerization. The product synthesis was evaluated with TEM, FTIR and later by $^1\text{H-NMR}$ to demonstrate that the protein quaternary structure remains unchanged, but with the presence of acrylic moieties on the surface. The bioconjugation of the HSF was critical to introduce reactive moieties that could undergo a grafting mechanism. MMA was selected as the most suitable bioconjugation reagent for the introduction of acrylic moieties, because it provides much more control of bioconjugation with 2.28 ± 0.38 modified lysine residues per subunit (~ 55 modified lysine residues per cage), which is in agreement with the literature.

Chapter 3 Rheological properties of polysaccharide-polymer blends

3.1 Introduction

The viscoelastic behavior of proteins originates by a combination of weak intermolecular forces (Appendix A). Therefore, the resulting interactions are not permanent.²⁰⁴ Functionalization of hydrogels has been of interest for biomaterial applications. By doing so, a protein polymer conjugate might have a change in the storage modulus (G'), thermosensitivity and softening properties.²⁰⁵ Protein-polymer blends are difficult to characterize. Usually, they behave as non-Newtonian fluids, making the η_{app} a function of many other factors, that have not been mentioned before such as gelling mechanisms, polymer molecular weight, polymer concentration, temperature, cross-linker activity, and humidity.¹²⁹ Furthermore, Lawrence *et al.* demonstrated that there is a relationship between protein sequence and the macroscopic properties of protein networks in terms of rheological behavior.²⁰⁶ In addition, relaxation mechanics could be controlled by altering the protein sequence if the percentage of protein content is approximately above 10% of a polymer-protein melt.^{204,206}

As previously mentioned, PEGDA is frequently employed as a crosslinking agent because of the non-toxicity of PEG itself and this reagent can be readily chemically modified; however, it is not suitable for bioprinting because of its relatively low viscosity. However, many PEGDA-based hydrogels have emerged.²⁰⁷ Kraut *et al.* successfully characterized PEGDA-Poloxamer 407 blends using the power law method, correlating apparent viscosity with shear rate.²⁰⁷ Furthermore, it was confirmed that PEDGA-based

hydrogels suffer from shear thinning behavior, which favors the formation of smooth hydrogel strands, facilitating the 3D bioprinting of constructs that are viable up to 180 minutes. While not characterizing the same type of system, Patel *et al.* indicated that as PEGDA content increases; hydrogels become firmer due to the higher number of polymer chains and behave more elastically.²⁰⁸ More so, the use of a synthetic crosslinker with a polysaccharide can improve the gel state properties, while reducing the degree of polysaccharide degradation when exposed to high shearing/high-pressure conditions.²⁰⁹

To gain further insight into the unique properties of the polymer-polysaccharide blend, numerous rheological studies were undertaken in this thesis research. Particular attention to the rheological properties of the prepolymer, preparation, and characterization of the 60 bioinks were made (varying their weight percentages of PEGDA and TA) with appropriate concentrations for bioprinting without the bioconjugated protein. The purpose of the chosen TA was to identify the optimal concentration at which each component delivers the fastest bioprinting, the highest bioprinting resolution, the lowest pressure required for bioprinting, and the extent of its facilitation of gel swelling.

To do this, small strain oscillatory flow measurements were carried out for each prepolymer as a function of the thickening agent's weight percent to determine the change of the viscoelastic properties as a function of PEGDA weight percent. All the measurements were adjusted to the Ostwald-de Waele approximation to determine the behavior of the viscosity as a function of the strain rate. Furthermore, the materials were classified according to their mechanical loss angle ($\tan \delta$), into viscoelastic or non-elastic bioinks. The last step was to analyze, by the use of image recognition software such as

FUJI, the best performing bioinks on which they bioprinted to analyze the deviation in the dimensions (width, height, and length) in order to determine the resolution of the bioprinted construct.

The results of these rheological analyses provide extensive details regarding the optimal composition of the desired bioink and offer a fascinating insight into the mechanisms that are involved in the gelation of the desired construct.

3.2 Materials and Methods

3.2.1 Materials

Sodium alginate (Alg), sodium carboxymethylcellulose (CMC), xanthan gum (XG), Pluronic F127 (PL), PEGDA 700, 2000, 6000, NAS and MMA were purchased from Aldrich (Milwaukee, USA) and used without further purification. Ethyl (2,4,6-trimethyl benzoyl)phenylphosphinate (CAS: 84434-11-7) was purchased from AK Scientific (Union City, CA; USA) and used without any further purification. Standard Regenerated Cellulose (RC) Membrane Dry Spectra/Por®4 Dialysis Tubing 12-14 kDa MWCO was purchased from Spectrum Labs (Rancho Dominguez, CA, USA).

3.2.2 Instrumentation

3.2.2.1 Rheometry measurements

The viscosity of the polymer solutions without UV polymerization was measured on a Bohlin CVO 100 digital rheometer (Viscometry mode, 4° cone/plate geometry, gap

= 150 μm). Dynamic viscosity measurements were conducted at 25 °C and in controlled shear rate (100–400 s^{-1}).

3.2.2.2 BioBots 1 Bioprinter

The bioprinting was carried out using a Biobots 1 3D bioprinter (Allevi, CA, USA) equipped with a single extruder system powered with a pneumatic air compressor system capable of providing 0-100 PSI (Figure 28). The bioprinter onset polymerization was carried out with a visible blue light lamp mounted on the lower section of the extruder cartridge [405 nm wavelength (λ) lamp (Light power = 10%, $I_0 = 10 \text{ mW/cm}^2$)] to cure biomaterials. The cartridge was set-up with a ten mL Luer-Lok syringe with a 1/4" straight cannula blunt end tip gauge either 30 or 32 from Fisnar (Germantown, Wisconsin, USA).

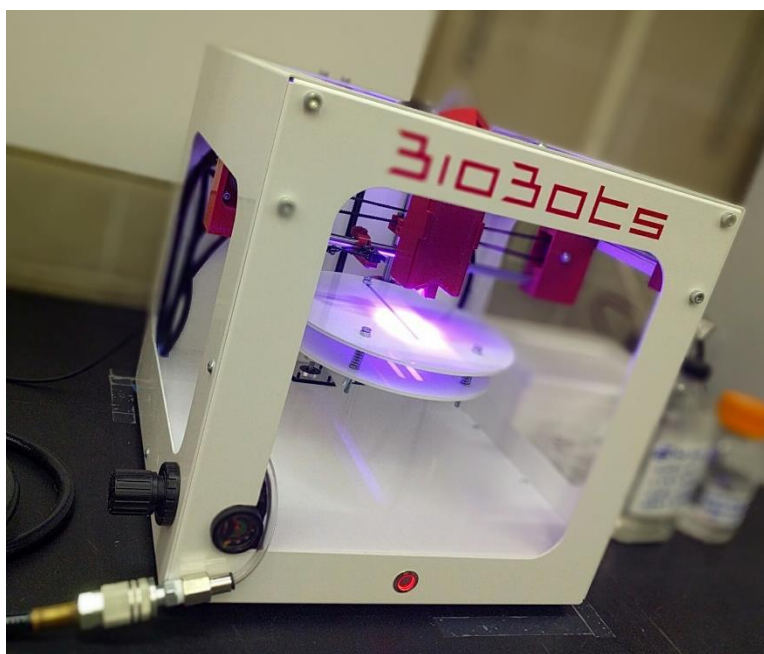


Figure 28. BioBots 1 bioprinter used for the studies of the aHSF-PEGDA-TF based bioinks.

3.2.3 Methods

3.2.3.1 Reagent synthesis

The initiator LAP was synthesized following the process described by Majima *et al.* via the Michaelis–Arbuzov reaction (Figure 29).^{210,211} Consequently, the synthesis begins with the addition of LiBr (2.482 g, 0.0285 mol; 4 eq) to 2-butanone (0.060 L) into a round bottomed flask with a magnetic stirrer. The resulting mixture was heated to 60 °C, and followed by the slow addition of ethyl (2,4,6-trimethyl benzoyl)phenylphosphinate (2.260 g, 0.0071 mol; 1 eq) to the mixture. The reaction was carried for 20 minutes and then cooled down for 2 hours without stirring. After the reaction reached room temperature, the precipitate was filtered using a 20 µm mesh size filter paper (Whatman, Maidstone, United Kingdom) protecting it from light during the filtration. The precipitate was washed twice with 2-butanone (0.050 L) and dried under vacuum at room temperature for 16 h to remove excess solvent.

Synthesis of the desired compound was verified using ¹H-NMR (300MHz, D₂O) δ 7.65 (m, 2H), 7.45 (m, 1H), 7.35 (m, 2H), 6.80 (s, 2H), 2.20 (s, 3H), 1.90 (s, 6H). These results are consistent with the information reported by Fairbanks *et al.*⁹⁶

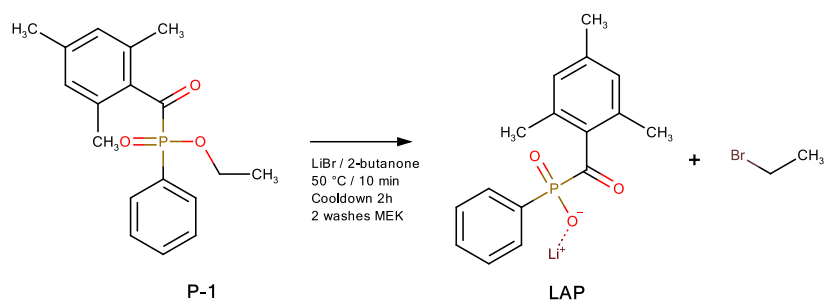


Figure 29. Synthesis proposed by Majima *et al.* to yield lithium acyl phosphinate from ethyl (2,4,6-trimethylbenzoyl)phenylphosphinate (P-1).²¹⁰

3.2.3.2 Study of bioinks without thickening agent

To determine the behavior of the bioink inside the bioprinter cartridge, a preparation varying the aHSF at a fixed concentration of the PEGDA was made. The photoinitiator, 0.17 mM lithium acylphosphinate, a reagent proposed by the manufacturer of the bioprinter, and 50% (v/v) PEGDA and aHSF (0.1 %, 1.20×10^{-4} mmol, 72 modified lysine residues per cage) stock solutions were made. Then, three separate bioinks with a fixed PEGDA concentration at 35% but varying the concentration of the aHSF (1.20×10^{-5} , 1.80×10^{-5} , 2.20×10^{-5} mmol) were prepared. Each bioink was exposed to 405 nm wavelength where the concentration of the photoinitiator was varied from 0.0017 M (0.05% v/v) to 0.17 M (5.00% v/v) in the following steps 1.72 mM, 3.44 mM, 17.22 mM, 34.44 mM, 86.10 mM and 172.20 mM. The characterization of the polymerization was made visually to determine if the polymerization had taken place.

3.2.3.3 Wetting agents for reduction of surface tension

To reduce the contact angle that occurs between the drop of bioink and the cannula of the printer syringe, wetting agents described by Moghimipour *et al.* such as glycerin, polysorbate 80 and Pluronic F-127 were evaluated.²¹² Stock solutions of the wetting agents were prepared at 20% weight/volume. Later, 1.50 mL of bioink was prepared containing either 0.50%, 2.50%, and 5.00% Pluronic F 127 (PL); 0.20%, 1.00% and 2.00% glycerin; or 0.10%, 0.25% and 0.50% of polysorbate 80. Then 1.00 mL from each bioink was placed inside the printer cartridge to assess further if the mixture of the wetting agents with the bioink was suitable for direct bioprinting using either 30 gauge 1/8" blunt end tips, or 100 µm Micron-S Micro Bore (Fisnar, USA) tips.

3.2.3.4 Thickening agent and pressure dependence

To assist in printability and resolution, thickening agents (TA) such as Alg, XG, CMC and PL were evaluated. Recommended values reported in the literature indicate that for increased viscosity, ranges between 1%-7% for Alg, 1.00%-5.00% for XG, 0.50%-3.00% for CMC and 10.00-20.00% for PL are recommended.²⁰⁷ Stock solutions of the TA of the highest value for the latter range were prepared. Then, preliminary blends were prepared to evaluate the pressure needed for bioink bioprinting as shown in Table 5.

Table 5. Preliminary evaluation of bioink printability at different pneumatic pressures

TA	Percentage	PEGDA	LAP	psi
ALG	6.03%	10.78%	0.06%	20
CMC	2.35%	16.35%	0.14%	15
CMC	2.59%	10.78%	0.06%	15
Pluronics	16.53%	13.79%	0.06%	18
XG	4.13%	13.79%	0.06%	5
XG	3.82%	19.10%	0.05%	5
XG	4.27%	10.69%	0.12%	25

3.2.3.5 TA-PEGDA bioink formulations

To determine the subset of bioinks with desirable features for extrusion bioprinting, 60 bioinks, with a volume of 10 mL each were prepared. To evaluate a representative spectrum of bioinks, the concentration of crosslinking and TA were varied according to Table 6. The range over which the crosslinking reagent was varied comprised four different weight/volume percentages (8, 12, 15, and 20%). Likewise, four different TA such as alginate (A), carboxymethylcellulose (CMC), xanthan gum (XG), and a triblock copolymer, Pluronics F127 (PL) were evaluated. The weight/volume percentages employed were Alg: (3, 5, 7, and 9%), CMC: (6, 8, 10, and 12%), XG: (2, 4, and 6%) and PL: (12, 14, 16, and 18%).

To guarantee the preparation of the bioinks, the liquid components were added first. That is, 10 mL of the PEGDA solution was added into a Corning® 15 mL centrifuge tube. Then, the thickening agent was quickly added followed by a thorough shaking process. Each bioink was allowed to rest 30 minutes on the bench to guarantee hydration

of the thickening agent before mechanical stirring with a spatula. To homogenize the bioink and remove the trapped air, two centrifugation steps at 5400 rpm (clinical centrifuge) were made. Each bioink was labeled and stored at 4°C for further evaluation.

Table 6. Composition of the initially tested bioinks for rheological studies

		Poly (ethylene glycol) diacrylate (P)			
		8%P	12%P	15%P	20%P
Alginate (A)	3%A	1	2	3	4
	5%A	5	6	7	8
	7%A	9	10	11	12
	9%A	13	14	15	16
Carboxy Methyl Cellulose (CMC)	6%CMC	17	18	19	20
	8%CMC	21	22	23	24
	10%CMC	25	26	27	28
	12%CMC	29	30	31	32
Xanthan Gum (XG)	2%XG	33	34	35	36
	4%XG	37	38	39	40
	6%XG	41	42	43	44
Pluronic F 127 (PL)	12%PL	45	46	47	48
	14%PL	49	50	51	52
	16%PL	53	54	55	56
	18%PL	57	58	59	60

3.2.3.6 Linear Viscoelastic region determination

The linear viscoelastic region (LVR) was determined using stress sweep rheometry measurements on each set of bioinks. To perform LVR measurements, the bioinks that are at the extreme values in Table 6 were selected. Furthermore, two of the middle bioinks were measured for each set to confirm the trend. Given this, the LVR was measured for XG samples: 33, 36, 38, 41, and 44; CMC samples: 17, 20, 23, 26, 29, and 32; PL samples: 45, 48, 50, 55, 57, and 60. Lastly, measured Alg samples were: 1, 3, 7, 10, and

15. To categorize the bioink's properties, an empirical classification was made based on their flow capacity.

This division of liquid and gels/solids was justified based on the concept that depending on the viscosity of the bioink, the defined maximum stress values will vary as shown in Table 7. Furthermore, all samples were measured using a CP4/40 LS cone-shaped plate spaced 150 μm from the sensing plate. Measurements were conducted at room temperature with a 5-second delay between measurements. All measurements were performed using stress sweep mode. In total, 30 steps were taken in-between the ranges of the frequency with an up/down frequency sweep.

Table 7. Settings for the Bholin Rheometer to measure the respective bioink's LVR

Material	Frequency Range	Stress Range(Pa)	Max Strain(Pa)
Alginate 3%	0.05-1 Hz	0.5-90	150
Alginate 5%	0.05-1 Hz	0.5-90	150
Alginate 7%	0.5-5 Hz	0.5-300	15
Alginate 9%	0.5-5 Hz	0.5-300	15
CMC 6%	0.05-1 Hz	0.5-90	150
CMC 8%	0.05-1 Hz	0.5-90	150
CMC 10%	0.5-5 Hz	0.5-300	15
CMC 12%	0.5-5 Hz	0.5-300	15
Pluronic F-127 12%	0.05-0.5 Hz	0.5-30	150
Pluronic F-127 14%	0.05-0.5 Hz	0.5-30	150
Pluronic F-127 16%	0.05-0.5 Hz	0.5-30	150
Pluronic F-127 18%	0.05-0.5 Hz	0.5-30	150
Xanthan Gum 2%	0.05-1 Hz	0.5-90	150
Xanthan Gum 4%	0.05-1 Hz	0.5-90	150
Xanthan Gum 6%	0.05-1 Hz	0.5-90	150

To determine the LVR of the different bioinks, a script in R was developed. The code was developed to scan each sample's measurements and determine the LVR, where there is a change in 10% of the slope from the relationship between G' concerning the logarithm of the stress. These results determined the adequate regions on which the oscillation sweeps could be made.

3.2.3.7 Oscillation sweeps determination

Oscillation sweeps were performed for all the bioinks described in Table 6 to determine their viscosity as a function of the strain rate, and relative position of the storage and loss modulus as a function of the strain rate. To perform these oscillation measurements, all materials were measured at room temperature using a CP4/40 LS cone plate. Furthermore, measurements were performed using oscillation mode. To do so, the rheometry was set for a continuous oscillation. In total, 15 frequencies were selected between the ranges of the frequency with an up/down frequency sweep. An interval of 10 seconds was given in-between measurements. Based on the LVR measurements, the maximum stress used for each sample is given in Table 8.

Table 8. Frequency range and Maximum Stress Values for Oscillation Experiments

Thickening Agent	Frequency Range	Max Stress(Pa)
Alginate 3%	0.1-1.5 Hz	1
Alginate 5%	0.1-1.5 Hz	1
Alginate 7%	0.1-5 Hz	10
Alginate 9%	0.1-5 Hz	10
CMC 6%	0.1-1.5 Hz	1
CMC 8%	0.1-1.5 Hz	1

Thickening Agent	Frequency Range	Max Stress(Pa)
CMC 10%	0.1-5 Hz	10
CMC 12%	0.1-5 Hz	10
Pluronics F-127 12%	0.05-0.5 Hz	0.4
Pluronics F-127 14%	0.05-0.5 Hz	0.4
Pluronics F-127 16%	0.05-0.5 Hz	0.4
Pluronics F-127 18%	0.05-0.5 Hz	0.4
Xanthan Gum 2%	0.1-1.5 Hz	1
Xanthan Gum 4%	0.1-1.5 Hz	10
Xanthan Gum 6%	0.1-1.5 Hz	10

The viscosity was plotted as a function of the frequency on a log scale for all samples. The equation of a line was fitted to each plot, and the slope of the line was recorded.

3.2.3.8 Bioprinting resolution experiments

Bioinks 6, 11, 14, 22, 26, 30, 34, 38, and 42 were selected for bioprinting based on the oscillation and linear viscoelasticity region measurements data. Furthermore, 1.72 mM of LAP was added to each bioink for the polymerization of the PEGDA as studied in section 3.2.3.1. Bioprinting conditions, as demonstrated in Appendix C, were set based on previous experiments and fixed for all samples. To bioprint with the selected bioinks, the air compressor pressure was adjusted to maintain a constant filament radius depending on the bioink at hand. To bioprint successfully, 5 psi, 15 psi, 25 psi and 40 psi were selected for XG, Alg, CMC and PL, respectively. To examine bioprinting resolution, a three-dimensional model, as shown in Figure 30, was bioprinted. It consists of an array of rectilinear objects varying in size and height. The exact dimension of each of the objects will depend on some layers that are stacked one on top of each other. The first layer

height is 0.150 mm and each extra layer adds 0.120 mm to the model. Also, the models side are for light blue: 0.250 cm, orange: 0.500 cm, green: 0.750 cm and purple: 1.00 cm. Following bioprinting, images of the model were taken and analyzed using the ImageJ software. Here, the sides and height of each object were measured and compared to their expected value. Furthermore, the radius of curvature for each of the corners was measured and averaged for each object. This value provided the metric for determining the angular sharpness of each object.

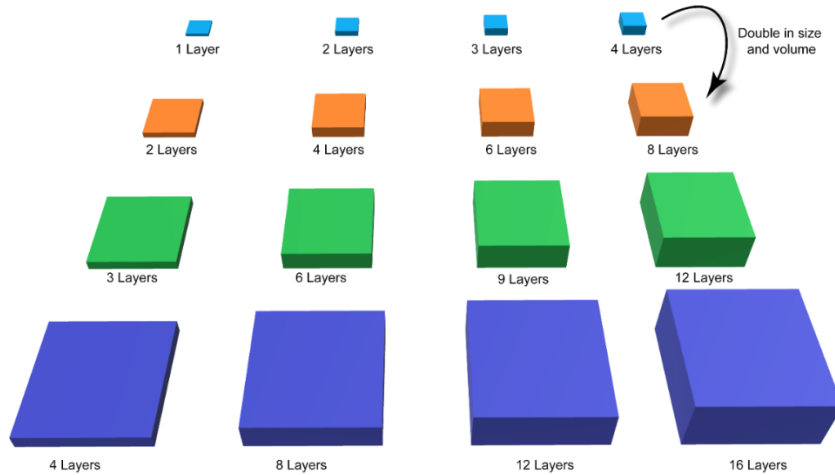


Figure 30. Schematic of bioprinting models used for testing resolution capabilities of the BioBots 1 bioprinter

3.3 Results and discussion

3.3.1 Linear dynamic viscoelastic properties

The purpose of this chapter was to analyze the rheological properties of the bioinks to be used in the extrusion-based bioprinting process. This analysis was explored first by a student under my supervision, Matthew Nguyen. To successfully bioprint any material, an initial screening of the bioprinter parameters was made (Appendix C). Initially, the bioinks were supposed to be a mixture of two components: a) aHSF, and b) PEGDA of different molecular weights ($MW_{\text{average}}=250, 700, 2000, \text{ and } 6000$). However, it was noticed during the initial bioprinting evaluations (section 3.2.3.1) that PEGDA bioinks were difficult to bioprint using extrusion systems. The reason was attributed to low viscosity from the solutions that could not withstand elongation forces needed for bioprinting.

The introduction of wetting agents that reduced the bioink viscosity, decreased surface tension and improved the flowability, was a solution to the difficulties encountered with the continuous bioprinting stream (section 3.2.3.3). The purpose was to reduce the behavior of the bioink droplet to stick to the side of the needle before touching the bioprinting platform surface. However, the addition of these agents not only did not facilitate the bioink bioprinting but also increased the spread on the solid bioprinting platform surface, decreasing the fidelity of the bioprinting. To allow this approach to work a hydrophilic surface to attract the droplet was needed instead of flat glass.²¹³ As a result, the research was focused on how to increase the bioink rheological properties.

A critical component to bioprint a bioink, as stated by Marques *et al.*, is the use of materials that increase the rheological properties of the PEGDA based prepolymer to be bioprinted.²⁰⁹ From here on, these materials are going to be addressed as TA. The purpose of the TA is to facilitate a mechanism to control the rheological properties of a given bioink. Furthermore, these materials need to allow the flow of the desired ink while reducing the spread of a given solution once is deposited on a surface of set inside a cartridge where shear stress was applied onto the bioink. To do so, the research was limited to investigation of the effect of three biodegradable polysaccharides and a synthetic triblock copolymer carboxymethylcellulose, alginate, xanthan gum and Poloxamer 407 (Pluronic F127), respectively (Figure 12). An initial screening of the adequate TA concentration was made (section 3.2.3.4). After this screening, the selection of 0.05% of initiator was made.⁹⁴

To further optimize the bioink composition, a set of 60 bioinks was prepared by varying the ratio between TA and PEGDA, which were the major components of the bioink (section 3.2.3.5). This was to optimize the bioprinting conditions, trading off over three variables: printability, viscosity, and pressure. The PEGDA percent range 8%-20% was chosen to maintain a suitable network pore size and matrix density reported by other authors.²¹⁴⁻²¹⁷

3.3.1.1 Linear viscoelastic region determination

It was necessary to analyze the bioinks and to determine their LVR (Appendix A). To determine the LVR, the rheometer was used in stress sweep mode, which applied a fix strain rate to the bioink. In return, the plate measured the stress, G' and G'' as a function of the total strain. All parameters were measured in a range of strain frequencies up to a user-specified maximum. The LVR was identified as the point where a deflection of 10% from a flat line was shown by plotting $\text{Log}(G'')$ versus $\text{Log}(\text{Stress})$ (Figure 31). The deflection of this flat region corresponded to the end of the LVR. However, the flat region of the G'' measure for the viscosity of the non-sheared sample. The analysis of the LVR at all frequencies was time-consuming (20-40 minutes depending on the sample), therefore, only a representative set of the bioinks was analyzed, as specified in section 3.2.3.6. The extreme values of the set of TA were selected (e.g., highest [PEGDA] and [CMC], lowest [PEGDA] and [CMC]). The reasons are that it is expected that the LVR range should vary proportionally as a function of the $[\text{TA}]/[\text{PEGDA}]$ weight percentage. By determining the LVR at the limiting values, we expected to obtain the LVR within the selected range. During the analysis of the bioinks, it was noted that the LVR is dependent on the [PEGDA] at low [TA], however, as [TA] increased, the contribution of [PEGDA] in the LVR decreased significantly. To demonstrate this, the two extremes of the PEGDA were also analyzed. Furthermore, the two middle elements of each set of bioinks were analyzed. This was to ensure that there was no local maximum/minimum when the LVR was varied as functions of both the thickening agent weight percent and the PEGDA.

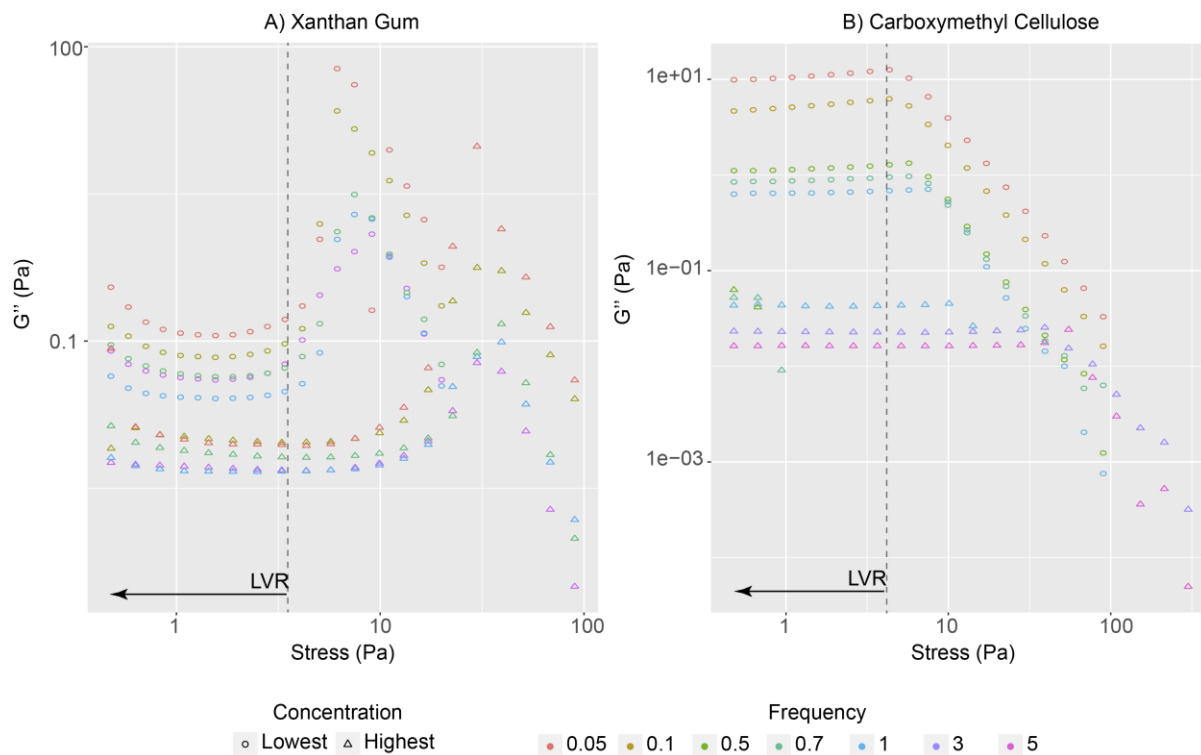


Figure 31. Log scale plot of the loss modulus as a function of the stress for a) XG and b) CMC at a range of frequencies 0.05-5.00[Hz], the LVR is indicated here.

It was noted that testing a less viscous sample using the high-frequency screening parameters might cause the liquid sample to burst from the equipment. Therefore, it was necessary to adjust the values of maximum stress value to guarantee that the analysis made was going to be representative depending on the viscosity behavior of the TAs. Once the LVRs, using stress sweep measurements, were performed the lowest value of all the LVR cutoffs was selected for each TA to guarantee that all the bioink mixtures kept their linear response and consolidated in Table 8 of section 3.2.3.7. Furthermore, the bioprinter, by design operated in the non-linear region of the LVR for the selected TAs.

3.3.1.2 Dynamic Oscillation Measurements

Dynamic Oscillation experiments involved applying a sinusoidal strain to the sample at varying frequencies. This frequency is proportional to the shear rate. The maximum stress value was set such that all samples were measured within the LVR. The purpose of oscillation measurements was to determine the dynamic properties of each material such as the loss (G'') and storage (G') moduli, which describe the viscoelastic properties of the material. Furthermore, similar information can be empirically determined from the phase shift between the applied oscillations of the plate to the oscillation in the material. This phase shift is referred to as the mechanical loss angle (δ), which is a relationship of the loss and storage moduli as $\tan \delta \equiv G''/G'$. It is confined to $0 \leq \delta \leq \pi/2 \text{rad}$ where 0 corresponds to the behavior of purely elastic, and $\pi/2 \text{rad}$, to the behavior of a purely viscous material. This is the cyclic integral of the shear stress response to small amplitude oscillatory shear, and concerns the shear strain.²¹⁸ Therefore, this measurement can be used to demonstrate how a bioink will behave, by comparing G' , G'' and δ . Specifically, these measurements provide information on the ease at which a bioink will flow once pressure is applied during bioprinting, and how quickly the network recover after the bioink has left the nozzle. To determine which of these events leads to the shear thinning or thickening, dynamic tests were conducted to determine the viscoelastic behavior of the material.

3.3.1.2.1 Viscosity Studies

The 60 bioink blends were analyzed to understand how the percentage of TA influences the viscosity of the bioinks. Analyses of the apparent viscosity of the bioink blends as a function of shear rate showed that all samples exhibited a high shear thinning behavior regardless of the TA and its concentration (Figure 32). Due to the sensitivity limits of the rheometer at low shear rates, the apparent viscosity of the TA-PEGDA bioinks were evaluated at shear rates above 0.1 Hz. To obtain relevant data, the viscosity and shear rate is usually plotted on a log scale; however, Cox and Merz, while doing a rheological analysis of polysaccharides, reported that the curve of apparent viscosity versus shear rate was very similar to the curve of complex viscosity versus frequency.²¹⁹ The Cox and Merz rule is not obeyed in semi dilute solutions and at lower frequencies and shear rates. Therefore it was essential to have concentration values above 1% of TA.²²⁰

First, as the frequency increases, some of the forces holding the gel structure together may weaken and as a result, decrease the viscosity of the hydrogel. The shear-thinning viscosity of the bioinks results from disaggregation of the network formed by the polysaccharide particles and PEGDA particles and the alignment of individual molecules in the direction of the flow.²²¹ Unfortunately, a zero shear viscosity was not determined to verify weight in the viscosity contribution of every component in the mixture. However, it was shown that the slopes of the plots became nearly proportional. This suggested that the polysaccharide content mainly dominated the intermolecular interactions that determine the viscosity from the TA network structure. A steeper slope was identified with

xanthan gum than with any other TA. It has been reported that the chain-chain association in xanthan gels can be modulated by salt content and temperature.²⁰⁵ Furthermore, it is widely known that for solutions with increased viscoelasticity, quick thinning due to a more particulate structure of dissolved xanthan will result. The reason is attributed to the large size of individual xanthan molecules (length $\sim 1 \mu\text{m}$) and a change in the density of junction zones of the elastic network formed by side-by-side associations.^{220,221}

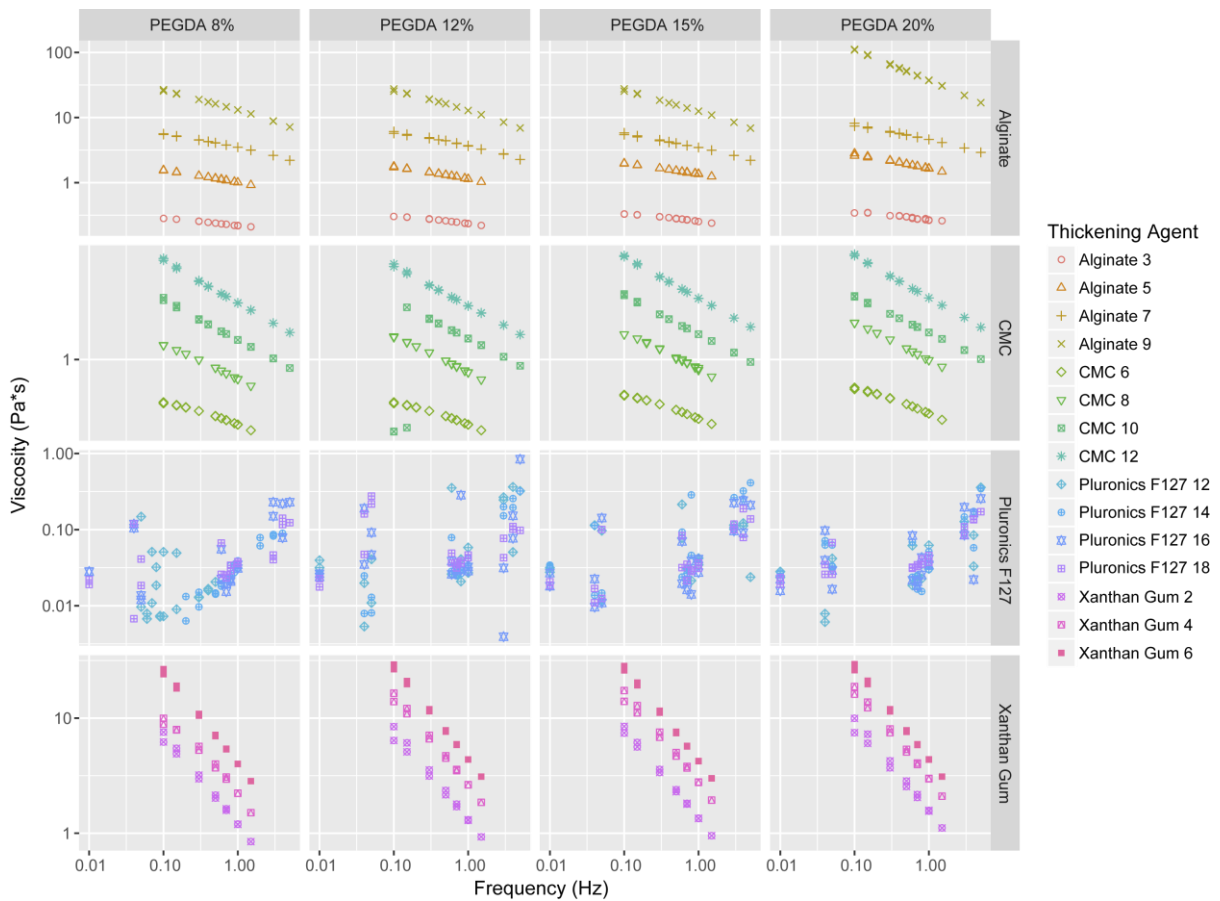


Figure 32. Log scale plot of the viscosity as a function of the frequency of the TA.

Determination of the viscoelasticity of Pluronics F127 could not be characterized at the frequency range previously mentioned. At 25 °C, the solutions underwent a crystalline transition. It has been reported that the rheological behavior of highly concentrated solutions in the crystalline phase of PEO–PPO–PEO are unsuccessful because of the presence of nonlinear viscoelastic regions. Hence the viscoelastic properties also change.¹¹²

It was found that the viscosity of neat PEGDA was independent of the applied frequency, whereas all TA-PEGDA dispersions exhibited notable shear thinning behavior, in agreement to what has been reported in the literature.²²¹ It was anticipated that varying the PEGDA concentration in the bioinks would result in a characteristic change of the rheological properties.²²² The applications of the viscosity determination were to allow us to customize the viscosity when the pneumatic compressor exerts pressure into the syringe. These measurements could be critical to the successful reduction of the printing pressure and to maximize the resolution of the bioprinting procedure. For example, bioinks with low viscosity could not sustain the pressing force and would extrude faster, while suspensions with very high viscosity could not be extruded easily. Therefore, adjusting the bioink viscosity to a proper range is an important step to achieving continuous extrusion. Typically, the viscosity (η) of the non-Newtonian fluids passing through a capillary can be adjusted by shear rate ($\dot{\gamma}$), and many authors have studied this. For this case, the power law method was selected (Appendix A).

3.3.1.2.2 Power Law Determination

The Power Law Model, also known as the Ostwald de Waele Model, is used to express a linear region over which apparent viscosity is plotted against shear stress over a logarithmic scale. In general, two useful values were acquired with this model: consistency (k) and power law index (n). These two values can be utilized to relate the shear rate at which a material is being exposed to the apparent viscosity at which the material will be sheared. The range at which these values oscillate will describe the rheological behavior of the blend. The value $n < 1$ as shear thinning, $n > 1$ as shear thickening and $n = 1$ will be used to characterize a Newtonian fluid. With the known values of other parameters, the viscosity can be estimated at any shear rate within the shear-thinning region. Nevertheless, the equation should not be used outside of the measured range of shear rates due to the possibility of the presence of Newtonian regions on either side of the measurement region, depending on the material being tested.

The slopes and intercepts of the plot of the viscosity as a function of the frequency for the TA from Figure 32 were acquired as a function of PEGDA weight percentage. It was desirable to adjust the acquired values to a predictive model that could be used to determine the change of k and n as a function of the percentage of thickening agent for each PEGDA weight percentage. Once these values were plotted, it was observed that the values followed a logarithmic trend, which could be adjusted to a linear model. More so, the values showed that the variation due to the PEGDA concentration was negligible. To support this statement a one-way ANOVA was conducted to compare the variation of the data among PEGDA concentrations for every TA. Normality checks and Levene's test

were carried out, and the assumptions met. There was no significant difference among the PEGDA concentrations for alginate, CMC or XG ($p\text{-value} > 0.05$ and $F > F_{\text{crit}}$). As expected, the variation of Pluronics was representative due to the difficulty in the reproducibility of the results ($p\text{-value} 0.05$).

Table 9. One Way ANOVA results for the variation of the linear regression for consistency as a function of TA percentage over a range of PEGDA concentrations

	<i>F(3,12)</i>	<i>p-value</i>
<i>Alginate</i>	0.067	0.9759
<i>CMC</i>	0.044	0.9871
<i>XG</i>	0.06679	0.976
<i>Pluronics F127</i>	3.0079	0.06841
<i>Fcrit(3,12)= 5.212</i>		

Post hoc comparisons using the Tukey test were carried out. There was no significant difference between the PEGDA concentrations over the range of 8% to 20% on the k or n values. As a result, it is expected that the concentration of the PEGDA minimally affects the rheometry measurements, namely the viscosity, as these properties vary mainly as functions of the percentage of thickening agent. Using the n and k over the range of TA percentages provides us with an efficient way to control the viscosity of the bioinks suitable for bioprinting by adjusting the nozzle diameter and extrusion rate as shown in Figure 33 for k values.²²¹

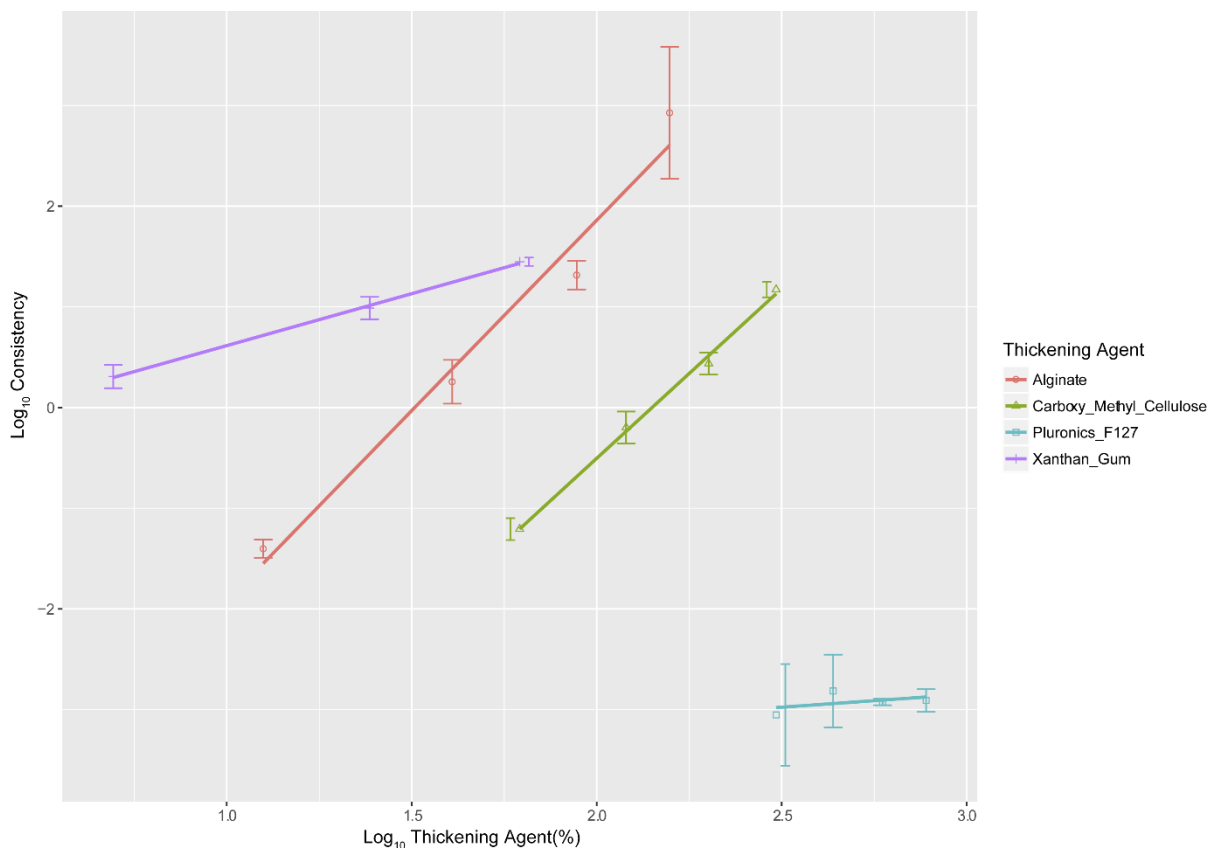


Figure 33. Dependency of Power Law model constants on thickening agent concentration.

As shown in Table 10 the n value for Alginate = 0.773 ± 0.025 , $CMC = 0.728 \pm 0.077$, Pluronic F 127 = 1.254 ± 0.174 , and XG = 0.23 ± 0.024 . Analyses of this data indicated that XG is the material that presents the highest shear thinning behavior, CMC and Alg behave similar to each other, and PL would be a shear thickening material. It has been reported that polymer solutions with chains larger than the molecular entanglement weight would behave as a pseudo-plastic fluid because of the chain entanglement.²²¹

Zhang *et al.* developed a 3D bioprinting system to optimize the flow and the porosity of scaffolds at the 100 μm resolution scale. To do so, they used a model shown in Equation 1 and Equation 2 to hypothetically determine the flow (Q) of a bioink based on their k and n values of a viscoelastic material. Furthermore, the experimental values were determined to show that the error between the experimental and the theoretical value is roughly 4%.²²³

$$Q = a(\Delta P)^b \quad \text{Equation 1}$$

$$a = \frac{n}{3n + 1} \pi \left(\frac{1}{2kL} \right)^{\frac{1}{n}} R^{\frac{3n+1}{n}}, b = \frac{1}{n} \quad \text{Equation 2}$$

The Zhang research group found that for 3% alginate solutions, employing an internal nozzle diameter of 0.25-0.41 mm and a pressure difference (ΔP) up to 1.5 bar, the flow of the bioink will not exceed 50 $\mu\text{L/s}$. Also, it was shown that for $\Delta P = 1$ Bar the flow of the bioink would be roughly 10 $\mu\text{L/s}$. Our findings show for this scenario in Table 10, the flow would be almost five times larger for a 0.15 mm ID nozzle (48,6 $\mu\text{L/s}$). This can be explained by the fact that the PEGDA concentration disrupts the entanglements among the bioink's polysaccharide network, causing a reduction in viscosity, and therefore increases the flow. Therefore, the nozzle extrusion pressure is proportional to the thickening agent concentration. As a result, too large of a TA concentration would exert excessive shear stresses on the cells inside. In contrast, if the thickening agent concentration was too low, the viscosity would also be too small resulting in a loss of bioprinting resolution.

Table 10. Power law model values for the determination of the viscosity as a function of shear stress

Type	Percentage (%)	ΔP (Bar)	Consistency (k)	Index (n)	a_{150}	a_{110}	$\mu L/s_{150}$	$\mu L/s_{110}$
Alginate	3	1	0.246±0.022	0.773±0.025	4.86E-05	1.28E-05	48.609	12.834
	5	1	1.293±0.281		5.68E-06	1.50E-06	5.681	1.500
	7	1	3.729±0.531		1.44E-06	3.81E-07	1.443	0.381
	9	1	18.681±12.224		1.79E-07	4.74E-08	0.179	0.047
Carboxymethylcellulose	6	2	0.299±0.033	0.728±0.077	2.86E-05	7.37E-06	74.192	19.109
	8	2	0.820±0.13		7.16E-06	1.84E-06	18.557	4.780
	10	2	1.548±0.169		2.99E-06	7.71E-07	7.753	1.997
	12	2	3.23±0.251		1.09E-06	2.81E-07	2.823	0.727
Pluronic F127	12	1.5	0.047±0.024	1.254±0.174	5.82E-03	1.79E-03	8044.258	2477.280
	14	1.5	0.060±0.022		7.64E-04	2.35E-04	1055.518	325.054
	16	1.5	0.054±0.002		8.31E-04	2.56E-04	1148.035	353.545
	18	1.5	0.055±0.006		8.19E-04	2.52E-04	1131.358	348.409
Xanthan Gum	2	0.5	1.361±0.158	0.23±0.024	1.57E-12	1.61E-13	7.71E-08	7.89E-09
	4	0.5	2.687±0.299		8.16E-14	8.35E-15	4.01E-09	4.10E-10
	6	0.5	4.257±0.176		1.10E-14	1.13E-15	5.42E-10	5.55E-11

Flow rates calculated for R= 0.150 and 0.110 mm ID and L=3.175 mm

3.3.1.2.3 G' , G'' , G^* Dependence on the thickening agent

Measurements of G' and G'' in frequency-dependent dynamic oscillatory experiments were used to examine the stability of bioink mixtures. It is possible to quantify the predominance of the solid or liquid character of a sample through these measurements.²²⁴ In general, a G' above G'' means that the elasticity is dominant, which suggests that a gelation process is prevailing. In contrast, G'' above G' represents a viscosity dominated solution-like material.²²¹ Polysaccharides are a highly polymeric material; therefore, we studied the G' and G'' of four TA in relation to frequency (0.1-5 Hz) at 2% strain to quantify viscoelasticity of the samples. Analysis of the plotted results of G' and G'' as a function of frequency on a logarithmic scale (Figure 34) indicated that the modulus G' and G'' values of all samples were increasing with increasing frequency. These results indicated that the four sets of bioinks were viscoelastic materials.

Analysis of dynamic testing indicated that at low frequency, the XG was predominantly a viscoelastic solid ($G' > G''$). This finding is in agreement with what Ki-Wong reported for xanthan gum solutions.¹¹¹ Where, over a whole range of angular frequencies, the linear viscoelastic functions exhibit an essentially similar behavior in both the G' and G'' ; and these values are gradually increased with an increase in polymer concentration. However, they demonstrated that a stable gel could not be obtained by just increasing the xanthan gum concentration.¹¹¹

Furthermore, alginate and CMC bioinks behave as viscoelastic fluids ($G'' > G'$). This was shown with a flat dependency of G' and G'' on frequency (f) ranging from about 10^{-2} to 10^2 with G' one or two orders of magnitude greater than G'' .¹⁰⁹ Even though the

study of the Pluronics-based bioinks provided inconclusive data, it appears that both curves G'' and G' intersect when the frequency reaches a certain value. This intersection is defined as a cross-over frequency; at this point, the bioink behaves more like a gel than a viscous liquid.²²⁴

For these bioinks, at the same TA weight concentration, both the G' and G'' moduli increase as the frequency increases. Nonetheless, as the TA weight % was increased, the rate at which G' rises was faster in comparison to G'' . This is indicative that more entanglements are being formed due to the presence of more hydrated polysaccharides. These trends indicate that the hydrogel is becoming firmer as the frequency is increased. Furthermore, as the bioink deforms, the polymer chains may begin to suffer from some anisotropy; however this is somewhat countered by overlapping chain entanglement.²⁰⁸ For bioprinting purposes it is desirable for the material to behave like a gel while resting in a cartridge to minimize the flow of the bioink, prevent flocculation and other forms of aggregation once it is blended with the materials of interest. However, it is also desirable that this bioink have a rapid shear thinning and a crossover transition at low frequencies (or shear strains) to facilitate the deposition of the bioink. In addition to this, a fast network recovery is desired in order to facilitate resolution and bioprinting fidelity.

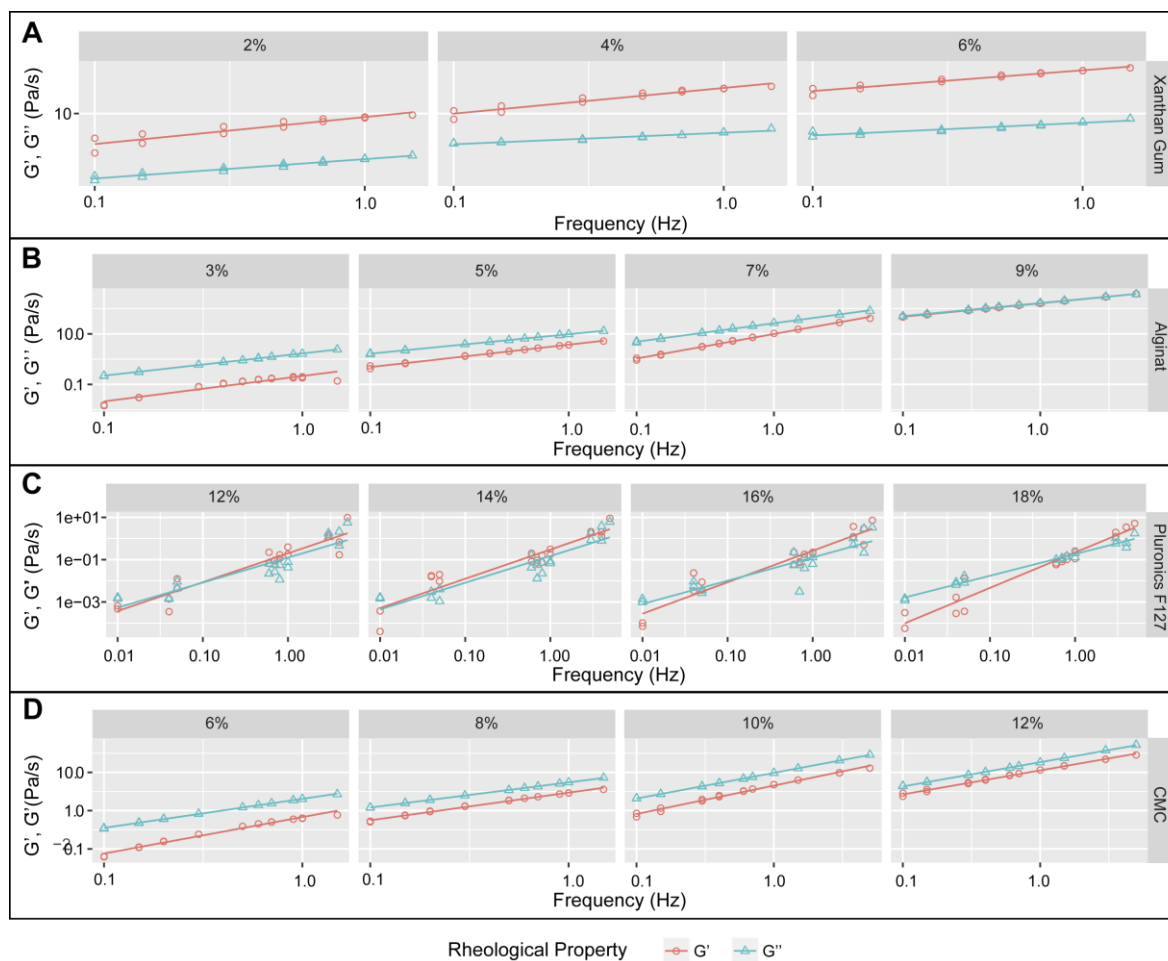


Figure 34. Evaluation of the viscoelastic properties G' and G'' for A) xanthan gum, B) alginate, C) Pluronic F127 and D) carboxymethylcellulose.

3.3.2 Bioprinting Fidelity

To assess the bioprinting fidelity and resolution of the bioinks, a student under my supervision, Matthew Nguyen evaluated a set of 9 bioinks according to section 3.2.3.8. The bioinks for bioprinting were selected with consistency values $K > 0.3$. Furthermore, the concentration chosen for PEGDA evaluation was 12%. The reason for this was twofold: attempt to increase the rheological properties of the hydrogels while maintaining cell viability and exploit the gel strengthening benefits of a PEGDA-TA based blend.^{216,225}

The hydrogels were to be formed from the bioink by UV photopolymerization. The rate of the FRP is expected to be dependent upon the formation of free radicals generated by photochemical reaction of LAP. LAP underwent a photofragmentation process to yield highly reactive aryl radicals, which initiated the polymerization by attacking the vinylic groups present in the PEGDA. This reaction resulted in the formation of two cross-linked patterns: linear chain formation and cross-linked structures, yielding a three-dimensional insoluble polymer network.²²⁶ In general, all the bioinks showed a transition shift, from a transparent-like blend in the viscous state to an opaque three-dimensional network. This behavior is attributed to the aggregation of the polymer strands in a disordered manner.²⁰⁴

The bioprinting conditions are given in Appendix C and the results are given in Table 11 and Table 12. Table 11 gives the measured side lengths of objects (4, 8, 12 layers) and Table 12 lists the heights measured for objects of decreasing height (12, 9, 6, 3. layers) according to the template shown in Figure 30. The percent deviations from the expected value are shown for each measured property.

A template was bioprinted and imaged (Figure 35) to evaluate the bioprinting fidelity. Furthermore, the images were analyzed using ImageJ to validate side and length deviations based on the desired dimensions. Also, the results for the highest alginate and CMC values (12P9A and 12P12CMC) are absent because they required more than 70 psi to bioprint, which exceeded the bioprinter limit. It is shown in Table 11 that for any given object series, as the object's theoretical side length decreases the deviation of the side increases. It was hypothesized that the trend is a result of increased evaporation rates and limitations of the bioprinter. As the object size decreases, the amount of water absorbed in the hydrogel structure decreases, enabling the shrinking processes that a specific object underwent. A similar trend was observed for the object height. It was expected that as we increase TA weight percent, the deviation of the object dimensions would decrease as a result of the increase of cross-linking density and enhancement of the mechanical properties. However, this was not what was found.

Regarding printability, as the TA weight percentage was increased, the deviation of the layer height increased as well. This behavior was the result of the varying extrusion pressures between bioinks. The starting bioprinting pressures are shown in Table 10, where 4% XG bioprinting pressure was 0.5 Bar in contrast for 6% XG an initial bioprinting pressure of 0.5 Bar was applied, but during the bioprinting process, it had to be increased to 1.0 Bar. This bioprinting pressure had to be progressively increased during the run to compensate for the clogging of the needle. The need to increase the pressure was to maintain the velocity profile at which the bioprinting was taking place. However, the

clogging of the needle was a phenomenon caused by the curing of the bioink in a layer-by-layer fashion inside the bioprinting needle. If the velocity profile was decreased, there was a more significant probability of polymerization within the tip at these regions caused by the UV-light. It was also noticed that the TA concentration influenced the clogging of the needle. More specifically, an increase of viscosity caused a decrease of the velocity profile inside the needle; therefore, the effective nozzle radius decreases as a function of time. Simultaneously, the extrusion filament width would also decrease as a function of time. Increasing the pressure aided in maintaining the same fluid flow rate, but not the filament width; hence lower resolution was the result.

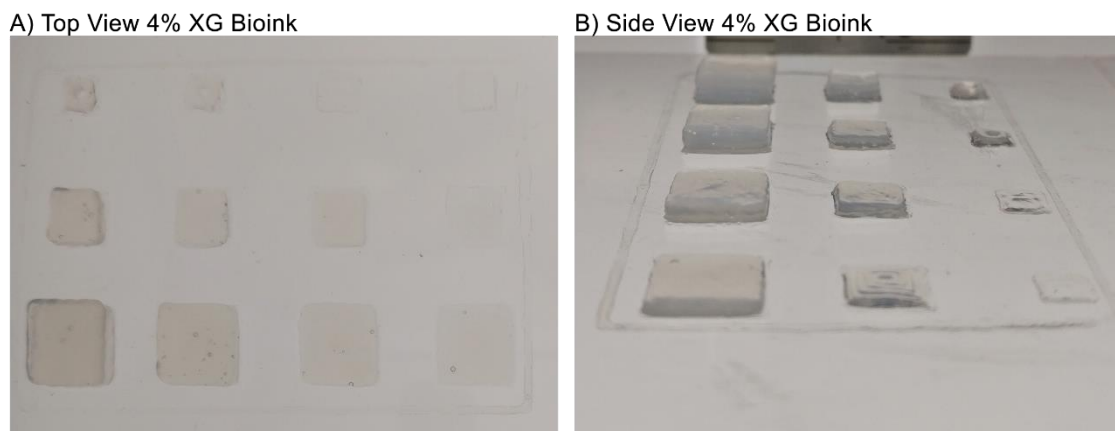


Figure 35. Images of A) top view and B) side view used to analyze the bioprinting fidelity of a 12% PEGDA and 4% XG gel using ImageJ.

From these nine bioink samples, 12P4XG and 12P10CMC were selected to be the best performing based on having the sharpest hydrogel constructs. It was noted that the highest thickening agent weight percent samples were unusable due to their extrusion pressure exceeding 3 bar. Comparing the remaining bioinks, we found that 12P4XG and

12P10CMC had similar deviations in their three-dimensional bioprinting resolutions. However, if we include the length and height deviations, then 12P4XG is preferred over 12P10CMC due to a smaller total sum of the errors. That is, the total error in the height and length measurements for 12P10CMC exceeded 12P4XG by 1.31 times. Furthermore, the total radius of curvature of 12P10CMC exceeded 12P4XG by 1.57 times.

Table 11.Length measurements for bioprinted features

Sample Name	Largest Side Length [cm] (% Deviation)	Middle Side Length [cm] (% Deviation)	Smallest Side Length [cm] (% Deviation)
12P2XG	0.814 (1.75%)	0.657 (9.50%)	0.343 (14.25%)
12P4XG	0.712 (11.00%)	0.485 (19.16%)	0.318 (20.50%)
12P6XG	0.716 (10.50%)	0.522 (13.00%)	0.388 (3.00%)
12P5A	0.710 (11.25%)	0.522 (13.00%)	0.217 (45.75%)
15P7A	0.743 (7.10%)	0.500 (16.66%)	0.227 (43.25%)
12P9A	-	-	-
12P8CMC	0.690 (13.75%)	0.451 (24.83%)	0.211 (47.25%)
12P10CMC	0.725 (9.375%)	0.522 (13.00%)	0.275 (31.25%)
12P12CMC	-	-	-

Table 12.Height Measurements for bioprinted Features

Sample Name	Object 12 Height [cm] (% Deviation)	Object 9 Height [cm] (% Deviation)	Object 6 Height [cm] (% Deviation)	Object 3 Height [cm] (% Deviation)
12P2XG	0.447 (10.60%)	0.236 (37.89%)	0.212 (15.20%)	0.035 (70.83%)
12P4XG	0.413 (17.40%)	0.269 (29.20%)	0.183 (26.80%)	0.134 (11.66%)
12P6XG	-	0.211 (44.50%)	0.084 (66.40%)	0.042 (65.00%)

Sample Name	Object 12 Height [cm] (% Deviation)	Object 9 Height [cm] (% Deviation)	Object 6 Height [cm] (% Deviation)	Object 3 Height [cm] (% Deviation)
12P5A	-	-	-	-
15P7A	0.410 (18.0%)	0.325 (14.50%)	0.193 (22.80%)	0.036 (70.00%)
12P9A	-	-	-	-
12P8CMC	0.477 (4.60%)	0.350 (7.8947%)	0.198 (20.80%)	0.116 (3.33%)
12P10CMC	0.440 (12.00%)	0.288 (24.20%)	0.152 (39.20%)	0.061 (49.16%)
12P12CMC	-	-	-	-

3.4 Conclusions

Here, it has been shown that bioink blends can be rheologically characterized to determine their adequacy for bioprinting applications. It was determined experimentally that concentration ranges of PEGDA between 8 to 20% presented little influence on the rheological properties for the extrusion-based bioprinting process. Therefore, it is expected that the bioprinting properties are dominated by the weight fraction of the TA, as explained in the rheological properties chapter, such as xanthan gum, alginate, and carboxymethylcellulose. Furthermore, it was experimentally determined that to have a satisfactory bioprinting material, the values of consistency (K) and the power law index (n) should be above 0.3 and ideally below 0.5, respectively. To facilitate the bioprinting of these materials, it is crucial to select shear thinning materials, that dramatically decrease their apparent viscosity inside the nozzle as the material is being bioprinted. Also, it was shown that there is a negative impact on the bioink bioprinting when high concentrations of TA are used due to low flowability. To prevent needle clogging, the use of a nozzle that requires less pressure and can withstand constant velocity profile of the bioink is advised. To finalize, it was demonstrated that the best bioink to be used for bioprinting is the 12% PEGDA with 4% xanthan gum because it exhibited the best resolution with 1.3x less error in length and height deviation and a 1.57x corner sharpness. However, 12% PEGDA and 10% CMC or 7% alginate can also be considered as bioink blends that will give satisfactory bioprinting.

Chapter 4 Bioprinting of bacterial cells on aHSF-based PEG hydrogels

4.1 Introduction

Current research on the development of bioinks are centered on tissue engineering applications, and focused on cell-seeded scaffolds for in vitro generation and posterior implantation.⁹⁷ As a result, it is desirable to fabricate mechanically robust 3D ECM's that can withstand these required applications.¹⁰¹ Traditionally, hydrogels have been used to fabricate these ECM due to their already diverse biomedical applications ranging from tissue engineering, drug delivery, and cell culture.²²⁷ However, the hydrogels require chemical modifications to fulfill a particular purpose. To expand the functionalities of the desired ECM and provide the biological functions, there has been an increased interest in attaching peptides and proteins to the gels themselves.²²⁸

There are multiple hydrogel modification techniques such as NHS ester activation, click chemistry, enzymatic ligation, and affinity binding for transient immobilization.²²⁸ Click chemistry has great attraction due to high yields, few byproducts, and the main advantage that this chemistry can be conducted under ambient conditions.²²⁹ In general, for protein and peptide attachment, the main advantage is that the thiol–ene coupling reaction is bioorthogonal with olefins on the surface directed to react specifically and exclusively with the thiols on the protein (cysteines).²³⁰ However, thiols can be problematic for conjugation chemistry because of their propensity to oxidize and form unreactive disulfide bridges, sulfones or sulfoxides.²²⁸

It is important to emphasize that ECMs cannot replicate the intricate architecture and arrangement of human native tissues and organs composed of multiple cell types. Therefore, a strategy to successfully organize the materials is to use dECMs. It has been considered a suitable strategy because the dECMs preserve a complex of functional and structural proteins from bioactive materials that are embedded in the natural ECMs while maintaining tissue homeostasis and promote the regeneration process needed to replicate a natural ECM.¹⁴⁹ To further the bioprinting requirements, cells are encapsulated in hydrogels or dECMs; therefore, for cell bioprinting, the choice of bioink is crucial and limited by the conditions on which the material is being bioprinted. Hospodiuk *et al.* presented a comprehensive review of most of the bioinks used for bioprinting.¹⁴¹ This review presents the myriad of approaches that can be made towards generating ECM. In general, a good bioink will provide customizable control to promote cellular behavior by modulating the stiffness, added functional groups, and surface morphology.²³¹

4.1.1 Bacterial cell bioprinting

The objective of a scaffold preparation was to develop a functional 3D structure using a bioink that will facilitate a cell bioprinting process with suitable rheological properties and have rapid crosslinking capabilities, without any additional steps required post/printing. To achieve this, our bioink, composed of a polysaccharide (10% carboxymethylcellulose, 7% alginate or 4% xanthan gum) was crosslinked with <1% of modified aHSF, in the presence of different ratios of PEGDA ($M_w=700$) under visible light (416 nm). The objective was to evaluate how the different crosslinking ratios would affect

the physical properties of the hydrogel construct such as protein declustering, diffusion of a substrate through the ferritin channels, the polymer network, swelling capacity, sol-gel partition, and scaffold porosity.

Furthermore, the bioprinting of *Eschericia coli* in hydrogel constructs has gained publicity lately due to its development into advanced applications such as pressure sensitive circuits and shape engineered 3D constructs.^{232,233} For example, Conell *et al.* demonstrated by using multibacterial colonies that it is possible to analyze the dynamics of the environmental conditions of a specific construct.¹⁰⁵ To fabricate these multicellularized scaffolds, gelatin-based microcontainers filled with *S. aureus* and *P. aeruginosa* at high cell density were fabricated using multi-photon lithography (MPL), a technique that allows one to bioprint an unlimited assortment of geometries. This approach facilitates micro positioning of desired bacterial colonies into a desired construct. However, using MPL is a costly and time consuming approach. As an alternative, Lehner *et al.* used *E. coli* as a rapid and inexpensive approach to assess an cell viability on bioprinted alginate-based bioinks.²³⁴ The incubated and bioprinted constructs were used to determine optimal conditions for bacterial colony growth. It was shown that within 48 hours incubated cells in non-bioprinted, liquid bioink reduced the viability of *E. coli* by approximately 50%, due to nutrient limitation. Bacterial cell loaded bioink extruded from a bioprinter increased the cell viability up to 200% due to the higher nutrient incorporation and lower bacterial density after bioprinting.

To verify cell viability, the most common method is to use the live/dead assay which is carried out by capturing images of cell-encapsulated mesh patterns right after bioprinting. This test is based on a fluorescence bioassay consisting of calcein AM to track living cells, and ethidium homodimer-1 to track dead cells which fluoresce in distinct wavelegths using confocal microscopy.¹⁰⁵

In this bioprinting study, *E. coli* spheroids were bioprinted in combination with the HSF-PEGDA-TA bioink selected previously as outlined in Chapter 3 to characterize the growth profile of *E. coli* containing a mutant form of the green fluorescent protein (GFP), specifically the His-tag GFP-S65T variant. There was an interest to understand the impact of seeding cells in incubated environments in comparison with bioprinted environments.

4.1.2 Hydrogel scaffold properties

4.1.2.1 Swelling experiments of HSF based hydrogels

4.1.2.1.1 Sol-gel

The sol-gel fraction was measured once the hydrogel was polymerized. This approach was undertaken to understand the influence of the PEGDA molar fraction on the modified ferritin cross-linking capacity. Xuzhen *et al.* used simple gravimetric analysis to characterize the sol-gel fraction in PEGDA hydrogels by merely leaching the unreacted fraction.²³⁵ The method is to quantify the weight difference between a dry sample (m_{dry}) just polymerized and a dry sample that was leached during at least 48 hours in a PBS solution (m'_{dry}) and using the Equation 3.

$$W_{gel}(\%) = \left(\frac{m_{dry}}{m'_{dry}} \right) * 100. \quad \text{Equation 4}$$

4.1.2.1.2 Swelling capacity of hydrogels

Many authors have measured the swelling capacity of hydrogels.^{103,226,236} The equilibrium-swelling ratio can be calculated using Equation 5.

$$Q = \frac{M_s - M_d}{M_d} \quad \text{Equation 5}$$

where Q is the equilibrium swelling ratio, and M_s and M_d are the masses in a swollen state and dried state, respectively. Swelling and hydration of the gels were measured by increasing the PEGDA concentration. It is expected that the polymers become more highly crosslinked and less flexible under increasing PEGDA concentrations. Mellot *et al.* carried out an experiment with a PEGDA- pentaerythritol triacrylate (PETA) system by varying the mole fraction of the constituents to confirm there was a two-fold decrease in the final volume change once the mole fraction of PETA is 1:1, reaching swelling equilibrium after approximately 20 minutes.²²⁶ To measure the sample weight equilibrium must be achieved, followed by blotting of the sample to remove any solution. To finalize the measurements, the dried sample weight was acquired by drying the sample under vacuum for 24 h and weighted again.²³⁷

4.1.2.2 Declustering of cross-linked protein cages for cargo release

Suttisansanee *et al.* studied the declustering mechanisms of HSF. Regarding stability, denaturation does not alter the shape and size of the 24mer significantly but

exposes protein chemical groups that were not exposed previously. It was reported that the cage structure is not stable under (I) protein concentrations <0.1 mg/mL; (II) $\text{pH}<2$ and $\text{pH}>10.6$; (III) presence of denaturants such as 9 M urea or 6 M guanidinium-hydrochloride solutions; (IV) temperature conditions above 93 °C, and (V) ionic strength <0.06 M NaCl.²⁴ Furthermore, Chen *et al.* reported a novel human ferritin nanocage which can undergo disassembly at $\text{pH} 4$ and reassembly at $\text{pH} 7.5$ by cleaving the last 23 amino acids of the protein amino acid sequence.²³⁸ This was accomplished by the complete removal of the E helix and the DE helix turn, sections which have no participation in the cage self-assembly process of HuFT and have no effect on the temperature stability.

4.1.2.3 Diffusion of cargo through the HSF channels

The diffusion of various proteins inside PEGDA hydrogels has been studied previously.^{94,239} At first, Cruise *et al.* reported that PEGDA hydrogels of molecular weights ranging from 2000 to 8000 (mesh size 15-35 Å) can only permeate proteins that are below 22 kDa, and PEGDA 20000 (mesh size 45-70 Å) can permeate proteins that are up to 45 kDa with concentrations ranging from 10% to 30% w/w.²³⁹ This approach employed the hydrogels as a membrane in between a solution that contained protein and a solution that was protein free. In contrast, Lee *et al.* evaluated diffusion by the Fickian diffusion model (Equation 6) by pre-making hydrogel disks, which were soaked in a protein solution (BSA, 4 mg mL^{-1}) for 15 hours to understand the behavior of protein unloading from PEGDA hydrogels (2000 to 10000 Da).⁹⁴ Zustiak *et al.* also followed the Fickian diffusion model in 4-arm-PEG polymers with Lysozyme, BSA, and Ig.²⁴⁰

$$\frac{M_t}{M_\infty} = 4 \left(\frac{Dt}{\pi a^2} \right)^{\frac{1}{2}} \quad \text{Equation 6}$$

For the diffusion determination, the formula used is useful only for short release times, to the extent of ~70% of total release. M_t is the accumulated protein release up to the time point t ; M_∞ is the accumulated protein release at the infinite time, which was determined by the protein accumulation; the fickian diffusion coefficient (D) of the BSA within the gel; and a is the gel diameter, and l is the gel thickness). It was shown that accepted values for the diffusion of proteins under 65 kDa in PEG-based hydrogels are in the range of $(1.0\text{--}2.5 \times 10^{-7} \text{ cm}^2 \text{ s}^{-1})$.^{94,240}

In our studies, one approach that was taken was to determine the kinetics of the release of iron from the aHSF system by using ascorbic acid as a reducing agent. Jones *et al.* reported that the release of iron using ascorbate followed a zero order reaction rate for iron-loaded ferritins. The explanation of the phenomena based on the complexation of the iron (III) by the 1,10-*o*-phenanthroline and the photo reduction of the iron (III) to the iron (II) complex.²³⁷ Furthermore, Sakuari *et al.* reported that to facilitate this reaction, ascorbate could reductively release ferritin iron only at high concentration and at pH 5 or below. In addition to iron extraction, the iron needs to be removed successfully from solution by the addition of PBS, pH 7.4, containing 10 mM disodium EDTA for 1 h at 4 °C. This was followed followed by a second dialysis after incubation in PBS without disodium EDTA for a further 3 h.²⁴¹ Therefore, D could be measured using an ascorbate solution,

followed by the O-phenanthroline reagent in combination with Fick's law for short times (under 180 minutes).

4.1.2.4 Porosity studies

An essential aspect of hydrogel matrices is the accessibility to the internal sites of the hydrogel. A method used to increase the accessibility of the hydrogel matrix is to add a porogen during the polymerization. Methods to create pores within hydrogels during polymerization include the use of salts, organic solvents, and inert molecules.²⁴² Another approach to increase the pore distribution, size and accessibility to the matrix could be by introducing co-polymers during polymerization. Liljeström *et al.* proposed the use of dendrimers as a co-polymer to increase the pore size with the advantage that they can be functionalized with a terminal amine.²⁴³ The applications of this reagents relied on utilizing the dendrimer's terminal amine group for chemical modification. The main advantage of this reagent is the similarity with a cage-like protein, where it resembled the diameter of the ferritin with a different profile of releasing potential. Likewise, Zustiak *et al.* used PEG derivatives (4-Arm PEG-VS) and employed click-chemistry (Michael-addition), and presented an elegant way of decreasing the cross-linking density and increasing the pore diameter at the microscopic level.²³⁷

Traditionally, to study porosity features, two accepted techniques have been used: Scanning electron Microscopy (SEM) and nitrogen Brunauer–Emmett–Teller (N₂ BET) isotherm analysis. HSF-based hydrogels have been studied by SEM studying the dependence of the crosslinking density on the porosity profile of the hydrogels.²⁴⁴ To

explore the morphology adequately, SEM studies of wet hydrogels are carried out using the backscattered electron detection (BSED) or the environmental scanning electron microscope (ESEM) at 10 kV.²⁴⁵ Furthermore, low pressure, a controlled low-temperature stage, and water vapor are needed to minimize the sublimation of the sample and sustain shape fidelity.²⁴⁶ Another acceptable method for porosity analysis is the freeze-drying of gels. However, it is difficult to guarantee that these methods precisely tune the pore size. Instead, freeze-drying a sample often results in the formation of a surface skin because the matrix may collapse at the scaffold–air interface due to the interfacial tension caused by solvent evaporation.²⁴⁷ Once the images have been acquired, an acceptable method is to analyze the samples using an imaging processing software package such as ImageJ on which it is possible to develop an algorithm to perform automated and high-throughput analysis of SEM images with quantification of fiber diameter, pore size, and fiber alignment of hydrogels.²⁴⁸

4.2 Materials and methods

4.2.1 Materials

Calcium chloride (CaCl_2), sodium chloride (NaCl), magnesium (II) sulfate (MgSO_4), monopotassium phosphate (KH_2PO_4), dipotassium phosphate (K_2HPO_4), ammonium chloride (NH_4Cl), disodium hydrogen phosphate heptahydrate ($\text{Na}_2\text{HPO}_4 \cdot 7\text{H}_2\text{O}$), sodium hydroxide (NaOH), glucose, bacto-tryptone, yeast extract, Alg, XG, CMC, PL, PEGDA (M_n : 700), NAS, MMA, and 1.5 cover glass were purchased from Aldrich (Milwaukee, USA), and used without further purification. CultureWell16 chambered cover glass was

purchased from Grace BioLabs (Oregon, USA). Blunt end tips (30" and 32") and Micron-S Micro Bore Dispensing Tips (150 and 50 μm) were purchased from Fisnar (WI, USA). Lithium acyl phosphinate was synthesized as described on section 3.2.3.1 and used without any further purification. *E. coli* (BL-21 cell line) containing the DNA coding for the variant His-tag GFP-S65T was expressed from a pET plasmid using isopropyl-beta-thiogalactopyranoside (IPTG) induction and was kindly provided by Dr. Jeanne Hardy (University of Massachusetts, Amherst).

4.2.1.1 Safety Statement

All bacterial samples were handled in accordance to level 1-safety laboratory facilities. After use, all bacterial samples were bleached or autoclaved to sterilize the media before disposal.

4.2.2 Instrumentation

4.2.2.1 Bioprinting Equipment

The equipment used for bioprinting is described in section 3.2.2.2

4.2.2.2 Thermogravimetric Analyzer

TGA was carried using a SDT Q600 (TA Instruments, PA, USA) in Thermal analysis mode using a 90 μL open ceramic cup.

4.2.2.3 Fluorescence Microscope

OMAX 40X-2500X Lab EPI-Fluorescence Trinocular Compound Microscope equipped with 14MP CMOS Camera Model A35100U (Omax Microscopes, Kitchener, ON, Canada) was employed. Image analysis was made using ToupView. Excitation wavelength 475 nm and emission wavelength at 509 nm was employed.

4.2.2.4 Confocal Microscope

Confocal images were obtained on a Zeiss Personal LSM 700 confocal microscope equipped with 405, 488, 555, and 639 nm lasers (Carl Zeiss MicroImaging GmbH, Germany).

4.2.3 Methods

4.2.3.1 Bioink stock formulations

To characterize the aHSF hydrogels, stock blends of TA-PEGDA were prepared. The bioinks were prepared by blending polysaccharide concentrations that delivered the optimal bioprinting conditions (0% thickening agent, 4% xanthan gum, 7% alginate and 10% carboxymethylcellulose), selected edge values of PEGDA (8% and 14%) and 0.05% LAP as shown on Table 13. This was followed by the addition of an aliquot of 0.200 mL of aHSF (25 mg/mL) and 0.005 mL of the *E. coli* bacterial cell solution ($OD_{600}=0.8$).

Table 13. Stock formulations for the hydrogel constructs to be analyzed.

Repetition	Thickening Agent	Thickening Agent Percentage	PEGDA Percentage	Protein Percentage	Ampicillin ($\mu\text{g/mL}$)	LAP	Cells
1	None	0.00%	8.00%	20.00%	60	0.05%	5.00%
2	Xanthan Gum	4.00%	8.00%	20.00%	60	0.05%	5.00%
3	Alginate	7.00%	8.00%	20.00%	60	0.05%	5.00%
4	Carboxymethylcellulose	10.00%	8.00%	20.00%	60	0.05%	5.00%
5	None	0.00%	14.00%	20.00%	60	0.05%	5.00%
6	Xanthan Gum	4.00%	14.00%	20.00%	60	0.05%	5.00%
7	Alginate	7.00%	14.00%	20.00%	60	0.05%	5.00%
8	Carboxymethylcellulose	10.00%	14.00%	20.00%	60	0.05%	5.00%

4.2.3.2 HSF based PEG hydrogel properties

4.2.3.2.1 Network composition of hydrogels determined by TGA

TGA was performed to obtain information on the composition of the HSF-based hydrogel scaffold. Methods used to determine the quantity of water that is being held by a hydrogel scaffold has been described before.²⁴⁹ However, we purposely used TGA to determine matrix composition and total amount of water in the sample. The sample was blotted over a tissue paper, followed by the extraction of a piece that was going to be placed in the sample cup. The average mass of the sample was 15 mg. Each sample was heated from 30-600 °C at a rate of 5 °C min⁻¹ under a 50 mL min⁻¹ N₂ flow. The final temperature was held for 20 minutes to guarantee that the sample had been fully

degraded. Subsequently, the first derivative of the network percentage with respect to the temperature was plotted using a spline-smoothing algorithm. To identify the peaks of the spectrum, the “peakfinder” function from Pracma, an R Studio package from CRAN was used to determine the amount of bound water (`findpeaks(Dataset,npeaks=6, minpeakheight = 0.0002, sortstr=TRUE, minpeakdistance = 500)`).

4.2.3.2.2 Swelling and Sol-gel studies

The swelling studies were carried out employing an approach previously described by Chavda *et al.*²³⁶ This strategy used dried hydrogels to determine their equilibrium-swelling ratio in distilled water. To obtain M_d , the hydrogel was lyophilized during 24 hours. Once dry, the weight was recorded. Then, it was immersed in excess of distilled water for swelling during 24 hours to guarantee hydration. The swollen hydrogel was put on an *in lab* designed grid, allowing a simple handling of the hydrogels in water while not altering the mechanical integrity. The hydrogel was removed from water; blotted using a tissue paper to remove the excess water and then weighed to record M_s . To analyze the variation of the swelling capacity, a spectrum of hydrogels encompassing a range of PEGDA concentrations of 8%,10%,12%, and 14% and an increasing amount of protein concentrations, 0, 5, 12.5, 20 mg/mL (Table 14) were weighed.

Table 14. Prepared HSF-based hydrogels for swelling studies.

PEGDA (%)	Amount of aHSF (mg/mL)			
	0 mg/mL	5 mg/mL	12.5 mg/mL	20 mg/mL
8%	1	2	3	4
10%	5	6	7	8
12%	9	10	11	12
14%	13	14	15	16

Hydrogel swelling studies were carried out to have a better understanding of the physical properties of the HSF-based hydrogels. To accomplish this, a 9-well plate was used to guarantee that all the hydrogels would have the same size and exposure to the UV-light.

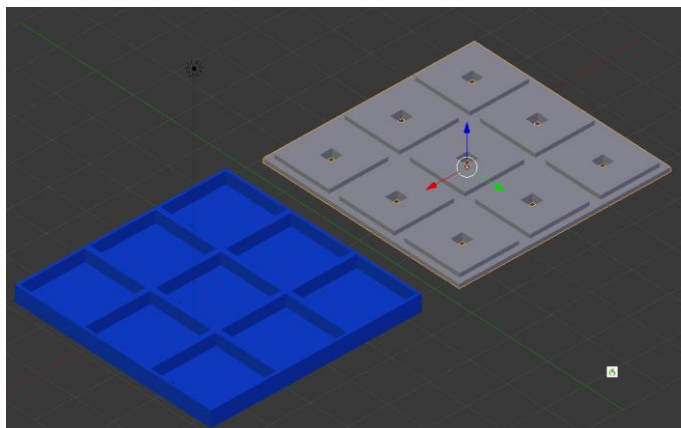


Figure 36. Designed nine plate well to guarantee gels with 12 mm wide, 12 mm long and 2 mm thick using the blender 2.76 program.

4.2.3.2.3 Cargo release through the HSF channels

The aHSF-based hydrogels were evaluated by measuring the rate at which ferritin subunits released their cargo through the inter-subunit channels. Two conditions were evaluated. First, the protein concentration was evaluated by testing a range of modified-HSF concentrations (0-20 mg/mL) at different ranges of PEGDA concentrations (8%-14%). Secondly, the effect of the polysaccharides was evaluated by fixing the modified-HSF concentration at 20 mg/mL, changing hydrogel composition (0% TA, 4% XG, 7% alginate and 10% CMC) at different PEGDA concentrations (8%-14%). To do so, 0.200 mL of each bioink was polymerized under UV light to generate the hydrogel constructs. The release of Fe²⁺ through the protein channels followed a procedure described by Jones *et al.* using ascorbic acid to facilitate the entry through the hydrophilic channels, followed by reduction of the Fe³⁺ core.²³⁷ Fe²⁺ was released from the cage protein by immersing the hydrogel scaffolds in an ascorbic acid solution (1.5 mM in 0.1 M citric acid buffer, pH 3), then a 50 µL aliquot was extracted every hour for 8 hours. During these experiments, the gels were placed in a shaker. The rate of diffusion was monitored using a spectrophotometer which was employed to detect the o-phenanthroline Fe²⁺ complex at 510 nm, as described by Vogel *et al.*, and then, this data was correlated to the initial ferritin concentration.²⁵⁰

A Soxhlet extraction apparatus was used during 48 hours to remove unbound ferritin from the hydrogel network (condenser temperature: 5 °C, evaporation temperature: 50 °C, and vacuum).

4.2.3.2.4 Cargo release by declustering of the HSF cage protein

The declustering potential of the HSF-based hydrogels was evaluated by measuring the rate at which ferritin subunits released their cargo under declustering conditions. A sample (0.200 mL) of each bioink was polymerized to generate the hydrogel constructs (~4 mg of modified protein). The declustering potential was studied in two stages. During the first stage, six 0.200 mL samples of HSF-based bioink (20 mg/mL of a 2 modified lysine per HSF, 20% PEGDA, 0.05% LAP) were polymerized under UV light to fabricate the hydrogel scaffolds. In addition, each scaffold was later immersed into one of the following declustering/denaturing conditions: a) 2% SDS, 6 M guanidine HCl and 9 M urea in 1 M acetate buffer pH 3; b) 50% DMF, c) 100 °C, and d) extreme pH, with HCl (1 M).²⁵¹ The second stage was used to analyze the influence of PEGDA concentration on the declustering capacity. Samples (0.200 mL) of the aHSF-based bioink (20 mg/mL 2 acrylated lysine residues per HSF, 0.05% LAP) ranging between 8%-14% PEGDA were evaluated under a) 1 M acetate buffer pH 3, b) 100 °C, c) HCl (0.1 M) and d) HCl (0.01 M). A control gel was set for each stage to analyze the maximum amount of Fe⁺² stored in a sample. One HSF-based construct was immersed into 2 mL of an iron reducing solution (1% NH₂OH, 1 M acetate buffer, pH 3) for 24 h. Later, an aliquot of 50 µL from the leachate was mixed with 50 µL of NH₂OH, 400 µL of an acetate buffer (1 M, pH 3) and 500 µL of O-phenanthroline solution (1% in ethanol) and measured.

A Soxhlet extraction apparatus was used during 48 hours to remove unbound ferritin from the hydrogel network (condenser temperature: 5 °C, evaporation

temperature: 50 °C, and vacuum). The rate of declustering was measured by the release of Fe³⁺ ions every 60 minutes for 8 hours at 510 nm. The samples were stirred before sampling to homogenize the solutions (Fe³⁺ ions) and monitored using o-phenanthroline, as described by Vogel *et al.*, and then, this data was correlated to the initial ferritin concentration.²⁵⁰

4.2.3.2.5 SEM studies

The porosity and the structure of the hydrogels were analyzed by SEM in order to ensure that hydrogels retain their structure. aHSF-based hydrogels were prepared by the photopolymerization of aqueous mixtures of 700 Da PEGDA and varying levels of TA (7% alginate, 10% carboxymethylcellulose, 4% xanthan gum and no thickening agent). Four distinct precursor solutions were prepared in dH₂O, each containing 8 or 14 wt % total of polymer (PEGDA). A photoinitiator consisting of a 0.5 wt % solution of LAP was added to each precursor solution at 10 µL/mL. All samples were polymerized by 6 minute exposure to longwave UV light (≈1 mW/cm², 405 nm). The samples were pre-frozen at -20°C using dry ice and then they were cut to expose their inner structure. They were then placed on the SEM chamber and analyzed using low vacuum mode, 30 kV electron beam, 3.0 spot size, using 2.0 mbar. The porosity was evaluated by processing captured images and analyzing them by Image J software using particle count values. The script is provided in Appendix I.

4.2.3.3 Cell growth conditions

Cell cultures were grown in Luria-Bertani (LB) broth (1% w/v tryptone, 0.5% yeast extract, 0.5% NaCl, pH 7.4 with NaOH), supplemented with ampicillin at a concentration of 100 µg/mL. To express the *E. coli* mutant His-tag GFP-S65T a starter culture was inoculated and left shaking at 37 °C overnight. When the OD₆₀₀ reached 1.0 O.D. the samples were taken and used for the hydrogel constructs.

4.2.3.4 Evaluation of the effect of growth media on *E. coli* casted bioink scaffolds

The efficiency of the bacterial growth was measured for bioinks described in section 4.2.3.1 by casting 200 µL of each bioink into a CultureWell16 chambered cover glass and copolymerized for 10 minutes at 25 °C by exposure with a 405 nm wavelength (λ) lamp (Light power = 10%, I₀ = 10mW/cm²). The samples sets (n=4) in a CultureWell were supplemented with 200 µL of a different growth media (two growth media: LB and M9; two levels: with or without 0.5 mM of IPTG). Each sample was measured by confocal microscopy at 3, 76 and 178 hours as described in section 4.2.3.6.

4.2.3.5 Casted and bio bioprinted scaffold effects on *E. coli* growth

The difference between bacterial growth on casted versus bioprinted scaffolds was measured for the bioinks described in section 4.2.3.1. For the casting hydrogel scaffolds, the procedure described in section 4.2.3.4 for LB was measured. For the bioprinted scaffolds, the bioprinter was placed in a type II laminar flow hood and sterilized using a UV light overnight. The bioink (1 mL) was loaded into a 10 mL Luer-Lok syringe and

placed in the bioprinter for the scaffold fabrication. The pressure was adjusted according to Table 10 and the model was bioprinted (13 layers, 0.8x0.8x0.2 cm³) for each sample on a 1.5 cover glass and copolymerized for the duration of the bioprinting at 25 °C. The scaffolds were placed in a 4 mL Petri dish with 2 mL of LB media. Each sample was blotted with a Kimwipe (Kimberly-Clark, Dallas, TX), placed on a clean 1.5 cover glass and read by confocal microscopy at 3, 76 and 178 hours as described in section 4.2.3.6.

4.2.3.6 Cell-laden hydrogel imaging acquisition

A z-stack of images ($n = 15$ per sample for a 50 μm cross-section), standardized to image through the entire thickness of the sample, was captured through the microscope slides using a resolution of 512 \times 512 pixels via a 20 \times Dry lens, 1% laser output using the 488 nm and a pinhole of 1 AU.

4.2.3.7 Cell-laden hydrogel imaging processing

Images were processed using ImageJ software using the script shown in Appendix J, where Z-stacks were compressed into one image using maximum intensity and subsequently subtracting the background. Later, images were converted to RGB using the ImageJ Cell Counter plugin and a scale was added. Viability was determined by counting the number of live cells determined by the presence of mutant-GFP cells.

4.2.3.8 Statistical Analysis

Comparisons between multiple samples were performed with single factor analysis of variance (ANOVA) with post hoc Tukey analysis was performed to determine statistical

significance in declustering experiments between Iron concentration vs PEGDA concentration (Appendix E). It was also used to determine statistical significance between groups in the bacterial cell viability data. All data are shown as mean \pm SEM, with $n = 4$ for declustering experiments and $n = 3$ for cell viability data. All graphs were plotted using R studio software. A p -value of less than 0.05 was considered statistically significant.

4.3 Results and Discussion

4.3.1 aHSF Hydrogel Properties

4.3.1.1 Network composition of the aHSF hydrogels

The thermal stability of the hydrogels and starting materials were characterized by TGA to determine the effect of aHSF concentration on the hydrogel networks (Figure 37). For the hydrogel formation the aHSF was subjected to PEGylation, in order to investigate the development of these biopolymers as interesting materials.²⁵² To establish a chemical fingerprint, the thermo-gravimetric transitions of the raw materials were measured. A narrow transition peak was found for Alginate (230 °C), xanthan gum (300 °C), and carboxymethylcellulose (320 °C); nonetheless, aHSF showed a broad distribution with a maximum at 380 °C. Furthermore, the PEGDA thermal transition is a two-peak signal in the range of 360-480 °C.

Likewise, the influence of the PEGDA ratio with the TA was investigated by comparing the thermal stability of the hydrogels having different molar ratios of PEGDA to TA. To elucidate the influence of the PEGDA, the thermal stabilities of hydrogels containing only PEGDA as the synthetic polymer were also studied and compared with the thermal stability of the hydrogels with different ratios of PEGDA/TA (7% Alginate, 4% XG and 10% CMC). The evaluated samples showed a rapid weight loss below 180°. This first degradation process could be assigned to the bound and unbound water that is held inside the hydrogel network (90 %, Appendix G). Subsequent weight loss is observed between 180 °C and 360 °C due to the decomposition of the TA matrix. It was intended

to use TGA analysis to quantify the amount of aHSF that was bound to the hydrogel after extensive washing of the hydrogel scaffold. However, the signal that was expected at 380 °C for aHSF was overlapped by the degradation of the PEG matrix. Hence, it was possible to use this analysis to show the stability of the polymeric matrix up to 280 °C, but it was not useful to determine the aHSF concentration. Furthermore, the last step in the degradation profile for each sample is most distinct in higher concentrations of PEGDA. Understanding the impact of PEGDA concentration on these melts is beneficial because Mazzoccoli *et al.* reported a negative correlation between PEGDA weight percent in a hydrogel with cell viability when the PEGDA concentration surpassed 20% w/v.¹⁰⁵ Furthermore, it has been reported also that an increment of the PEGDA chain length will favor an increase in the network stability due to an increase in crosslinking density.²⁵³ The analysis of the melt gave a residual mass at 600 °C of 1.3 %, which corresponded to the iron oxide cores of the protein. The melt decomposed at 430 °C, compared with aHSF. Perryman *et al.* previously reported that aHSF-based hydrogels decompose, leaving behind 1% of inorganic matter.⁸⁸

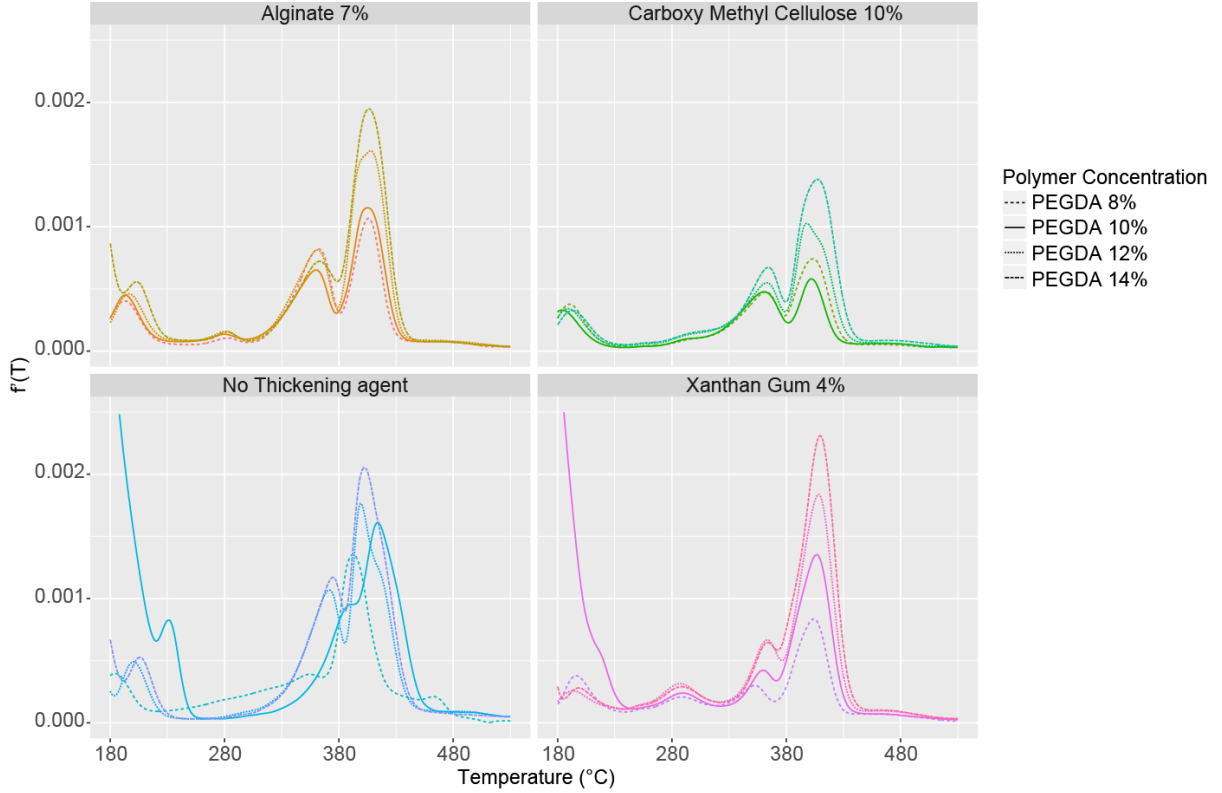


Figure 37. Thermo-gravimetric profile of PEGDA M_n 700 variation in aHSF-PEGDA hydrogels prepared with different TA.

4.3.1.2 Swelling potential of aHSF-based hydrogels

The swelling ratio of hydrogels is a property that defines the amount of water that a scaffold can hold, therefore it is linked to the ability of a scaffold to foster cell viability. Effects of the protein concentration on the aHSF constructs were studied by swelling cycles as described in section 4.2.3.2.1. The measurement of the swelling was made immediately after the polymerization was carried out, then it was followed by freeze-drying at $-40\text{ }^\circ\text{C}$ to calculate the degree of swelling using the equation in section Equation 4. Swelling tests showed an inverse correlation between increasing the amount of aHSF

and the amount of swelling capacity that the aHSF-based hydrogel has (72 lysine residues per subunit). A possible explanation could be that the modified ferritin has a lower cross-linking density than a pure PEGDA hydrogel. In addition, a protein-based hydrogel would have no ether groups but amino acids with negatively charged carboxylate groups such as Glu and Asp, at pH 7.4, which should increase the amount of water that could be absorbed by the hydrogel.²⁵⁴

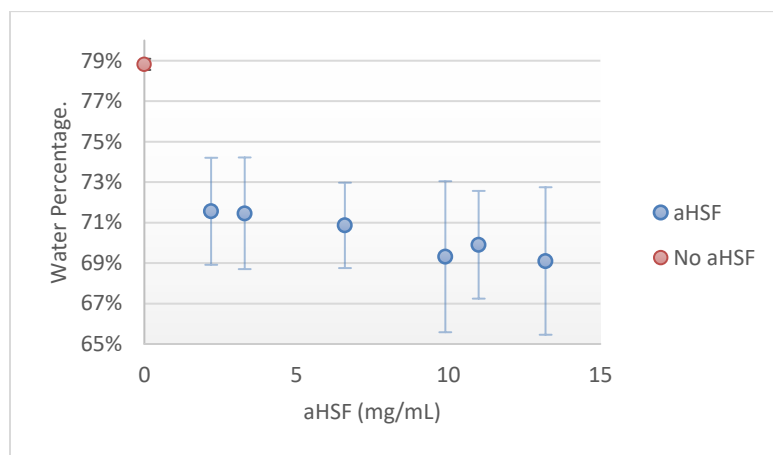


Figure 38. Protein concentration effect on aHSF-based hydrogels.

The characterization of the swelling behavior as a function of the concentration of aHSF in the hydrogels with no TA (Figure 38) showed that at low aHSF concentration the swelling potential of hydrogels remained similar. However, the method itself presented some variations that accounted for the large error for each measurement. In general, the samples were blotted over a tissue paper, which might account for those differences. Instead, the samples were measured using TGA as described on section 4.2.3.2.1, which gave a repeatable result for swelling. For the TGA analysis, the samples were equilibrated

for 24 hours in PBS buffer (0.1 M, pH 7.4) to guarantee that the samples were fully hydrated. This represented an increase of 10% for water an aHSF hydrogel can hold. Furthermore, two trends may be observed. First, an increase in the amount of PEGDA in the hydrogels, results in a decrease of the bound water to the aHSF-PEGDA scaffold. Second, TA hydrogels have an increased swelling ratio. This behavior is more prone on CMC-based networks perhaps due to the fact that CMC has a large electronic repulsion of carboxyl groups within the polysaccharide network.²⁵⁵ It was also shown that XG presents a large variation on the swelling ratio. This can be explained by the tangling between the PEGDA strands and the XG strands. It was previously shown (Figure 12) that XG has the largest repeating unit in comparison with the other TA. This repeating unit entangles with the PEGDA strands. While larger mechanical strength is achieved by higher entanglement of the strands, less water appears to be held inside the hydrogel construct. Furthermore, the hydration level was controlled by the TA of choice, as shown in Figure 39.

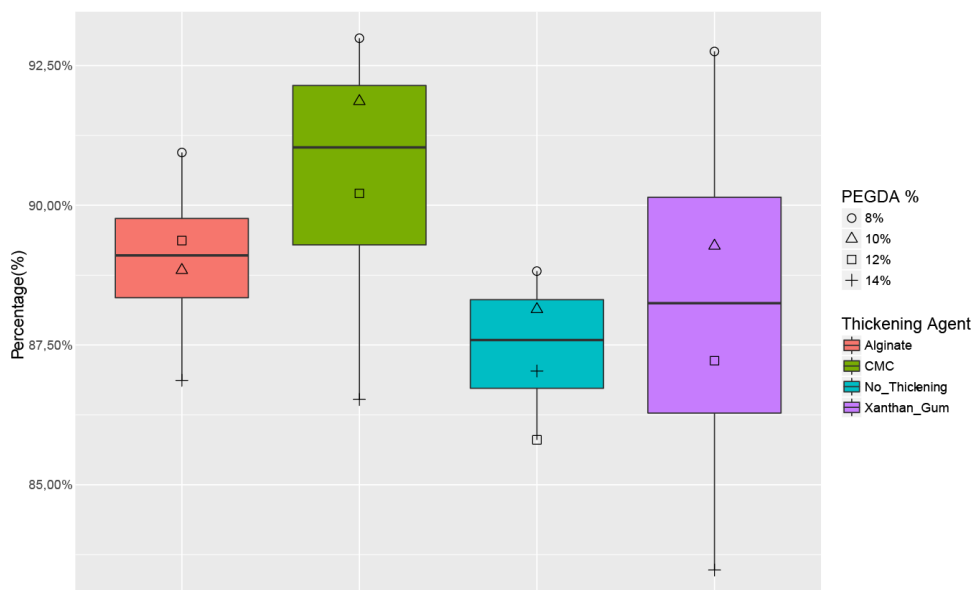


Figure 39. Swelling of PEGDA Based Hydrogels by TA (Appendix G).

4.3.1.3 Fe²⁺ diffusion through the channels of a loaded aHSF embedded into the hydrogel network

The synthesized scaffold containing a capsule protein provides a host component that might offer opportunities for controlled cargo release. One key element is to use the intrasubunit channels to extract a desired material. A direct correlation between the amount of guest that is loaded into the aHSF hydrogel and the diffusion time of Fe²⁺ could be plotted to determine the diffusion coefficient of a given guest within the hydrogel (D). A different approach to measure diffusion is to measure the penetration of a substance in a hydrogel network. Such studies have been done in polyacrylamide hydrogels that were photo patterned.²⁵⁶ To determine the extent of the penetration into the hydrogels,

fluorescent solutes were flowed into specific channels and monitored using a camera while making note of the absorption of the gels over time.

In the present investigation, the ferritin is loaded with solid iron(III) hydrate cores, which can be released by the use of reducing agents to release Fe^{2+} which could diffuse through the aHSF hydrogel network and be monitored. Iron release from ferritin cages has been successfully achieved, as previously discussed, by the use of nicotinamide adenine dinucleotide-flavin mononucleotide (NADH/FMN) as a reducing system from the Fe^{3+} to Fe^{2+} . The system presents the advantage of being able to be measured using a spectrophotometer. Where oxidized nicotinamide (NAD^+) absorbs strongly at 260 nm, and the reduced nicotinamide (NADH) compound absorbs strongly at 340 nm ($16,900 \text{ M}^{-1}\text{cm}^{-1}$).²⁵⁷ Another method was proposed by Vladimirova *et al.* using a potentiometric titration of the release of Fe^{2+} with the aid of potentiometric titration using Ce^{4+} as an oxidizing titrant.²⁵⁸ However, we envisioned that the best method to do the release of the iron cores was to utilize an ascorbate solution in an acidic buffer with the determination of the released Fe^{2+} by formation of its *o*-phenanthroline complex with measurement at 510 nm.²³⁷ During the experiments, it was necessary to guarantee that swelling equilibrium was achieved, because the hydrogel water content will affect the release profile. This behavior occurs because water in the matrix is the medium through which cargo will diffuse. Water content and swelling are obviously related as both are dependent on the amount of water the hydrogel can uptake when hydrated and thus should demonstrate similar trends.²²⁶

Furthermore, it was necessary to wash each hydrogel sample to guarantee that the measured iron corresponded exclusively to encapsulated iron release. The exposure of aHSF to UV light could adversely affect the stability of the protein as demonstrated by the reduction in activity of some enzymes when exposed to UV light.²²⁶ Increasing the PEGDA concentration in hydrogels resulted in a decrease of D within the hydrogel, as shown on Figure 40. Furthermore, as stated by Mellot *et al.* the addition of PEGDA will create a more highly crosslinked hydrogel network which will physically allow less water to diffuse in the hydrogel, thus resulting in a lower iron diffusion from the aHSF cores.²²⁶

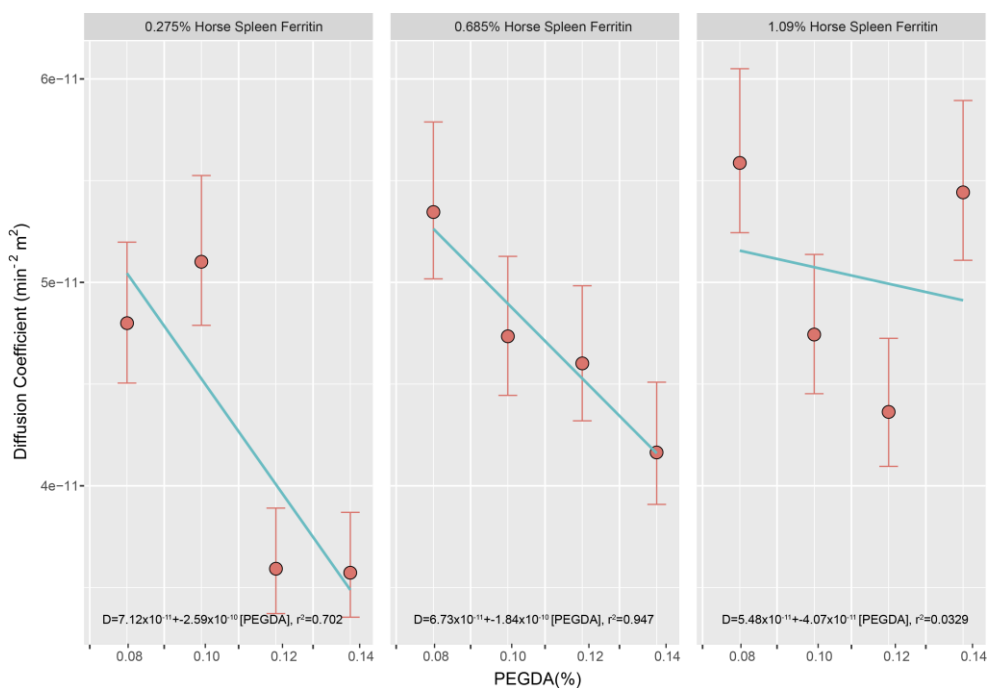


Figure 40. HSF concentration dependency on Fe²⁺ diffusion of aHSF PEGDA-based hydrogel networks

The diffusion rates for PEGDA hydrogels have been characterized for materials that have been loaded previously in the hydrogel matrix. Usually the values reported for dextran diffusion in 4-6% of PEGDA 10000 are close to $0.1 \times 10^{-5} \text{ cm}^2/\text{s}$.²⁵⁶ For BSA in 10-20% PEG 2500 values are on the order of $1 \times 10^{-7} \text{ cm}^2/\text{s}$.⁹⁴ In the case for the iron diffusivity measured for our aHSF network, the obtained values for no TA aHSF-hydrogels are on the order of $4 \times 10^{-11} \text{ cm}^2/\text{s}$. Furthermore, as represented on Figure 41, as the TA weight percentage increases, there is an increase in D. This behavior favored the reducing agent penetration, which as a result gave rates on the order of $1 \times 10^{-10} \text{ cm}^2/\text{s}$. It has been reported that alginate hydrogels present the disadvantage that they can complex with Fe^{2+} , which in turn can affect the diffusion of divalent ions from the aHSF-PEGDA-alginate hydrogels.²⁵⁹ However, our findings suggest that the diffusion of Fe^{2+} is favored with the alginate hydrogels due to the fact that it presented the highest diffusion rates from the aHSF-hydrogels studied.

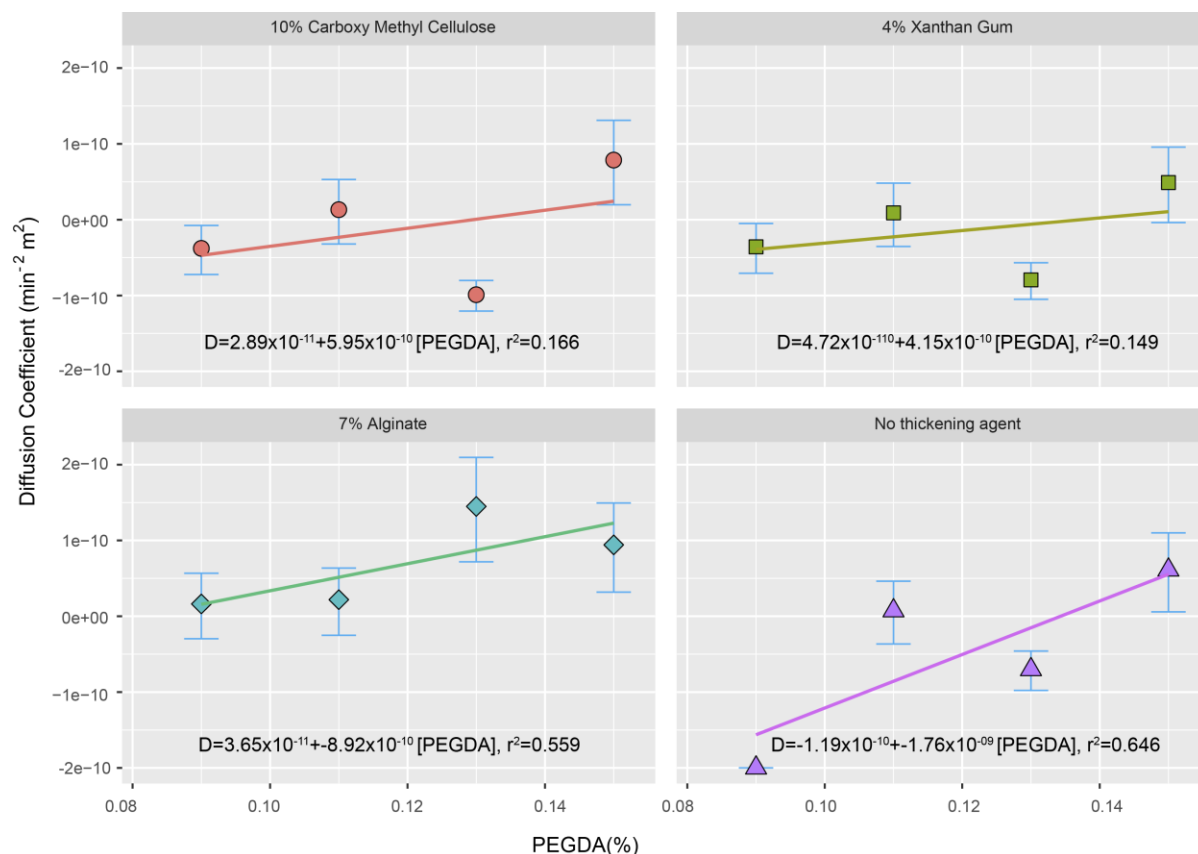


Figure 41. PEGDA concentration dependency on Fe²⁺ diffusion from HSF bioconjugated PEGDA-Based hydrogels for A) CMC, B) XG, C) ALG and D)NTA (Data shown in Appendix F).

4.3.1.4 Fe³⁺ release from a loaded aHSF embedded into the hydrogel network by cage declustering

The purpose of the development of the bioink was to exploit the cage protein capabilities in a printed hydrogel. One well-known capability that can be harnessed is the declustering potential of the 24-mer to release a cargo of interest. This behavior has been studied with HSF in solution by Sutisansanee *et al.*²⁴ There is no study, to our knowledge,

that involved the study of the protein declustering within a hydrogel network. To understand mass transport within PEGDA hydrogels, Lee *et al.* stated that large macromolecular solutes do not penetrate hydrogel networks easily.²⁵⁶ More in depth, there is a threshold value of mesh size for PEGDA hydrogels on which a solute (e.g., a large protein such as ferritin) that is encapsulated within a hydrogel network will not be able to diffuse into the network due to restrictive entanglements with the hydrogel network. PEGDA hydrogels (M_w 575–20000) have mesh sizes less than 0.1–10 nm, respectively.²⁶⁰

The first approach in our current investigation was to select an appropriate method to understand the cargo release from the hydrogels. Traditionally, the release of cargo from hydrogels was measured using dextran-fluorescein isothiocyanate solutions. Theoretically, it could be possible to encapsulate dextran ($R_h < 4$ nm) within a ferritin protein cage.²⁶¹ However, It has been shown that for diffusive studies the dextran-fluorescein isothiocyanate molecule has a negative behavior because it is a linear and flexible polymer, which behaves differently than globular substrates.⁹⁴ To our benefit, aHSF has loaded iron cores, which can be quantified using a colorimetric assay with non complexating buffers such as MES or MOPS (0.1-1 M).¹⁸⁹ Therefore the method employing the o-phenanthroline/ Fe^{2+} complex was selected.

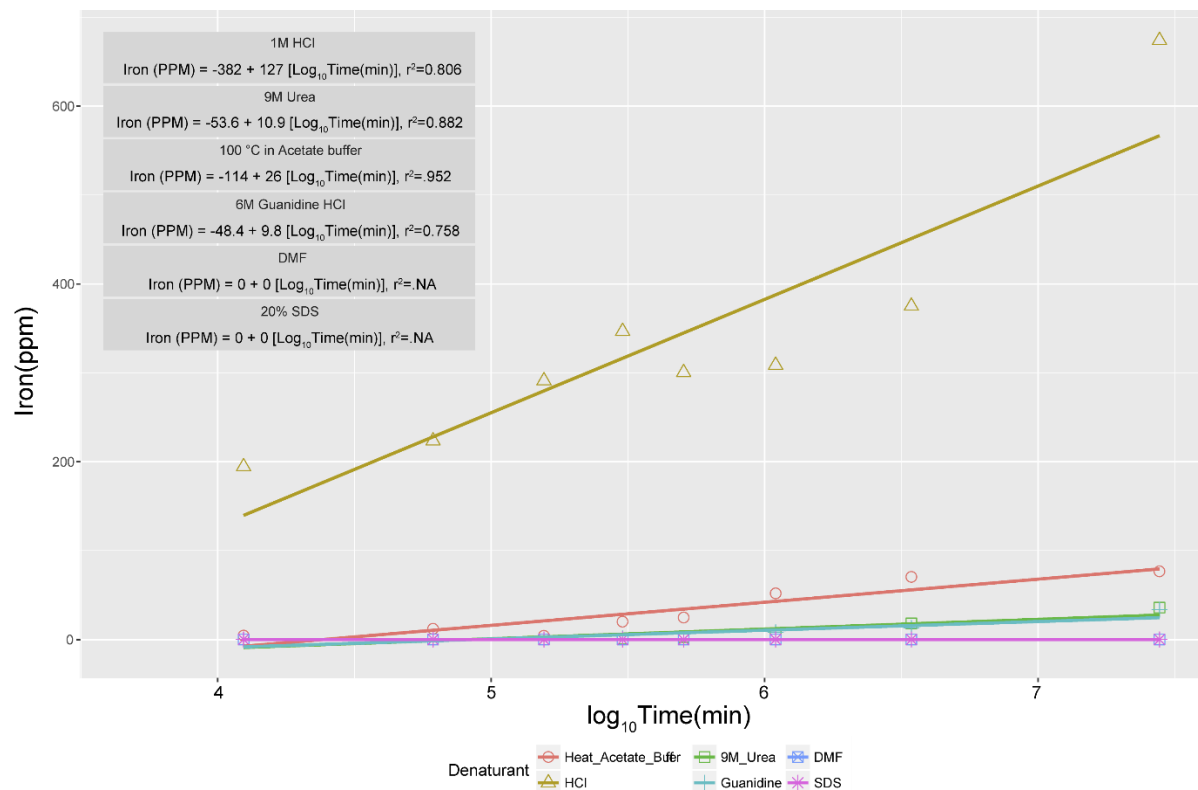


Figure 42. Coarse-declustering profiles of bioconjugated HSF in PEGDA networks for denaturing conditions.

The analysis was carried out in two stages. In the first stage (Figure 42) aHSF-PEGDA hydrogels were immersed in high concentration of declustering agents to to determine the critical factors required for cage declustering. In the second stage (Figure 43), the aHSF-PEGDA hydrogels were to be immersed in lower concentrations of the chaotropic solutions that showed declustering behavior in the first stage. From the first stage, it was shown that as expected, the declustering in 1.0 M HCl solutions is noticeable ($127 \text{ mg L}^{-1} \text{ min}^{-1}$). Heat treatment in acetate buffer (1 M, pH 3) revealed a 5-fold reduction of the declustering rate ($26 \text{ mg L}^{-1} \text{ min}^{-1}$), and high salt concentration presented a 10-fold

reduction of the declustering rate in comparison with HCl with 9 M urea solution (10.9 mg L⁻¹ min⁻¹) and 6 M guanidine-HCl (9.8 mg L⁻¹ min⁻¹). However, high organic solvent percentage and detergent concentrations of SDS 20% did not showed declustering potential.

Low pH provided the best conditions to decluster an aHSF hydrogel. However, the pH is unfeasible for biomedical applications, although could be useful for non-medical applications. To decluster the aHSF hydrogel, the temperature used was 100 °C, temperature at which the cargo was released. This is promising for the use of aHSF thermal sensitivity for rapid drug release using thermal ablation temperature ranges.²⁵⁵ Finally, high salt concentrations revealed a change among the aHSF interactions. It has been reported that high concentrations of urea can cause partial opening of aHSF 4-fold channels through localized unfolding of this protein while keeping its shell-like structure.⁹⁰

In the second stage, four conditions were analyzed to study milder conditions for the aHSF hydrogel. It was shown, that low pH is still the most efficient way to decluster the capsule protein. However, as the HCl is decreased to 0.1 M there is a 25-fold decrease in the rate of declustering and even further when the HCl concentration is decreased to 0.01 M. Finally, heat treatment (pH 7) and acetate buffer (1.0 M, pH 3) gave the lowest declustering ratio.

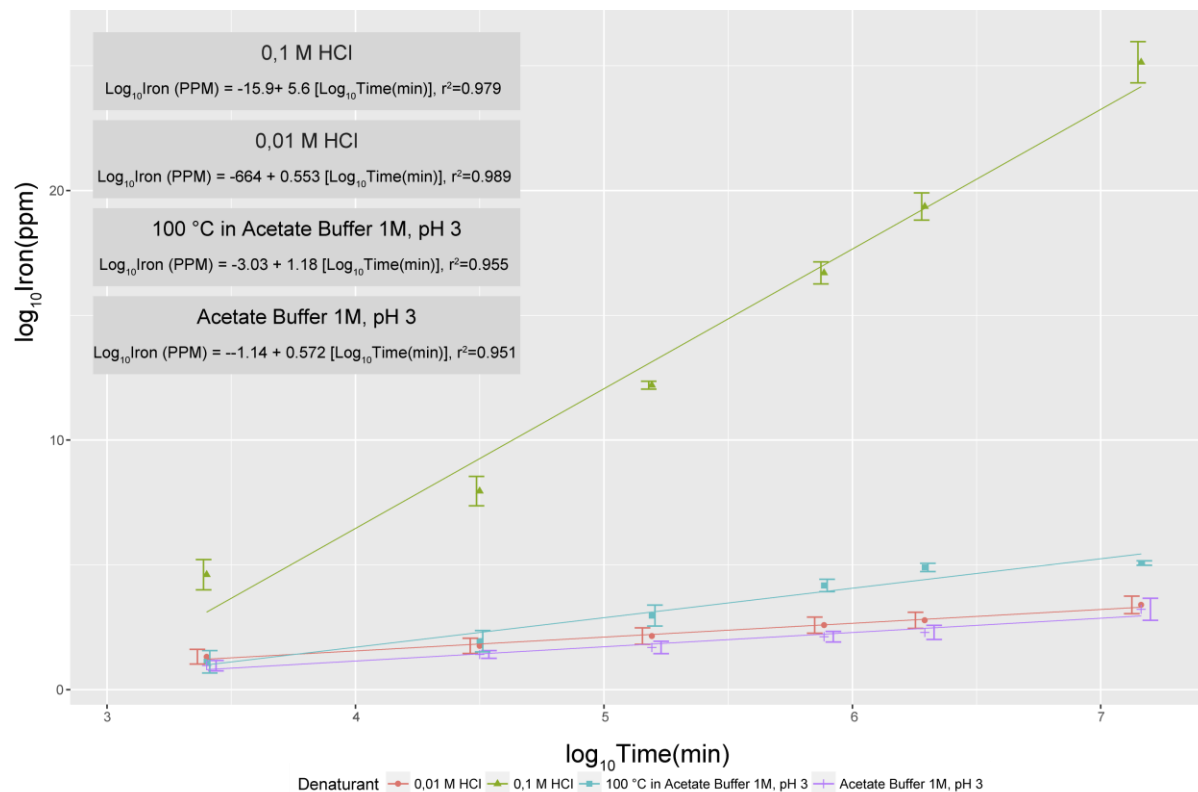


Figure 43. Detailed-declustering profiles of bioconjugated HSF in PEGDA networks.

4.3.1.5 Porosity studies on aHSF hydrogel networks

SEM was used to examine surface morphology and the internal structures of the hydrogel constructs. In the early stages of the research, the samples were lyophilized for 24 hours and then they were cut to expose their inner structure. This was followed by placing the slides in the SEM chamber and analyzing these slices using high vacuum, 10 kV electron beam, 1.0 spot size, using 0.2 mbar conditions. However, no apparent network was identified from these experiments. The hydrogels formed a smooth film due

to collapse of the network. This behavior has been reported previously in the literature for preparation of samples for imaging PEGDA hydrogels.

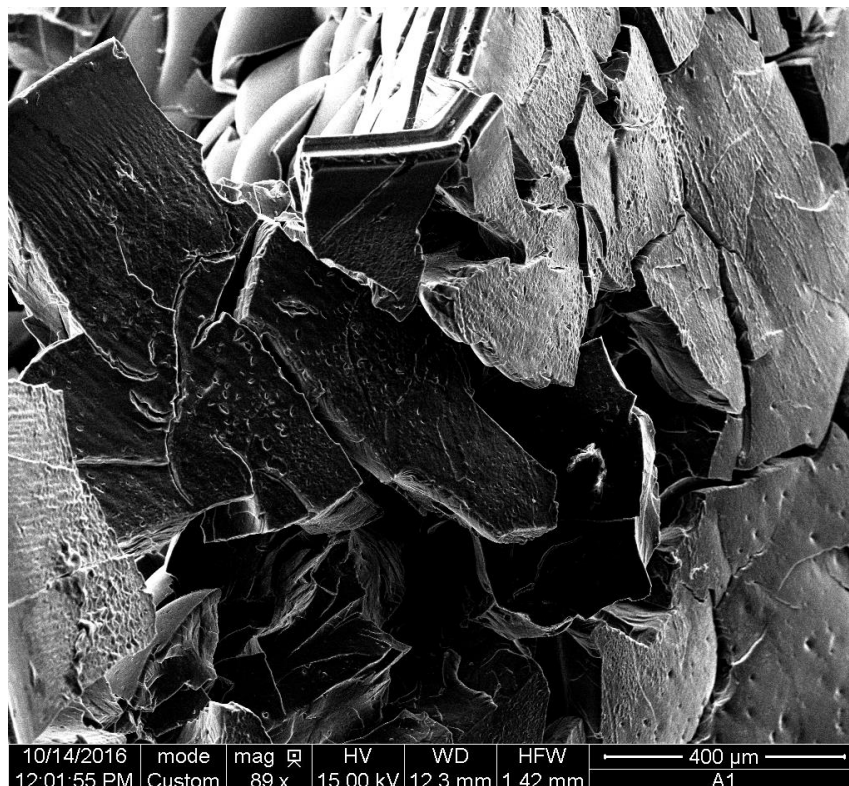


Figure 44. SEM image of a 20% PEGDA-aHSF hydrogel (400- μ m image recorded in ESEM mode, high vacuum, 30 kV)

Therefore, it was hypothesized that wet samples were needed to structurally preserve the hydrogel network. In the literature, environmental secondary electron detector (ESED) or gaseous secondary electron detectors (GSED) are used to analyze wet samples, in combination with low temperatures, H₂O vapor rich atmosphere and low laser power.²⁶³ The hydrogels were frozen at -20 °C and kept at that temperature until they were measured. Once measured the hydrogels showed a random honeycomb

network structure, which was not observed when freeze-dried gels were analyzed (Figure 45).

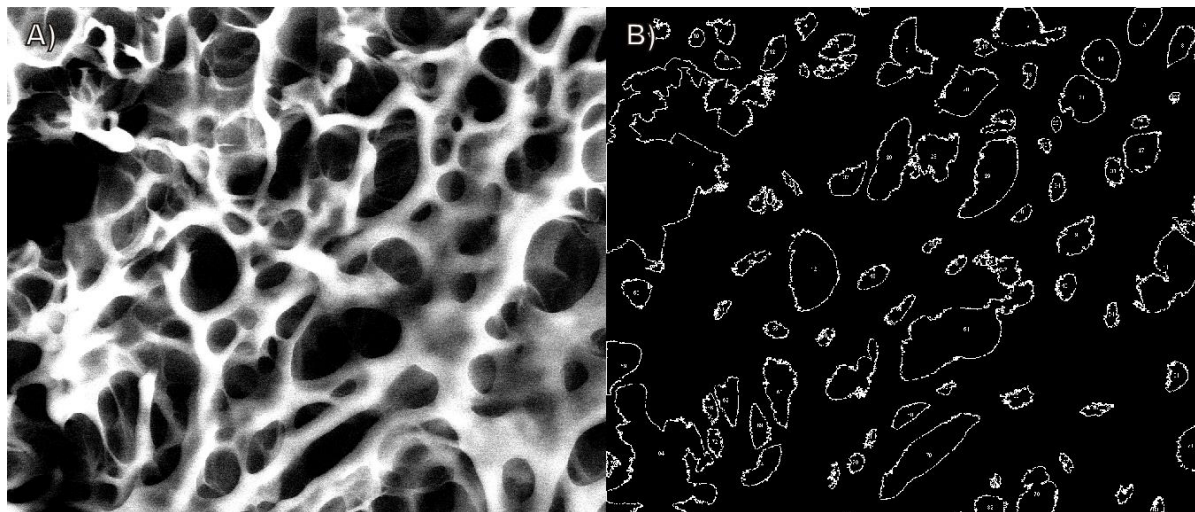


Figure 45. Images for A) 100 μm image recorded in ESEM mode, low vacuum and 30 kV, and B) Negative threshold pore identification by the ImageJ software for porosity determination.

To analyze the pore size distribution, a script was developed using ImageJ, threshold values, object counter and the particle analyzer as shown in Appendix I. The images were acquired using the ESEM detector and the backscatter detector (BSD). Interestingly, as previously mentioned, pure PEGDA hydrogels (Mw 575–20000) have mesh sizes less than 0.1–10 nm, respectively.²⁶⁰ This pore size is not suitable for cell viability due to the prevention of cell migration. Therefore, it was of interest to determine the effect of the polysaccharides in the pore size of the hydrogels constructs.

Each sample was imaged using the regular ESEM detector and the BSD. A variation is observed and the lowest mean pore value for 7% CMC hydrogel with 14% PEGDA is $39.6 \pm 3.0 \mu\text{m}$, which is significantly higher than the reported values for PEGDA: Furthermore, the CMC pore size varies significantly. Barbucci *et al.* reported a pore size distribution change (15-90 μm) when the CMC weight percentage is increased by 1% in hydrogels.²⁵⁵ Alginate showed mean pore sizes of $125.1 \pm 5.0 \mu\text{m}$ in agreement with what has been reported for alginate mean pore size (20-250 μm) in the literature.²⁶⁴ This observation suggests that the pore size is dominated by the polysaccharide content. As the polysaccharide content is increased there is a decrease in structural strength; hydrogels containing higher than 12% TA did not form. Therefore, further improvement in the porosity of aHSF-PEGDA hydrogels by using polysaccharides is limited. It was observed that the incorporation of TA acted as a porogen, which increased the pore size and facilitated structural integrity of the hydrogels.

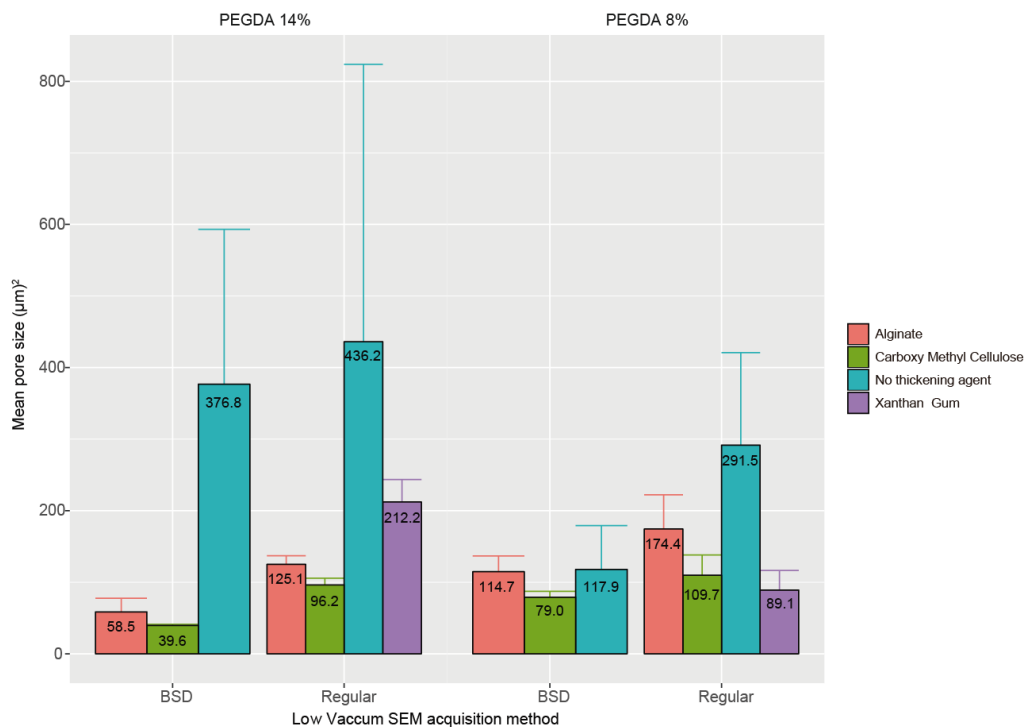


Figure 46. Pore size dependency of HSF-PEGDA based hydrogels on the presence of thickening agent.

It was shown for hydrogels, which do not have TA present into the construct, that the greatest error is due to fast H₂O evaporation. Therefore, it was challenging to acquire repeatable results when lower TA concentrations were evaluated using SEM due to low water retention. To reduce the effects of the H₂O evaporation, it might be possible to substitute the solution with low-vapour-pressure liquids allowing SEM examination of infiltrated samples.²⁶⁵

4.3.2 *E. coli* growth on aHSF hydrogel networks

To check the feasibility of the proposed hydrogel system, it was decided to investigate the encapsulation of bacterial cells by the hydrogel combinations selected in Chapter 3 and to bioprint these employing our visible light bioprinting system. The total fabrication time for PEGDA blends with 10% CMC, 7% Alg and 4% XG was about 15 minutes per 0.7x0.7x0.2 cm³ construct. As a result, to guarantee an excellent bioprinting process with an adequate cell viability and good bioprinting fidelity a thorough optimization was undertaken.²⁶⁶

Traditionally, to determine cell viability following encapsulation, a Live/Dead staining assay is used. Its functionality allows one to count the live (staining green) and dead cells (staining red) in every experimental condition. Furthermore, the samples are imaged multiple times in random fields with a desired thickness to guarantee that a representative sample has been acquired.²²⁵ However, there was an interest to exploit the properties of the *E. coli* mutant His-tag GFP-S65T cell lines available in the laboratory in order to have a reference fluorescence signal confirming that we were imaging cell growth inside the hydrogel construct. The His-tag GFP-S65T variant allowed for a controlled expression of the protein enabling imaging of cells in the green channel. We characterized the unseeded cell hydrogel scaffold and the cell seeded hydrogel. In this case, the cells were not selected to eliminate the untransfected cells, allowing us to visualize different levels of expression.

A preliminary assay was made with hydrogel constructs to evaluate the sedimentation profile. A 124.0 μm cross section of an 8% PEGDA-aHSF hydrogel with a cell density of 2.5×10^4 cells cm^{-3} was imaged using a confocal microscope at the maximum excitation/emission spectra of the GFP-*E. coli* cells at 400nm/460 nm. It was shown on Figure 47 that cell distribution was uniform. This allowed us to detect the cell attachment in the hydrogels by fluorescence imaging.

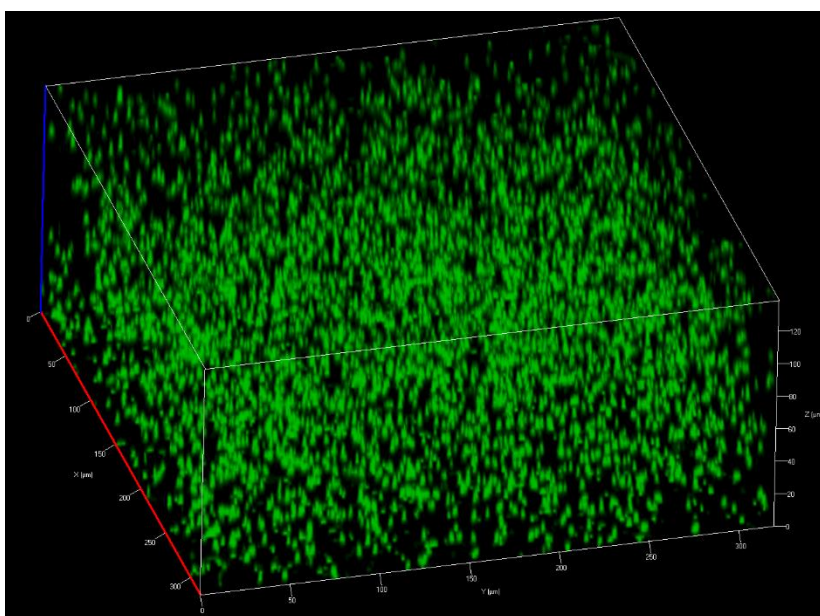


Figure 47. Qualitative assessment of GFP-*E. coli* growth on 124.0 μm cross section of aHSF-8% PEGDA-Based hydrogel construct.

The purpose of blending hydrogels with cells is to protect the cells from the shear force generated in the bioprinting process while maintaining their biological functions.²³¹ As mentioned in Chapter 3, these hydrogels modulated the viscosity and printability of these bioinks. In general, high viscosity bioinks offer excellent printability and shape

fidelity with the drawback of low cell viability. In contrast, low viscosity bioinks have an enhanced cell viability with a collapsed 3D structure as printed in a layer by layer process.¹⁴⁷ Furthermore, bioinks undergo a non-Newtonian behavior while bioprinting (e.g., shear thinning, yielding, or shear thickening) therefore; the effectiveness of the resulting construct will be very dependent upon material rheology regarding both printability and bioprint quality. As a result it was necessary for us to try to understand the differences in cell growth within the hydrogel scaffolds.

4.3.2.1 *E. coli* growth on PEGDA-based scaffolds

As previously mentioned, cell-loaded bioinks are subject to cell-bioink interactions while direct bioprinting. Therefore, it is important to control three aspects when pneumatic or piston driven direct-write bioprinting is employed: (A) cell sedimentation, which can lead to inhomogeneous cell distribution and needle clogging; (B) changes in the flow profiles which can disrupt the cell membrane; and (C) the curing conditions, which compromise cell viability by dehydration or exposure to crosslinking reagents.⁹⁹

To analyze matrix's impact on cell growth, an encapsulation of *E. coli* was made in PEGDA-based hydrogels. It was also desirable to determine the feasibility of the His-tag GFP-S65T variant as an imaging probe in the system. Four factors were selected to analyze the hydrogel system behavior: cell density, influence of PEGDA weight percentage, presence of aHSE and addition of a protein expression promoter (IPTG). Encapsulation of bacterial cells has been previously reported, where it was stated that hydrogels used for *E. coli* bioprinting required low pore sizes to prevent the escape of the

cells from within the gel (2.0 μm).²⁶⁷ A decrease of the pore size of low cross-linked materials (pore size > 40.0 μm) was achieved by adding a second polymer to the network, which increased the matrix entanglements (e.g., bacterial cellulose $8.4 \pm 2.5 \mu\text{m}$ decreases the pore size to 1.0 μm once silk fibroin is added).²⁶⁷

Hydrogel stiffness can affect cell spheroid viability and growth rate. Therefore, it was clear that there is a correlation between network structure of the cell-laden PEG-based hydrogels and PEGDA concentrations. Furthermore, when assessing cell arrangements inside hydrogel constructs, it has been reported that, within non-adhesive soft materials such as agarose and unmodified PEG hydrogels, the cells aggregate into multicellular spheroids over time.²⁶⁸ An incremental increase in PEGDA concentration results in an increase in crosslinking within the hydrogel. However, there was no apparent difference on cell viability for the hydrogel constructs if the PEGDA percentage was increased from 8% to 14%. This behavior suggested that the pore size was successfully reducing cell migration from the hydrogel construct due to close crosslinking of the polymer network. Furthermore, there is no clear evidence that aHSF had the potential to increase the pore size of the hydrogel construct.

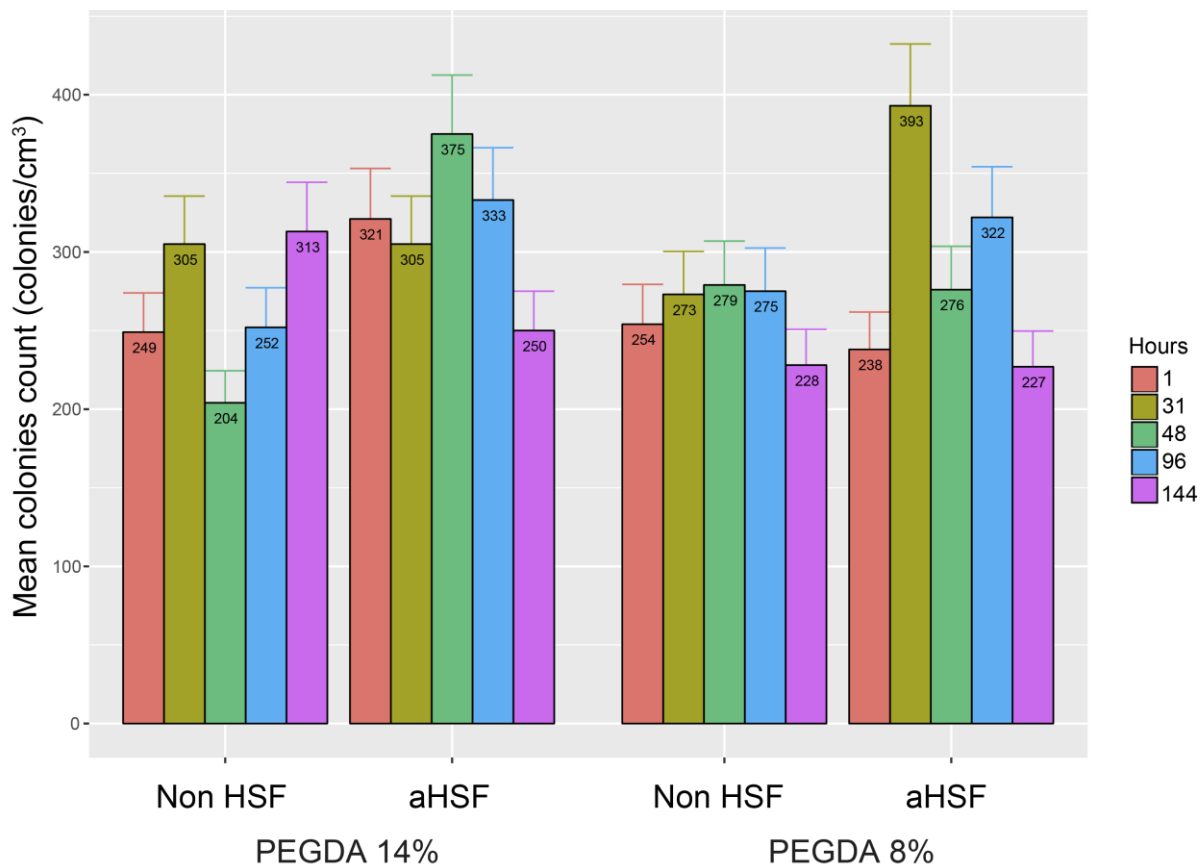


Figure 48. Evaluation of the effects of PEGDA concentration on cell density of a 1.25×10^5 cells cm^{-3} hydrogels construct immersed in LB with 0.5 mM of IPTG for 96 hours.

With respect to cell density, four concentrations were evaluated (5.0×10^3 , 2.4×10^4 , 1.25×10^5 , and 2.5×10^5 cells cm^{-3}). Nonetheless, the lowest cell density gave inconsistent results throughout the analysis. As a result, it was determined to exclude 5.0×10^3 cells cm^{-3} concentrations for the cell probing capabilities of *E. coli* cells within the hydrogel constructs. It is evident in Figure 49 that as a higher concentration of cell colonies were added to a bioink, more cell colonies were going to be detected. However,

it was unexpected to see no marked change in the number of cell colonies within the same concentrations over a range of 96 hours. It was difficult to successfully address cells that are migrating inside the hydrogel networks within the same cell density. In fact, on panel B of Figure 49, the 25 μL aliquot (1.25×10^5 cells cm^{-3}) showed no apparent change over 96 hours. To support this lack of change, the same behavior was observed for the 5 μL aliquot (2.4×10^4 cells cm^{-3}) on the same panel, where no clear trend was observed. In terms of cell identification capabilities, constructs that were immersed in 0.5 mM IPTG solution seem to be more consistent for cell identification. This could be attributed to the overexpression of GFP inside the *E. coli* cells, which would increase the intensity of the detected cells as measured by using confocal microscopy. Conversely, the overall cell growth was not successfully monitored by measuring the mean cell count that was growing inside a hydrogel construct. It was hypothesized that, hydrogel pore size might prevent the migration of the *E. coli* cells; as a result, a better way to identify cell growth and viability was by correlating the cell count with the associated intensity of such cells in the hydrogel construct.

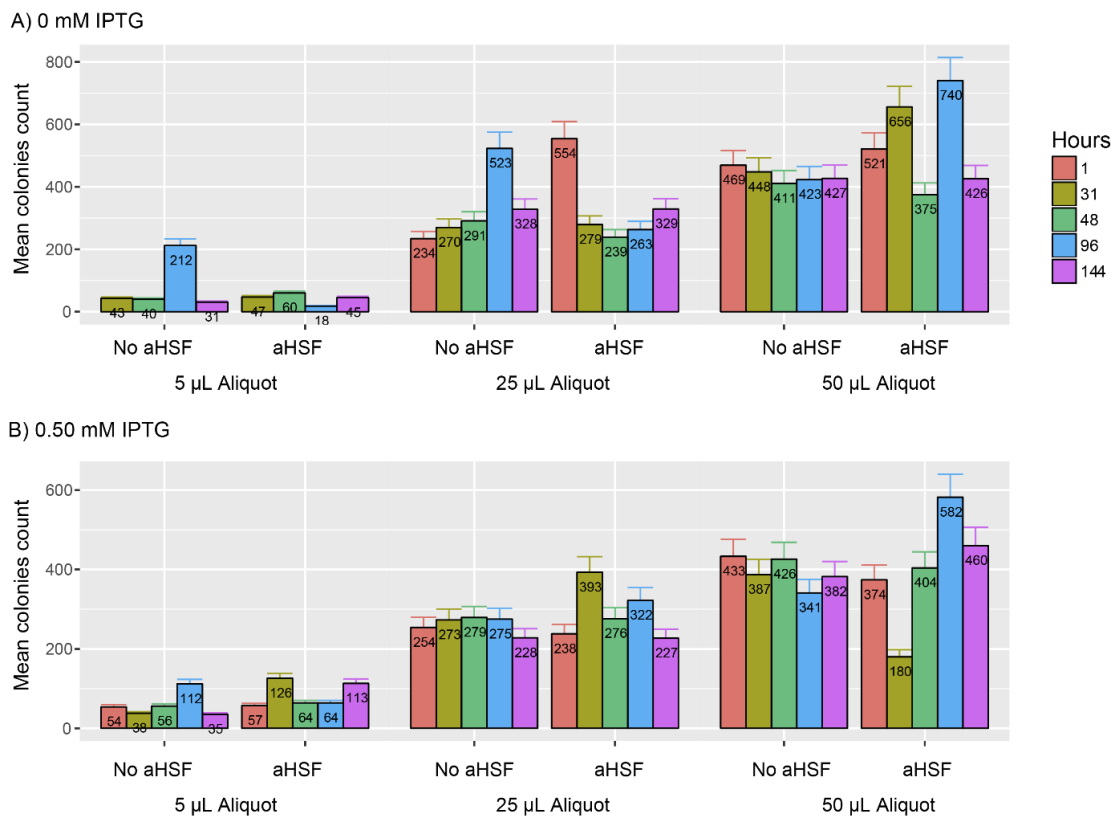
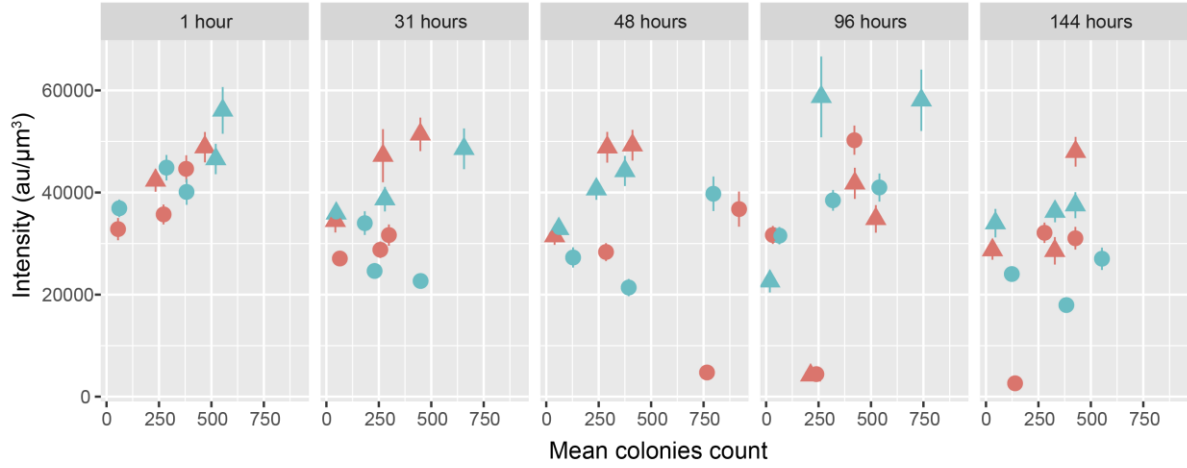


Figure 49. Evaluation of the effects on cell density (2.4×10^4 , 1.25×10^5 , and 2.5×10^5 cells cm^{-3}) for 8 % PEGDA hydrogels immersed in A) LB with 0 mM of IPTG and B) LB with 0.5 mM of IPTG.

The intensity was plotted over time for the PEGDA-based hydrogel constructs as shown in Figure 50. The mean intensity was directly correlated with the presence of the GFP produced within each *E.Coli* cell; therefore, as the mean intensity increased, more cells should be located within the hydrogel construct. Furthermore, it was identified that the intensity of the spheroids within the hydrogel construct had a maximum fluorescence threshold for the selected window of the confocal microscope data (800 gain, $312 \mu\text{m} \times 312$ and 1 au) of $60000 \text{ au } \mu\text{m}^{-2}$ that accounted for the maximum mean fluorescence a

hydrogel construct could show. As shown in Figure 51, there is no clear explanation for rate at which cell intensity grew over time inside the hydrogel constructs. It was presumed that cell diffusion was restricted for the spheroids; therefore, the cell growth profile will be characterized for the spheroids volume. It has been shown, that there is no evident differentiation in the cell intensity depending on the PEGDA weight percentage in the hydrogel for 4 days. To support this statement, a similar characterization was made by Lee *et al.* These authors characterized cells in PEGDA networks during 20 days on which the intensity of the measured signal did not vary; however, the size of the spheroid dramatically changed over time.²⁶⁸ To verify that the spheroid volume changed over time in our cases, an assessment of the PEGDA casted hydrogels was made plotting spheroid volume over time (Figure 51). A decreasing volume over time was supported by the detection of fewer GFP fluorescence signals. The explanation for this phenomenon was attributed to the *E. coli* death inside the casted gels due to low nutrient and oxygen exchange. Furthermore, Steff *et al.* reported two possibilities that can cause reduced GFP fluorescence within cells. First, cytosolic acidification (pH decrease 0.4 U during the apoptotic process) which will degrade the protein. Second, the possibility that the redox changes that occurred during the apoptotic process reduced the access of molecular oxygen needed for the oxidation of Tyr66 to generate the chromophore complex.²⁶⁹

A) 0 mM IPTG



B) 0.50 mM IPTG

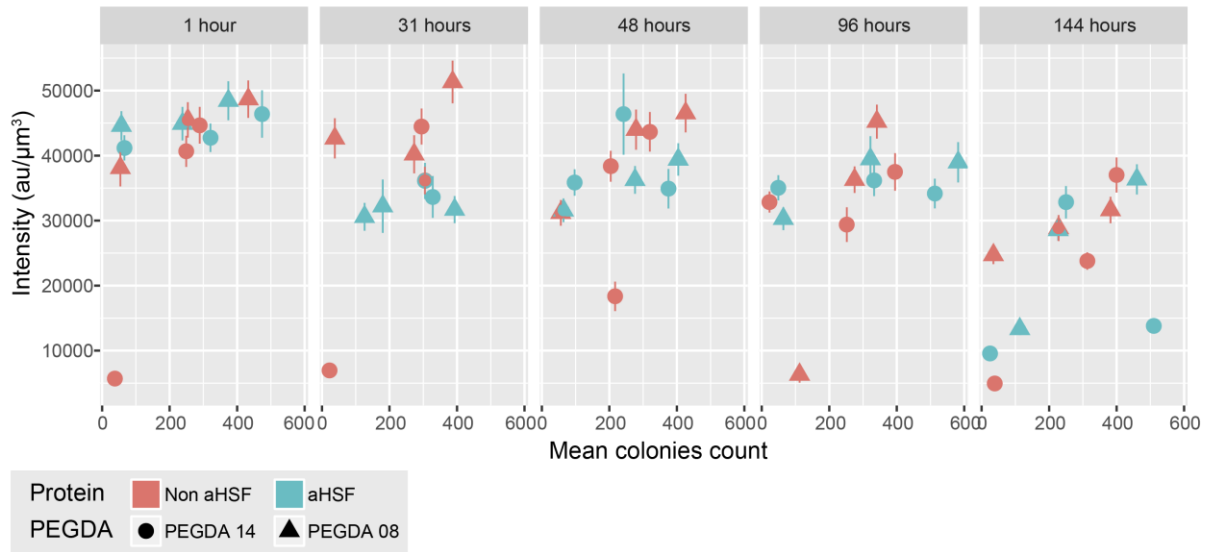


Figure 50. Time dependency for mean intensity versus cell colonies count for PEGDA hydrogels (Red: without protein and Blue: with protein) immersed in A) LB with 0 mM of IPTG and B) LB with 0.5 mM of IPTG.

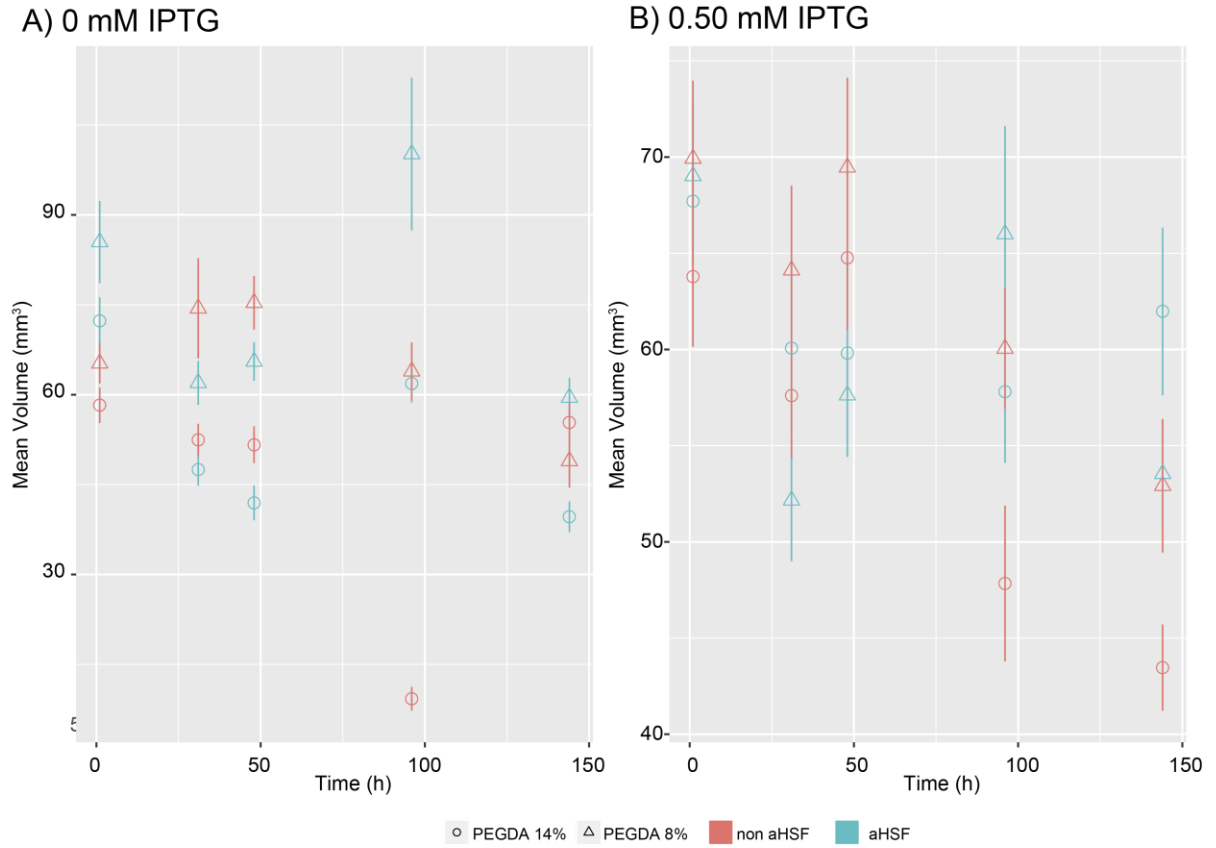


Figure 51. Time dependency for mean volume for PEGDA hydrogels (Red: without protein and Blue: with protein) immersed in A) LB with 0 mM of IPTG and B) LB with 0.5 mM of IPTG.

4.3.2.2 Effect of the delivery of the bioink

Three-dimensional bioprinting is a promising technique to deliver cell seeded bioinks; however, bioprinting is not only about structurally functional constructs, but also, these constructs need to foster normal functioning of the cells. Zheng *et al.* has reported that it is difficult to obtain a homogeneous distribution of cells within a viscous hydrogel and subsequently into the scaffolds.²⁷⁰ This statement indicated that cells distribution within the hydrogels without damaging cells was challenging to quantify.

To understand the impact of the bioprinting process for the hydrogel constructs, each bioink was bioprinted and compared to the results with a casted hydrogel. Both constructs were designed to have the same dimensions. When comparing each process, it was noticed that the layer-by-layer approach gave better curing to hydrogel constructs because it cures 0.150 mm at a time, allowing a better mechanical integrity in comparison with the casted gels in the press-to-seal silicon molds. Furthermore, it has been known that curing potential of a hydrogel is greatly influenced by the thickness of the layer that is being cured.²⁷¹

In our experiments, all the bioinks were loaded with a cell density of 1.25×10^5 cells/mL. Furthermore, each hydrogel scaffold was required 0.2 mL per experiment. Therefore, it was a good approximation that each hydrogel construct had 2.50×10^4 cells. As previously mentioned, these hydrogels were cured by the actuation of a FRP under a 405 nm wavelength. It has been reported by Vermeulen *et al.* that long exposure to radiation has a negative impact on cell survival and that it can be quantified using the

equation $S/S_0 = e^{-2.3026P_2(\lambda)D}$, where initial cell concentration (S_0), final cell concentration (S), dose (D) and an effective wavelength ($P_2(\lambda)$) were correlated to give an approximation of S .²⁷² Furthermore, it is known that increasing solution viscosity results in a decrease of radical diffusivity, which can decrease cell mortality.²⁷³ This suggested a possibility that radical diffusivity affected the cell viability by radical species interaction. It was desirable to understand the effects of prolonged exposure of the printed scaffold under this wavelength. For all the constructs (bioprinted and casted) it was estimated that S was about 20% for a 12 minute exposure at an intensity of 10 mW/cm² for a 405nm wavelength.

Once the hydrogels were fabricated, they were immersed into the culture media to facilitate cell growth. It was noticed that after 6 hours, especially for low PEGDA weight percentage, the hydrogel's mechanical structure was compromised over time because of increased swelling. This behavior was more evident for CMC based bioprinted hydrogels. The CMC hydrogels are not as intricate as Alg- or XG- based hydrogels. Perhaps, the addition of biodegradable hydrophobic polymers could be done to enhance the mechanical properties of purely hydrophilic hydrogels. For example, Annabi *et al.* reported that the mechanical properties of natural bioinks fabricated by electrospinning were dramatically increased with the addition of 10% PCL without use of any chemical crosslinker.²⁴⁷ It was noticed that casted CMC gels have good mechanical integrity in contrast with the ones that were printed in a layer-by-layer fashion, suggesting that it might be useful to consider this bioink as one that could be used with the help of a

sacrificial mold and then casted into this mold. Once the hydrogels were incubated for 6 hours, each sample was analyzed using CM and analyzed using ImageJ with the script provided in the Appendix J.

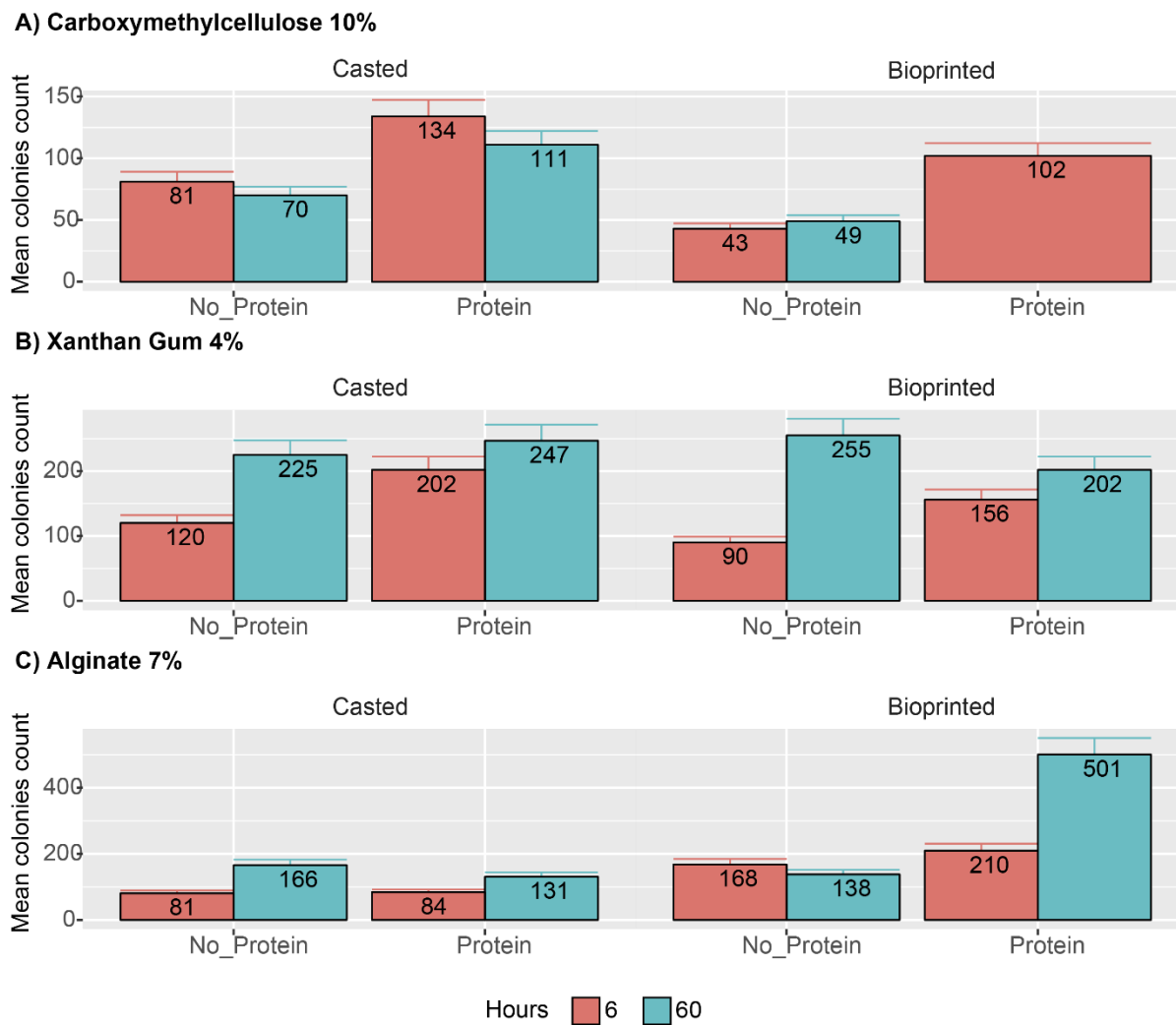


Figure 52. Time dependency of the cell growth inside A) Carboxymethylcellulose 10%, B) Xanthan Gum 4% and C) Alginate 7% hydrogel constructs with and without aHSF.

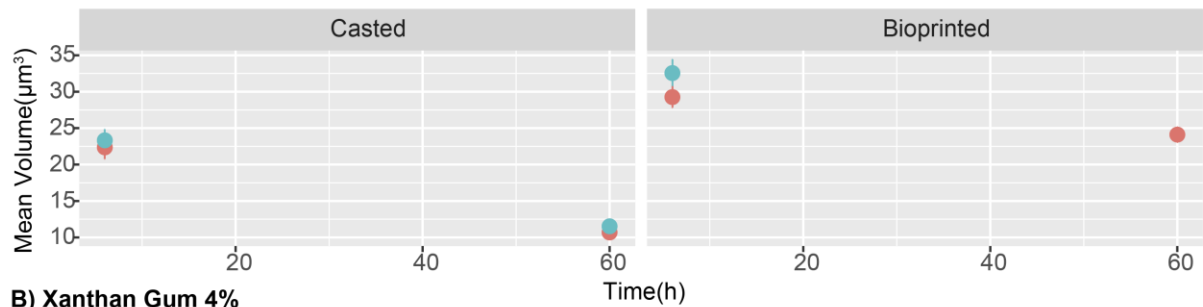
As shown in Figure 52, the mean colonies count for the first measurement is below the values reported for casted PEGDA-based hydrogel constructs from section 4.3.2.1 for 2.5×10^5 Cells/mL. The approximate values that were expected were of 200 mean colonies per $312 \times 312 \times 30 \mu\text{m}^3$ hydrogel construct. This difference was attributed to the fact that PEGDA-based bioink constructs are not as viscous as a TA-PEGDA-based bioink, making difficult the reduction of the particle spheroid size and a homogeneous distribution of them. Furthermore, because the TA-PEGDA-based hydrogels have increased pore sizes, it will facilitate cell diffusion from the hydrogel construct to the culture media, decreasing the signal measured with the CM. To our benefit, it was theorized that the presence of aHSF inside the TA-PEGDA-based hydrogels showed no alteration of the rate at which cells grew within the hydrogel construct. This could be harnessed by depositing an enhancing material of interest inside the cage protein to be released through its intrasubunit channels or by the declustering of the aHSF, as previously shown.

In terms of cell proliferation, it seems, that because the pore size of the hydrogels are bigger, it facilitates the cell replication and the creation of new spheroids due to cell diffusion. However, there is not a clear differentiation among the casted and the printed hydrogel constructs. From the data shown in Figure 52 panels B and C for the bioprinted scaffolds, an assumption can be made on which the cell replication is increased due to a higher porosity gel being present. More so, this can be attributed to the interplanar spacing that occurs when the layers are printed one on top of each other.

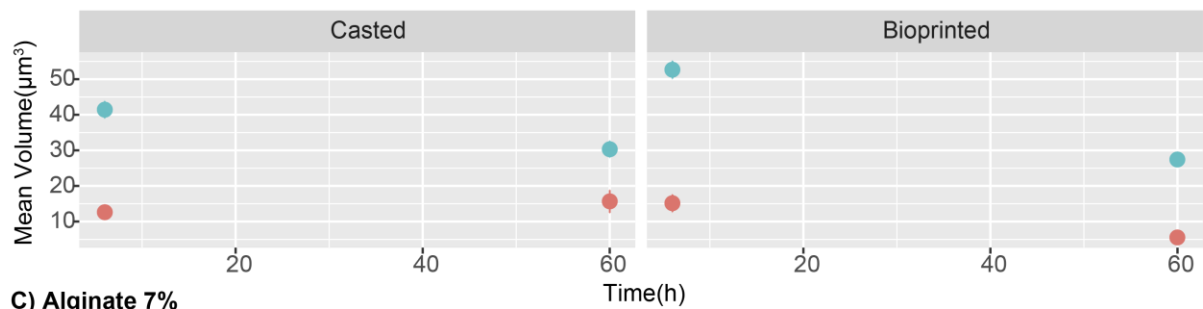
To support the evidence of cell diffusion, as shown in Figure 53, for all the panels that the spheroid volume decreases over time. This evidence appears to support the idea that cell migration is enhanced for TA-based hydrogels. Furthermore, the pore size order distribution, as shown on section 4.3.1.5 is Alg<CMC<XG. These observations are met by the Alg and XG hydrogels, where volume reduction is more distinct in XG hydrogels in comparison with Alg hydrogels. This trend is not followed by the CMC gels, because the mechanical stability of the gels were compromised, therefore it had more surface area exposed for cell diffusivity over time.

However, the criteria for a suitable network remains unclear and should be evaluated in future studies involving cell proliferation and migration rates within these networks. Overall, it will depend upon the desired application. The thickening agent concentration ranges were selected due to previously determined limits in printability. The stability of a vascularization network within hydrogels also needs evaluation for the *E. coli* to survive sufficiently long for any future applications.

A) Carboxymethylcellulose 10%



B) Xanthan Gum 4%



C) Alginate 7%

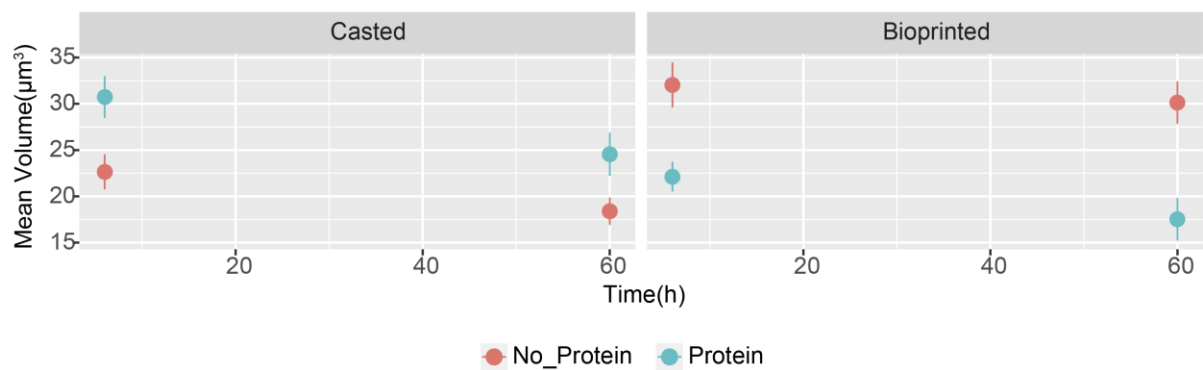


Figure 53. Spheroid volume change over time inside A) Carboxymethylcellulose 10%, B) Xanthan Gum 4% and C) Alginate 7% hydrogel constructs with and without aHSF.

4.4 Conclusions

We successfully identified a series of obstacles for 3D bioprinting of aHSF-TA-PEGDA based bioink. In terms of the bioink capabilities, it was extremely important to understand how the protein polymer conjugate behaved in terms of the cross-linking density, swelling properties, porosity and declustering potential. Furthermore, we developed these bioinks to facilitate the growth of His-tag GFP-S65T and be used as an imaging probe. It was shown that vascularization within the hydrogel constructs was critical to supply oxygen, nutrients and bioactive agents otherwise the His-tag GFP-S65T mutant was not suitable for cell viability studies. Furthermore, it was shown that the mechanism of hydrogel formation affects the way the cells grew inside these hydrogel constructs by the 3D bioprinting process. From the experimental results for particle and volume increase over time, a precise control of particle size and monodispersity were needed to guarantee an adequate use of the His-tag GFP-S65T variant as an imaging probe in the system. Our findings suggest that 14% PEGDA based bioinks with either 7% Alg or 4% XG will give the best printability with the highest cell proliferation capabilities. Furthermore, if it was desirable to minimize cell diffusion, while enhancing cell proliferation, and in order to take advantage of the host-guest interaction capabilities of HSF, the optimal bioink for bioprinting selected was found to be a 14% PEGDA, 4% XG based bioink with 0.1% aHSF.

Chapter 5 Future directions

5.1 Introduction

Despite the work that has been performed to develop the HSF-hydrogel bioink for 3D bioprinting, there are many opportunities to further the understanding of how cage like protein can be exploited within a three-dimensional network. Two projects are outlined below to develop new applications for the HSF-polymer networks. It was shown in Chapter 2 that PEGDA concentrations in a range of 8-20% weight were unsuccessful in tuning the mechanical properties of the bioinks. It showed that their primary function was to operate as a structural surrogate that will hold a 3D structure together. However, to improve the bioink formulation, the possibility of leaving out the PEGDA component of the bioink appears attractive. Reducing the components of the bioinks will facilitate the ability to control the mechanical properties of the hydrogel in a controlled manner. Furthermore, while modifying the polysaccharides used to fabricate the bioink, it is possible to fabricate a stimuli-responsive hydrogel. These points are discussed below.

Another way to increase the contribution of the cage-like protein is by changing the grafting approach that is being utilized on the protein-polymer conjugate. The resulting approach, elaborated upon below, could be used to either facilitate the control over the concentration of the protein that is being used within the hydrogel or, customize the mechanical properties for bioprinting processes. Furthermore, this control of the deposition can be extended to the ability to bioprint multicellular scaffolds one on top of the other.

5.1.1 Evaluation of modified polysaccharides for three-dimensional network generation

To enable the crosslinking of polysaccharides into three-dimensional networks, various approaches had been reported in the literature according to the type of material that is being modified. Crucial to this strategy is to determine the crosslinking mechanism that is the most adequate for the system.

For xanthan gum, we recommend two paths. A two-step modification could be used for thermal-inkjet bioprinting methods employing xanthan gum. The first would be a condensation process occurring by the mixing citric acid and XG at 165 °C (a temperature at which both reagents are stable) and would involve dehydration and ester linkages formation between these two components.²⁷⁴ To further the functionalization, this sacrificial scaffold could be followed by a subsequent etherification of the alkoxy groups with a vinyl halide to graft the modified HSF into the hydrogel network.²⁷⁵ However, an approach that could be undertaken with our existing equipment is possible; therefore, this approach is reported. A pH-responsive hydrogel has been successfully synthesized by modifying Arabic gum, a xanthan gum analog, with GMA to fabricate an Arabic Gum-Methacrylate hydrogel (AG-MA) having a water intake that is pH dependent due to the increase in the ionized groups of glucuronic acid segments.²⁷⁶ This hydrogel can undergo FRP using the acrylic moieties of the GMA.

In the case of CMC, a derivatization of the carboxyl moieties with aminoethyl methacrylamide hydrochloride (AEM) and EDC is possible. The result of this reaction is

a vinyl-modified CMC which could undergo FRP with a methacrylate-modified HSF under aqueous conditions.²⁷⁷ Likewise, the sodium salt of alginate could be modified using EDC and a potentially reactive amine. AEM could be used as a feasible reagent for polysaccharide modification. A similar approach has been used to attach azide groups on to alginate by the EDC/NHS reaction of alginate with an NH₂-PEG-N₃ analog.²⁷⁸ Once the polysaccharides have been modified, it would then be necessary to evaluate the rheological properties of the hydrogels such as G', G'', phase shift and creep time to recover the polymer network. This will further our understanding of how the polymer will reform and shear once it is extruded from the pneumatic system of a 3D bioprinter. These variables will impact the resolution of the polysaccharide-containing bioprinting scaffolds. Also, it would be of paramount importance to verify if the modified polysaccharides hydrogels could store large amounts of water compared to with their dry weight. A more thorough analysis has to be made to understand the critical protein concentration that can be added into the protein gel without modifying the rheological properties of the scaffold.

Furthermore, an assessment of the gel's cytotoxicity to various cells is needed to verify that the developed network can be used for bioprinting prior to and after protein incorporation, with evaluation of the effect of the presence of the incorporated polysaccharide. Therefore, cell-scaffold interaction studies would be required using RealTime-Glo MT in combination with LIVE/DEAD imaging to validate how a cell population spreads inside the proposed hydrogels. This approach could be used to quantitatively and continually measure cell proliferation during the first 72 hours of being

seeded into a 3D scaffold, with further quantification of cell viability after six days of seeding.²⁷⁹ This technique could allow one to measure virtually any cell line that might be of interest. In general, this strategy could provide unique and highly specific functionalities for modification of the bioink.

5.1.2 Variation of the polymer-protein conjugate approach

Employing a different mechanism to graft the HSF into the network would expand the possibilities of using the hydrogel scaffold as a platform for nanotechnology. A simple variation from a grafting-to to a grafting-from approach could change the polymer properties dramatically. Grafting a given polymer from the HSF subunit has been evaluated before, and a water-soluble polymer was employed in that study.⁸⁶ However, grafting-from the HSF using ATRP and combining it with a further step of FRP could aid in controlling the spatial localization of each ferritin subunit within the gel. Nanostructured hybrid micro-gels have been previously prepared by incorporating well-defined poly(oligo (ethylene oxide) monomethyl ether methacrylate) (POEO₃₀₀MA) by ATRP, followed by a derivatization of the pendant hydroxyl groups from the amino acid residues with methacrylated groups to generate photo-reactive nanospheres.²⁸⁰

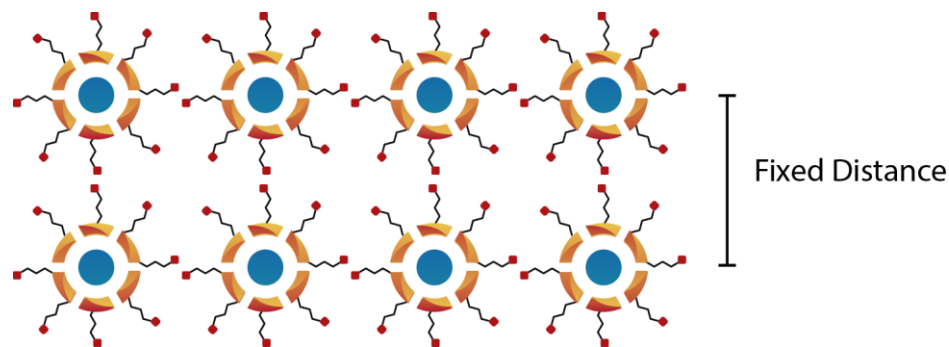


Figure 54. Diagram of an aHSF-based hydrogel with controlled aHSF concentration.

By generating a photoreactive ferritin nanosphere, it could be possible to estimate the hydrodynamic radius of the particle (R_H) and as a result, the density of loaded ferritin molecules that a specific hydrogel construct could store. To further this control, the ferritin-based hydrogel framework could be used as an iron templating scaffold. To characterize the HSF distribution, it is possible to use a UV-Ozone oxidation to remove all the polymeric material. Later, using AFM it could be possible to reconstruct the three-dimensional spacing using the deposited monolayer of iron cores.²⁸¹ Once the ferritin density within the hydrogel is characterized, it could be used to bioprint a scaffold, as a system could be used to encapsulate a given material in a specific density with a controlled distance between hydrogel centers. Furthermore, It might also be used to generate a template for quantum dots controlled arrays of quantum dots, a potentially useful material for cancer imaging in vivo environments.²⁸²

Letters of Copyright Permissions

Permission 1. Copyright use for Figure 2.

29/11/2017

RightsLink Printable License

ELSEVIER LICENSE TERMS AND CONDITIONS

Nov 29, 2017

This Agreement between 330 Phillip Str. ("You") and Elsevier ("Elsevier") consists of your license details and the terms and conditions provided by Elsevier and Copyright Clearance Center.

License Number	4238371122214
License date	Nov 29, 2017
Licensed Content Publisher	Elsevier
Licensed Content Publication	Journal of Molecular Biology
Licensed Content Title	Quasi-equivalent viruses: a paradigm for protein assemblies 1 1 Edited by T. Richmond
Licensed Content Author	John E Johnson, Jeffrey A Speir
Licensed Content Date	Jul 27, 1997
Licensed Content Volume	269
Licensed Content Issue	5
Licensed Content Pages	11
Start Page	665
End Page	675
Type of Use	reuse in a thesis/dissertation
Portion	figures/tables/illustrations
Number of figures/tables/illustrations	1
Format	both print and electronic
Are you the author of this Elsevier article?	No
Will you be translating?	No
Original figure numbers	Figure 6
Title of your thesis/dissertation	Cage-like Proteins as Bioink Components for 3D Bioprinting
Expected completion date	Jan 2018
Estimated size (number of pages)	260
Requestor Location	330 Phillip Str. 636Cp Waterloo, ON N2L3W9 Canada Attn: 330 Phillip Str.
Total	0.00 CAD
Terms and Conditions	

INTRODUCTION

1. The publisher for this copyrighted material is Elsevier. By clicking "accept" in connection with completing this licensing transaction, you agree that the following terms and conditions apply to this transaction (along with the Billing and Payment terms and conditions

<https://s100.copyright.com/AppDispatchServlet>

1/5

Permission 2. Copyright use for Figure 3.

29/11/2017

Rightslink® by Copyright Clearance Center



RightsLink®

Home

Account Info

Help



Structure



Title: Structures of the native and swollen forms of cowpea chlorotic mottle virus determined by X-ray crystallography and cryo-electron microscopy

Author: Jeffrey A Speir, Sanjeev Munshi, Guoji Wang, Timothy S Baker, John E Johnson

Publication: Structure

Publisher: Elsevier

Date: January 1995

Copyright © 1995 Elsevier Science Ltd. All rights reserved.

Logged in as:
Adrian Delgado

LOGOUT

Order Completed

Thank you for your order.

This Agreement between 330 Phillip Str. ("You") and Elsevier ("Elsevier") consists of your license details and the terms and conditions provided by Elsevier and Copyright Clearance Center.

Your confirmation email will contain your order number for future reference.

[printable details](#)

License Number	4238380556687
License date	Nov 29, 2017
Licensed Content Publisher	Elsevier
Licensed Content Publication	Structure
Licensed Content Title	Structures of the native and swollen forms of cowpea chlorotic mottle virus determined by X-ray crystallography and cryo-electron microscopy
Licensed Content Author	Jeffrey A Speir, Sanjeev Munshi, Guoji Wang, Timothy S Baker, John E Johnson
Licensed Content Date	Jan 1, 1995
Licensed Content Volume	3
Licensed Content Issue	1
Licensed Content Pages	16
Type of Use	reuse in a thesis/dissertation
Portion	figures/tables/illustrations
Number of figures/tables/illustrations	1
Format	both print and electronic
Are you the author of this Elsevier article?	No
Will you be translating?	No
Original figure numbers	Figure 2
Title of your thesis/dissertation	Cage-like Proteins as Bioink Components for 3D Bioprinting
Expected completion date	Jan 2018
Estimated size (number of pages)	260
Requestor Location	330 Phillip Str. 636Cp
	Waterloo, ON N2L3W9 Canada Attn: 330 Phillip Str.
Total	0.00 USD

[ORDER MORE](#)

[CLOSE WINDOW](#)

<https://s100.copyright.com/AppDispatchServlet>

1/2

Permission 3. Copyright use for Figure 4.

29/11/2017

Rightslink® by Copyright Clearance Center



RightsLink®

Home

Account Info

Help



Title: X-ray structures of ferritins and related proteins
Author: Robert R. Crichton, Jean-Paul Declercq
Publication: Biochimica et Biophysica Acta (BBA) - General Subjects
Publisher: Elsevier
Date: August 2010
Copyright © 2010 Elsevier B.V. All rights reserved.

Logged in as:
Adrian Delgado

LOGOUT

Order Completed

Thank you for your order.

This Agreement between 330 Phillip Str. ("You") and Elsevier ("Elsevier") consists of your license details and the terms and conditions provided by Elsevier and Copyright Clearance Center.

Your confirmation email will contain your order number for future reference.

[printable details](#)

License Number	4238381248457
License date	Nov 29, 2017
Licensed Content Publisher	Elsevier
Licensed Content Publication	Biochimica et Biophysica Acta (BBA) - General Subjects
Licensed Content Title	X-ray structures of ferritins and related proteins
Licensed Content Author	Robert R. Crichton, Jean-Paul Declercq
Licensed Content Date	Aug 1, 2010
Licensed Content Volume	1800
Licensed Content Issue	8
Licensed Content Pages	13
Type of Use	reuse in a thesis/dissertation
Portion	figures/tables/illustrations
Number of figures/tables/illustrations	1
Format	both print and electronic
Are you the author of this Elsevier article?	No
Will you be translating?	No
Original figure numbers	Figure 1
Title of your thesis/dissertation	Cage-like Proteins as Bioink Components for 3D Bioprinting
Expected completion date	Jan 2018
Estimated size (number of pages)	260
Requestor Location	330 Phillip Str. 636Cp Waterloo, ON N2L3W9 Canada Attn: 330 Phillip Str.
Total	0.00 USD

[ORDER MORE](#)

[CLOSE WINDOW](#)

Copyright © 2017 Copyright Clearance Center, Inc. All Rights Reserved. [Privacy statement](#). [Terms and Conditions](#).
Comments? We would like to hear from you. E-mail us at customer@copyright.com

<https://s100.copyright.com/AppDispatchServlet>

1/1

Permission 4. Copyright use for Figure 5 and Figure 6.

29/11/2017

Rightslink® by Copyright Clearance Center



RightsLink®

Home

Account Info

Help



Title: Ferritin: A Versatile Building Block for Bionanotechnology
Author: Günther Jutz, Patrick van Rijn, Barbara Santos Miranda, et al
Publication: Chemical Reviews
Publisher: American Chemical Society
Date: Feb 1, 2015
Copyright © 2015, American Chemical Society

Logged in as:
Adrian Delgado

LOGOUT

PERMISSION/LICENSE IS GRANTED FOR YOUR ORDER AT NO CHARGE

This type of permission/license, instead of the standard Terms & Conditions, is sent to you because no fee is being charged for your order. Please note the following:

- Permission is granted for your request in both print and electronic formats, and translations.
- If figures and/or tables were requested, they may be adapted or used in part.
- Please print this page for your records and send a copy of it to your publisher/graduate school.
- Appropriate credit for the requested material should be given as follows: "Reprinted (adapted) with permission from (COMPLETE REFERENCE CITATION). Copyright (YEAR) American Chemical Society." Insert appropriate information in place of the capitalized words.
- One-time permission is granted only for the use specified in your request. No additional uses are granted (such as derivative works or other editions). For any other uses, please submit a new request.

If credit is given to another source for the material you requested, permission must be obtained from that source.

BACK

CLOSE WINDOW

Copyright © 2017 Copyright Clearance Center, Inc. All Rights Reserved. [Privacy statement](#). [Terms and Conditions](#).
Comments? We would like to hear from you. E-mail us at customer care@copyright.com

Permission 5. Copyright use for Figure 7.

29/11/2017

Rightslink® by Copyright Clearance Center



RightsLink®



Title: Multiple chaperonins in bacteria – why so many?
Author: Lund, Peter A.
Publication: FEMS Microbiology Reviews
Publisher: Oxford University Press
Date: 2009-07-01
Copyright © 2009, Oxford University Press

Logged in as:
Adrian Delgado

LOGOUT

Order Completed

Thank you for your order.

This Agreement between 330 Phillip Str. ("You") and Oxford University Press ("Oxford University Press") consists of your license details and the terms and conditions provided by Oxford University Press and Copyright Clearance Center.

Your confirmation email will contain your order number for future reference.

[printable details](#)

License Number	4238390693553
License date	Nov 29, 2017
Licensed Content Publisher	Oxford University Press
Licensed Content Publication	FEMS Microbiology Reviews
Licensed Content Title	Multiple chaperonins in bacteria – why so many?
Licensed Content Author	Lund, Peter A.
Licensed Content Date	Jul 1, 2009
Licensed Content Volume	33
Licensed Content Issue	4
Type of Use	Thesis/Dissertation
Requestor type	Educational Institution/Non-commercial/ Not for-profit
Format	Print and electronic
Portion	Figure/table
Number of figures/tables	1
Will you be translating?	No
Order reference number	
Title of your thesis / dissertation	Cage-like Proteins as Bioink Components for 3D Bioprinting
Expected completion date	Jan 2018
Estimated size(pages)	260
Requestor Location	330 Phillip Str. 636Cp Waterloo, ON N2L3W9 Canada Attn: 330 Phillip Str.
Publisher Tax ID	GB125506730
Billing Type	Invoice
Billing address	330 Phillip Str. 636Cp Waterloo, ON N2L3W9 Canada Attn: 330 Phillip Str.
Total	0.00 USD

[ORDER MORE](#)

[CLOSE WINDOW](#)

<https://s100.copyright.com/AppDispatchServlet>

1/2

Permission 6. Copyright use for Figure 8.

29/11/2017

Rightslink® by Copyright Clearance Center



RightsLink®

Home

Account Info

Help



Title: Targeting the N terminus for site-selective protein modification
Author: Christian B Rosen, Matthew B Francis
Publication: Nature Chemical Biology
Publisher: Nature Publishing Group
Date: Jun 20, 2017
Copyright © 2017, Rights Managed by Nature Publishing Group

Logged in as:
Adrian Delgado
Account #:
3001223565

LOGOUT

Order Completed

Thank you for your order.

This Agreement between 330 Phillip Str. ("You") and Nature Publishing Group ("Nature Publishing Group") consists of your license details and the terms and conditions provided by Nature Publishing Group and Copyright Clearance Center.

Your confirmation email will contain your order number for future reference.

[printable details](#)

License Number	4238410470996
License date	Nov 29, 2017
Licensed Content Publisher	Nature Publishing Group
Licensed Content Publication	Nature Chemical Biology
Licensed Content Title	Targeting the N terminus for site-selective protein modification
Licensed Content Author	Christian B Rosen, Matthew B Francis
Licensed Content Date	Jun 20, 2017
Licensed Content Volume	13
Licensed Content Issue	7
Type of Use	reuse in a dissertation / thesis
Requestor type	academic/educational
Format	print and electronic
Portion	figures/tables/illustrations
Number of figures/tables/illustrations	1
High-res required	no
Figures	Figure 1
Author of this NPG article	no
Your reference number	
Title of your thesis / dissertation	Cage-like Proteins as Bioink Components for 3D Bioprinting
Expected completion date	Jan 2018
Estimated size (number of pages)	260
Requestor Location	330 Phillip Str. 636Cp Waterloo, ON N2L3W9 Canada Attn: 330 Phillip Str.
Billing Type	Invoice
Billing address	330 Phillip Str. 636Cp Waterloo, ON N2L3W9 Canada Attn: 330 Phillip Str.

<https://s100.copyright.com/AppDispatchServlet>

1/2

Permission 7. Copyright use for Figure 9.

29/11/2017

Rightslink® by Copyright Clearance Center

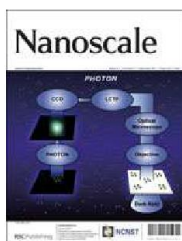


RightsLink®

Home

Account Info

Help



Title: Functionalization of protein-based nanocages for drug delivery applications

Author: Lise Schoonen, Jan C. M. van Hest

Publication: Nanoscale

Publisher: Royal Society of Chemistry

Date: May 9, 2014

Copyright © 2014, Royal Society of Chemistry

Logged in as:
Adrian Delgado
Account #:
3001223565

LOGOUT

Order Completed

Thank you for your order.

This Agreement between 330 Phillip Str. ("You") and Royal Society of Chemistry ("Royal Society of Chemistry") consists of your license details and the terms and conditions provided by Royal Society of Chemistry and Copyright Clearance Center.

Your confirmation email will contain your order number for future reference.

[printable details](#)

License Number	4238410645594
License date	Nov 29, 2017
Licensed Content Publisher	Royal Society of Chemistry
Licensed Content Publication	Nanoscale
Licensed Content Title	Functionalization of protein-based nanocages for drug delivery applications
Licensed Content Author	Lise Schoonen, Jan C. M. van Hest
Licensed Content Date	May 9, 2014
Licensed Content Volume	6
Licensed Content Issue	13
Type of Use	Thesis/Dissertation
Requestor type	academic/educational
Portion	figures/tables/images
Number of figures/tables/images	1
Distribution quantity	1
Format	print and electronic
Will you be translating?	no
Order reference number	
Title of the thesis/dissertation	Cage-like Proteins as Bioink Components for 3D Bioprinting
Expected completion date	Jan 2018
Estimated size	260
Requestor Location	330 Phillip Str. 636Cp Waterloo, ON N2L3W9 Canada Attn: 330 Phillip Str.
Billing Type	Invoice
Billing address	330 Phillip Str. 636Cp Waterloo, ON N2L3W9

<https://s100.copyright.com/AppDispatchServlet>

1/2

Permission 8. Copyright use for Figure 10.

29/11/2017

Rightslink® by Copyright Clearance Center



RightsLink®

Home

Account
Info

Help



Title: Peptide Coupling Reagents, More than a Letter Soup

Author: Ayman El-Faham, Fernando Albericio

Publication: Chemical Reviews

Publisher: American Chemical Society

Date: Nov 1, 2011

Copyright © 2011, American Chemical Society

Logged in as:

Adrian Delgado

Account #:

3001223565

LOGOUT

PERMISSION/LICENSE IS GRANTED FOR YOUR ORDER AT NO CHARGE

This type of permission/license, instead of the standard Terms & Conditions, is sent to you because no fee is being charged for your order. Please note the following:

- Permission is granted for your request in both print and electronic formats, and translations.
- If figures and/or tables were requested, they may be adapted or used in part.
- Please print this page for your records and send a copy of it to your publisher/graduate school.
- Appropriate credit for the requested material should be given as follows: "Reprinted (adapted) with permission from (COMPLETE REFERENCE CITATION). Copyright (YEAR) American Chemical Society." Insert appropriate information in place of the capitalized words.
- One-time permission is granted only for the use specified in your request. No additional uses are granted (such as derivative works or other editions). For any other uses, please submit a new request.

If credit is given to another source for the material you requested, permission must be obtained from that source.

BACK

CLOSE WINDOW

Copyright © 2017 Copyright Clearance Center, Inc. All Rights Reserved. [Privacy statement](#). [Terms and Conditions](#). Comments? We would like to hear from you. E-mail us at customer care@copyright.com

Permission 9. Copyright use for Figure 14, Figure 15 and Figure 16.

29/11/2017

Rightslink® by Copyright Clearance Center



RightsLink®



Title: Protein-polymer conjugates: synthetic approaches by controlled radical polymerizations and interesting applications
Author: Gregory N Grover, Heather D Maynard
Publication: Current Opinion in Chemical Biology
Publisher: Elsevier
Date: December 2010
 Copyright © 2010 Elsevier Ltd. All rights reserved.

Logged in as:
 Adrian Delgado
 Account #: 3001223565

LOGOUT

Order Completed

Thank you for your order.

This Agreement between 330 Phillip Str. ("You") and Elsevier ("Elsevier") consists of your license details and the terms and conditions provided by Elsevier and Copyright Clearance Center.

Your confirmation email will contain your order number for future reference.

[printable details](#)

License Number	4238420359899
License date	Nov 29, 2017
Licensed Content Publisher	Elsevier
Licensed Content Publication	Current Opinion in Chemical Biology
Licensed Content Title	Protein-polymer conjugates: synthetic approaches by controlled radical polymerizations and interesting applications
Licensed Content Author	Gregory N Grover, Heather D Maynard
Licensed Content Date	Dec 1, 2010
Licensed Content Volume	14
Licensed Content Issue	6
Licensed Content Pages	10
Type of Use	reuse in a thesis/dissertation
Portion	figures/tables/illustrations
Number of figures/tables/illustrations	1
Format	both print and electronic
Are you the author of this Elsevier article?	No
Will you be translating?	No
Original figure numbers	Figure 2
Title of your thesis/dissertation	Cage-like Proteins as Bioink Components for 3D Bioprinting
Expected completion date	Jan 2018
Estimated size (number of pages)	260
Requestor Location	330 Phillip Str. 636Cp Waterloo, ON N2L3W9 Canada Attn: 330 Phillip Str.
Total	0.00 CAD

[ORDER MORE](#) [CLOSE WINDOW](#)

Copyright © 2017 Copyright Clearance Center, Inc. All Rights Reserved. [Privacy statement](#). [Terms and Conditions](#).
 Comments? We would like to hear from you. E-mail us at customercare@copyright.com




<https://s100.copyright.com/AppDispatchServlet>


1/2

Permission 10. Copyright use for

Figure 17.

29/11/2017 Rightslink® by Copyright Clearance Center

  [Home](#) [Account Info](#) [Help](#) 



Title: 3D bioprinting of structural proteins
Author: Małgorzata K. Włodarczyk-Biegun, Aránzazu del Campo
Publication: Biomaterials
Publisher: Elsevier
Date: July 2017
Copyright © 2017, Elsevier

Logged in as:
Adrian Delgado
Account #: 3001223565
[LOGOUT](#)

Order Completed
Thank you for your order.

This Agreement between 330 Phillip Str. ("You") and Elsevier ("Elsevier") consists of your license details and the terms and conditions provided by Elsevier and Copyright Clearance Center.

Your confirmation email will contain your order number for future reference.

[printable details](#)

License Number	4238411318680
License date	Nov 29, 2017
Licensed Content Publisher	Elsevier
Licensed Content Publication	Biomaterials
Licensed Content Title	3D bioprinting of structural proteins
Licensed Content Author	Małgorzata K. Włodarczyk-Biegun, Aránzazu del Campo
Licensed Content Date	Jul 1, 2017
Licensed Content Volume	134
Licensed Content Issue	n/a
Licensed Content Pages	22
Type of Use	reuse in a thesis/dissertation
Portion	figures/tables/illustrations
Number of figures/tables/illustrations	1
Format	both print and electronic
Are you the author of this Elsevier article?	No
Will you be translating?	No
Original figure numbers	Figure 3
Title of your thesis/dissertation	Cage-like Proteins as Bioink Components for 3D Bioprinting
Expected completion date	Jan 2018
Estimated size (number of pages)	260
Requestor Location	330 Phillip Str. 636Cp Waterloo, ON N2L3W9 Canada Attn: 330 Phillip Str.
Total	0.00 CAD

[ORDER MORE](#) [CLOSE WINDOW](#)

Copyright © 2017 [Copyright Clearance Center, Inc.](#) All Rights Reserved. [Privacy statement](#). [Terms and Conditions](#).
Comments? We would like to hear from you. E-mail us at customercare@copyright.com

Permission 11. Copyright use for Figure 19.

18/12/2017

Rightslink® by Copyright Clearance Center

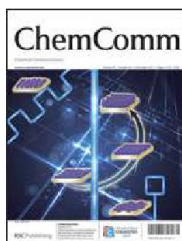


RightsLink®

Home

Account Info

Help



Title: Chemoselective derivatization of a bionanoparticle by click reaction and ATRP reaction
Author: Qingbing Zeng, Tao Li, Brandon Cash, Siqi Li, Fang Xie, Qian Wang
Publication: Chemical Communications (Cambridge)
Publisher: Royal Society of Chemistry
Date: Jan 25, 2007
Copyright © 2007, Royal Society of Chemistry

Logged in as:
Adrian Delgado
Account #:
3001223565

LOGOUT

Order Completed

Thank you for your order.

This Agreement between 330 Phillip Str. ("You") and Royal Society of Chemistry ("Royal Society of Chemistry") consists of your license details and the terms and conditions provided by Royal Society of Chemistry and Copyright Clearance Center.

Your confirmation email will contain your order number for future reference.

[printable details](#)

License Number	4252140004617
License date	Dec 18, 2017
Licensed Content Publisher	Royal Society of Chemistry
Licensed Content Publication	Chemical Communications (Cambridge)
Licensed Content Title	Chemoselective derivatization of a bionanoparticle by click reaction and ATRP reaction
Licensed Content Author	Qingbing Zeng, Tao Li, Brandon Cash, Siqi Li, Fang Xie, Qian Wang
Licensed Content Date	Jan 25, 2007
Licensed Content Volume	0
Licensed Content Issue	14
Type of Use	Thesis/Dissertation
Requestor type	academic/educational
Portion	figures/tables/images
Number of figures/tables/images	1
Distribution quantity	5
Format	print and electronic
Will you be translating?	no
Order reference number	
Title of the thesis/dissertation	Cage-like Proteins as Bioink Components for 3D Bioprinting
Expected completion date	Jan 2018
Estimated size	260
Requestor Location	330 Phillip Str. 636Cp Waterloo, ON N2L3W9 Canada Attn: 330 Phillip Str.
Billing Type	Invoice
Billing address	330 Phillip Str. 636Cp Waterloo, ON N2L3W9

<https://s100.copyright.com/AppDispatchServlet>

1/2

Bibliography

- (1) Uchida, M.; Klem, M. T.; Allen, M.; Suci, P.; Flenniken, M.; Gillitzer, E.; Varpness, Z.; Liepold, L. O.; Young, M.; Douglas, T. *Adv. Mater.* **2007**, *19* (8), 1025.
- (2) Walker, J. M. In *Protein Nanotechnology*; Gerrard, J. A., Ed.; Humana Press: New Zealand, 2013; pp 1–19.
- (3) Liu, A.; Verwegen, M.; de Rooter, M. V.; Maassen, S. J.; Traulsen, C. H.-H.; Cornelissen, J. J. L. M. *J. Phys. Chem. B* **2016**, *120* (26), 6352.
- (4) Douglas, T.; Allen, M.; Young, M. *Biopolym. Online* **2005**, 405.
- (5) Flenniken, M. L.; Uchida, M.; Liepold, L. O.; Kang, S.; Young, M. J.; Douglas, T. *Current Topics in Microbiology and Immunology*. Springer, Berlin, Heidelberg 2009, pp 71–93.
- (6) Sasaki, E.; Böhringer, D.; van de Waterbeemd, M.; Leibundgut, M.; Zschoche, R.; Heck, A. J. R.; Ban, N.; Hilvert, D. *Nat. Commun.* **2017**, *8*, 14663.
- (7) Flynn, C.; Lee, S.-W.; Peelle, B.; Belcher, A. *Acta Mater.* **2003**, *51* (19), 5867.
- (8) Zipper, P.; Schubert, D.; Vogt, J. *Eur. J. Biochem.* **1973**, *36* (2), 301.
- (9) Heddle, J. G.; Chakraborti, S.; Iwasaki, K. *Current Opinion in Structural Biology*. Elsevier Current Trends April 1, 2017, pp 148–155.
- (10) Douglas, T.; Young, M. *Nature* **1998**, *393* (6681), 152.
- (11) Comellas-Aragonès, M.; Engelkamp, H.; Claessen, V. I.; Sommerdijk, N. A. J. M.;

- Rowan, A. E.; Christianen, P. C. M.; Maan, J. C.; Verduin, B. J. M.; Cornelissen, J. J. L. M.; Nolte, R. J. M. *Nat. Nanotechnol.* **2007**, 2 (10), 635.
- (12) Johnson, J. E.; Speir, J. A. *J. Mol. Biol.* **1997**, 269 (5), 665.
- (13) Fuenmayor, J.; Gòdia, F.; Cervera, L. *N. Biotechnol.* **2017**, 39, 174.
- (14) Speir, J.; Munshi, S.; Wang, G.; Baker, T.; Johnson, J. *Structure* **1995**, 3 (1), 63.
- (15) Arosio, P.; Ingrassia, R.; Cavadini, P. *Biochim. Biophys. Acta - Gen. Subj.* **2009**, 1790 (7), 589.
- (16) Jutz, G.; van Rijn, P.; Santos Miranda, B.; Böker, A. *Chem. Rev.* **2015**, 115, 1653.
- (17) Ebrahimi, K. H.; Hagedoorn, P.; Hagen, W. R. *Chem. Rev.* **2015**, 115, 295.
- (18) Crichton, R. R.; Declercq, J. P. *Biochim. Biophys. Acta - Gen. Subj.* **2010**, 1800 (8), 706.
- (19) Andrews, S. C. *Biochim. Biophys. Acta - Gen. Subj.* **2010**, 1800 (8), 691.
- (20) He, D.; Marles-Wright, J. *N. Biotechnol.* **2015**, 32 (6), 651.
- (21) Harrison, P.; Arosio, P. *Biochim. Biophys. Acta - Bioenerg.* **1996**, 1275 (3), 161.
- (22) Boyd, D.; Vecoli, C.; Belcher, D. M.; Jain, S. K.; Drysdale, J. W. *J. Biol. Chem.* **1985**, 260 (21), 11755.
- (23) Zhang, Y.; Orner, B. P. *Int. J. Mol. Sci.* **2011**, 12 (8), 5406.
- (24) Suttisansanee, U. Biochemistry in bacterioferritin (Unpublished master thesis), University of Waterloo, 2006.

- (25) Bou-Abdallah, F. *Biochim. Biophys. Acta* **2010**, 1800 (8), 719.
- (26) Sato, D.; Ohtomo, H.; Yamada, Y.; Hikima, T.; Kurobe, A.; Fujiwara, K.; Ikeguchi, M. *Biochemistry* **2016**, 55 (2), 287.
- (27) Kim, M.; Rho, Y.; Jin, K. S.; Ahn, B.; Jung, S.; Kim, H.; Ree, M. *Biomacromolecules* **2011**, 12 (5), 1629.
- (28) Linder, M. C.; Kakavandi, H. R.; Miller, P.; Wirth, P. L.; Nagel, G. M. *Arch. Biochem. Biophys.* **1989**, 269 (2), 485.
- (29) Crichton, R. R.; Bryce, C. F. *Biochem. J.* **1973**, 133 (2), 289.
- (30) Treffry, A.; Bauminger, E. R.; Hechel, D.; Hodson, N. W.; Nowik, I.; Yewdallt, S. J.; Harrisont, P. M. *Biochem. J* **1993**, 296, 721.
- (31) Chasteen, D.; Harrison, P. *J. Struct. Biol.* **1999**, 126 (3), 182.
- (32) Hilton, R. J.; David Andros, N.; Watt, R. K. *BioMetals* **2012**, 25 (2), 259.
- (33) Barnes, C. M.; Petoud, S.; Cohen, S. M.; Raymond, K. N. *J. Biol. Inorg. Chem.* **2003**, 8 (1–2), 195.
- (34) Sun, S.; Chasteen, N. D. *J. Biol. Chem.* **1992**, 267 (35), 25160.
- (35) Bakker, G. R.; Boyer, R. F. *J. Biol. Chem.* **1986**, 261 (28), 13182.
- (36) Cavallo, S.; Mei, G.; Stefanini, S.; Rosato, N.; Finazzi-Agró, A.; Chiancone, E. *Protein Sci.* **2008**, 7 (2), 427.
- (37) Honarmand Ebrahimi, K.; Bill, E.; Hagedoorn, P.-L.; Hagen, W. R. *Nat. Chem. Biol.*

- 2012**, 8 (11), 941.
- (38) Mehlenbacher, M.; Poli, M.; Arosio, P.; Santambrogio, P.; Levi, S.; Chasteen, N. D.; Bou-Abdallah, F. *Biochemistry* **2017**, 56 (30), 3900.
- (39) May, C. A.; Grady, J. K.; Laue, T. M.; Poli, M.; Arosio, P.; Chasteen, N. D. *Biochim. Biophys. Acta - Gen. Subj.* **2010**, 1800 (8), 858.
- (40) Rother, M.; Nussbaumer, M. G.; Renggli, K.; Bruns, N. *Chem. Soc. Rev.* **2016**, 45 (22), 6213.
- (41) Lund, P. A. *FEMS Microbiol. Rev.* **2009**, 33 (4), 785.
- (42) Yébenes, H.; Mesa, P.; Muñoz, I.; Montoya, G.; Valpuesta, J. *Trends Biochem. Sci.* **2011**, 36 (8), 424.
- (43) Xia, P.-F.; Zhang, G.-C.; Liu, J.-J.; Kwak, S.; Tsai, C.-S.; Kong, I. I.; Sung, B. H.; Sohn, J.-H.; Wang, S.-G.; Jin, Y.-S. *Biotechnol. Bioeng.* **2016**, 113 (10), 2149.
- (44) Ojha, B.; Fukui, N.; Hongo, K.; Mizobata, T.; Kawata, Y. *Sci. Rep.* **2016**, 6 (1), 31041.
- (45) Stephanopoulos, N.; Francis, M. B. *Nat. Chem. Biol.* **2011**, 7 (12), 876.
- (46) Meredith, G. D.; Wu, H. Y.; Allbritton, N. L. *Bioconjug. Chem.* **2004**, 15 (5), 969.
- (47) King, N. P.; Bale, J. B.; Sheffler, W.; McNamara, D. E.; Gonen, S.; Gonen, T.; Yeates, T. O.; Baker, D. *Nature* **2014**, 510 (7503), 103.
- (48) Rudolf, G.; Heydenreuter, W.; Sieber, S. *Curr. Opin. Chem. Biol.* **2013**, 17 (1), 110.

- (49) Spicer, C. D.; Davis, B. G. *Nat. Commun.* **2014**, *5* (4740), 1.
- (50) Hermanson, G. T. In *Bioconjugate Techniques*; Elsevier: California, 2013; pp 233–234.
- (51) Hermanson, G. T. In *Bioconjugate Techniques*; Elsevier: California, 2008; pp 168–169.
- (52) Anderson, G. W.; Callahan, F. M.; Zimmerman, J. E. *J. Am. Chem. Soc.* **1967**, *89* (1), 178.
- (53) Studart, A. R. *Chem. Soc. Rev.* **2016**, *45* (2), 359.
- (54) Rosen, C. B.; Francis, M. B. *Nat. Chem. Biol.* **2017**, *13* (7), 697.
- (55) Chen, D.; Disotuar, M. M.; Xiong, X.; Wang, Y.; Chou, D. H.-C. *Chem. Sci.* **2017**, *8* (4), 2717.
- (56) Couto, C.; Vitorino, R.; Daniel-da-Silva, A. L. *Crit. Rev. Biotechnol.* **2017**, *37* (2), 238.
- (57) de Graaf, A. J.; Kooijman, M.; Hennink, W. E.; Mastrobattista, E. *Bioconjug. Chem.* **2009**, *20* (7), 1281.
- (58) Schoonen, L.; van Hest, J. C. M. *Nanoscale* **2014**, *6* (13), 7124.
- (59) Koniev, O.; Wagner, A. *Chem. Soc. Rev.* **2015**, *44* (15), 5495.
- (60) Larda, S. T.; Pichugin, D.; Prosser, R. S. *Bioconjug. Chem.* **2015**, *26* (12), 2376.
- (61) Rayment, I. *Methods in Enzymology*. Academic Press January 1, 1997, pp 171–

179.

- (62) El-Faham, A.; Albericio, F. *Chem. Rev.* **2011**, *111* (11), 6557.
- (63) Baslé, E.; Joubert, N.; Pucheault, M. *Chem. Biol.* **2010**, *17* (3), 213.
- (64) Baldwin, A. D.; Kiick, K. L. *Bioconjug. Chem.* **2011**, *22* (10), 1946.
- (65) Fontaine, S. D.; Reid, R.; Robinson, L.; Ashley, G. W.; Santi, D. V. *Bioconjug. Chem.* **2015**, *26* (1), 145.
- (66) Steen Redeker, E.; Ta, D. T.; Cortens, D.; Billen, B.; Guedens, W.; Adriaensens, P. *Bioconjug. Chem.* **2013**, *24* (11), 1761.
- (67) Gauthier, M. A.; Klok, H. A. *Chem Commun* **2008**, 2591.
- (68) Krall, N.; da Cruz, F. P.; Boutureira, O.; Bernardes, G. J. L. *Nat. Chem.* **2015**, *8* (2), 103.
- (69) Tilley, S. D.; Francis, M. B. *J. Am. Chem. Soc.* **2006**, *128* (4), 1080.
- (70) Sato, S.; Nakamura, K.; Nakamura, H. *ACS Chem. Biol.* **2015**, *10* (11), 2633.
- (71) Boutureira, O.; Bernardes, G. J. L. *Chem. Rev.* **2015**, *115* (5), 2174.
- (72) de Turrís, V.; Cardoso Trabuco, M.; Peruzzi, G.; Boffi, A.; Testi, C.; Vallone, B.; Celeste Montemiglio, L.; Georges, A. Des; Calisti, L.; Benni, I.; Bonamore, A.; Baiocco, P. *Nanoscale* **2017**, *9* (2), 647.
- (73) Zhen, Z.; Tang, W.; Todd, T.; Xie, J. *Expert Opin. Drug Deliv.* **2014**, *11* (12), 1913.
- (74) He, D.; Marles-Wright, J. *N. Biotechnol.* **2015**, *32* (6), 651.

- (75) Johnson, E.; Cascio, D.; Sawaya, M. R.; Gingery, M.; Schröder, I. *Structure* **2005**, 13 (4), 637.
- (76) Williams, S.-M.; Chandran, A.-V.; Prakash, S.; Vijayan, M.; Chatterji, D. *Structure* **2017**, 25 (9), 1449.
- (77) Domínguez-Vera, J. M.; Welte, L.; Gálvez, N.; Fernández, B.; Gómez-Herrero, J.; Zamora, F. *Nanotechnology* **2008**, 19 (2), 25302.
- (78) Halfer, T.; Rei, A.; Ciacchi, L. C.; Treccani, L.; Rezwani, K. *Biointerphases* **2014**, 9 (3), 31018.
- (79) Jung, B.; Theato, P. *Adv. Polym. Sci.* **2012**, 5 (2012), 1.
- (80) Gálvez, N.; Fernández, B.; Sánchez, P.; Morales-Sanfrutos, J.; Santoyo-González, F.; Cuesta, R.; Bermejo, R.; Clemente-León, M.; Coronado, E.; Soriano-Portillo, A.; Domínguez-Vera, J. M. *Solid State Sci.* **2009**, 11 (4), 754.
- (81) Kishida, Y.; Olsen, B. R.; Berg, R. A.; Prockop, D. J. *J. Cell Biol.* **1975**, 64 (2), 331.
- (82) Hu, Y.; Samanta, D.; Parelkar, S. S.; Hong, S. W.; Wang, Q.; Russell, T. P.; Emrick, T. *Adv. Funct. Mater.* **2010**, 20 (20), 3603.
- (83) Spa, S. J.; Bunschoten, A.; Rood, M. T. M.; Peters, R. J. B.; Koster, A. J.; van Leeuwen, F. W. B. *Eur. J. Inorg. Chem.* **2015**, 2015 (27), 4603.
- (84) Wonga, K. K. W.; Cölfen, H.; Whilton, N. T.; Douglas, T.; Mann, S. *J. Inorg. Biochem.* **1999**, 76 (3–4), 187.

- (85) Bhattacharyya, S.; Sinturel, C.; Salvetat, J. P.; Saboungi, M.-L. *Appl. Phys. Lett.* **2005**, *86* (11), 113104.
- (86) Mougín, N. C.; van Rijn, P.; Park, H.; Müller, A. H. E.; Boker, A. *Adv. Funct. Mater.* **2011**, *21* (13), 2470.
- (87) Danon, D.; Goldstein, L.; Marikovsky, Y.; Skutelsky, E. *J. Ultrastruct. Res.* **1972**, *38* (5–6), 500.
- (88) Perriman, A. W.; Cölfen, H.; Hughes, R. W.; Barrie, C. L.; Mann, S. *Angew. Chemie Int. Ed.* **2009**, *48* (34), 6242.
- (89) Yang, R.; Chen, L.; Zhang, T.; Yang, S.; Leng, X.; Zhao, G. *Chem. Commun.* **2014**, *50* (4), 481.
- (90) Yang, R.; Chen, L.; Yang, S.; Lv, C.; Leng, X.; Zhao, G. *Chem. Commun.* **2014**, *50* (22), 2879.
- (91) Bryant, S. J.; Anseth, K. S. *J. Biomed. Mater. Res.* **2002**, *59* (1), 63.
- (92) Le Goff, G. C.; Srinivas, R. L.; Hill, W. A.; Doyle, P. S. *Eur. Polym. J.* **2015**, *72*, 386.
- (93) Kodadek, T.; Zhang, Z.; Zhu, W. *Nat. Biotechnol.* **2000**, *18* (1), 71.
- (94) Lee, S.; Tong, X.; Yang, F. *Acta Biomater.* **2014**, *10* (10), 4167.
- (95) Masuma, R.; Kashima, S.; Kurasaki, M.; Okuno, T. *J. Photochem. Photobiol. B Biol.* **2013**, *125*, 202.
- (96) Fairbanks, B. D.; Schwartz, M. P.; Bowman, C. N.; Anseth, K. S. *Biomaterials* **2009**,

30 (35), 6702.

- (97) Fathi, A.; Lee, S.; Breen, A.; Negahi-Shirazi, A.; Valtchev, P.; Dehghani, F. *Eur. Polym. J.* **2014**, *59*, 161.
- (98) Wang, X.; Ao, Q.; Tian, X.; Fan, J.; Tong, H.; Hou, W.; Bai, S. *Polymers (Basel)*. **2017**, *9* (9), 401.
- (99) Dubbin, K.; Tabet, A.; Heilshorn, S. C. *Biofabrication* **2017**, *9* (4), 44102.
- (100) DeKosky, B. J.; Dormer, N. H.; Ingavle, G. C.; Roatch, C. H.; Lomakin, J.; Detamore, M. S.; Gehrke, S. H. *Tissue Eng. Part C. Methods* **2010**, *16* (6), 1533.
- (101) Ingavle, G. C.; Gehrke, S. H.; Detamore, M. S. *Biomaterials* **2014**, *35* (11), 3558.
- (102) Lee, H.; Stoffey, D. Polyethylene glycol diacrylate. US3769336 A, 1973.
- (103) Tana, F.; Liu, J.; Liu, M.; Wang, J. *Mater. Sci. Eng. C* **2017**, *76*, 330.
- (104) Munoz-Pinto, D. J.; Grigoryan, B.; Long, J.; Grunlan, M.; Hahn, M. S. *J. Biomed. Mater. Res. Part A* **2012**, *100A* (10), 2855.
- (105) Mazzoccoli, J. P.; Feke, D. L.; Baskaran, H.; Pintauro, P. N. *J. Biomed. Mater. Res. A* **2010**, *93* (2), 558.
- (106) Browning, M. B.; Cosgriff-Hernandez, E. *Biomacromolecules* **2012**, *13* (3), 779.
- (107) Komorowska, P.; Róžańska, S.; Róžański, J. *Cellulose* **2017**, *24* (10), 4151.
- (108) Webber, R. E.; Shull, K. R. *Macromolecules* **2004**, *37* (16), 6153.
- (109) Moresi, M.; Mancini, M.; Bruno, M.; Rancini, R. *J. Texture Stud.* **2001**, *32* (5–6),

375.

- (110) Ma, L.; Barbosa-canovas, G. V. *J. Food Sci.* **1997**, 62 (6), 1124.
- (111) Song, K. W.; Kuk, H. Y.; Chang, G. S. *Korea Aust. Rheol. J.* **2006**, 18 (2), 67.
- (112) Habas, J.-P.; Pavie, E.; Lapp, A.; Peyrelasse, J. *Rheol. Acta* **2008**, 47 (7), 765.
- (113) Baloglu, E.; Karavana, S. Y.; Senyigit, Z. A.; Guneri, T. *Pharm. Dev. Technol.* **2011**, 16 (6), 627.
- (114) Bercea, M.; Darie, R. N.; Niță, L. E.; Morariu, S. *Ind. Eng. Chem. Res.* **2011**, 50 (7), 4199.
- (115) de Sousa Costa, L. A.; Inomata Campos, M.; Izabel Druzian, J.; de Oliveira, A. M.; de Oliveira Junior, E. N. *Int. J. Polym. Sci.* **2014**, 2014, 1.
- (116) Gross, B. C.; Erkal, J. L.; Lockwood, S. Y.; Chen, C.; Spence, D. M. *Anal. Chem.* **2014**, 86 (7), 3240.
- (117) Chia, H. N.; Wu, B. M. *J. Biol. Eng.* **2015**, 9 (1), 4.
- (118) Bajaj, P.; Schweller, R. M.; Khademhosseini, A.; West, J. L.; Bashir, R. *Annu. Rev. Biomed. Eng.* **2014**, 16 (1), 247.
- (119) Müller, M.; Becher, J.; Schnabelrauch, M.; Zenobi-Wong, M. *Biofabrication* **2015**, 7, 35006.
- (120) Li, J.; Chen, M.; Fan, X.; Zhou, H. *J. Transl. Med.* **2016**, 14 (1), 271.
- (121) Shafiee, A.; Atala, A. *Annu. Rev. Med.* **2017**, 68 (1), 29.

- (122) Mosadegh, B.; Xiong, G.; Dunham, S.; Min, J. K. *Biomed. Mater.* **2015**, *10* (3), 34002.
- (123) Colosi, C.; Shin, S. R.; Manoharan, V.; Massa, S.; Costantini, M.; Barbetta, A.; Dokmeci, M. R.; Dentini, M.; Khademhosseini, A. *Adv. Mater.* **2015**, *28*, 677.
- (124) Jessop, Z.; Al-Sabah, A.; Gardiner, M.; Combellack, E.; Hawkins, K.; Whitaker, L. *J. Plast. Reconstr. Aesthetic Surg.* **2017**, *70* (9), 1155.
- (125) Huang, Y.; Zhang, X.-F.; Gao, G.; Yonezawa, T.; Cui, X. *Biotechnol. J.* **2017**, *12* (8), 1600734.
- (126) Adepu, S.; Dhiman, N.; Laha, A.; Sharma, C.; Ramakrishna, S.; Khandelwal, M. *Curr. Opin. Biomed. Eng.* **2017**, *2*, 22.
- (127) Jose, R. R.; Rodriguez, M. J.; Dixon, T. A.; Omenetto, F.; Kaplan, D. L. *ACS Biomater. Sci. Eng.* **2016**, *2* (10), 1662.
- (128) K.Włodarczyk-Bieguna, M.; del Campo, A. *Biomaterials* **2017**, *134*, 180.
- (129) Patra, S.; Young, V. *Cell Biochem. Biophys.* **2016**, *74* (2), 93.
- (130) de Obaldia, E. E.; Jeong, C.; Grunenfelder, L. K.; Kisailus, D.; Zavattieri, P. *J. Mech. Behav. Biomed. Mater.* **2015**, *48*, 70.
- (131) Skardal, A.; Atala, A. *Ann. Biomed. Eng.* **2015**, *43* (3), 730.
- (132) Mandrycky, C.; Wang, Z.; Kim, K.; Kim, D.-H. *Biotechnol. Adv.* **2016**, *34* (4), 422.
- (133) Zhang, X.; Zhang, Y. *Cell Biochem. Biophys.* **2015**, 777.

- (134) Jonathan, G.; Karim, A. *Int. J. Pharm.* **2016**, 499 (1), 376.
- (135) Murphy, S. V.; Atala, A. *Nat. Biotechnol.* **2014**, 32 (8), 773.
- (136) Dababneh, A. B.; Ozbolat, I. T. *J. Manuf. Sci. Eng.* **2014**, 136 (6), 61016.
- (137) Ozbolat, I. T.; Hospodiuk, M. *Biomaterials* **2016**, 76, 321.
- (138) Wang, Z.; Abdulla, R.; Parker, B.; Samanipour, R.; Ghosh, S.; Kim, K. *Biofabrication* **2015**, 7 (4), 45009.
- (139) Sun, A. X.; Lin, H.; Beck, A. M.; Kilroy, E. J.; Tuan, R. S. *Front. Bioeng. Biotechnol.* **2015**, 3, 115.
- (140) Hölzl, K.; Lin, S.; Tytgat, L.; Van Vlierberghe, S.; Gu, L.; Ovsianikov, A. *Biofabrication* **2016**, 8 (3), 32002.
- (141) Hospodiuk, M.; Dey, M.; Sosnoski, D.; Ozbolat, I. T. *Biotechnol. Adv.* **2017**, 35 (2), 217.
- (142) Zhang, Z.; Wang, B.; Hui, D.; Qiu, J.; Wang, S. *Compos. Part B Eng.* **2017**, 123, 279.
- (143) Raphael, B.; Khalil, T.; Workman, V. L.; Smith, A.; Brown, C. P.; Streuli, C.; Saiani, A.; Domingos, M. *Mater. Lett.* **2017**, 190, 103.
- (144) El-Sherbiny, I.; Yacoub, M. *Glob. Cardiol. Sci. Pr.* **2013**, 2013 (3), 316.
- (145) DeSimone, E.; Schacht, K.; Jungst, T.; Groll, J.; Scheibel, T. *Pure Appl. Chem.* **2015**, 87 (8), 737.

- (146) Moller, L.; Krause, A.; Dahlmann, J.; Gruh, I.; Kirschning, A.; Drager, G. *Int. J. Artif. Organs* **2011**, *34* (2), 93.
- (147) Ahn, G.; Min, K.-H.; Kim, C.; Lee, J.-S.; Kang, D.; Won, J.-Y.; Cho, D.-W.; Kim, J.-Y.; Jin, S.; Yun, W.-S.; Shim, J.-H. *Sci. Rep.* **2017**, *7* (1), 8624.
- (148) Jakus, A. E.; Laronda, M. M.; Rashedi, A. S.; Robinson, C. M.; Lee, C.; Jordan, S. W.; Orwig, K. E.; Woodruff, T. K.; Shah, R. N. *Adv. Funct. Mater.* **2017**, *27* (34), 1700992.
- (149) Kim, B. S.; Kim, H.; Gao, G.; Jang, J.; Cho, D.-W. *Biofabrication* **2017**, *9* (3), 34104.
- (150) Anasiz, Y.; Ozgul, R. K.; Uckan-Cetinkaya, D. *Stem Cell Rev. Reports* **2017**, *13* (5), 587.
- (151) Yu, Y.; Moncal, K. K.; Li, J.; Peng, W.; Rivero, I.; Martin, J. A.; Ozbolat, I. T. *Sci. Rep.* **2016**, *6* (1), 28714.
- (152) Norotte, C.; Marga, F. S.; Niklason, L. E.; Forgacs, G. *Biomaterials* **2009**, *30* (30), 5910.
- (153) Gu, Q.; Zhu, H.; Li, J.; Li, X.; Hao, J.; Wallace, G. G.; Zhou, Q. *Natl. Sci. Rev.* **2016**, *3* (3), 331.
- (154) Leppiniemi, J.; Lahtinen, P.; Paajanen, A.; Mahlberg, R.; Metsä-Kortelainen, S.; Pinomaa, T.; Pajari, H.; Vikholm-Lundin, I.; Pursula, P.; Hytönen, V. P. *ACS Appl. Mater. Interfaces* **2017**, *9* (26), 21959.
- (155) Duarte Campos, D. F.; Blaeser, A.; Korsten, A.; Neuss, S.; Jäkel, J.; Vogt, M.;

- Fischer, H. *Tissue Eng. Part A* **2015**, 21 (3–4), 740.
- (156) Diamantides, N.; Wang, L.; Pruiksmá, T.; Siemiatkoski, J.; Dugopolski, C.; Shortkroff, S.; Kennedy, S.; Bonassar, L. J. *Biofabrication* **2017**, 9 (3), 34102.
- (157) Demirtaş, T. T.; Irmak, G.; Gümüşderelioğlu, M. *Biofabrication* **2017**, 9 (3), 35003.
- (158) Cubo, N.; Garcia, M.; del Cañizo, J. F.; Velasco, D.; Jorcano, J. L. *Biofabrication* **2016**, 9 (1), 15006.
- (159) Wang, X.; Yan, Y.; Pan, Y.; Xiong, Z.; Liu, H.; Cheng, J.; Liu, F.; Lin, F.; Wu, R.; Zhang, R.; Lu, Q. *Tissue Eng.* **2006**, 12 (1), 83.
- (160) Poldervaart, M. T.; Goversen, B.; de Ruijter, M.; Abbadessa, A.; Melchels, F. P. W.; Öner, F. C.; Dhert, W. J. A.; Vermonden, T.; Alblas, J. *PLoS One* **2017**, 12 (6), e0177628.
- (161) Snyder, J. E.; Hamid, Q.; Wang, C.; Chang, R.; Emami, K.; Wu, H.; Sun, W. *Biofabrication* **2011**, 3 (3), 34112.
- (162) Gioffredi, E.; Boffito, M.; Calzone, S.; Giannitelli, S. M.; Rainer, A.; Trombetta, M.; Mozetic, P.; Chiono, V. *Procedia CIRP* **2016**, 49, 125.
- (163) Bertassoni, L. E.; Cardoso, J. C.; Manoharan, V.; Cristino, A. L.; Bhise, N. S.; Araujo, W. A.; Zorlutuna, P.; Vrana, N. E.; Ghaemmaghami, A. M.; Dokmeci, M. R.; Khademhosseini, A. *Biofabrication* **2014**, 6 (2), 24105.
- (164) Pereira, R. F.; Bártolo, P. J. *J. Appl. Polym. Sci.* **2015**, 132 (48), n/a.

- (165) Kanczler, J. M.; Mirmalek-Sani, S.-H.; Hanley, N. A.; Ivanov, A. L.; Barry, J. J. A.; Upton, C.; Shakesheff, K. M.; Howdle, S. M.; Antonov, E. N.; Bagratashvili, V. N.; Popov, V. K.; Oreffo, R. O. C. *Acta Biomater.* **2009**, 5 (6), 2063.
- (166) Poh, P. S. P.; Chhaya, M. P.; Wunner, F. M.; De-Juan-Pardo, E. M.; Schilling, A. F.; Schantz, J. T.; van Griensven, M.; Hutmacher, D. W. *Advanced Drug Delivery Reviews*. Elsevier December 15, 2016, pp 228–246.
- (167) Kim, B. S.; Jang, J.; Chae, S.; Gao, G.; Kong, J.-S.; Ahn, M.; Cho, D.-W. *Biofabrication* **2016**, 8 (3), 35013.
- (168) Van der Ven, A. M. In *Protein Engineering of Bacterioferritin: Applications to Bionanotechnology (Unpublished master thesis)*; 2014; Vol. 1, p 42.
- (169) Kumari, S.; Kulkarni, A.; Kumaraswamy, G.; Sen Gupta, S. *Chem. Mater.* **2013**, 25 (23), 4813.
- (170) Zhao, W.; Liu, F.; Chen, Y.; Bai, J.; Gao, W. *Polymer (Guildf)*. **2015**, 66, A1.
- (171) Kramer, R. M.; Shende, V. R.; Motl, N.; Pace, C. N.; Scholtz, J. M. *Biophys. J.* **2012**, 102 (8), 1907.
- (172) Vanparijs, N.; Maji, S.; Louage, B.; Voorhaar, L.; Laplace, D.; Zhang, Q.; Shi, Y.; Hennink, W. E.; Hoogenboom, R.; De Geest, B. G. *Polym. Chem.* **2015**, 6 (31), 5602.
- (173) Tebaldi, M. L.; Charan, H.; Mavliutova, L.; Böker, A.; Glebe, U. *Macromol. Chem. Phys.* **2017**, 218 (11), 1600529.

- (174) Grogna, M.; Cloots, R.; Luxen, A.; Jérôme, C.; Passirani, C.; Lautram, N.; Desreux, J.-F.; Detrembleur, C. *J. Polym. Sci. Part A Polym. Chem.* **2011**, *49* (17), 3700.
- (175) Falatach, R.; McGlone, C.; Al-Abdul-Wahid, M. S.; Averick, S.; Page, R. C.; Berberich, J. A.; Konkolewicz, D. *Chem. Commun.* **2015**, *51* (25), 5343.
- (176) Zhou, T.; Qi, H.; Han, L.; Barbash, D.; Li, C. Y. *Nat. Commun.* **2016**, *7*, 11119.
- (177) Grover, G. N.; Maynard, H. D. *Curr. Opin. Chem. Biol.* **2010**, *14* (6), 818.
- (178) Zhong, M.; Wang, Y.; Krys, P.; Konkolewicz, D.; Matyjaszewski, K. *Macromolecules* **2013**, *46* (10), 3816.
- (179) Borchmann, D. E.; Carberry, T. P.; Weck, M. *Macromol. Rapid Commun.* **2014**, *35* (1), 27.
- (180) Xu, D.; Tonggu, L.; Bao, X.; Lu, D.; Liu, Z. *Soft Matter* **2012**, *8* (6), 2036.
- (181) Crowley, T. E.; Kyte, J.; Crowley, T. E.; Kyte, J. In *Experiments in the Purification and Characterization of Enzymes*; Elsevier, 2014; pp 25–102.
- (182) Cayot, P.; Tainturier, G. *Anal. Biochem.* **1997**, *249* (2), 184.
- (183) Zhang, Y.; Ardejani, M. S. In *Protein Cages: Methods and Protocols*; Humana Press, New York, NY, 2014; pp 101–113.
- (184) Hui, G.; Huang, W.; Song, Y.; Chen, D.; Zhong, A. *Korean J. Chem. Eng.* **2013**, *30* (8), 1609.
- (185) Wetz, K.; Crichton, R. *Eur. J. Biochem.* **1976**, *61* (2), 545.

- (186) Zeng, Q.; Li, T.; Cash, B.; Li, S.; Xie, F.; Wang, Q. *Chem. Commun. (Camb)*. **2007**, 1 (14), 1453.
- (187) Zeng, Q.; Reuther, R.; Oxsher, J.; Wang, Q. *Bioorg. Chem.* **2008**, 36 (5), 255.
- (188) Roy, R.; Tropper, F. D.; Morrison, T.; Boratynski, J. *J. Chem. Soc. Chem. Commun.* **1991**, No. 7, 536.
- (189) Bradburne, J. A.; Godfrey, P.; Choi, J. H.; Mathis, J. N. *Appl. Environ. Microbiol.* **1993**, 59 (3), 663.
- (190) Bondos, S. E.; Bicknell, A. *Anal. Biochem.* **2003**, 316 (2), 223.
- (191) Walker, J. M. *Mass Spectrometry of Proteins and Peptides Series*, 2nd ed.; Pasatolic, L., Lipton, M. S., Eds.; Humana Press: Hatfield, Hertfordsire, 2009.
- (192) Shinjyo, S.; Abe, H.; Masuda, M. *Biochim. Biophys. Acta* **1975**, 411, 165.
- (193) Li, Q.; Wang, D. A.; Elisseeff, J. H. *Macromolecules* **2003**, 36 (7), 2556.
- (194) Huang, B. X.; Kim, H.-Y.; Dassb, C. *J. Am. Soc. Mass Spectrom.* **2004**, 15 (8), 1237.
- (195) Carter, D. C.; Ho, J. X. *Adv. Protein Chem.* **1994**, 45 (C), 153.
- (196) Yan, Q.; Zheng, H.-N.; Jiang, C.; Li, K.; Xiao, S.-J. *RSC Adv.* **2015**, 5 (86), 69939.
- (197) Lim, C. Y.; Owens, N. A.; Wampler, R. D.; Ying, Y.; Granger, J. H.; Porter, M. D.; Takahashi, M.; Shimazu, K. *Langmuir* **2014**, 30 (43), 12868.
- (198) Klykov, O.; Weller, M. G. *Anal. Methods* **2015**, 7 (15), 6443.

- (199) Ghirlando, R.; Mutsikova, R.; Schwartz, C. *Nanotechnology* **2016**, 27 (4), 45102.
- (200) Sengonul, M.; Ruzicka, J.; Attygalle, A. B.; Libera, M. *Polymer (Guildf)*. **2007**, 48 (13), 3632.
- (201) Ipatieff, V. N.; Thompson, W. W.; Pines, H. *J. Am. Chem. Soc.* **1948**, 70 (4), 1658.
- (202) Kitano, H.; Nakada, H.; Mizukami, K. *Colloids Surfaces B Biointerfaces* **2008**, 61 (1), 17.
- (203) Mruk, R.; Prehl, S.; Zentel, R. *Macromol. Chem. Phys.* **2004**, 205 (16), 2169.
- (204) Katsuta, K.; Kinsella, J. E. *J. Food Sci.* **1990**, 55 (5), 1296.
- (205) Pham, T. T. H.; Snijkers, F.; Storm, I. M.; de Wolf, F. A.; Cohen Stuart, M. A.; van der Gucht, J. *Int. J. Polym. Mater. Polym. Biomater.* **2016**, 65 (3), 125.
- (206) Dooling, L. J.; Tirrell, D. A. *ACS Cent. Sci.* **2016**, 2 (11), 812.
- (207) Kraut, G.; Yenchesky, L.; Prieto, F.; Tovar, G. E. M.; Southan, A. *J. Appl. Polym. Sci.* **2017**, 134 (29), 45083.
- (208) Patel, P. N.; Smith, C. K.; Patrick, C. W. *J. Biomed. Mater. Res. Part A* **2005**, 73A (3), 313.
- (209) Marques, P. T.; Pérégo, C.; Le Meins, J. F.; Borsali, R.; Soldi, V. *Carbohydr. Polym.* **2006**, 66 (3), 396.
- (210) Majima, T.; Schnabel, W.; Weber, W. *Die Makromol. Chemie* **1991**, 192 (10), 2307.
- (211) Faralli, A.; Melander, F.; Larsen, E. K. U.; Chernyy, S.; Andresen, T. L.; Larsen, N.

- B. *Adv. Healthc. Mater.* **2015**, 244.
- (212) Moghimipour, E.; Salimi, A.; Rezaee, S.; Balack, M.; Handali, S. *Jundishapur J. Nat. Pharm. Prod.* **2014**, 9 (2), e12716.
- (213) Rattle, S.; Hofmann, O.; Price, C. P.; Kricka, L. J.; Wild, D. In *The Immunoassay Handbook*; Elsevier, 2013; pp 175–202.
- (214) Shanjani, Y.; Pan, C. C.; Elomaa, L.; Yang, Y. *Biofabrication* **2015**, 7 (4), 45008.
- (215) Liao, H.; Munoz-Pinto, D.; Qu, X.; Hou, Y.; Grunlan, M. A.; Hahn, M. S. *Acta Biomater.* **2008**, 4 (5), 1161.
- (216) Rennerfeldt, D. A.; Renth, A. N.; Talata, Z.; Gehrke, S. H.; Detamore, M. S. *Biomaterials* **2013**, 34 (33), 8241.
- (217) Raeber, G. P.; Lutolf, M. P.; Hubbell, J. A. *Biophys. J.* **2005**, 89 (2), 1374.
- (218) Fu, Y.; Xu, K.; Zheng, X.; Giacomini, A. J.; Mix, A. W.; Kao, W. J. *Biomaterials* **2012**, 33 (1), 48.
- (219) Dealy, J. M.; Wang, J. In *Melt Rheology and its Applications in the Plastics Industry*; Springer, Dordrecht: Dordrecht , 2013; pp 19–47.
- (220) Milas, M.; Rinaudo, M.; Knipper, M.; Schuppiser, J. L. *Macromolecules* **1990**, 23 (9), 2506.
- (221) Hou, K.; Li, Y.; Liu, Y.; Zhang, R.; Hsiao, B.-S. S.; Zhu, M. *Polymer (Guildf)*. **2017**, 123, 55.

- (222) Munoz-Pinto, D. J.; Jimenez-Vergara, A. C.; Gharat, T. P.; Hahn, M. S. *Biomaterials* **2015**, *40*, 32.
- (223) Zhang, B.; Gao, L.; Gu, L.; Yang, H.; Luo, Y.; Ma, L. *Procedia CIRP* **2017**, *65*, 219.
- (224) Li, L.; Liao, B. Y.; Thakur, K.; Zhang, J. G.; Wei, Z. J. *Int. J. Biol. Macromol.* **2017**, *In Press*, 11.
- (225) Mazzoccoli, J. P.; Feke, D. L.; Baskaran, H.; Pintauro, P. N. *J. Biomed. Mater. Res. A* **2010**, *93* (2), 558.
- (226) Mellott, M. B.; Searcy, K.; Pishko, M. V. *Biomaterials* **2001**, *22* (9), 929.
- (227) Wang, X.; Ao, Q.; Tian, X.; Fan, J.; Tong, H.; Hou, W.; Bai, S. *Polymers (Basel)*. **2017**, *9* (9), 401.
- (228) Fisher, S. A.; Baker, A. E. G.; Shoichet, M. S. *J. Am. Chem. Soc.* **2017**, *139* (22), 7416.
- (229) Nair, D. P.; Podgórski, M.; Chatani, S.; Gong, T.; Xi, W.; Fenoli, C. R.; Bowman, C. N. *Chem. Mater.* **2014**, *26* (1), 724.
- (230) Hoyle, C. E.; Bowman, C. N. *Angew. Chemie - Int. Ed.* **2010**, *49* (9), 1540.
- (231) Li, J.; Chen, M.; Fan, X.; Zhou, H. *J. Transl. Med.* **2016**, *14* (1), 271.
- (232) Cao, Y.; Feng, Y.; Ryser, M. D.; Zhu, K.; Herschlag, G.; Cao, C.; Marusak, K.; Zauscher, S.; You, L. *Nat. Biotechnol.* **2017**, *35* (11), 1087.
- (233) Pascalie, J.; Potier, M.; Kowaliw, T.; Giavitto, J.-L.; Michel, O.; Spicher, A.; Doursat,

- R. *ACS Synth. Biol.* **2016**, 5 (8), 842.
- (234) Lehner, B. A. E.; Schmieden, D. T.; Meyer, A. S. *ACS Synth. Biol.* **2017**, 6 (7), 1124.
- (235) Xuzhen, Q.; Qianqian, H.; Guanghui, G.; Shuang, G. *Chem. Res. Chin. Univ* **2015**, 31 (6), 1046.
- (236) Chavda, H. V.; Patel, R. D.; Modhia, I. P.; Patel, C. N. **2012**, 2 (3), 3.
- (237) Jones, M. M.; Johnston, D. O. *Nature*. Nature Publishing Group November 4, 1967, pp 509–510.
- (238) Chen, H.; Zhang, S.; Xu, C.; Zhao, G. *Chem. Commun.* **2016**, 52 (46), 7402.
- (239) Cruise, G. M.; Scharp, D. S.; Hubbell, J. A. *Biomaterials* **1998**, 19 (14), 1287.
- (240) Zustiak, S. P.; Leach, J. B. *Biotechnol. Bioeng.* **2011**, 108 (1), 197.
- (241) Sakurai, K.; Nabeyama, A.; Fujimoto, Y. *BioMetals* **2006**, 19 (3), 323.
- (242) Saez-Martinez, V.; Atorrasagasti, G.; Olalde, B.; Madarieta, I.; Morin, F.; Garagorri, N. *Int. J. Polym. Mater.* **2013**, 62 (9), 502.
- (243) Liljeström, V.; Seitsonen, J.; Kostianen, M. A. *ACS Nano* **2015**, 9 (11), 11278.
- (244) Lee, E. J.; Ahn, K. Y.; Lee, J. H.; Park, J. S.; Song, J. A.; Sim, S. J.; Lee, E. B.; Cha, Y. J.; Lee, J. *Adv. Mater.* **2012**, 24 (35), 4739.
- (245) Tronci, G.; Grant, C. A.; Thomson, N. H.; Russell, S. J.; Wood, D. J. *J. R. Soc. Interface* **2015**, 12 (102), 20141079.
- (246) Cameron, R. E.; Donald, A. M. *J. Microsc.* **1994**, 173 (3), 227.

- (247) Annabi, N.; Nichol, J. W.; Zhong, X.; Ji, C.; Koshy, S.; Khademhosseini, A.; Dehghani, F. *Tissue Eng. Part B. Rev.* **2010**, *16* (4), 371.
- (248) Saldin, L. T.; Cramer, M. C.; Velankar, S. S.; White, L. J.; Badylak, S. F. *Acta Biomater.* **2017**, *49*, 1.
- (249) Meakin, J. R.; Hukins, D. W. L.; Imrie, C. T.; Aspden, R. M. *J. Mater. Sci. Mater. Med.* **2003**, *14* (1), 9.
- (250) Vogel, A.; Svehla, G. *Vogel's qualitative inorganic analysis*, 5th ed.; Pearson, 1979.
- (251) Smith, B. J. In *Basic Protein and Peptide Protocols*; Humana Press: New Jersey, 1994; pp 39–48.
- (252) Zhang, Q.; Li, M.; Zhu, C.; Nurumbetov, G.; Li, Z.; Wilson, P.; Kempe, K.; Haddleton, D. M. *J. Am. Chem. Soc.* **2015**, *137* (29), 9344.
- (253) Hamid, Z. A. A.; Lim, K. W. *Procedia Chem.* **2016**, *19*, 410.
- (254) Xu, M. Development of protein-based hydrogels as encapsulation matrices for *Lactobacillus casei*, McGill University, 2015.
- (255) Shen, X.; Shamshina, J. L.; Berton, P.; Gurau, G.; Rogers, R. D. *Green Chem.* **2016**, *18* (1), 53.
- (256) Lee, A. G.; Arena, C. P.; Beebe, D. J.; Palecek, S. P. *Biomacromolecules* **2010**, *11* (12), 3316.
- (257) Jones, T.; Spencer, R.; Walsh, C. *Biochemistry* **1978**, *17* (19), 4011.

- (258) Vladimirova, L. S.; Kochev, V. K. *Anal. Biochem.* **2010**, *404* (1), 52.
- (259) Shahid Akhlaq, M.; Schuchmann, H.-P.; Sonntag, C. Von. *Environ. Sci. Technol* **1990**, *24*, 379.
- (260) Canal, T.; Peppas, N. A. *J. Biomed. Mater. Res.* **1989**, *23* (10), 1183.
- (261) Armstrong, J. K.; Wenby, R. B.; Meiselman, H. J.; Fisher, T. C. *Biophys. J.* **2004**, *87* (6), 4259.
- (262) Yacob, N.; Hashim, K. *AIP Conf. Proc.* **2014**, *1584* (153), 153.
- (263) Yi, W. S.; Qin, L. H.; Cao, J. B. *Scanning* **2011**, *33* (6), 450.
- (264) Mohan, N.; Nair, P. D. *Trends Biomater. Artif. Organs* **2005**, *18* (January), 219.
- (265) Ensikat, H. J.; Barthlott, W. *J. Microsc.* **1993**, *172* (3), 195.
- (266) Sweeney, M.; Campbell, L. L.; Hanson, J.; Pantoya, M. L.; Christopher, G. F. *J. Mater. Sci.* **2017**, *52* (22), 13040.
- (267) Drachuk, I.; Harbaugh, S.; Geryak, R.; Kaplan, D. L.; Tsukruk, V. V.; Kelley-Loughnane, N. *ACS Biomater. Sci. Eng.* **2017**, *3* (10), 2278.
- (268) Lee, B. H.; Kim, M. H.; Lee, J. H.; Seliktar, D.; Lay, N. J. C.; Tan, P. *PLoS One* **2015**, *10* (2), e0118123.
- (269) Steff, A.-M.; Fortin, M.; Arguin, C.; Hugo, P. *Cytometry* **2001**, *45* (4), 237.
- (270) Zhang, H.-B.; Xing, T.-L.; Yin, R.-X.; Shi, Y.; Yang, S.-M.; Zhang, W.-J. *Chinese J. Traumatol.* **2016**, *19* (4), 187.

- (271) Lee, J. H.; Prud'homme, R. K.; Aksay, I. A. *J. Mater. Res.* **2001**, *16* (12), 3536.
- (272) Vermeulen, N.; Keeler, W. J.; Nandakumar, K.; Leung, K. T. *Biotechnol. Bioeng.* **2008**, *99* (3), 550.
- (273) Lin, C.-C.; Raza, A.; Shih, H. *Biomaterials* **2011**, *32* (36), 9685.
- (274) Bueno, V. B.; Bentini, R.; Catalani, L. H.; Siqueira-Petri, D. F. *Carbohydr. Polym.* **2013**, *92* (2), 1091.
- (275) Cumpstey, I. *ISRN Org. Chem.* **2013**, *2013*, 1.
- (276) Reis, A. V.; Guilherme, M. R.; Cavalcanti, O. A.; Rubira, A. F.; Muniz, E. C. *Polymer (Guildf)*. **2006**, *47* (6), 2023.
- (277) Reeves, R.; Ribeiro, A.; Lombardo, L.; Boyer, R.; Leach, J. B. *Polymers (Basel)*. **2010**, *2* (3), 252.
- (278) Leary, R. J.; Kinde, I.; Diehl, F.; Schmidt, K.; Clouser, C.; Duncan, C.; Antipova, A.; Lee, C.; McKernan, K.; De La Vega, F. M.; Kinzler, K. W.; Vogelstein, B.; Diaz, L. A.; Velculescu, V. E. *Sci. Transl. Med.* **2010**, *2* (20), 3122.
- (279) Tan, Y. J.; Yeong, W. Y.; Tan, X.; An, J.; Chian, K. S.; Leong, K. F. *J. Mech. Behav. Biomed. Mater.* **2016**, *57*, 246.
- (280) Bencherif, S.; Siegwart, D.; Srinivasan, A.; Horkay, F.; Hollinger, J.; R. Washburna, N.; Matyjaszewski, K. *Biomaterials* **2009**, *30* (29), 5270.
- (281) Hosein, H.-A.; Strongin, D. R.; Allen, M.; Douglas, T. *Langmuir* **2004**, *20* (23),

10283.

- (282) Iwahori, K.; Yoshizawa, K.; Muraoka, M.; Yamashita, I. *Inorg. Chem.* **2005**, *44* (18), 6393.
- (283) Barnes, H. A. *A handbook of elementary rheology*; University of Wales, Institute of Non-Newtonian Fluid Mechanics, 2000.
- (284) Dolz, M.; Delegido, J.; Casanovas, A.; Hernández, M.-J. *J. Chem. Educ.* **2005**, *82* (3), 445.
- (285) Rohrig, B. *ChemMatters* **2017**, *1* (2017), 8.
- (286) Chhabra, R. P. In *Rheology of Complex Fluids*; Springer New York: New York, NY, 2010; pp 3–34.
- (287) Sochi, T. *Polymer (Guildf)*. **2010**, *51* (22), 5007.
- (288) Kawase, Y.; Halard, B.; Moo-Young, M. *Chem. Eng. Sci.* **1987**, *42* (7), 1609.
- (289) Gutierrez-Lemini, D. In *Engineering Viscoelasticity*; Springer US: Boston, MA, 2014; pp 1–21.
- (290) Dealy, J. M.; Wissbrun, K. F. In *Melt Rheology and Its Role in Plastics Processing*; Springer US: Boston, MA, 1990; pp 42–102.
- (291) Gutierrez-Lemini, D. *Engineering viscoelasticity*, 1st ed.; Roylance, D., Ed.; Department of Materials Science and Engineering: Cambridge, 2014.
- (292) Starkova, O.; Aniskevich, A. *Mech. Time-Dependent Mater.* **2007**, *11* (2), 111.

(293) Schmidt-rob, K. *Contract* **2004**, 1 (21), 1734.

Appendix

Appendix A. Rheology Theory

Rheology is defined as the science that studies the flow and deformation of materials. To fully characterize a material, it is essential to understand the molecular mechanisms that govern it. Two key components are studied by rheology: flow and deformation. There are two types of flow: *shear* and *elongational* flows. In shear flow the elements flow over or past each other, while elongational flows move away or towards each other. ²⁸³

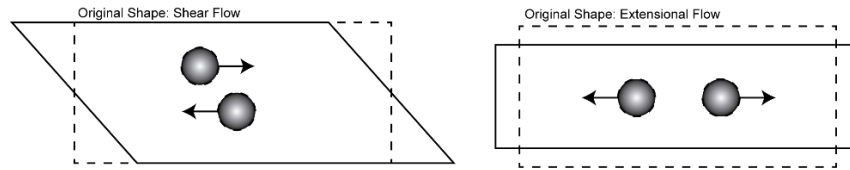


Figure 55. Particle motion profile for shear and extensional flow.²⁸³

Basic concepts that are used in rheology are the concept of viscosity (η), a proportionality constant used in the study of the relationships of flow and shearing, the study of change of force per unit of area (shear stress, σ), and the velocity gradient that is applied to a specific fluid (shear rate, γ).²⁸⁴

$$\gamma = \frac{dV}{dh} = \eta \cdot$$

Equation 7

$$\sigma = \eta \frac{F}{A} = \eta \cdot \gamma$$

Equation 8

To understand shear flow rheology, Newtonian and non-Newtonian fluids are being continuously characterized. Newtonian fluids follow a decreasing trend in their viscosity when the surrounding temperature is increased, but their viscosity remains constant despite the change in shear rate. While for non-Newtonian fluids, factors other than temperatures, such as agitation or pressure will affect the apparent viscosity of the

fluid.²⁸⁵ Another fundamental term is needed for non-Newtonian fluids, the apparent viscosity, η_{app} , which is a ratio of the shear stress and shear rate.²⁸⁴ Therefore, to have a relevant value, useful for comparison, it is necessary to report apparent viscosities stating the shear rate at which they have been measured.²²¹

$$\eta_{app}(\dot{\gamma}) = \frac{\sigma}{\dot{\gamma}} \quad \text{Equation 9}$$

Sochi *et al.* has presented a comprehensive review on non-Newtonian fluids, where they are classified as time-independent, viscoelastic and time-dependent.²²¹ Time-independent fluid behavior is that for which the strain rate of the fluid is only dependent on the shear stress applied at that specific point.²²¹ The fluid would be described as shear thinning if the apparent viscosity decreases as the shear rate increases. Conversely, the fluid would be described as shear thickening if the apparent viscosity increases with the increase of the shear rate.²²¹

Viscoelastic fluid behavior is the one that is characterized by the need of a threshold stress, called the yield stress (σ_0), which is needed to let a material flow. Therefore, a viscoelastic fluid will behave as an elastic solid if a $\sigma < \sigma_0$ is applied, but it will behave as a liquid if $\sigma > \sigma_0$.²⁸⁶

Time-dependent fluid behaviors have a complex component because their η_{app} are a function of σ , $\dot{\gamma}$, and the time for which the fluid has been subjected to shearing.²⁸⁶ Furthermore, because it has been acknowledged that reversible structural change causes this phenomenon during the flow process, they have been classified into two types:

thixotropic and rheopectic depending upon whether the stress decreases or increases with time at a given strain rate and constant temperature.²²¹

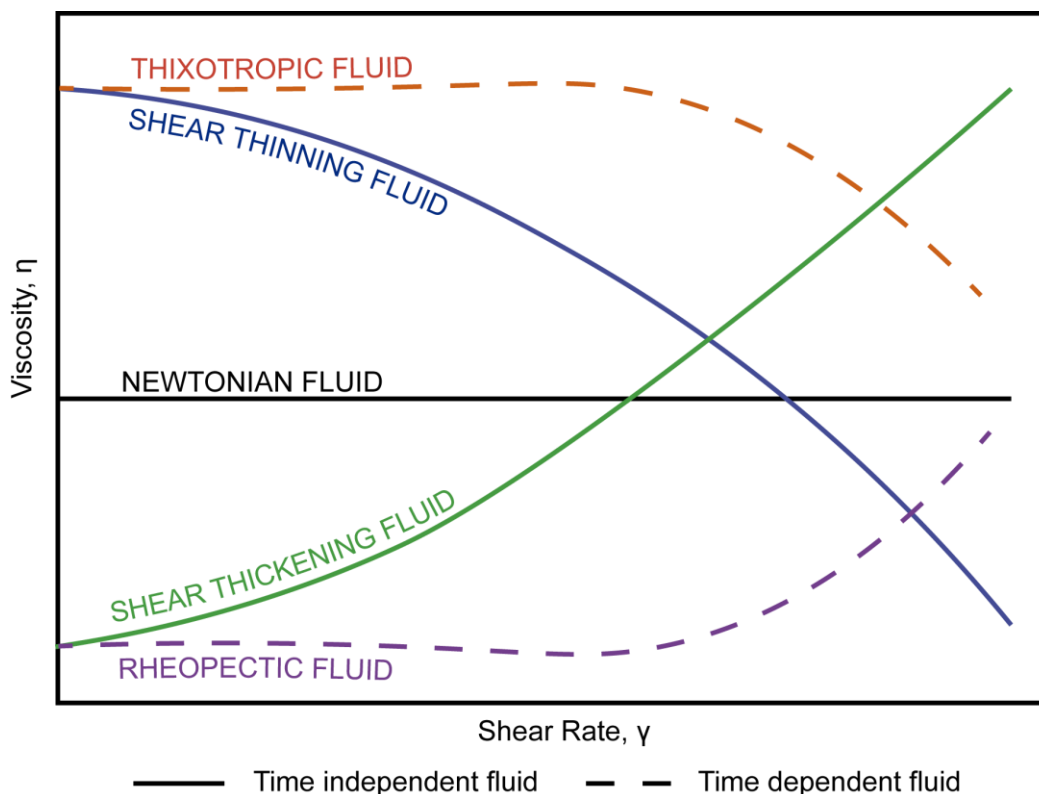


Figure 56. Viscosity as a function of shear rate for time dependent and time independent non-Newtonian fluids.

It is common knowledge that low shear rates of non-Newtonian fluids cause that the viscosity appears to be Newtonian.²²¹

Furthermore, It has also been reported that some Newtonian fluids, such as low polystyrene solutions, can present both Newtonian behaviors at low shear rates and non-Newtonian behavior when higher shear rates are applied to them.²⁸⁴ More so, to compare the behavior of non-Newtonian fluids, many methods have been developed such as the

power law method, Ellis method, and Carreau method.²⁸⁷ However, the power law method, also known as the Ostwald-de Waele method (Equation 10) has been selected to analyze the behavior of the non-Newtonian blends because it has been accepted as a power law method for shear-dependent viscosities.²⁸⁸

$$\sigma = K \cdot \dot{\gamma}^n \quad \text{Equation 10} \quad \eta_{app}(\dot{\gamma}) = K \cdot \dot{\gamma}^{n-1} \quad \text{Equation 11}$$

In this method, K is called the consistency and n the power law index. Furthermore, Equation 10 and Equation 11 can also be used to successfully reproduce Newtonian flow when the values of $n = 1$ and $K = \eta$. As a general rule, when values of $n > 1$ of the power index correspond to shear thickening fluids, while values of $n < 1$ correspond to shear-thinning fluids.²⁸⁴

To understand elongational flows, it is necessary to define it as the one in which fluid elements are subjected to extensions and compressions without being rotated or sheared.²⁸³ It has not been characterized extensively. However, the extensional viscosity function is often qualitatively different from that of the shear viscosity. This behavior result of interest with highly elastic polymer solutions, which often show a decrease in viscosity with shear while exhibiting an increase in the extensional viscosity (Trouton viscosity, μ_x) in function of the extension rate.²⁸⁷

A material exhibits a viscoelastic behavior if the response to external stimuli encompasses characteristics of viscous and elastic behaviors.²⁸⁹ According to Chhabra *et al.* for an ideal elastic solid, stress in a sheared state is proportional to the strain.²⁸⁶ Therefore, the most straightforward viscoelastic behavior would be the one that can be

described as a linear system, such as linear viscoelasticity, in which an applied deformation is sufficient to disturb the particles from their equilibrium, but returning to their equilibrium state due to Brownian motion.²⁹⁰

It is vital to characterize materials to determine their rheological capabilities. Therefore, uniaxial tests are carried out continuously. For example, one test studies the applied stress until it exceeds the yield stress of the examined material, achieving a faster anisotropic effect than a recovery. This study is called the *creep* test.²⁸⁹ This phenomenon is usually described as a time-dependent strain, mathematically described as $\epsilon(t) = d(t)/L_0$ (ϵ being the strain, d being the deformation, and L_0 being the initial length), which results directly from the applied uniaxial stress (σ_0) to a particular material.²⁹¹

Creep is an advantageous phenomenon and it is measured over extended periods, however, it is inaccurate for shorter times. Therefore, another method needs to be used to characterize the response for the microstructures. The oscillatory shear motion also called the dynamic loading or small strain oscillatory flow is a dynamic test in which the stress from a sinusoidal strain is measured.²⁹¹ To measure this phenomenon, a plate, in this case, a 4° dynamic cone and a static plate were used. The top plate oscillates at a constant frequency of ω , where $x = \delta \sin \omega t$, the plate velocity will be given by $\Omega = \omega \delta \sin \omega t$. As a result, shear rate and shear stress are defined as:

$$\gamma = \frac{d\gamma}{dt} = \gamma_0 \omega \cos \omega t = \gamma_0 \omega \sin \left(\frac{\pi}{2} + \omega t \right) \quad \text{Equation 12}$$

$$\sigma = \eta\dot{\gamma} = \eta\gamma_0\omega \sin\left(\frac{\pi}{2} + \omega t\right) = \sigma_0\omega \sin\left(\frac{\pi}{2} + \omega t\right) \quad \text{Equation 13}$$

It is evident that the shear stress is out of phase by $\pi/2$. Therefore, we can use the phase shift (δ) as a method to characterize if a material has a purely elastic ($\delta=0$) response or a purely viscous response ($\delta=1$).²⁸⁶

The linear viscoelastic region (LVR), is defined by Starkova *et al.* as the maximum level of stress or strain, independent of time and action of external factors, above which actual behavior deviates 10% from behavior predicted based on linearity assumption.²⁹²

In the LVR, it is possible to define the complex viscosity (η^*) as follows $\eta^* = \eta' + i\eta''$

The part that is in phase with the strain is used to define the storage viscosity (η''), and the part that is in phase with the strain rate is termed dynamic viscosity (η').²⁸⁶

It is possible to relate the storage and dynamic viscosities to the loss (G'') and storage (G') moduli, which are related as:

$G' = \omega\eta''$	Equation	$G'' = \omega\eta'$	Equation
	14		15

These are functions of the frequency, and they are collectively referred to as the *dynamic properties* of the fluid.²⁹³

Appendix B. Iron determination of ferritin hydrogels

Materials:

The reagents $(\text{NH}_4)_2\text{SO}_4 \cdot \text{FeSO}_4 \cdot 6\text{H}_2\text{O}$, hydroxylamine($\text{NH}_2\text{OH} \cdot \text{HCL}$), O-phenanthroline, Acetic acid (CH_3COOH), Ethanol($\text{CH}_3\text{CH}_2\text{OH}$), NaOH were purchased from Sigma-Aldrich (Milwaukee, USA) and used without further purification. Transparent Corning 96-well plate was acquired from Corning (New York, USA)

Iron Calibration Standards:

Accurately weighed 0.05 g of reagent $(\text{NH}_4)_2\text{SO}_4 \cdot \text{FeSO}_4 \cdot 6\text{H}_2\text{O}$ and dissolved in 10 mL of water. An aliquot (1.00 mL) of the latter solution was diluted 10 times to make the standard iron solution of 0.005 g $(\text{NH}_4)_2\text{SO}_4 \cdot \text{FeSO}_4 \cdot 6\text{H}_2\text{O}$ /mL or 0.712 mg Fe /mL.

Acetate Buffer:

A 1M acetate buffer, pH 3 was prepared. To do so, 30.01 mL of acetic acid (CH_3COOH) was measured using a graduated cylinder, dissolved in 450 mL deionized water.

Hydroxylamine hydrochloride solutions:

A 10% hydroxylamine-HCl solution was prepared by weighting on the top-loading balance 1.01 g of hydroxylamine hydrochloride $\text{NH}_2\text{OH} \cdot \text{HCL}$ and dissolving it in 10mL water. Furthermore, A 2.00 ml aliquot of the 10.1% Hydroxylamine-HCl solution was dissolved in 8.00 mL of deionized water to make up for a 2.02% Hydroxylamine-HCl solution.

o-Phenanthroline solution:

A 1.00% o-phenanthroline solution was prepared by accurately weighting 0.1039 g of o-phenanthroline and dissolving it in a 100 mL of a 50% aqueous ethanol solution.

Preparation of Calibration Curve:

To produce the standards a specific quantity of the Fe²⁺ stock solution denoted in the Table 15 was added, followed by 50 µL of hydroxylamine-HCl. Then an adequate amount of 1 M acetate buffer pH 3 was added followed by 500 µL of 1% o-phenanthroline and waited 10 minutes to favor the complete development of the calorimetric complex generated by the Iron-O-Phenanthroline complex. Adjusted final volume 1.00 mL of each solution with water and vortexed to guarantee complete dissolution.

Table 15. Calibration curve for the iron determination in ferritin based hydrogel.

Std.	IronStd (mL)	Hydroxylamine-HCl (mL)	O-Phenanthroline (mL)	Acetate buffer (mL)	Fe Concentration (mg/mL)
1	0.0000	0.05	0.5	0.450	0.0000000
2	0.0050	0.05	0.5	0.445	0.0035597
3	0.0100	0.05	0.5	0.440	0.0071195
4	0.0250	0.05	0.5	0.425	0.0177986
5	0.0500	0.05	0.5	0.400	0.0355973
6	0.1000	0.05	0.5	0.350	0.0711945
7	0.2000	0.05	0.5	0.250	0.1423890
8	0.3000	0.05	0.5	0.150	0.2135835

Absorbance Reading:

To determine the maximum absorption of the iron colorimetric complex, an absorption sweep of different iron concentrations was made, as shown in Figure 57 using

a 96-well plate. It was experimentally determined that the maximum absorption is at 510 nm for the calibration standards, which was used to prepare a calibration curve of concentration of Fe (Beer-Lambert plot) vs absorbance.

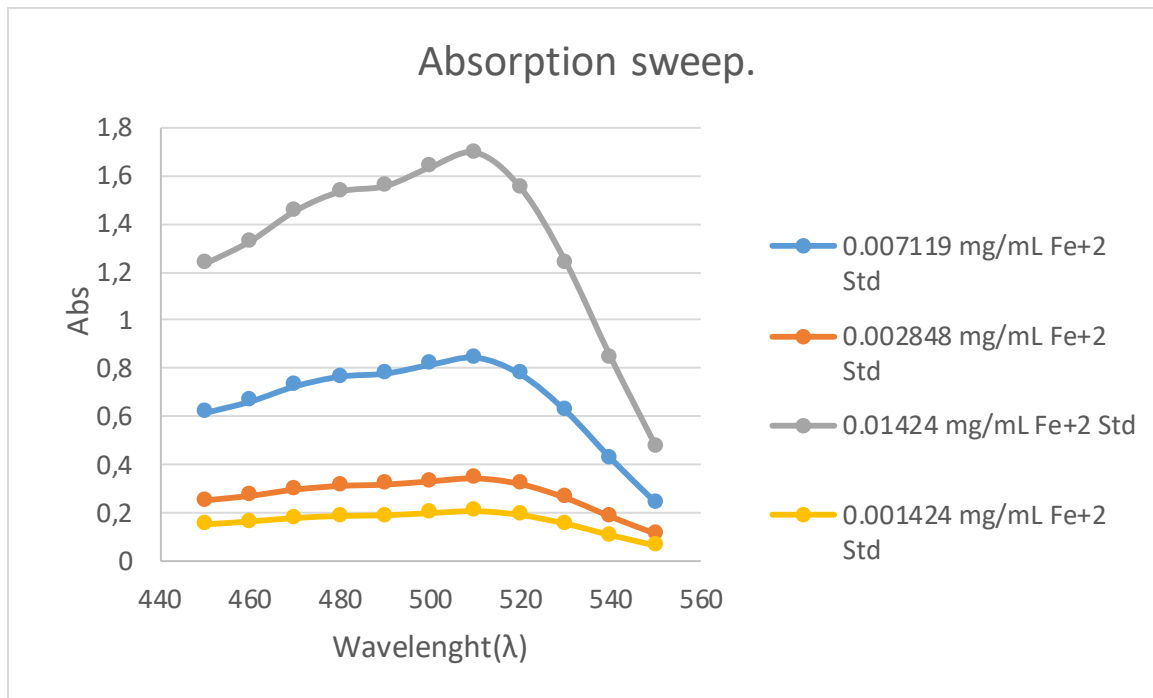


Figure 57. Absorption sweep for the determination of the wavelength of maximum absorption of the Iron-Phenanthroline complex.

All the standards were measured at 510 nm to generate the calibration curve shown in Figure 58. Then calculated the iron concentration of ferritin solution using the generated line equation.

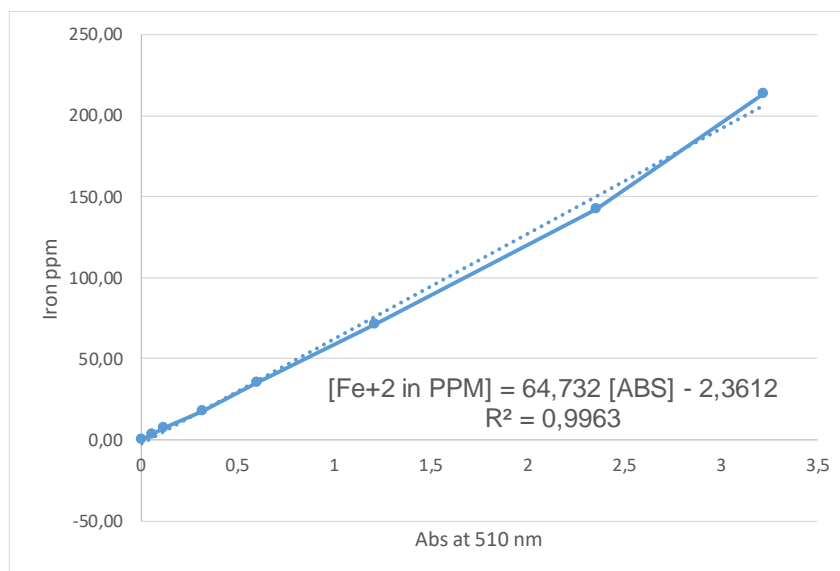


Figure 58. Iron absorbance determination at 510 nm for the Fe²⁺-O-phenanthroline complex.

For further understanding of the results of the colorimetric assay, the F-statistic was determined in Table 16 to demonstrate that the set of values, under the current degrees of freedom, fails the null hypothesis that the dataset follows a zero-slope relationship.

Table 16. Statistical results of linear regression for the iron absorbance determination at 510 nm for the Fe²⁺-O-Phenanthroline complex.

Slope	64.732	-2.361	Intercept
Slope Std. Deviation	1.600	2.391	Intercept Std. Deviation
r ²	0.996	5.084	Std. Error for the y estimate.
F	1636.114	6	degrees of freedom

Appendix C. Bioprinting Conditions

Layer Height
Layer Height: 0.115mm
First Layer Height 0.15mm

Vertical Shells
Perimeters (minimum): 0
Spiral vase: OFF

Horizontal Shells
Solid Layers:
Top: 1
Bottom: 1

Quality (slower slicing)
Extra perimeter if needed ON
Avoid crossing perimeter (slow): OFF
Detect thin walls: ON
Detect bridging perimeters: ON

Advanced
Seam position: Aligned
External perimeters first: OFF

Infill
Fill Density: 100%
Fill Pattern: Concentric
Top/bottom Fill Pattern: Concentric

Reducing Print Time
Combine infill every: 1
Only infill where needed: OFF

Advanced
Solid infill every: 2
Fill angle: 45
Only retract when crossing perimeters: ON
Infill before perimeters: OFF

Speed for Print Moves:
Perimeters: 10
Small perimeters: 3
External perimeters: 3
Infill: 5
Solid infill: 5
Top solid infill: 5
Support material: 3
Support material; interface: 3
Bridges: 3
Gap fill: 3

Speed for non-print moves
Travel: 20

Modifiers:
First layer speed: 85%

Acceleration control (advanced)
Perimeters: 0
Infill: 0

Bridge: 0
First layer: 0
Default: 0

Skirt
Loops: 1
Distance from object: 2
Skirt height: 1
Minimum extrusion length: 0

Brim
Brim width: 0

Support Material
Generate support material: OFF
Overhang threshold: 0
Enforce support for the first: 0

Raft
Raft layers: 0

Options for Support Material and Raft
Pattern: rectilinear
Pattern spacing: 2.5
Pattern angle: 0
Interface layers: 3
Interface pattern spacing: 0
Don't support bridges: ON

Extrusion Width
Default extrusion width: 0
First layer: 200
Perimeters: 0
Infill: 0
Solid infill: 0
Top solid infill: 0
Support material: 0

Flow
Bridge flow ratio: 1

Other
Threads: 2
Resolution: 0

Appendix D. ANOVA for k and n determinations

```
[1] "#####Alginate#####"  
PEGDA 08 PEGDA 12 PEGDA 15 PEGDA 20  
0.57 0.63 0.67 1.08  
[1] "Chi-Sq: 10.0351749229298 |P-Value: 0.981730510018466"
```

```
Call:  
lm(formula = log(y1) ~ x1, data = StatData)
```

```
Residuals:  
Min 1Q Median 3Q Max  
-2.38530 -0.93822 0.03164 0.95535 2.53225
```

```
Coefficients:  
Estimate Std. Error t value Pr(>|t|)  
(Intercept) 0.56884 0.89133 0.638 0.535  
x1PEGDA 12 0.05813 1.26053 0.046 0.964  
x1PEGDA 15 0.10108 1.26053 0.080 0.937  
x1PEGDA 20 0.51023 1.26053 0.405 0.693
```

```
Residual standard error: 1.783 on 12 degrees of freedom  
Multiple R-squared: 0.0167, Adjusted R-squared: -0.2291  
F-statistic: 0.06793 on 3 and 12 DF, p-value: 0.9759
```

```
Tukey multiple comparisons of means  
95% family-wise confidence level
```

```
Fit: aov(formula = m.interaction)
```

```
$x1  
diff lwr upr p adj  
PEGDA 12-PEGDA 08 0.05812896 -3.684253 3.800511 0.9999627  
PEGDA 15-PEGDA 08 0.10108369 -3.641298 3.843466 0.9998041  
PEGDA 20-PEGDA 08 0.51023103 -3.232151 4.252613 0.9765688  
PEGDA 15-PEGDA 12 0.04295473 -3.699427 3.785337 0.9999849  
PEGDA 20-PEGDA 12 0.45210207 -3.290280 4.194484 0.9834351  
PEGDA 20-PEGDA 15 0.40914734 -3.333235 4.151529 0.9875903
```

```
[1] "#####Carboxy_Methyl_Cellulose#####"  
PEGDA 08 PEGDA 12 PEGDA 15 PEGDA 20  
-0.04 -0.04 0.09 0.17  
[1] "Chi-Sq: 18.0093940721518 |P-Value: 0.999562108231058"
```

```
Call:  
lm(formula = log(y1) ~ x1, data = StatData)
```

Residuals:

	Min	1Q	Median	3Q	Max
	-1.27175	-0.57266	0.07817	0.59027	1.17403

Coefficients:

	Estimate	Std. Error	t value	Pr(> t)
(Intercept)	-0.037824	0.505358	-0.075	0.942
x1PEGDA 12	-0.006832	0.714683	-0.010	0.993
x1PEGDA 15	0.131709	0.714683	0.184	0.857
x1PEGDA 20	0.211070	0.714683	0.295	0.773

Residual standard error: 1.011 on 12 degrees of freedom
 Multiple R-squared: 0.01089, Adjusted R-squared: -0.2364
 F-statistic: 0.04402 on 3 and 12 DF, p-value: 0.9871

Tukey multiple comparisons of means
 95% family-wise confidence level

Fit: aov(formula = m.interaction)

\$x1

	diff	lwr	upr	p	adj
PEGDA 12-PEGDA 08	-0.006832232	-2.128657	2.114992	0.9999997	
PEGDA 15-PEGDA 08	0.131708692	-1.990116	2.253533	0.9976523	
PEGDA 20-PEGDA 08	0.211069544	-1.910755	2.332894	0.9905736	
PEGDA 15-PEGDA 12	0.138540923	-1.983284	2.260366	0.9972723	
PEGDA 20-PEGDA 12	0.217901776	-1.903923	2.339726	0.9896557	
PEGDA 20-PEGDA 15	0.079360853	-2.042464	2.201185	0.9994812	

[1] "#####Plurronics_F127#####"
 PEGDA 08 PEGDA 12 PEGDA 15 PEGDA 20
 -3.40 -2.79 -2.80 -2.92

[1] "Chi-Sq: 0.183295240552238 |P-Value: 0.0197601280994389"

Call:

lm(formula = log(y1) ~ x1, data = StatData)

Residuals:

	Min	1Q	Median	3Q	Max
	-0.82112	-0.12399	-0.02297	0.10195	0.51724

Coefficients:

	Estimate	Std. Error	t value	Pr(> t)
(Intercept)	-3.3982	0.1636	-20.777	8.94e-11 ***
x1PEGDA 12	0.6061	0.2313	2.620	0.0224 *

```
x1PEGDA 15 0.6003 0.2313 2.595 0.0234 *
x1PEGDA 20 0.4795 0.2313 2.073 0.0603 .
```

Signif. codes: 0 '***' 0.001 '**' 0.01 '*' 0.05 '.' 0.1 ' ' 1

Residual standard error: 0.3271 on 12 degrees of freedom
Multiple R-squared: 0.4349, Adjusted R-squared: 0.2937
F-statistic: 3.079 on 3 and 12 DF, p-value: 0.06841

Tukey multiple comparisons of means
95% family-wise confidence level

Fit: aov(formula = m.interaction)

\$x1

	diff	lwr	upr	p adj
PEGDA 12-PEGDA 08	0.60613282	-0.08059601	1.2928617	0.0904614
PEGDA 15-PEGDA 08	0.60027337	-0.08645546	1.2870022	0.0943659
PEGDA 20-PEGDA 08	0.47953709	-0.20719174	1.1662659	0.2164090
PEGDA 15-PEGDA 12	-0.00585945	-0.69258829	0.6808694	0.9999938
PEGDA 20-PEGDA 12	-0.12659573	-0.81332457	0.5601331	0.9455111
PEGDA 20-PEGDA 15	-0.12073628	-0.80746512	0.5659926	0.9521579

[1] "#####Xanthan_Gum#####"

PEGDA 08 PEGDA 12 PEGDA 15 PEGDA 20
0.80 0.91 0.93 1.01

[1] "Chi-Sq: 13.8383367224405 |P-Value: 0.99686632959551"

Call:

lm(formula = log(y1) ~ x1, data = StatData)

Residuals:

Min	1Q	Median	3Q	Max
-0.63650	-0.57025	0.07752	0.48048	0.58808

Coefficients:

	Estimate	Std. Error	t value	Pr(> t)
(Intercept)	0.8014	0.3334	2.404	0.0429 *
x1PEGDA 12	0.1073	0.4715	0.228	0.8257
x1PEGDA 15	0.1239	0.4715	0.263	0.7994
x1PEGDA 20	0.2098	0.4715	0.445	0.6681

Signif. codes: 0 '***' 0.001 '**' 0.01 '*' 0.05 '.' 0.1 ' ' 1

Residual standard error: 0.5774 on 8 degrees of freedom
Multiple R-squared: 0.02443, Adjusted R-squared: -0.3414

F-statistic: 0.06679 on 3 and 8 DF, p-value: 0.976

Tukey multiple comparisons of means
95% family-wise confidence level

Fit: aov(formula = m.interaction)

\$x1

	diff	lwr	upr	p adj
PEGDA 12-PEGDA 08	0.10729706	-1.402463	1.617057	0.9955039
PEGDA 15-PEGDA 08	0.12388291	-1.385877	1.633643	0.9931405
PEGDA 20-PEGDA 08	0.20983814	-1.299922	1.719599	0.9687495
PEGDA 15-PEGDA 12	0.01658585	-1.493175	1.526346	0.9999830
PEGDA 20-PEGDA 12	0.10254108	-1.407219	1.612301	0.9960667
PEGDA 20-PEGDA 15	0.08595524	-1.423805	1.595716	0.9976665

Appendix E. ANOVA for detailed declustering studies.

```
[1] "#####0,01 M HCl#####"
```

Call:

```
lm(formula = log(Iron) ~ PEGDA, data = StatData)
```

Residuals:

```
   Min     1Q  Median     3Q    Max
-0.65888 -0.22578  0.05979  0.21049  0.51215
```

Coefficients:

```
      Estimate Std. Error t value Pr(>|t|)
(Intercept)  0.94362   0.14297   6.600 1.98e-06 ***
PEGDA10%    -0.29285   0.20219  -1.448  0.163
PEGDA12%    -0.05522   0.20219  -0.273  0.788
PEGDA14%    -0.26862   0.20219  -1.329  0.199
```

Signif. codes: 0 '***' 0.001 '**' 0.01 '*' 0.05 '.' 0.1 ' ' 1

Residual standard error: 0.3502 on 20 degrees of freedom

Multiple R-squared: 0.1388, Adjusted R-squared: 0.009629

F-statistic: 1.075 on 3 and 20 DF, p-value: 0.3823

Tukey multiple comparisons of means

95% family-wise confidence level

Fit: aov(formula = m.interaction)

\$PEGDA

```
      diff      lwr      upr    p adj
10%-08% -0.29284669 -0.8587574 0.2730640 0.4855213
12%-08% -0.05521505 -0.6211258 0.5106956 0.9926535
14%-08% -0.26862010 -0.8345308 0.2972906 0.5563177
12%-10%  0.23763164 -0.3282791 0.8035423 0.6487628
14%-10%  0.02422660 -0.5416841 0.5901373 0.9993632
14%-12% -0.21340504 -0.7793157 0.3525057 0.7195728
```

```
[1] "#####0,1 M HCl#####"
```

Call:

```
lm(formula = log(Iron) ~ PEGDA, data = StatData)
```

Residuals:

Min	1Q	Median	3Q	Max
-1.1321	-0.4293	0.1387	0.4482	0.7708

Coefficients:

	Estimate	Std. Error	t value	Pr(> t)
(Intercept)	2.54962	0.25775	9.892	3.8e-09 ***
PEGDA10%	-0.07366	0.36451	-0.202	0.842
PEGDA12%	-0.04983	0.36451	-0.137	0.893
PEGDA14%	-0.01083	0.36451	-0.030	0.977

Signif. codes: 0 '***' 0.001 '**' 0.01 '*' 0.05 '.' 0.1 ' ' 1

Residual standard error: 0.6313 on 20 degrees of freedom
Multiple R-squared: 0.002639, Adjusted R-squared: -0.147
F-statistic: 0.01764 on 3 and 20 DF, p-value: 0.9967

Tukey multiple comparisons of means
95% family-wise confidence level

Fit: aov(formula = m.interaction)

\$PEGDA

	diff	lwr	upr	p adj
10%-08%	-0.07366319	-1.0939026	0.9465763	0.9969796
12%-08%	-0.04982608	-1.0700655	0.9704134	0.9990563
14%-08%	-0.01083082	-1.0310703	1.0094086	0.9999902
12%-10%	0.02383711	-0.9964024	1.0440766	0.9998960
14%-10%	0.06283237	-0.9574071	1.0830718	0.9981166
14%-12%	0.03899526	-0.9812442	1.0592347	0.9995462

[1] "#####100 °C in Acetate Buffer 1M, pH 3#####"

Call:

lm(formula = log(iron) ~ PEGDA, data = StatData)

Residuals:

Min	1Q	Median	3Q	Max
-1.2631	-0.4001	0.1445	0.4617	0.6848

Coefficients:

	Estimate	Std. Error	t value	Pr(> t)
(Intercept)	1.1119	0.2582	4.306	0.000344 ***
PEGDA10%	-0.1294	0.3651	-0.354	0.726786
PEGDA12%	0.1353	0.3651	0.370	0.714929

PEGDA14% -0.1772 0.3651 -0.485 0.632732

Signif. codes: 0 '***' 0.001 '**' 0.01 '*' 0.05 '.' 0.1 ' ' 1

Residual standard error: 0.6325 on 20 degrees of freedom
Multiple R-squared: 0.04245, Adjusted R-squared: -0.1012
F-statistic: 0.2955 on 3 and 20 DF, p-value: 0.8282

Tukey multiple comparisons of means
95% family-wise confidence level

Fit: aov(formula = m.interaction)

\$PEGDA

	diff	lwr	upr	p adj
10%-08%	-0.1293901	-1.1514185	0.8926384	0.9842947
12%-08%	0.1352757	-0.8867527	1.1573042	0.9821411
14%-08%	-0.1772096	-1.1992380	0.8448189	0.9614773
12%-10%	0.2646658	-0.7573627	1.2866943	0.8860224
14%-10%	-0.0478195	-1.0698480	0.9742090	0.9991696
14%-12%	-0.3124853	-1.3345138	0.7095432	0.8271647

[1] "#####Acetate Buffer 1M, pH 3#####"

Call:

lm(formula = log(iron) ~ PEGDA, data = StatData)

Residuals:

Min	1Q	Median	3Q	Max
-0.84077	-0.30475	0.05342	0.24224	0.61193

Coefficients:

	Estimate	Std. Error	t value	Pr(> t)
(Intercept)	0.6947943	0.1758473	3.951	0.000789 ***
PEGDA10%	-0.2284415	0.2486856	-0.919	0.369253
PEGDA12%	0.0009927	0.2486856	0.004	0.996855
PEGDA14%	-0.2002024	0.2486856	-0.805	0.430263

Signif. codes: 0 '***' 0.001 '**' 0.01 '*' 0.05 '.' 0.1 ' ' 1

Residual standard error: 0.4307 on 20 degrees of freedom
Multiple R-squared: 0.07, Adjusted R-squared: -0.06951
F-statistic: 0.5018 on 3 and 20 DF, p-value: 0.6854

Tukey multiple comparisons of means
95% family-wise confidence level

Fit: aov(formula = m.interaction)

\$PEGDA

	diff	lwr	upr	p	adj
10%-08%	-0.228441465	-0.9244966	0.4676137	0.7952749	
12%-08%	0.000992661	-0.6950625	0.6970478	1.0000000	
14%-08%	-0.200202381	-0.8962576	0.4958528	0.8512784	
12%-10%	0.229434126	-0.4666211	0.9254893	0.7931795	
14%-10%	0.028239084	-0.6678161	0.7242943	0.9994577	
14%-12%	-0.201195042	-0.8972502	0.4948601	0.8494385	

Appendix F. Iron diffusion from PEGDA-Based hydrogels

Measurement	Thickening Agent*	PEGDA (%)	Protein (%)	Diffusion Coefficient (min⁻² m²)
1	NTA	8%	0.000%	0.00E+00
2	NTA	8%	0.275%	4.80E-11
3	NTA	8%	0.685%	5.35E-11
4	NTA	8%	1.097%	5.59E-11
5	NTA	10%	0.000%	0.00E+00
6	NTA	10%	0.275%	5.10E-11
7	NTA	10%	0.685%	4.74E-11
8	NTA	10%	1.097%	4.74E-11
9	NTA	12%	0.000%	0.00E+00
10	NTA	12%	0.275%	3.59E-11
11	NTA	12%	0.685%	4.60E-11
12	NTA	12%	1.097%	4.36E-11
13	NTA	14%	0.000%	0.00E+00
14	NTA	14%	0.275%	3.57E-11
15	NTA	14%	0.685%	4.16E-11
16	NTA	14%	1.097%	5.44E-11
17	NTA	8%	0.323%	0.00E+00
18	4% XG	8%	0.323%	8.21E-11
19	7% ALG	8%	0.323%	1.08E-10

Measurement	Thickening Agent*	PEGDA (%)	Protein (%)	Diffusion Coefficient (min⁻² m²)
20	10% CMC	8%	0.323%	8.10E-11
21	NTA	10%	0.323%	1.04E-10
22	4% XG	10%	0.323%	1.05E-10
23	7% ALG	10%	0.323%	1.11E-10
24	10% CMC	10%	0.323%	1.07E-10
25	NTA	12%	0.323%	6.49E-11
26	4% XG	12%	0.323%	6.03E-11
27	7% ALG	12%	0.323%	1.72E-10
28	10% CMC	12%	0.323%	5.05E-11
29	NTA	14%	0.323%	1.31E-10
30	4% XG	14%	0.323%	1.25E-10
31	7% ALG	14%	0.323%	1.47E-10
32	10% CMC	14%	0.323%	1.39E-10

*ALG: Alginate. CMC: Carboxymethylcellulose. NTA: No Thickening Agent. XG: Xanthan Gum

Appendix G. Swelling Capacity of Hydrogels determined by TGA.

Type*	PEGDA ⁺	Temperature(°C)	Temperature Standard deviation	Water Volume (%)
ALG	PEGDA 8%	174.45	±35.90	90.94%
	PEGDA 10%	179.67		88.84%
	PEGDA 12%	179.80		89.37%
	PEGDA 14%	249.60		86.87%
CMC	PEGDA 8%	176.36	±6.11	92.99%
	PEGDA 10%	163.64		91.86%
	PEGDA 12%	175.98		90.21%
	PEGDA 14%	175.05		86.53%
NTA	PEGDA 8%	158.86	±54.41	88.82%
	PEGDA 10%	274.09		88.14%
	PEGDA 12%	189.14		85.80%
	PEGDA 14%	255.60		87.04%
XG	PEGDA 8%	192.76	±31.56	92.75%
	PEGDA 10%	249.54		89.27%
	PEGDA 12%	176.83		87.22%
	PEGDA 14%	196.97		83.48%

*ALG: Alginate (7% w/v); CMC:Carboxymethylcellulose (10% w/v); NTA:No thickening agent; XG:Xanthan Gum (3%)

*PEGDA: Poly(ethylene glycol) diacrylate average MW:700

Appendix I. ImageJ Code to analyze porosity SEM images

```
dir = getDirectory("Choose a Directory ");
count = 1;

listFiles(dir);

function listFiles(dir) {
  list = getFileList(dir);
  for (i=0; i<list.length; i++) {
    if (endsWith(list[i], ".tif")){
      listFiles(""+dir+list[i]);
    }else if (endsWith(list[i], ".tif")) {
      print((count++) + ": " + dir + list[i]);
      //Calls the function that iterates over the files
      Porosity(dir,list[i]);
      //print(list[i]);

    }else{
      print("Not what we are looking for");
    }
  }
}

//setBatchMode(false);
cleanUp();
}
```



```
//Check the string to be there to process either 400 or 100 um filesize
function checkForMatches(fragSeq,checkSeq){
  numMatchesFound=0;

  //print("fragSeq="+fragSeq+" checkSeq="+checkSeq);
  if(lengthOf(fragSeq)>lengthOf(checkSeq)){
    return false;
  }
  for(i=0;i<=lengthOf(checkSeq)-lengthOf(fragSeq);i++){
    if(matches(fragSeq,substring(checkSeq,i,i+lengthOf(fragSeq)))){
      numMatchesFound++;
    }
  }
}
```



```

    }
    print(numMatchesFound);
    if(numMatchesFound>0){
        return true;
    }else{
        return false;
    }
}

```

```

function Porosity(dir,Name){

    setBatchMode(true);

    //Define the new variable
    SaveName = substring(Name,0,lengthOf(Name)-4);
    Name=SaveName+".tif";
    Address=dir+Name;

    //Open the filename
    open(Address);

    //Set the scale
    if (checkForMatches("100", SaveName)>0){
        run("Set Scale...", "distance=245.3370 known=3.83 pixel=100 unit=um");
    }else{
        run("Set Scale...", "distance=382.6760 known=5.98 pixel=400 unit=um");
    }

    //Set the measurements
    run("Set Measurements...", "area mean standard min centroid bounding fit shape integrated skewness redirect=None
decimal=3");
    //Set Threshold
    run("Threshold...");
    setThreshold(0, 9000);
    //setAutoThreshold("Default stack");
    run("Convert to Mask");

```

```

//Analyze the particles
run("Analyze Particles...", "size=5-Infinity show=Outlines display include summarize in_situ");
//Save the results
saveAs("Results", dir+SaveName+"-Particles.csv");

//Analyze the distance optional
//run("ND ", "entrada=6");

//Save it on the folder
Location=dir+SaveName+"-Distance.csv";
saveAs("Results",Location);

//Close results window
if (isOpen("Results")) {
    selectWindow("Results");
    run("Close");
}

//Save it as an EPS Image: run("EPS ...", "save=["+dir+SaveName+".eps"+"]");
selectWindow(Name);
run("Input/Output...", "jpeg=100");
saveAs("Jpeg", dir+SaveName+".jpg");

setBatchMode(false);
close();

}

// Closes the "Results" and "Log" windows and all image windows
function cleanUp() {
    // requires("1.30e");
    if (isOpen("Results")) {
        selectWindow("Results");
        run("Close" );
    }
    if (isOpen("Log")) {
        selectWindow("Log");
        run("Close" );
    }
}

```

```
while (nImages()>0) {  
  selectImage(nImages());  
  run("Close");  
}  
}
```

Appendix J. ImageJ Code to analyze confocal images

```
dir = getDirectory("Choose a Directory ");
count = 1;

listFiles(dir);

function listFiles(dir) {
  list = getFileList(dir);
  print(list.length);
  for (i=0; i<list.length; i++) {
    if (endsWith(list[i], ".")){
      listFiles(""+dir+list[i]);
    }else if (endsWith(list[i], ".czi")) {
      print((count++) + ". " + dir + list[i]);
      //Calls the function that iterates over the files
      ConfocalProcessing(dir,list[i]);
      run("Close All");
      print("Done5");
    }else{
      print("Not what we are looking for");
    }
  }
}

//setBatchMode(false);
}

//Define all functions
function ConfocalProcessing(dir,Name){

  setBatchMode(true);

  //Define the new variable
  Name=File.getName(dir+Name);
  dir=replace(dir,"/", "\\");
  print(dir+Name);
  SaveName = substring(Name,0,lengthOf(Name)-4);
  print(SaveName);
  //Name=SaveName+".czi";
  //Define Object Counter Settings//show_numbers white_numbers
```

```
run("3D OC Options", "volume nb_of_obj._voxels integrated_density std_dev_gray_value minimum_gray_value  
close_original_images_while_processing_(saves_memory) dots_size=10 font_size=14 redirect_to=none");
```

```
//Analyze the Data in Object Counter  
run("Bio-Formats", "open=["+dir+Name+"]autoscale color_mode=Default view=Hyperstack stack_order=XYZCT");  
run("3D Objects Counter", "threshold=250 slice=10 min.=10 max.=22020096 exclude_objects_on_edges objects  
statistics");  
saveAs("Results", dir+SaveName+".csv");
```

```
//Stack the Z and add the Scale Bar  
selectWindow("Objects map of"+ " "+ Name);  
run("Scale Bar...", "width=50 height=8 font=28 color=White background=None location=[Lower Right] bold overlay");  
run("Z Project...", "projection=[Max Intensity]");
```

```
//Save it as an EPS Image: run("EPS ...", "save=["+dir+SaveName+".eps"+"]);  
selectWindow("MAX_Objects map of"+ " "+ Name);  
run("Input/Output...", "jpeg=100");  
saveAs("Jpeg", dir+SaveName+".jpg");  
print("DONE");
```

```
//Close results window  
if (isOpen("Results")) {  
    selectWindow("Results");  
    run("Close");  
}
```

```
//Give me the zstacks of cell distribution  
selectWindow("Objects map of"+ " "+ Name);
```

```
//Z stack  
run("Plot Z-axis Profile");
```

```
//Open a file and store it  
selectWindow("Objects map of"+ " "+ Name+"-0-0");
```

```
//Open a file and store it  
Plot.getValues(x, y);  
//Loads the results on the tables  
for (i=0; i<x.length; i++)  
    setResult("Microns", i, x[i]);
```

```
for (i=0; i<y.length; i++)
  setResult("Mean", i, y[i]);
print("DONE2");
//Save it on the folder
Location=dir+SaveName+"-Plot Values.csv";
saveAs("Results",Location);
print("DONE3");

setBatchMode(false);
}
```